



OWL Instrument Concept Study

T-OWL

Thermal Infrared Instrument for OWL

PI: Rainer Lenzen

Co-PI: Bernhard Brandl



Version 1 (20. October 2005)

Document No.: OWL-CSR-ESO-00000-0161



T-OWL Concept Level Study

Doc : OWL-CSR-ESO-00000-0161



Version 1
Date: 20/10/2005
Page: 2/175

Document change record

Issue	Date		Sec./Paragr. affected	Reasons/Remarks
Version 1.0	22/09/05			First version
Version 1.1	26.9.2005		p21	Contributor deleted
	“		Tab. 3	Values corrected
	“		all	Type errors
	04/10/05		p47	New chapter
	“		p57	Sensitivity new
			Table 3	Min. Telescope diameters
	05/10/05		P63	New chapter
Version 1.2	10/10/05		All	Div typing errors
	“		p17	Reference completed
	“		p143	Table completed
	“		P159	Sentence added
	“		P171	Wording changed
	“		p29	Double sentence erased
Version 1	20/10/05			ESO revision # rounding



T-OWL Concept Level Study

Doc : OWL-CSR-ESO-00000-0161



Version 1
Date: 20/10/2005
Page: 3/175

Table of Contents

1 APPLICABLE AND REFERENCE DOCUMENTS	15
1.1 Applicable Documents.....	15
1.2 Reference Documents.....	15
2 ACRONYMS	19
3 CONTRIBUTORS	20
3.1 Section authors.....	20
3.2 Main contributors to the technical part of this study are: (in alphabetical order).....	20
3.3 Additional contributors: (in alphabetical order)	20
4 SUMMARY	22
5 SCIENCE DRIVERS	23
5.1 Solar System.....	23
5.1.1 Seismology of the Giant Planets.....	23
5.1.2 Cold Volcanism in the Outer Solar System: Triton and the Kuiper Belt.....	25
5.1.3 Comets and the Ice and Dust Composition in the Outer Solar System.....	26
5.2 Exo-Planets.....	29
5.2.1 EPICS Follow-Up.....	29
5.3 Proto-Planetary Disks.....	31
5.3.1 Signatures of Planet Formation.....	31
5.3.2 Evolution of Dust Grains.....	34
5.3.3 Chemical Evolution of Gas in Disks.....	36
5.3.4 Organic Molecules in the Planet-Forming Zones.....	39
5.4 Proto-Stars.....	42
5.5 The Galactic Center.....	43
5.6 The IMF in Star-Bursts.....	46
5.6.1 Dynamical Masses of Super Star Clusters.....	47
5.6.2 Star-burst modelling.....	49
5.7 Active Galactic Nuclei at Low Redshift.....	50
5.8 Ultra-Luminous IR Galaxies (ULIRGs).....	53
5.9 Active Galactic Nuclei at High Redshift.....	56
5.10 Gamma-Ray Bursts.....	59



T-OWL Concept Level Study

Doc : OWL-CSR-ESO-00000-0161



Version 1
Date: 20/10/2005
Page: 4/175

5.11 Summary of the Science Requirements.....	61
5.11.1 Conclusions Concerning Aperture Diameter	61
5.11.2 Conclusions Concerning T-OWL Capabilities	61
6 STUDY OF SEEING / AO REQUIREMENTS	64
6.1 Chromatic Atmospheric Effects	64
6.2 Strehl Ratio.....	66
6.3 Isoplanatic Patch	68
7 DETAILED BEST EFFORT CALCULATIONS OF PERFORMANCE	69
7.1 Instrumental Background.....	69
7.2 Atmospheric Transmission.....	69
7.3 Atmospheric Emission.....	71
7.3.1 Atmospheric Background for BB Imaging	71
7.3.2 Atmospheric Background for Spectroscopy.....	72
7.4 Atmospheric Dispersion.....	73
7.5 Instrumental Polarization.....	74
8 T-OWL SENSITIVITY	76
8.1 Preface: Point Source Versus Extended Source Sensitivity.....	76
8.2 Imager Sensitivity.....	76
8.3 Spectrograph Sensitivity.....	77
8.3.1 Introduction.....	77
8.3.2 Low Resolution R=300 Spectrograph	80
8.3.3 Medium Resolution R = 3000 Spectrograph.....	82
8.3.4 High Resolution R = 50000 Spectrograph.....	84
8.3.5 Conclusions.....	86
9 COMPARISON TO GROUND BASED FACILITIES AND SPACE MISSIONS.....	89
9.1 Mid Infrared Instrumentation at 8m-Class Telescopes.....	89
9.2 Expected Contemporaries of T-OWL.....	90
9.2.1 Introduction	90
9.2.2 James Web Space Telescope.....	90
9.2.3 SAFIR.....	93
9.2.4 ALMA.....	94
9.2.5 Darwin.....	94
9.2.6 VLTI.....	94
9.2.7 WISE	94
9.2.8 Summary.....	98
10 SCOPE OF THE IDEAL INSTRUMENT.....	98



T-OWL Concept Level Study

Doc : OWL-CSR-ESO-00000-0161



Version 1
Date: 20/10/2005
Page: 5/175

10.1 Wavelength Range	98
10.2 Imaging Mode	98
10.2.1 Pixel Scale.....	98
10.2.2 Chronagraphy.....	100
10.2.3 Pupil Masking.....	100
10.2.4 Low Resolution Spectroscopy.....	100
10.3 Spectroscopic Mode	100
10.3.1 General Spectroscopic Concept (Spectral Modes).....	100
10.3.2 IFU Versus Long-slit	101
10.3.3 Atmospheric Windows.....	102
10.3.4 Efficiency Considerations.....	102
10.3.5 Spatial Sampling.....	105
10.4 Use of the Instrument with an Incomplete M1.....	107
10.4.1 PSF of Progressively Filled Aperture	107
10.4.2 PS Sensitivity for a Progressively Filled Aperture	111
11 OBSERVATIONAL TECHNICALITIES.....	112
11.1 Field- and Pupil Rotation.....	112
11.1.1 Instrumental De-Rotation.....	113
11.1.2 Detector De-Rotation.....	113
11.1.3 Optical De-Rotation.....	113
11.1.4 De-Rotation by Post-Processing.....	113
11.2 Chopping	114
12 INSTRUMENT CONCEPT DESIGN	115
12.1 Top Level Requirements.....	115
12.2 General Concept Considerations.....	115
12.3 General Instrument Concept in Optical Train.....	119
12.4 Imager Design Details.....	123
12.4.1 Optical Design of the Imager.....	123
12.4.2 Entrance Window.....	126
12.4.3 Tunable Atmospheric Dispersion Corrector (TADC).....	128
12.4.4 Filters.....	131
12.4.5 Dispersive Elements.....	133
12.4.6 Detector.....	134
12.4.7 Wave Front Sensor.....	137
12.5 Spectrograph Design Details.....	138
12.5.1 Spectrometer Concept.....	138
12.5.2 IFU.....	138
12.5.3 Medium Resolution Spectrometer.....	140
12.5.4 HR Spectroscopy.....	143
12.5.5 Dichroic Separation.....	152
12.5.6 Opto-Mechanical Design.....	153
12.5.7 Parallel Observing Modes.....	156
12.5.8 General Observation Issues.....	156
12.6 Cryo-Mechanical Concept.....	157



T-OWL Concept Level Study

Doc : OWL-CSR-ESO-00000-0161



Version 1
Date: 20/10/2005
Page: 6/175

12.6.1 Packing of the Whole Instrument	157
12.6.2 Imager Cooling Requirements.....	157
12.6.3 Thermal Consideration for Spectrometer.....	158
12.6.4 Motor Drives.....	160
12.6.5 Minimizing Flexure Effects.....	160
13 DATA RATES.....	160
13.1 Data Rates for the Imager.....	160
13.2 Data Rates for the Spectrograph.....	160
14 CALIBRATION: SKETCH OF REQUIREMENTS AND SOLUTIONS.....	161
14.1 Introduction.....	161
14.2 Background Subtraction.....	161
14.3 Flat Fielding.....	163
14.4 Photometric Calibration.....	164
14.5 PSF Calibration.....	164
14.6 Spectroscopic Calibration.....	164
14.6.1 Wavelength Calibration.....	164
14.6.2 PSF Calibration.....	164
14.6.3 Flux Calibration and Flat-Fielding.....	165
15 CONCLUSIONS.....	166
15.1 Consistency with OWL Interface Document.....	166
15.2 Main Design Conclusions.....	167
15.3 Schedule.....	167
15.4 Weight of MIR Imaging Instrument	168
15.5 Budget for MIR Imager and Spectrograph.....	169
16 IMPORTANT ASPECTS FOR MORE FUTURE RESEARCH.....	171
17 APPENDIX A: OPTICAL MATERIAL DATA.....	172

Table of Figures

Fig. 1: Schematics of the inner structure of Jupiter.....	24
Fig. 2: Penetration of seismic wave through Jupiter.....	24
Fig. 3: Geysier vents on Neptune's moon Triton.....	26
Fig. 4: Dust Plume, created by the artificial cratering experiment "Deep Impact" on July 4th, 2005 as seen from the fly-by spacecraft ~15min after fly-by. For comparison the PSF of T-OWL at 3.5 μm is indicated. It is obvious that T-OWL would have been capable to spatially resolve the nucleus and the dust ejecta.....	27
Fig. 5: Volatile primordial ices in Comet Hale-Bopp.	29
Fig. 6: Dust mineralogy in Comet C/2001Q4 (NEAT) (Wooden et al. 2004) shows thermal emission models compared with observed spectra of Comet C/2001Q4 (NEAT). (a)2004 May 11.25, (b) 2004 May 11.30. Five minerals are modelled: amorphous carbon (dashed line), amorphous pyroxene (thin solid line), amorphous olivine (long-dashed – dotted line), crystalline olivine (dotted line), crystalline ortho-pyroxene dashed-dotted line). The thick-solid line shows the fit of the mineralogical mixing model to the observations.	29
Fig. 7: Simulated detectability of a nearby solar system with T-OWL	30
Fig. 8: Response of a gaseous disk to an embedded planet. [Wolf 2001 (data from W. Kley)].....	32
Fig. 9: Simulations of the re-emitted light at 10 microns, assuming an undisturbed disk and a disk with a hole with a radius of 2AU and 4 AU, respectively, convolved with the 100m-OWL point spread function. The star is assumed to be a Herbig Ae star at 140pc with $T=10,000\text{K}$, and $L=46L_{\odot}$; the disk parameters are those of the Butterfly star (Wolf, Padget, & Stapelfeldt 2003; flared disk, Shakura-Sunyaev type; disk mass: 0.01 M_{\odot}), but with a smaller radius of 100AU. The dust properties in terms of grain size distribution and chemical composition are those of typical interstellar medium dust. The simulated region corresponds to 60 AU x 60 AU.....	33
Fig. 10: Simulated radial brightness profile of the configuration shown in the previous Figure. For simplicity, only the case of an inclination $i=0$ is considered here. However, since T-OWL provides full u-v-plane coverage instantaneously (as opposite to e.g. VLTI) this will be most important for inclinations where the disk is not face-on.....	34
Fig. 11: Continuum-subtracted 10 μm silicate emission bands observed toward a selected sample of isolated Herbig Ae stars with ISO-SWS. For reference, the silicate bands of interstellar medium dust and comet C/1995 O1 Hale-Bopp are included. The dotted line indicates the position of the 9.8 μm amorphous silicate band observed in the interstellar medium. The solid lines indicate the best-fit models using a mixture of amorphous and crystalline material with different grain sizes. The sharp 11.3 μm feature is evidence for crystallization, the shift toward longer wavelengths hints grain growth (Bouwman et al. 2001).....	35
Fig. 12: CO $v=1-0$ line profiles at 4.7 mm obtained with Keck-NIRSPEC at $R=25,000$, produced by averaging over all low-J levels (left panels) and high-J levels (right panels). The green lines represent disk model fits to the data (Blake & Boogert 2004). T-OWL can both spatially and spectrally resolve the CO emission.....	37
Fig. 13: Spitzer-IRS spectrum at $R=600$ toward the edge-on disk IRS46 in Oph (Lahius et al. 2005).	40

Fig. 14: ISO-SWS spectrum of the Herbig Ae/Be star HD 97048. The strength of the various PAH emission features – predominantly those at 3.3, 6.2, 7.6, 7.8 and 8.6 μ m – makes them important diagnostics tool (van Kerckhoven et al. 2002). The features at 3.3 and 8.6 μ m are easily observable from the ground. 41

Fig. 15: Rotational diagrams of CO molecules in the hot cores in massive star forming regions. Multiple line observation works as a thermometer (Goto 2005)..... 42

Fig. 16: The Galactic Center: Color composite using filters centered at 8.6 μ m (coded blue), 12.8 μ m (coded green) and 19.5 μ m (coded red). Each pixel subtends 0.127 arcsec and the total field of view is ~ 33 x 33 arcsec (North at the top and East to the left). Total integration times were 300, 160 and 300s for the 3 filters, respectively..... 43

Fig. 17: Broad band spectrum of Sgr A* produced by a jet model, with a power-law(PL) and a relativistic Maxwellian (MW) electron distribution, compared to radio and IR observations (From F. Melia and H. Falcke, 2001) 44

Fig. 18. Today’s highest spatial resolution SED of the nucleus of NGC 1068, based on NACO, MIDI and VLBA data (crosses). X-ray data from Chandra and EXOSAT is also included. The effect of large-aperture data is illustrated with the tick-line which outlines extracted nuclear fluxes from HST/NICMOS, ISO and IRAS. Diamonds are Keck mid-IR nuclear fluxes extracted from deconvolved images. Compilation by A. Prieto..... 45

Fig. 19: Spitzer-IRAC colour composite of the 3.6 μ m, 4.5 μ m, and 8 μ m filter bands..... 47

Fig. 20: HST-WFPC2 image (below) and a larger scale DSS image showing the tales that gave it its nickname..... 47

Fig. 21: HST/NICMOS image of R136 re-binned by factors of two (from left to right: x2, x4, x8) to simulate greater distances (Brandl et al. 2004). 48

Fig. 22: The core radius derived by a simple Gaussian fit to the cluster at a given “distance”..... 48

Fig. 23: The [Ne III]/[Ne II] line ratio as a function of infrared luminosity for a large variety of sources as measured by the ISO-SWS (Thornley et al. 2000)..... 50

Fig. 24: The relevant length scales of structures around an AGN (from Robson 1996, Fig. 9.9).... 51

Fig. 25: VISIR map of NGC 1068 in the [Ne II] line..... 52

Fig. 26: Spatially integrated VLTI/MIDI N-band spectrum of the nuclear region of NGC 1068 (Jaffe et al. 2004)..... 53

Fig. 27: VLTI/MIDI N-band spectrum of the very center of NGC 1068 (Jaffe et al. 2004)..... 53

Fig. 28: A zoom-in on the nuclear region of the nearest ULIRG, Arp220. At a resolution of 0.02”, the detailed structure of the central power source can be resolved..... 54

Fig. 29: [Ne II] velocity map of the starburst/Seyfert galaxy NGC 7582, taken with VLT/VISIR in HR mode (Wold et al. 2005)..... 55

Fig. 30: K-band spectra of typical AGN, including NGC 1068 on the top (adapted from Reunanen et al. 2003). The coronal lines [Si VI]1.6 μ m and [Si VII]2.4 μ m are the strongest lines in these spectra. These lines shift into the 10–20 μ m range for $z > 4$ 57

Fig. 31: Illustration of the detectability of the strongest coronal lines within the atmospheric windows for a wide range in redshift. The atmospheric windows are the ones listed in Tab. 13. 58

Fig. 32: GRB flux density as a function of redshift for different observing wavelengths and times after the burst started (Ciardi & Loeb 2000)..... 60

Fig. 33: GRB number counts as a function of flux density for different observing wavelengths (Ciardi & Loeb 2000).....	60
Fig. 34 Model spectra of C ₂ H ₂ at 900K and HCN at 600K (assumed Doppler broadening ~4km/s) at a resolutions of R=2000 (Fig. provided by F. Lahuis).	63
Fig. 35: Model spectra of C ₂ H ₂ at 900K and HCN at 600K (assumed Doppler broadening ~4km/s) at a resolutions of R=50000 (Figure provided by F. Lahuis).	63
Fig. 36: Schematic ray path to demonstrate chromatic atmospheric effect.....	66
Fig. 37: Strehl ratio versus wavelength assuming a Fried parameter of 20cm at 0.5μm. This wavelength dependence is given for different numbers of actuators N. To reach the goal of 20% SR at 0.5μm, at least 10000 actuators are required.	67
Fig. 38: Atmospheric transmission from 1 to 6 μm at mid-latitude in summer and winter time for a moderate elevation of 2km.....	70
Fig. 39: Atmospheric transmission from 7 to 27μm at mid-latitude in summer and winter time for a moderate elevation of 2km.....	70
Fig. 40: Variation of 20-30μm atmospheric transmission with elevation of observing site, Zenith mid-latitude winter standard model.	71
Fig. 42: Atmospheric radiance at mid-latitude in summer and winter time for the 5 to 30μm region. Observatory height of 3500m is assumed.	72
Fig. 43: Atmospheric refractivity versus wavelength. The blue graph represents the data given in Mathar (2004), the red one is the generally accepted (Joint Commission for Spectroscopy 1952) one as represented by Edlén's formula given in Edlén (1953) (for details see text).	73
Fig. 44: Instrumental polarization produced by M6 (20deg incidence angle) for pure silver coating. Polarization for protected silver coating will be somewhat higher, however significantly depending on the materials used for over-coating.	74
Fig. 45: Point source sensitivity of a 100m-telescope under medium atmospheric conditions (typical for Paranal).	76
Fig. 46 – 10-σ continuum point source sensitivity in L and M-band at R = 300 for one hour wall clock observing time.....	81
Fig. 47 – 10-σ continuum point source sensitivity in N-band at R = 300 for one hour wall clock observing time.....	81
Fig. 48 – 10-σ continuum point source sensitivity in Q-band at R = 300 for one hour wall clock observing time.....	82
Fig. 49 – 10-σ continuum sensitivity to a point source in LM-band at R = 3000 within one hour wall clock time.....	82
Fig. 50 – 10-σ line sensitivity to a point source in LM-band at R = 3000 within one hour wall clock time.....	83
Fig. 51 – 10-σ continuum point source sensitivity in N-band at R = 3000 within one hour wall clock time.....	83
Fig. 52 – 10-σ line sensitivity to a point source in N-band at R = 3000 within one hour wall clock time.....	83
Fig. 53 – 10-σ continuum point source sensitivity in Q-band at R = 3000 within one hour wall clock time.....	84

Fig. 54 – 10- σ line sensitivity to a point source in Q-band at R = 3000 within one hour wall clock time.....	84
Fig. 55 – 10- σ line sensitivity to a point source around the Br- α line (4.05 μ m) in L-band at R = 50000 within one hour wall clock time.....	85
Fig. 56 – 10- σ line sensitivity to a point source around the [Ar III] line (8.99 μ m) in N-band at R = 50000 within one hour wall clock time.....	85
Fig. 57 – 10- σ line sensitivity to a point source around the [Ne II] line (12.81 μ m) in N-band at R = 50000 within one hour wall clock time.....	85
Fig. 58 – 10- σ line sensitivity to a point source in the short wavelength part of the Q-band at R = 25000 within one hour wall clock time. Numerous spectral features, such as the H ₂ S(1) line, fall into windows of good atmospheric transmission and can be observed at unsurpassed sensitivity.	86
Fig. 59 – 10- σ line sensitivity to a point source around the H ₂ S(1) line (17.03 μ m) in Q-band at R = 25000 within one hour wall clock time.....	86
Fig. 60 – Impact of the telescope aperture size on the N-band line sensitivity (10 σ in 1hr) at R=3000.	87
Fig. 61 – Comparison of the line sensitivity between existing and future T-OWL spectrograph “competitors” (courtesy Alistair Glasse).	88
Fig. 62: JWST placative description.....	90
Fig.63: JWST MIRI Optical Module.....	91
Fig. 64: Sensitivity of WISE	95
Fig. 65: Comparison of point source detectivity of contemporary IR and sub-millimeter instrumentations to a MIR instrumentation at OWL.	96
Fig. 66: Comparison of spatial resolution of contemporary IR to sub-millimeter projects to MIR-instrumentation at OWL.	96
Fig. 67: Comparison of point-source detectivity versus spatial resolution of IR to sub-millimeter contemporaries to an OWL MIR-instrument.....	97
Fig. 68: Comparison of possible field of observational capabilities of T-OWL compared to those of JWST/MIRI and Spitzer.	97
Fig. 69: Over-sampling rate (compared to Nyquist sampling) for 3mas (respectively 6mas) pixel size within the 1-5 μ m (respectively 7-25 μ m) region.	99
Fig. 70: As example, the Airy pattern broadening with wavelength for JWST compared to a slice width of 0.2 arcsecond.....	103
Fig. 71: The recovery of lost light as function of oversizing in the post slice optics for the slice of Fig. 70.....	103
Fig. 72: The efficiency loss as function of slice width for various degrees of oversizing.....	104
Fig. 73: The dependence of spatial resolution elements as function of wavelength for a 100 meter telescope (solid black line). The sampling in spectral direction by the slices (coloured lines), and the proposed spatial sampling by 1.5* λ min*D (dots).....	106
Fig. 74: PSF of OWL at 10 μ m, broad band R=10, 2arcsec x 2 arcsec), completely filled M1 and M2.	108

Fig. 75: 10 μ m point spread function of OWL during progressive filling of aperture: top row one year after start of mirror mounting, lower row final configuration. First column: filling from margin to center. Second column: filling from center to margin. Third column: Starting with 100m x100m cross. Image size is 2 x 2 arcsec. 109

Fig. 76: Comparison of PSF for a continuously growing M1 filling from margin to center)..... 110

Fig. 77: Comparison of PSF for a continuously growing M1 filled from center to margin (see text).
..... 110

Fig. 78: Comparison of PSF for different filling models after one year (see text). 111

Fig. 79: Comparison of PSF for different filling modes after two years (see text). 111

Fig. 80: Maximum (at meridian) field rotation versus declination for Paranal. 112

Fig. 81: Schematic showing conflicts between versatility, complexity, cost and mass limitation, reliability and scientific requirements. 116

Fig.82: Comparison of multi-optics design to the monolithic design. The same FOV is shown in similar scale. 118

..... 119

..... 119

..... 119

Fig.83: Schematic overview of the CONICA-approach: The first collimated beam is used for all analysing optics, including spectroscopy. Advantage: Very compact overall design, optics completely common for imaging and spectroscopic mode. No trade-offs for imaging mode. Disadvantage: Pupil-stop identical to grating/grism-position. No separate pixel scale optimization, spectroscopic resolution is limited. 119

Fig. 84: VISIR approach: the detectors are not shared between imager and spectrograph; this could indeed be an advantage of the design if there were different detectors to pick from..... 120

..... 120

Fig. 85: The SUBARU-Approach: Cold fore-optics, common detector for slit-viewer and imaging mode, separate detector for spectroscopy. Advantage: Imager used as slit-viewer. Pre-optics until slit position is common. Disadvantage: Two detectors required (slit-viewer detector not optimized), additional re-imaging optics in imaging mode. 121

Fig. 86: Proposed T-OWL approach: Common pre-optics including entrance window, cold pupil stop, chopper, ADC and de-rotator(if required) within a common cryostat, however, imaging and spectroscopic instrument are entirely separated, additional detectors are required. 122

Fig. 87: Pure reflective imaging optics of the T-OWL Imager, attached to the telescope. 123

Fig. 88: Conceptual optical design of the T-OWL imager. 124

Fig. 89: Image quality of T-OWL-imager: Strehl ratio for different field positions versus wavelength
..... 125

Fig. 90: Pupil image quality (cryogenic pupil)..... 125

Fig. 91: T-OWL imager with low resolution grism..... 126

Fig. 92: Schematic distribution of entrance windows 128

Fig. 93: Residual atmospheric dispersion effects using optimized TADC concepts of different material combinations (two components, 2-5 μ m region). Zenith distance of 60 deg, atmospheric temperature 293K, 1013mbar (ground layer).	129
Fig. 94: As an example, one TIR TADC double wedge plate of the TADC is shown (CsBr/Amtir1)	130
Fig. 95: MIR filter set proposed for VISIR by the VAFC (see webpage given above)	131
Fig. 96: Spectral distribution over the chip for proposed grisms.	133
Fig. 97: Historical development of pixel sizes for optical and infrared detector arrays.	134
Fig. 98: General lay-out of the spectrometer.....	138
Fig. 99: Schematic representation of the pre-optics for the spectrometers.....	140
Fig. 100: Global design parameters for the medium resolution spectrometer channels.....	141
Fig. 101: The wavelength coverage in the four channels with their different exposures.....	143
Fig. 102: The change of the resolution for different wavelength in the four spectrometer channels.	143
Fig. 103: Mapping of information in N-band channels on the detectors. The Decker mask can be changed to block the outer IFU slices, to free two detectors for cross-dispersion. "Common" refers to common to both MR and HR mode. Blue refers to HR mode, red to MR mode.....	145
Fig. 104: Estimate of the beam parameters for the high resolution N-band spectroscopy, scaled version from VISIR.....	145
Fig. 105: Echelle mode and cross dispersion for the N-band.....	147
Fig. 106: Possible optical design for the HR spectroscopy.....	148
Fig. 107: Spectral coverage of the HR-mode for the N-band. Full coverage with 16 exposures. Still unequal overlap in SW and LW channels. Can be further optimized with additional fine tuning..	148
Fig. 108: Resolution drop within the N-band channels.....	148
Fig. 109: Echelle mode and cross dispersion for the Q-band.....	149
Fig. 110: Spectral coverage of the HR-mode for the Q-band. Full coverage within 8 exposures..	150
Fig. 111: Mapping of information in Q-band on detector. The Decker mask can be changed to block the outer IFU slices, to free three quarters of the two detectors for the cross-dispersion orders.....	150
Fig. 112: Echelle mode and dispersion parameters for the L+M-band.....	151
Fig. 113: Paraxial design of the Q-band spectrometer.....	154
Fig. 114: Optical design for the Q-band channel camera.....	155
Fig. 115: Spot diagrams for the Q-band channel camera.....	155
Fig. 116: Packaging the whole T-OWL in one cryostat.....	157
Fig. 117 – Ratio between thermal background from within the cryostat (internal) to the background from atmosphere and telescope (sky) as a function of wavelength for the high resolution spectrograph (R=70000 at 7 μ m).....	159
Fig. 118: Transmission of AgCl	172
Fig. 119: External transmission of 10mm CsBr	172



T-OWL Concept Level Study

Doc : OWL-CSR-ESO-00000-0161



Version 1
Date: 20/10/2005
Page: 13/175

Fig. 120: External transmission of 5mm CsI.....	173
Fig. 121: External transmission of 1mm CVD Diamond	173
Fig 122: Transmission of KBr.....	174
Fig. 123: External transmission of KRS5	174
Fig. 124: External transmission of ZnSe.	175
Fig. 125: Reflectivity of JANOS gold coating.....	175

List of Tables

Table 1: Techniques used as probes of gas and dust in disks.	36
Table 2 The main spectral diagnostics for star-bursts in the L, M, N and Q bands.....	49
Table 3: Summary of scientific requirements on a TIR/MIR instrument for OWL.	62
Table 4: Expected Strehl ratio for TIR and MIR bands extrapolated from a given Strehl ratio at 0.5 μ m	67
Table 5: Instrumental Background conditions.....	69
Table 6: Background flux for broad band applications.	71
Table 7 Parameters used in the spreadsheet for the spectrograph sensitivity calculations.....	77
Table 8: Observational capabilities of MIR-instrumentations at existing 8m-class telescopes	89
Table 9: Sensitivity estimates for the MIRI Imager and Spectrometer.....	93
Table 10: Comparison of the main MIR competitors of T-OWL.....	95
Table 11: F-ratio of re-imaging beam required for Nyquist sampling at different wavelengths and for three most common pixel sizes. Most favourable combinations are highlighted in yellow.	99
Table 12: Top level technical requirements for the spectrometer.....	101
Table 13: Spectral ranges.....	102
Table 14: Spectral ranges that should be covered by T-OWL.....	104
Table 15: Effect of angular resolution on required number of detectors for full spatial sampling of an 1*1 square arcsec FOV.....	105
Table 16: Advantages (and disadvantages) of the multi-optics concept.	117
Table 17: Window materials for the thermal and mid-infrared wavelength region, materials useful beyond 25 μ m are high-lighted (grey).	127
Table 18: List of proposed filters.....	132
Table 19: Main parameters of proposed Grisms.....	133
Table 20: List of available TIR and MIR detector arrays.....	137
Table 21: Slicing and sampling parameters.....	139
Table 22: Details for the different exposures in all channels and the grating parameters.....	142
Table 23: Overview of the HR spectrometer parameters.....	152
Table 24: Dichroic scheme from the MR spectrograph.....	153
Table 25: List of proposed dichroics.....	153
Table 26: Chopping frequency measurements with the AAT in New South Wales (Allen 1981) and at La Silla (Käufl 1991). A wavelength dependence is clearly visible.....	161
Table 27 Dependence of the chopping frequency from the telescope diameter.....	162
Table 28: List of consistencies with OWL interface document.....	166
Table 29: Estimated mass of T-OWL.....	168
Table 30: Hard-ware cost break down for T-OWL.....	170

1 Applicable and Reference Documents

1.1 Applicable Documents

- (1) OWL Telescope-Instruments Interface Control Document, ESO internal document, ref. OWL-CSR-00000-0139, 30 September 2004-10-05
- (2) OWL Instrumentation: Technical Specification and Statement of Work, OWL-SPE-ESO-00000-0151, Nov19, 2004-12-09
- (3) Framework of OWL instrument concept design studies, OWL-CSR-ESO-00000-0147, Vers. 24.09.2004

1.2 Reference Documents

- (1) A'Hearn, M., Space Science Reviews, Volume 117, Issue 1-2, pp. 1-21
- (2) Allen D. et al. "A study of sky noise", 1.5um - 5um; PASP 93:381-384, 1981
Alonso-Herrero et al. 2004, AJ 126, 81
- (3) G. Avila, G. Rupprecht, J.M. Beckers, "Atmospheric dispersion Correction for the FORS Focal Reducers at the ESO VLT", SPIE Vol 2871, p1135 (2001)
- (4) A. Ardeberg, "Diffraction-limited light collection: promises and challenges of a 50-m ELT", SPIE 5489 p23 (2004)
- (5) A. Ardeberg, P. Linde, "Evolution of distant galaxies from cluster photometry: a program for a 50-m ELT", SPIE 5489, p72 (2004)
- (6) Aristidi E. et al "Site testing study based on weather balloons measurements"; (in preparation)
- (7) Bezawada, N., Ives, D., "Characterization of VISTA IR detectors", SPIE 5499, p23 (2004)
- (8) Bouwman, J., Meeus, G., de Koter, A., et al., A&A, 375, 950 (2001)
- (9) E. Brunetto et al., "Progress of ESO's 100-m OWL optical telescope design", Proc. 2nd Bäckaskog Workshop on ELTs (2004)
- (10) Colavita, M. Mark; Swain, Mark R.; Akeson, Rachel L.; Koresko, Christopher D.; "Effects of Atmospheric Water Vapor on Infrared Interferometry", PASP 116,876 (2004)
- (11) Dierickx, P., Brunetto, E.T., Comeron, F., Gilmozzi, R., Gonté, F.Y.J., Koch, F., le Louarn, M., Monnet, G.J., Spyromilio, J. Surdej, I., Verinaud, Ch., Yaitskova, N., "OWL phase A status report", SPIE 5489, p391 (2004)
- (12) Dutta, S.I., Hall Reno, M., Sarcevic, I., "Black hole detection with the OWL-Airwatch telescope", Phys. Rev. Dvol. 66, issue 3, 2002



T-OWL Concept Level Study

Doc : OWL-CSR-ESO-00000-0161



Version 1
Date: 20/10/2005
Page: 16/175

- (13) Gilmozzi, R., Dierickx, P., Monnet, G., “Science and Technology of a 100-m Telescope: The OWL Concept”, conference 2002 Rome
- (14) Edlén, B., “The dispersion of standard air”, J. Opt. Soc. Am, 43, p339, 1953
- (15) Eisenhauer, F., Tecza, M., Thatte, N., Mengel, S., Hofmann, R., Genzel, r., “Near-infrared-spectroscopy with Extremely Large telescopes: Integral-field- versus multi-object-instruments”, ELT conference in Backaskog, 2000
- (16) Gilmozzi R., “Science and Technology Drivers for Future Giant Telescopes”, Proc. SPIE 5489, June 2004-10-05
- (17) Cotera, A., Morris, M., Ghez, M., Becklin, E.E., Tanner, A.M., Werner, M.W., Stolovy, S.R., “Mid-Infrared Imaging of the Central Parsec with Keck”, ASP Conference Series, Vol 186, p240, 1999
- (18) Hawarden, T., “Extremely Large Ground-based Telescopes (ELTs): Performance Comparisons with 8-m class Space Telescopes”, ISAS report No. 14, (2000)
- (19) Hawarden, T.G., Gilmozzi, R., Hainaut, O., “Using a 100-meter ELT (e.g. “OWL”) for Extrasolar Planet and Extrasolar Life Detection” 25th meeting of the IAU, Sidney 2003
- (20) Holcombe, R.S., Hoffman, A.W., Love, P.J., “Mosaic packaging for large-format infrared devices” SPIE 5499, p526
- (21) Hook, I.M., “Highlights from the science case for a 50- to 100-m extremely large telescope”, SPIE 5489, p35, 2004
- (22) Hoffman, A.W., Love, P.J., Ando, K.J., Corrales, E., “Large infrared and visible arrays for low-background applications: an overview”, SPIE 5499, p240 (2004)
- (23) Hoffman, A.W., Corrales, E., Love, P.J., Rosbeck, J., Merrill, M., Fowler, A., McMurtry, C., “2K x 2K InSb for Astronomy”, SPIE 5499, p59, (2004)
- (24) Käufel et.al. A sky-noise measurement and its implication for ground-based infrared astronomy in the 10 micron atmospheric window; Experimental Astronomy2, 115-122, 1991
- (25) Käufel et al., “Combining optical interferometry with lunar occultation”, Proc. SPIE Vol. 3350, p. 267-274 (1998)
- (26) Käufel, u., et al., M. Proceedings of the SPIE, Volume 4841, pp. 117-128 (2003)
- (27) Lenzen F. et.al “Robust Reconstruction from chopped and noded images”; A&A (submitted) 2005 astro-ph/0508184
- (28) Love, P.J., Hoffman, A.W., Lum, N.A., Ando, K.J., Ritchie, W.D., Therrien, N.J., Toth, A.G., Holcombe, R.S., “1Kx1K Si:As IBC detector arrays for JWST MIRI and other applications”, SPIE 5499, p86 (2004)
- (29) Lucas C., et al., “New 8-13 micrometer Si:Ga/DRO hybrid arrays for very large telescopes”, Experimentel Astronomy, Vol. 3, No. 1-4, p273 (1994)
- (30) Marconi, A. et al. 1994, A&A 291, 18
- (31) Masciadri, E., “Near Ground wind simulations by a meso-scale atmospheric model for the extremely large telescope site selection”, Rev. Mex. De Astr. Y Astrof. 39, p249 (2003)
- (32) Masciadri et al. 2000, SPIE, 4006, 1136; Thompson, Moran, Swenson, “Interferometry and Synthesis in Radio Astronomy”, John Wiley & Sons, 1986



T-OWL Concept Level Study

Doc : OWL-CSR-ESO-00000-0161



Version 1
Date: 20/10/2005
Page: 17/175

- (33) Mathar, R.J., “Calculated refractivity of water vapour and moist air in the atmospheric window at 10 μ m”, Applied Optics 43, p928 (2004)
- (34) McClelland, R.S., Content, D.A., « Design Manufacture and test of a cryo-stable Offner relay using aluminium foam core optics”, SPIE 4451, p77
- (35) Melia, F., Falcke, H., “The super-massive Black Hole at the galactic center”, Annu. Rev. Astron. Astrophys.2001.39 p309
- (36) Michelle User Manual
- (37) Miyata T. MICS: A new mid-infrared camera and spectrometer for ground-based astronomy; PASP 111:750-764, 1999
- (38) Moerchen, M., Varosi, F., Gezari, D., Telesco, C., Dwek, E., “The Heating of Dust in the Central Parsec of the Galaxy from Mid-IR Imaging with T-Recs” AAS meeting 205 (2004)
- (39) Monnet G. and D’Odorico S., “Towards Instrumentation for ELTs: the OWL case”, Proc. SPIE 5492-22, June 2004
- (40) Mosser, B. Et al., Icarus, Vol. 121, p. 331-340 (1996)
- (41) M. Owner-Petersen and A. Gontcharov, “Multi-conjugate Adaptive Optics for the Swedish ELT, Investigation of the Effects of Laser Guid Stars at a finite Distance”, Venice 2001
- (42) Okamoto, Y.K., Kataza, H., Honda, M. et al., Nature, 431, 660 (2004)
- (43) T. Peacocke, S.P. Todd, E. Atad, T.G. Hawarden, “Will ELT segmentation effects conceal exo-Earths? A physical optics simulation as a test of Fourier methods”, SPIE 5497 p338 (2004)
- (44) R. Penndorf, “Tables of the refractive index for standard air and the Rayleigh scattering coefficient for the spectral region between 0.2 and 20.0 μ m and their application to atmospheric optics”, JOSA 47, p176 (1957)
- (45) Penston et al, 1984 MNRAS 208, 347
- (46) Pentericci, Fan, Rix et al. (2002, AJ 123, 2151)
- (47) Prieto et al. 2005, MNRAS in press
- (48) Prieto & Viegas, 2000, ApJ 532, 238
- (49) R. Ragazzoni, J. Farinato, E. Marchetti: “Adaptive Optics for 100m class telescopes: New Challenges require New Solutions” Adaptive Systems Technology, P. Wiziniwich, Proc. SPIE. 4007, 1076-1087 (March 2000)
- (50) R. Ragazzoni, C. Arcidiacono, E. Diolaiti, J. Farinato, A. Moore, R. Soci, “A Smart Fast Camera”, SPIE 5492, p121 (2004)
- (51) Ramsay, H.S., Mountain, M., Wright, G., Hastings, P., “A near-infrared 3D spectrograph for an ELT” ELT conference in Backaskog, Sweden 2000
- (52) Reunanen et al. 2003, MNRAS 343, 192
- (53) F. Roddier and C Roddier: “Modeling atmospheric effects in adaptive optics systems for astronomical telescopes”, SPIE Vol. 628, p298 (1986)
- (54) Rodriguez-Ardila et al. 2002, ApJ 579, 214
- (55) Rodriguez-Ardila et al. 2004, Proceedings of the IAU 222, Ho, C. & Schmitt, H. eds., Cambridge University Press, 2004., p. 283



T-OWL Concept Level Study

Doc : OWL-CSR-ESO-00000-0161



Version 1
Date: 20/10/2005
Page: 18/175

- (56) A.P.G. Russell, G. Monnet, A. Quirrenbach, R. Bacon, M. Redfern, T. Andersen, A. Ardeberg, E. Atad-Etchedgui, T. G. Hawarden, "Instruments for a European Extremely Large Telescope: The challenges of designing instruments for 30-100m telescopes", 2004, SPIE 5492, p1796
- (57) A.P.G. Russell, Hawarden, T.G., Timothy, G., "Instrumentation studies for a European extremely large telescope: a straw man instrument suite and implications for telescope design", SPIE 5382, p684, 2004
- (58) R. J. Sarlot, D. W. McCarthy, "A Cryogenic, 1 – 5 "Micron Atmospheric Dispersion Corrector for Astronomical Adaptive Optics", SPIE 4441, p72 (2001)
- (59) Schütz, O., Meeus, G., Sterzik, M., A&A, 431, 165 (2005)
- (60) Schütz, O., Meeus, G., Sterzik, M., A&A, 431, 175 (2005)
- (61) P.K. Seidelmann, "Refraction and numerical integration" section 3.281 in Exo-planetary Supplement to the Astronomical Almanac, PP 141-143, University Science Books, Mill Valley, (1992)
- (62) Siebenmorgen et al. 2005, A&A 436, L5
- (63) Sturm et al. 2000, A&A 358, 481
- (64) Tarrus A. et.al. "The struggle against sky noise in ground based and air-borne observatories"; Proc. of the 2nd ESO IR Workshop p.159, 1982
- (65) Taylor, K., McLean, I.S., "Instrumentation for the California Extremely Large Telescope", SPIE 4841, P55, 2003
- (66) Wooden et al., 2004, AJ812, L77)
- (67) Visir User Manual
- (68) Yaitskova, N., Dohlen, K., Dierickx, P., "Diffraction in OWL: Effects of segmentation and segments edge mis-figure", SPIE 4840, 2003
- (69) Yan et al. 2005, ApJ in press



T-OWL Concept Level Study

Doc : OWL-CSR-ESO-00000-0161



Version 1
Date: 20/10/2005
Page: 19/175

2 Acronyms

AD	Applicable Document
ADC	Atmospheric dispersion corrector
AO	Adaptive optics
AR	Anti-reflection
CCC	Closed Cycle Cooler
DIT	Detector Integration Time
FWHM	Full width half maximum
IFU	Integral field unit
ITC	Integration Time Calculator
JFC	Jupiter Family of Comets
JWST	James Webb Space Telescope
MCAO	Multi-conjugate adaptive optics
MIR	Mid-infrared region (6 – 30 μ m)
MIDI	VLT Mid-IR Interferometer
MIRI	Mid-infrared Instrument for JWST
MPIA	Max-Planck-Institut für Astronomie
MPS	Max-Planck-Institut für Sonnensystemforschung
NIR	Near infrared region (1 – 2.5 μ m)
OWL	Overwhelming large telescope
PSF	Point spread function
RD	Reference Document
RO	read-out
SAFIR	Single aperture FIR satellite
TADC	Tunable atmospheric dispersion corrector
TIR	Thermal infrared region (2.5 – 6 μ m)
TIRC	Thermal Infrared Camera
TMA	Three mirror anastigmat
T-OWL	Thermal infrared instrument for OWL
ULIRG	Ultra-luminous infrared Galaxy
VISIR	VLT spectrometer and IR imager
VLT	ESO's Very Large Telescope



T-OWL Concept Level Study

Doc : OWL-CSR-ESO-00000-0161



Version 1
Date: 20/10/2005
Page: 20/175

3 Contributors

3.1 Section authors

The main contributors to the science case are listed by sections:

- Science Drivers (overall): Bernhard Brandl & Wolfgang Brandner
- Solar system: Hermann Bönhard, Ulli Käufl
 - Exo-planets: Wolfgang Brandner, Kees Dullemond, Elena Masciadri, Stephan Kellner
 - Proto-planetary disks: Ewine van Dishoeck, Wolfgang Brandner, Miwa Goto, Cornelis Dullemond, Oliver Schütz, Sebastian Wolf
 - Proto-stars: Ewine van Dishoeck
 - The Galactic center: Rainer Lenzen
 - The IMF in Star-bursts: Bernhard Brandl
 - AGN at low redshift: Paul van der Werf
 - ULIRGs: Paul van der Werf
 - AGN at high redshift: Almudena Prieto, Peter Barthel
 - Gamma-ray bursts: Ralf Wijers, Bernhard Brandl
 - Summary: Bernhard Brandl

3.2 Main contributors to the technical part of this study are: (in alphabetical order)

- Bernhard Brandl (U. Leiden)
- Wolfgang Brandner (MPIA)
- Wolfgang Gässler (MPIA)
- Ulli Käufl (ESO)
- Stefan Kellner (MPIA)
- Rainer Lenzen (MPIA)
- Elena Masciadri (MPIA)
- Lars Venema (Astron)
- Jan-Willem Pel (Astron/U. Groningen)

3.3 Additional contributors: (in alphabetical order)

- Thijs de Graauw (SRON/U. Leiden)
- Pascal Hallibert (U. Leiden)
- Dietrich Lemke (MPIA)
- Michael Meijers (Astron)



T-OWL Concept Level Study

Doc : OWL-CSR-ESO-00000-0161



Version 1
Date: 20/10/2005
Page: 21/175

- Johan Pragt (Astron)
- Andreas Quirrenbach (U. Leiden)
- Ronald Roelfsema (Astron)
- Ton Schoenmaker (Astron)
- Xander Thielens (U. Groningen)

4 Summary

This document summarizes the concept study for T-OWL, an instrument for imaging and spectroscopy in the thermal- and mid-IR wavelength regime (3 – 30 μm). This instrument concept study is part of ESO's OWL telescope feasibility study, and was done jointly by MPIA with partners Leiden University and ASTRON with more than 25 contributors from these institutions and from MPS.

The scientific perspective provided by the collecting power and resolution of a 100m telescope raises mid-IR astronomy to a new level. With orders of magnitude higher sensitivity than any previous instrument and a spatial resolution better than what astronomers are used to from the Hubble Space Telescope in the optical, T-OWL will certainly deliver breakthrough science in many fields of Galactic and extragalactic astronomy. This document presents ten most exciting science examples that can only (or best) be done with T-OWL; amongst those are the study of extrasolar planets and their formation, and the centers of active galaxies. However, the discovery space of T-OWL is by no means limited to these examples, but opens up new areas that have not been considered for MIR observations, such as Galactic pulsars or gamma-ray bursts at high-redshift.

From these science cases the top level requirements for T-OWL were derived:

T-OWL shall cover the 3 – 20 μm (LMNQ bands) wavelength range (goal: 3 - 27 μm) with four different modules:

1. A diffraction-limited camera for broad and narrow-band imaging over a 7"×7" FOV
2. A low-resolution (R=300) long-slit spectrograph
3. An integral-field medium-resolution (R=3000) spectrograph
4. A high-resolution (R=50000) Echelle spectrograph

The field of highest spatial resolution is of special interest for background limited application as sensitivity for unresolved sources increases with D^2 . Thus, TIR and MIR observations from the ground should concentrate on highest spatial resolution.

General design considerations as well as more detailed optical calculations are included.

The document discusses the requirements on telescope, adaptive optics performance, and atmospheric properties. For a site at 4000m altitude detailed performance estimates are provided. T-OWL turns out to be comparable in sensitivity even to cryogenic space missions like JWST, but at the same time quite complementary: while limited to the atmospheric windows, T-OWL will have 15 times better spatial resolution than JWST/MIRI, and its high-resolution spectrograph provides access to kinematic studies at sensitivities that will be unique for at least one or two generations of astronomers.

5 Science Drivers

A 100m OWL telescope will provide a dramatic improvement in sensitivity and spatial resolution compared to all previous ground based observing facilities. With T-OWL the infrared Universe can be seen at a resolution better than what astronomers got used to with the Hubble Space Telescope in the optical observations – but now at $10\mu\text{m}$! This will be the dawn of a new era for mid-infrared astronomy, mainly enabled through the large collecting area of OWL and the availability of large format MIR detector arrays.

However, observations in the TIR and MIR regime are background limited due to the thermal emission of the atmosphere and the telescope itself. Cooled space observatories which can avoid the terrestrial thermal background, have much higher sensitivity for a given aperture size. The next generation space telescope JWST, with its $5 - 28\mu\text{m}$ MIR instrument MIRI and the $1 - 5\mu\text{m}$ instruments NIRCAM and NIRSPEC, will likely be operating in orbit by the time OWL achieves first light with the full aperture.

Hence, this document focuses on those science cases that cannot, or at least not as well, be addressed by other facilities. Specifically, such observations require:

- highest angular resolution
- very high spectral resolution
- quick response times (< 1 day)

This chapter illustrates that the science that can be done with T-OWL includes several “killer applications” that will bring MIR astronomy on the newspaper front pages. The following discussion of selected science cases is organized by increasing distance, not priority:

1. Solar System
2. Exo-planets
3. Proto-planetary Disks
4. Proto-stars
5. The Galactic Center
6. The IMF in Star-bursts
7. AGN at Low Redshift
8. Ultra-Luminous Infrared Galaxies
9. AGN at High Redshift
10. Gamma-Ray Bursts

Section 5.11 of this chapter summarizes the science cases and derives the basic instrument parameters on which the rest of this study is based.

5.1 Solar System

5.1.1 Seismology of the Giant Planets

Science context: The interior of the outer planets in the solar system is hidden under an extended (thousands of km), dense, opaque atmosphere of clouds, not accessible neither for direct observations from Earth nor for spacecraft in-situ experiments. Understanding of the interior structure of the giant



T-OWL Concept Level Study

Doc : OWL-CSR-ESO-00000-0161



Version 1
Date: 20/10/2005
Page: 24/175

planets has great impact on the formation scenarios of our and other planetary systems. Nonetheless, the intrinsic structure of giant planets is basically unconstrained by observations and it can only be hypothesized by model estimations.

The present models predict an inner core of the typical size of the Earth in the center which should consist mostly of Fe and Si in the very inner part, and a layer of ices further outside. In Jupiter and Saturn, a large layer (thickness of about 2/3 of the planet radius) of metallic H mixed with He, O, C, N should exist above the inner core. The outer 10 percent of the radius of these two planets comprise clouds of H₂, H, O, C, N. In Uranus and Neptune, a metallic H layer is not expected to exist, and the inner core should be surrounded by the molecular H₂ dominated atmosphere as in the case of Jupiter and Saturn.

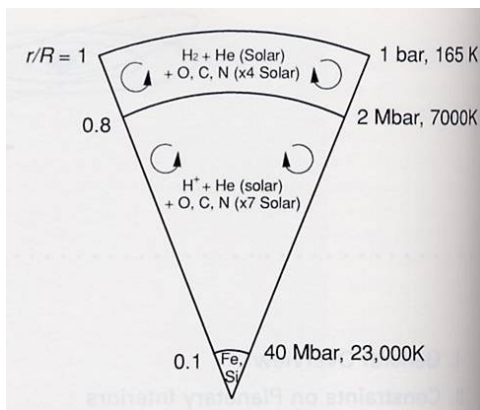


Fig. 1: Schematics of the inner structure of Jupiter

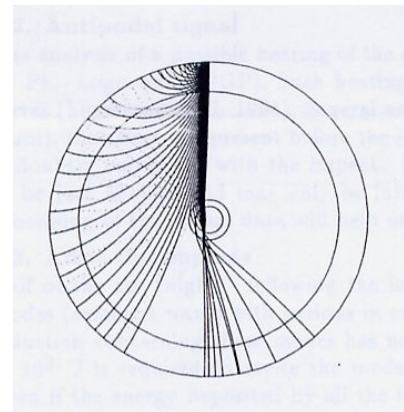


Fig. 2: Penetration of seismic wave through Jupiter

Methodology: Seismology is the pathway to sense the interior of planets. However, the traditional approach through seismic surface sensors is excluded for the gas giants in the solar system. Remote sensing of the thermal heating of the outer (visible) atmosphere, produced by seismic waves from a major impact on a gas giant (like the one of Comet Shoemaker-Levy 9 on Jupiter in 1994) or through the intrinsic oscillations of a planet, are the only ways to assess the internal structure of the gas giants in the solar system. So far, attempts to measure seismic waves on Jupiter (impact induced and eigen modes) have been unsuccessful or at best inconclusive. For the case of Shoemaker-Levy 9, Mosser et al, (1996) have analyzed the data of a multi-site mid-infrared observing campaign, spanning several days, albeit finding no seismic signatures. However, they describe thoroughly the methodology. The expectations are that the low-degree pressure modes should have amplitudes of less than 0.5 m/s (comparing to temperature changes of a few 10 mK) and frequencies in the mHz range.



T-OWL Concept Level Study

Doc : OWL-CSR-ESO-00000-0161



Version 1
Date: 20/10/2005
Page: 25/175

Note on design requirements

Observation type	MIR-imaging
Spatial resolution	50mas
FOV	5" – 10"
Spectral resolution	-
Wavelength range	8 - 20 μ m
Min. telescope size	30m
Special requirements	none
comments	

5.1.2 Cold Volcanism in the Outer Solar System: Triton and the Kuiper Belt

Science context: Volcanism among the moons of the major planets is a surprising phenomenon. While for Io at Jupiter the volcanic activity is driven by tidal interaction with the host planet, this mechanism is not considered to be efficient for the geyser-like phenomena encountered on the surface of Neptune's largest moon, Triton. Instead, the cryo-volcanism found there seems to be driven by intrinsic phenomena, most likely related to the ice chemistry (N_2 and CH_4) and constitution, possibly triggered by solar illumination. There is no doubt: Triton's geysers are mysterious by their nature and origin, and it is not even known if they are long-lasting, since they were only observed during a single spacecraft fly-by so far. Nonetheless, the mechanism that drives the cryo-volcanism on Triton is also very likely to play a significant role for the surface constitution and evolution of Kuiper Belt objects, which are at similar distance from the Sun and have most likely a constitution similar to Triton (actually, Triton is considered to be a Pluto-size Kuiper Belt object that was captured by Neptune). The deposits of the activity, most likely condensed gas from the eruptions, change the surface chemistry and layering at least on a local, if not on a global scale. Gas expelled during the eruptions can contribute to the weak transient or maybe even permanent atmospheres seen around Triton and Pluto. However, it is completely unknown so far which chemistry is dominant in the geyser activity on Triton.

Methodology: The study of the cryo-volcanism on Triton requires (1) the detection of geyser phenomena by high resolution imaging in the thermal infrared for the eruption or by high resolution imaging in the near-IR up to 5 μ m for the surface deposits and (2) the follow-up measurement of the spectral signatures of the detected features by low-dispersion spectroscopy over the widest possible wavelength range from about 3 – 20 μ m.

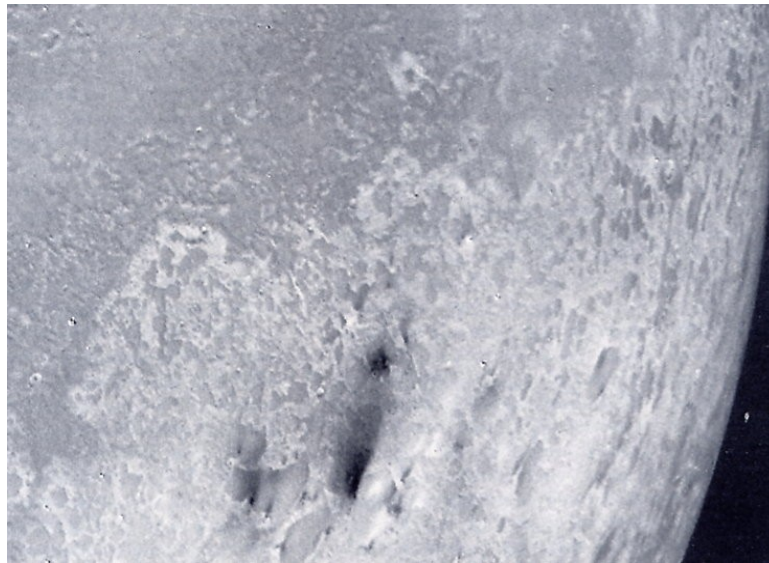


Fig. 3: Geyser vents on Neptune's moon Triton

Note on design requirements

Observation type	TIR/MIR imaging/spectroscopy
Spatial resolution	50mas
FOV	1"
Spectral resolution	300
Wavelength range	3 - 20 μ m
Min. telescope size	60m
Special requirements	High SNR
comments	

5.1.3 Comets and the Ice and Dust Composition in the Outer Solar System

Science context: The structure and composition are key for the understanding of the formation and evolution of matter within the early solar system. Ices are especially sensitive to temperature and to radiation processing. Comets are made of these ices and are considered to represent the most primordial bodies accessible to Earth-based observations to date. Comets likely formed at diverse distances from the sun and for sure outside the 'frost line' in the solar nebula (~5AU) out to the Kuiper Belt (40-50AU). The temperature regime of the formation region ranged from 200 K near Jupiter to about 30 K at Neptune. Other conditions also varied with location in the proto-planetary disk. The original dust from the proto-stellar collapse was exposed to the local physical conditions by the time when it was enclosed into cometary nuclei. Depending on the temperature – thus the distance - of the formation region, dust alteration from amorphous to crystalline forms may have occurred.

Thus, the composition of a comet in its icy and dusty components contains the signatures from the formation period.

Today, comets, the icy and dusty planetesimals, reside in two reservoirs: the Oort Cloud (OC) far beyond, and the Kuiper Belt at the edge of the planetary system. The OC contains the long-periodic and ‘dynamically new’ comets, the Kuiper Belt is the main source for the short-periodic comets (the so called Jupiter family of comets; JFC). Interestingly, dynamical models predict that about half of the OC comets should originate from the region between Jupiter and Neptune, the rest from further out. Thus, it can be expected that diversity in chemical and constitutional composition of the ices and dust may be measurable in comets, leading in the long term to better constraints on the region of their formation and the physical conditions therein.

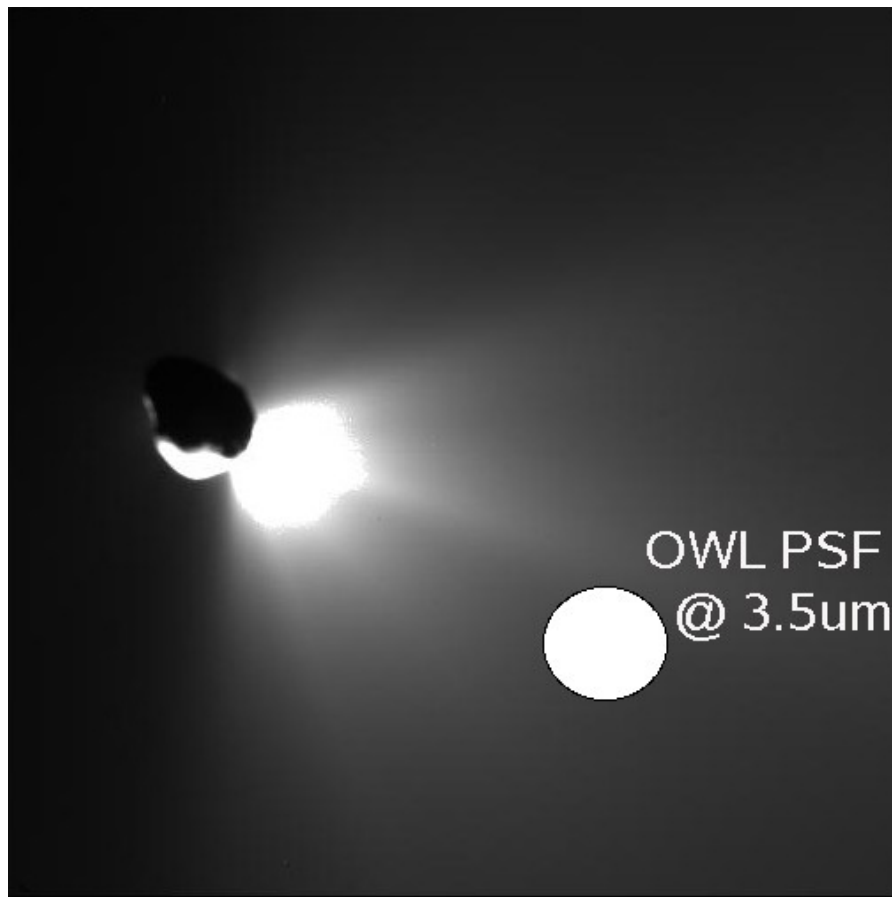


Fig. 4: Dust Plume, created by the artificial cratering experiment "Deep Impact" on July 4th, 2005 as seen from the fly-by spacecraft ~15min after fly-by. For comparison the PSF of T-OWL at 3.5 μm is indicated. It is obvious that T-OWL would have been capable to spatially resolve the nucleus and the dust ejecta.

The properties of cometary nuclei and the conditions which lead to active zones on cometary surfaces after the NASA Deep Impact Mission (see M. A'Hearn 2005) appear even more enigmatic than before. However, a detailed understanding of these issues is important to judge and calibrate the 'weathering' cometary nuclei have undergone since their formation, to use them as reliable tracers for the conditions of the Solar System during formation.



T-OWL Concept Level Study

Doc : OWL-CSR-ESO-00000-0161



Version 1
Date: 20/10/2005
Page: 28/175

Methodology: Chemical and constitutional differences in comets are revealed when parent volatiles from the ices and the dust component are studied directly. The richest wavelength domain for volatile studies is the near-IR between 3 and 5 μm , for the dust the 7-23 μm range. Using high-dispersion spectroscopy in the former case a number of parent gas species from cometary ices (H_2O , CO , NH_3 , CH_4 , C_2H_2 , C_2H_6 , CH_3OH , HCN) can be measured. The constitutional structure and composition of the dust is revealed by low- to medium resolution spectroscopy. Both techniques are successfully applied with the respective instrumentation at 8-10m class telescopes. However, for sensitivity reasons they are limited to bright comets only. The goal to establish a map of the formation regions and conditions for comets in the solar system is only reachable using similar instrumentation at a telescope of larger light collecting power since only this way a much larger sample of comets, in particular the barely represented JFCs, can be measured.

Infrared Spectroscopy of gas outflow in the 3-5 μm region allows to measure the nuclear spin statistics of protons in H_2O and NH_3 . This is considered a reliable thermometer preserving a temperature reading over $>10^6$ years. It must, however, be debated, if the spin statistics is not altered by interaction with the solar radiation, once the molecules are released from the nucleus. The high spatial resolution, which can be achieved with T-OWL in long slit spectroscopy will allow for a study of the gas within seconds after it has left the surface so that the "true" spin temperature can be derived.

Note on design requirements

Observation type	TIR-spectroscopy
Spatial resolution	50mas
FOV	Up to 1 arcmin
Spectral resolution	300, 50000
Wavelength range	3 - 5 μm
Min. telescope size	30m
Special requirements	Long-slit
comments	

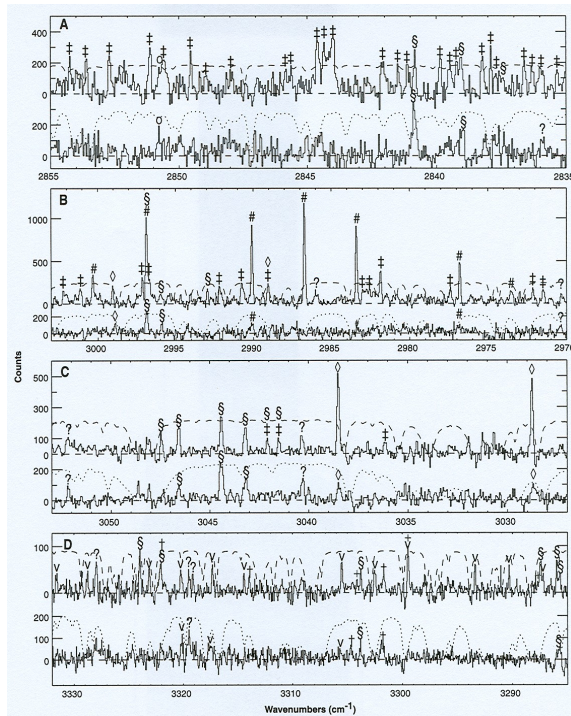


Fig. 5: Volatile primordial ices in Comet Hale-Bopp.

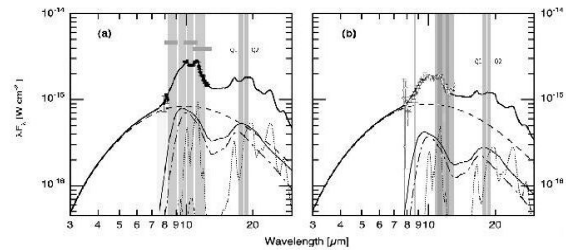


Fig. 6: Dust mineralogy in Comet C/2001Q4 (NEAT) (Wooden et al. 2004) shows thermal emission models compared with observed spectra of Comet C/2001Q4 (NEAT). (a) 2004 May 11.25, (b) 2004 May 11.30. Five minerals are modelled: amorphous carbon (dashed line), amorphous pyroxene (thin solid line), amorphous olivine (long-dashed – dotted line), crystalline olivine (dotted line), crystalline ortho-pyroxene dashed-dotted line). The thick-solid line shows the fit of the mineralogical mixing model to the observations.

5.2 Exo-Planets

5.2.1 EPICS Follow-Up

Science Context: More than 140 exo-planetary systems have been identified by now using indirect methods like radial velocity measurements, pulsar-timing, transits, micro-lensing or astrometry. (Santos et al , 2003, Marcy et al., 2005) The direct detection of exo-planets, i.e., the photometric, spectroscopic and/or polarimetric analysis of radiation emanating from an exo-planet , and hence the detailed characterization of the chemical and physical properties of exo-planets is the next logical step.

Methodology: T-OWL will be the ideal instrument for follow-up studies of new exo-planetary systems discovered by EPICS. EPICS is expected to easily detect giant exo-planets around hundreds of stars within a few 100 pc to the Sun, and to detect terrestrial planets around stars within 10-20 pc. The N-star data base lists 100 stars within 7.2 pc to the Sun.

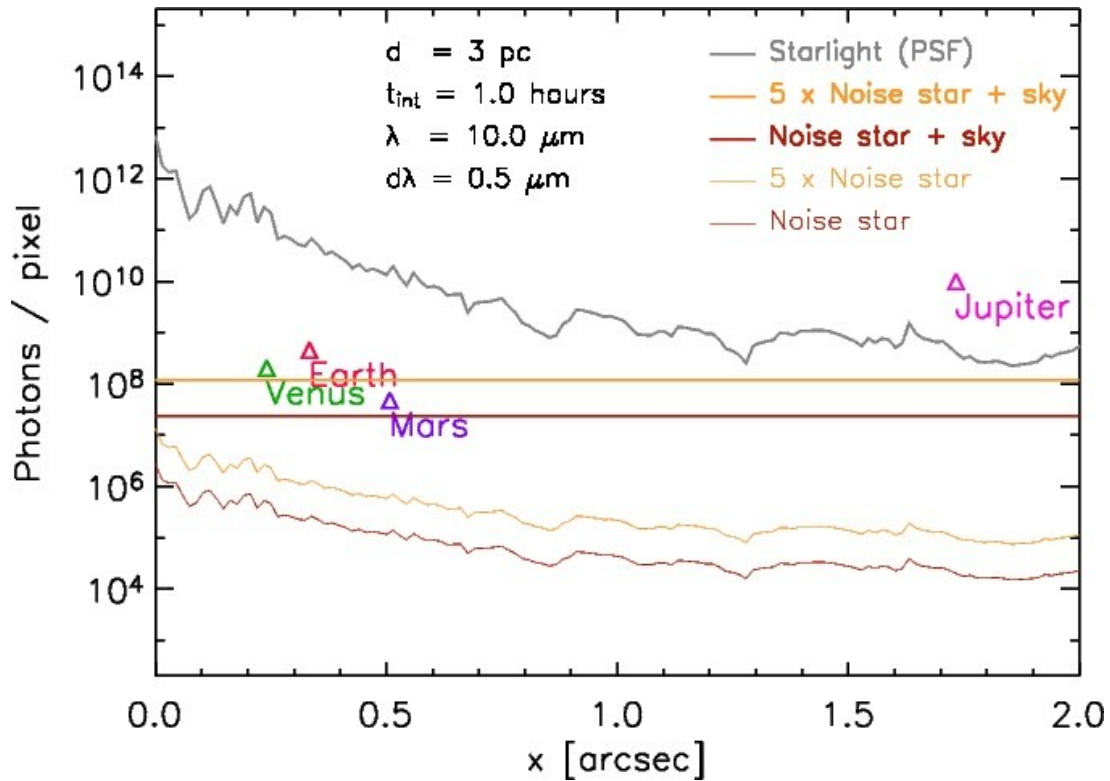


Fig. 7: Simulated detectability of a nearby solar system with T-OWL

Simulations (see Fig. 7) indicate that at a wavelength of 10 micron, the giant and terrestrial exoplanets around these most nearby stars could clearly stand out above the residual photon noise from the stellar point spread function and the thermal background, *provided* a telescope with a sufficiently large aperture ($\geq 100\text{m}$) is used. As observations at 10 micron probe the thermal emission from exoplanets, they can be used to study the properties of the exo-planet atmosphere (opacity, presence of dust). Low-resolution spectroscopy would be the ideal tool to study the main gas constituents of the planets atmospheres (like CO, H₂O, ...), while high-resolution spectroscopy could be employed to search for bio-markers like Ozone.

Since T-OWL will already benefit from the baseline adaptive optics system of OWL with a high quality PSF with a Strehl ratio $\geq 95\%$ at 10 micron, T-OWL could carry out a pilot exo-planet search programme by surveying 30 to 40 of the most nearby stars even before EPICS becomes fully operational.

Instrumentation: A telescope diameter of at least 100m (better 160m) would be required for the direct detection of Earth-like planets in Earth-like orbits around the most nearby stars. The direct imaging requires intermediate band 10 micron filters with a width of around 0.5 micron. Low-resolution spectroscopy with $R \leq 100$ should be sufficient to probe the main constituents of the exo-planet atmospheres, while the detection of bio-markers requires a much higher resolution of $R \sim 50,000 - 100,000$ and exposure times of about 100 hours.

Note on design requirements

Observation type	MIR-imaging
Spatial resolution	diffraction
FOV	2"
Spectral resolution	100, 50000
Wavelength range	8 - 12 μ m
Min. telescope size	100m
Special requirements	High contrast, SR
comments	

5.3 Proto-Planetary Disks

In addition to studying exoplanets, understanding their origin has become one of the major questions in modern astrophysics.

Circumstellar disks are a natural by-product of the star formation process. The material in these disks comprises the building blocks for future planetary systems (e.g., Lissauer 1993, Beckwith et al. 2000). Virtually all of the planets detected to date are gaseous Jupiter-like planets, which are thought to form in disks within 1-10 Myr after the formation of the parent star (Pollack et al. 1996). Over time, the gas in the disk will dissipate and the small grains will coagulate or be blown away. In particular Herbig Ae/Be stars ($t = 1-5$ Myr) in the later stages of their evolution are the immediate progenitors of classical debris disks like, e.g., Vega (A0V, $t \sim 100$ Myr), β Pic (A5V, 20 Myr), and Fomalhaut (A3V, 100 Myr). After ~ 20 Myr, disks become optically thin at ultraviolet and infrared wavelengths, and are called debris disks. The dust grains in the debris disks are of secondary origin, replenished by collisions of larger objects. This implies the presence of asteroid-sized bodies, the so-called planetesimals. In the core-accretion model, rocky planets with masses comparable to those of the Moon or Earth form by gradual accretion of planetesimals, and only the heaviest of these cores, with masses of 10-20 Earth masses, can attract gas to form a gas-rich planet.

The transition phase from gas-rich to gas-poor disks is clearly a pivotal period in planet formation and direct observations of the gas content and composition are key to constrain the processes and time-scales involved. In particular, the bulk of the disk mass is in the gas, not in the dust.

5.3.1 Signatures of Planet Formation

Proto-planetary disks have now been imaged from the optical/near-infrared to the millimeter wavelength range around low-mass YSOs (T Tauri stars, e.g. Dutrey et al. 1994, 1998; Burrows et al. 1996), intermediate-mass YSOs (Herbig Ae/Be stars, e.g. Mannings & Sargent 1997, 2000), and possibly also around massive stars (Fontani et al. 2004; see also Chini et al. 2004, Shepherd et al. 2004, Schreyer et al. 2002).

Inner Holes and Gaps

An inner dust disk radius of ~ 4 AU has been measured in the 10 Myr old proto-planetary disk around TW Hydrae (Calvet et al. 2002). Other examples are the object Coku Tau/4 with an evacuated inner zone of radius ~ 10 AU (D'Alessio et al. 2005, Quillen et al. 2004) and GM Aur with a significant decrease of the dust re-emission inside ~ 4 AU around the central star (Rice et al. 2003). This “gap” is characterized by a depletion of at least the population of small dust grains, which are responsible for the near-to-mid-infrared flux. The confirmation of these indirectly (via SED modelling) determined gaps, as well as examining other disks for the existence / non-existence of similar gaps will provide valuable constraints on the evolution of the planet-forming region and thus on the process of planet formation itself.

Once (proto-)planets have been formed, they may significantly alter the surface density profile of the disk and thus create signatures in the disk that are much easier to find than the planets themselves (see Fig. 8). The appearance and type of these signatures depend on the mass and orbit of the planet, but even more on the evolutionary stage of the circumstellar disk. While the spatial structure of optically thick, young circumstellar disks around Herbig Ae/Be and T Tauri stars is dominated by gas dynamics, the much lower optical depth and gas-to-dust mass ratios in debris disks (Zuckermann, Forveille, & Kastner 1995; Dent et al. 1995; Artymowicz 1997; Liseau & Artymowicz 1998; Greaves, Coulson, & Holland 2000) make the Poynting-Robertson effect and stellar wind drag, in addition to gravitation, responsible for the resulting disk density distribution.

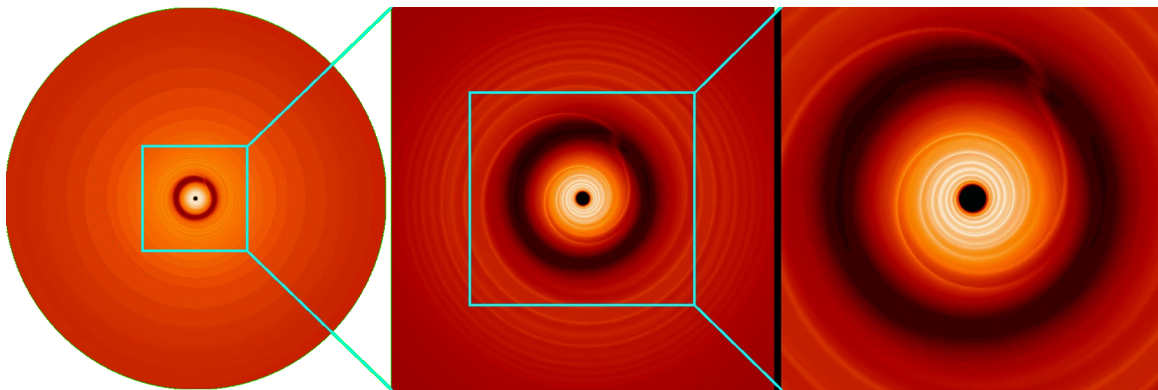


Fig. 8: Response of a gaseous disk to an embedded planet. [Wolf 2001 (data from W. Kley)]

Hydrodynamic simulations of gaseous, viscous proto-planetary disks with an embedded proto-planet show that the planet may open and maintain a significant gap (e.g., Bryden et al. 1999; Kley 1999, 2000; D'Angelo et al. 2003). This gap, which is located along the orbit of the planet, may extend to several astronomical units in width, depending on the mass of the planet and the hydrodynamical properties of the disk. The gas accretion on the planet can continue to planet masses up to $\sim 10 M_{\text{Jupiter}}$, at which point tidal forces are sufficiently strong to prevent further gas flow into the gap. The simulations also show that only planets with masses $> 0.1 M_{\text{Jupiter}}$ produce significant perturbations in the disk's surface density (Bate et al. 2003). Paardekooper & Mellema (2004) found that for typical disk masses (e.g., $0.01 M_{\odot}$ within 100 AU) the strong spiral shocks near the planet are able to decouple the larger particles (0.1 mm) from the gas. This leads to the formation of an annular gap in the dust, even if there is no significant gap in the gas density. As the opacity at longer wavelengths is dominated by these larger particles, the signatures of low-mass planets in disks can be stronger than

previously thought. The minimum mass for a planet to open a gap this way was found to be 0.05 $M(\text{Jupiter})$ – corresponding to ~ 16 Earth masses – for 1 mm particles.

The dominant observable quantity originating from the inner disk region ($r < 10\text{-}20\text{AU}$) is the emission of MIR continuum radiation by hot dust. Given the typical distance of nearby star-forming regions of $\sim 140\text{-}200$ pc and the spatial resolution achievable with a $\sim 100\text{m}$ telescope in the mid-infrared wavelength range of up to $\sim 10\text{mas}$, T-OWL will facilitate studying the planet-forming region in circumstellar disks. The instrumental requirements are diffraction limited imaging capability over a 1 to 2 arcsec field of view through wide and intermediate band filters ranging from 3 to 20 micron.

Fig. 9 presents a simulation of a circumstellar disk around a Herbig Ae star (for details see figure caption). The simulation clearly shows that gaps in the disks around intermediate mass stars at a distance of 140 pc can be detected with T-OWL assuming a 100m aperture.

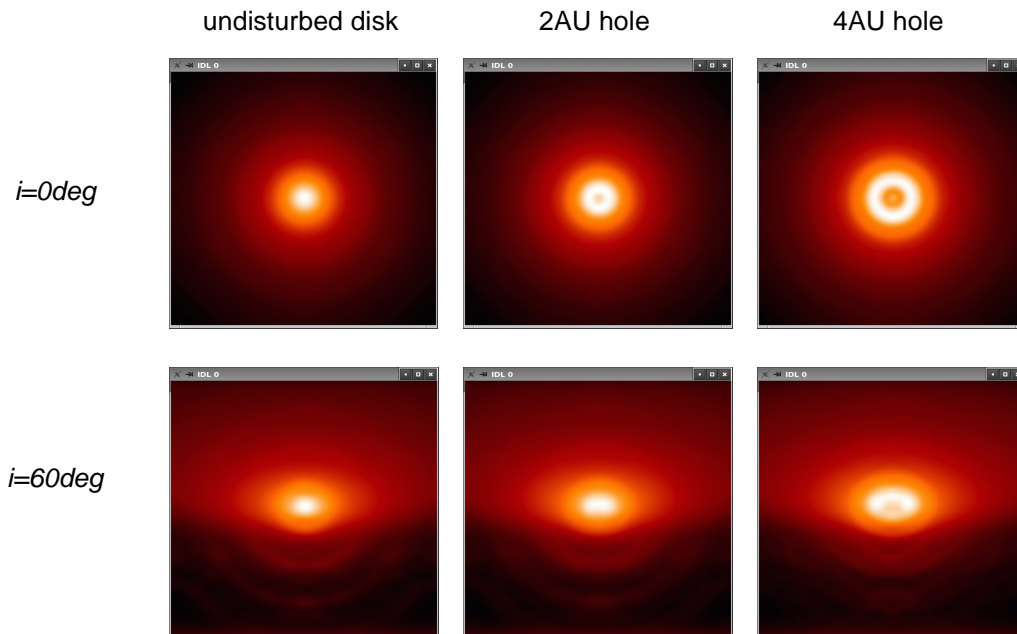
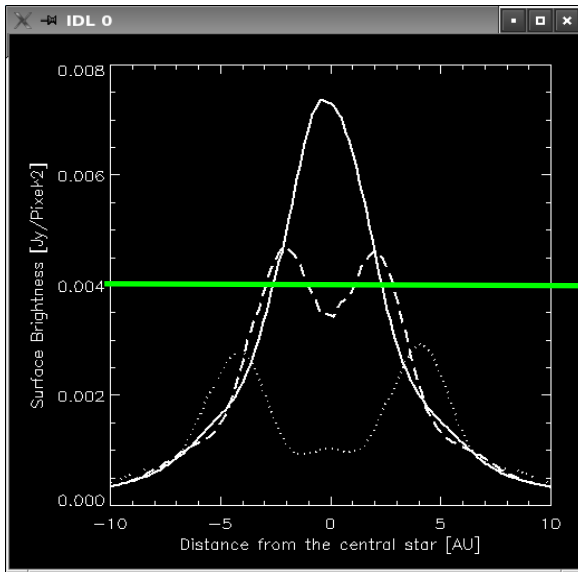


Fig. 9: Simulations of the re-emitted light at 10 microns, assuming an undisturbed disk and a disk with a hole with a radius of 2AU and 4 AU, respectively, convolved with the 100m-OWL point spread function. The star is assumed to be a Herbig Ae star at 140pc with $T=10,000\text{K}$, and $L=46L_{\odot}$; the disk parameters are those of the Butterfly star (Wolf, Padget, & Stapelfeldt 2003; flared disk, Shakura-Sunyaev type; disk mass: $0.01M_{\odot}$), but with a smaller radius of 100AU. The dust properties in terms of grain size distribution and chemical composition are those of typical interstellar medium dust. The simulated region corresponds to 60 AU x 60 AU.

In Fig. 10 the flux-calibrated brightness distribution along a horizontal cut in the middle of these images is shown and compared to the limiting N band background. As indicated in Fig. 10, the gap in a distance of 2 AU / 4 AU could be detected. For T Tauri stars the detection of a inner hole via this method is more challenging.



Solid line: undisturbed disk
Dashed line: inner hole with radius 2AU
Dotted line: inner hole with radius 4AU

Result:
882 Jy/arcsec²
[N band background: 250 Jy/arcsec²]
=> detectable

Fig. 10: Simulated radial brightness profile of the configuration shown in the previous Figure. For simplicity, only the case of an inclination $i=0$ is considered here. However, since T-OWL provides full u - v -plane coverage instantaneously (as opposite to e.g. VLTI) this will be most important for inclinations where the disk is not face-on.

Note on design requirements

Observation type	MIR-imaging
Spatial resolution	diffraction
FOV	4"
Spectral resolution	--
Wavelength range	3 - 20 μ m
Min. telescope size	50m
Special requirements	none
comments	

5.3.2 Evolution of Dust Grains

In the N-band we can see characteristic emission from warm silicate dust grains. Possible science targets include pre-main sequence stars with circumstellar disks or solar-system comets. By modelling the *entire* N-band spectrum we can conclude on the level of dust evolution (grain growth and crystallization), which is of particular interest in young circumstellar disks within the framework of planet formation. The evolution of dust grains is illustrated in Fig. 11. In this case, the spectral N-band coverage per single setting is of higher interest than spectral resolution.

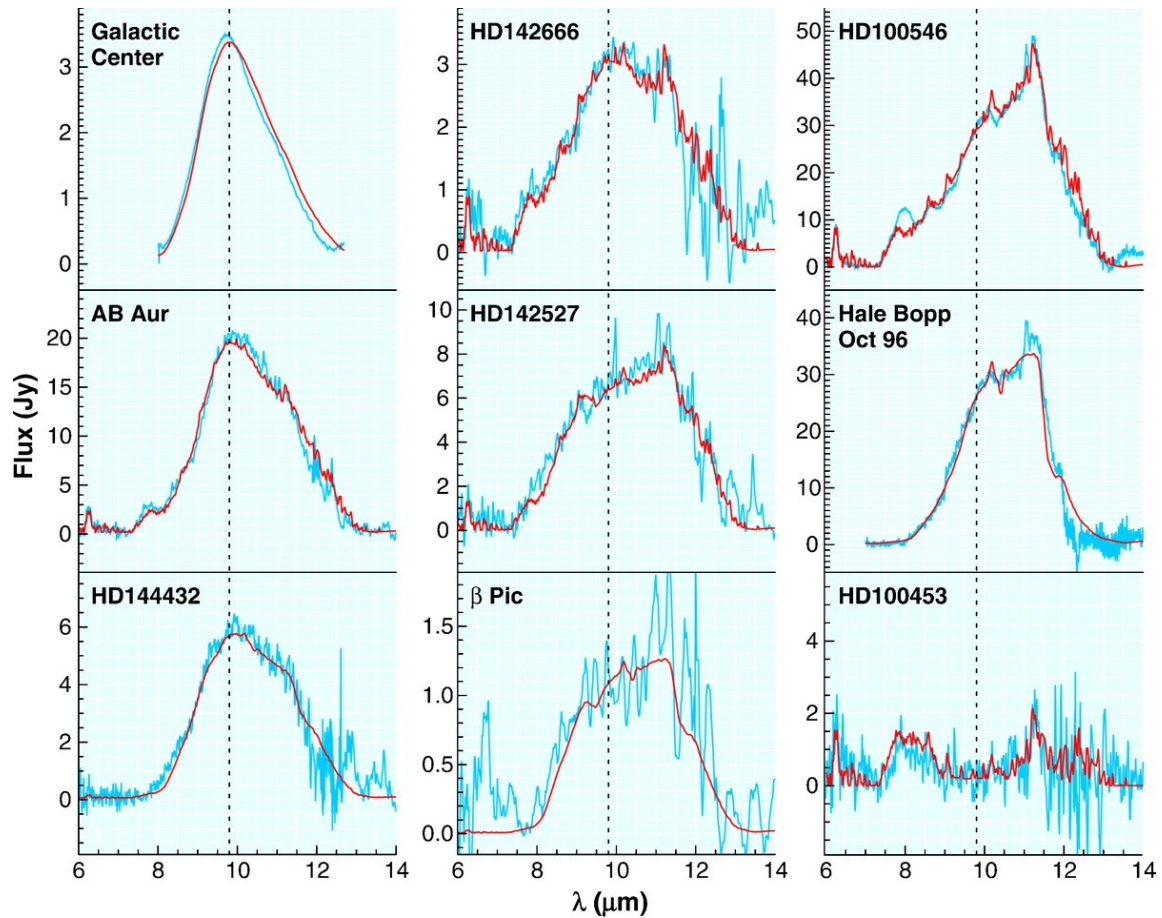


Fig. 11: Continuum-subtracted $10\mu\text{m}$ silicate emission bands observed toward a selected sample of isolated Herbig Ae stars with ISO-SWS. For reference, the silicate bands of interstellar medium dust and comet C/1995 O1 Hale-Bopp are included. The dotted line indicates the position of the $9.8\mu\text{m}$ amorphous silicate band observed in the interstellar medium. The solid lines indicate the best-fit models using a mixture of amorphous and crystalline material with different grain sizes. The sharp $11.3\mu\text{m}$ feature is evidence for crystallization, the shift toward longer wavelengths hints grain growth (Bouwman et al. 2001).

Currently resolved imaging spectroscopy can only be done for a very small number of nearby disks. Nevertheless, the spatially resolved spectroscopy of silicate and PAH has opened the completely new field of mineralogy inside circumstellar disks (van Boekel et al. 2004a, 2004b; Okamoto et al. 2004; Habart et al. 2004). Spatially resolved spectroscopy in molecular lines will facilitate the study of the evolving disk chemistry. Okamoto et al. (2004) performed this for the large disk around beta Pictoris using COMICS at the SUBARU telescope. By resolving the locations of ongoing dust replenishment they concluded on the position of three planetesimal belts at certain distances from the star. This technique hence witnesses indirectly the formation of planets. T-OWL will be able to study disks at much larger distances, hence creating a statistically relevant sample of disks. While spatially resolved mid-IR spectroscopy could, in principle, also be acquired with the VLTI, only very few disks are bright enough to be observable by MIDI.

Note on design requirements

Observation type	MIR-spectroscopy
Spatial resolution	diffraction
FOV	2"
Spectral resolution	300
Wavelength range	8 - 12 μ m
Min. telescope size	60m
Special requirements	none
comments	

5.3.3 Chemical Evolution of Gas in Disks

There are various techniques that can be used as probes of gas and dust in disks.

Table 1: Techniques used as probes of gas and dust in disks.

Method	Tracer	Probe
CO radio spectroscopy	cold molecules 10 – 30 K	~100AU
Sub-mm continuum	cold dust 10 – 30 K	~100AU
UV-vis scattered light	dust grains (coronagraph)	~100AU
MIR dust continuum	warm dust 100K	~30AU
UV-vis spectroscopy	atoms close to photosphere	~1 – 10 R_{star}

Unfortunately, none of these methods probes the gas in the most crucial 0.1-10 AU region where planet formation is thought to occur. Mid-infrared spectroscopy, however, is a powerful means to probe this important region. So far, most information on this region comes from studies of warm dust, but the gas and dust temperatures are not well coupled (e.g., Gorti & Hollenbach 2004). Typical gas temperatures in the 1-10 AU range are 100-1000 K, which is sufficient to excite the vibration-rotation lines of molecules. In the following, the direct gas probes that can be observed with T-OWL are summarized.

H₂ pure rotational lines in the MIR

H₂ is the main gaseous reservoir in disks, and an essential ingredient for building gas giant planets. The pure-rotational mid-IR lines are the lowest possible transitions to search for, but they are extremely difficult to detect because they are intrinsically very weak and always superposed on a strong continuum, the tentative detections by Thi et al. (2001) have not been confirmed (Sako et al. 2005). The high spectral and spatial resolution of T-OWL will mitigate both these problems. For a typical sensitivity of 10^{-16} erg s⁻¹ cm⁻² at 17 μ m (10σ , 1hr), T-OWL can detect $\sim 10 M_{\text{Earth}}$ of H₂ gas in a disk at 150 pc. For a disk at the distance of the TW Hya association (56 pc), models predict S(1) and S(2) fluxes around 2×10^{-15} erg s⁻¹ cm⁻² if the star has excess UV radiation (Nomura & Millar 2005), readily detectable with T-OWL. A key T-OWL program would be to survey the S(1) 17 μ m and S(2) 12 μ m lines in a large set of disks of various evolutionary stages, taken from samples defined, e.g., by

Spitzer. The integral field unit will be very important for these studies. Its resolution is well matched to the size of disks ($10 \text{ AU} = 0.07''$ at typical distances of 150 pc for T Tauri stars in Oph, Cha, or Lupus).

CO fundamental band at $4.7 \mu\text{m}$

The CO $v=1-0$ fundamental vibration-rotation transitions at $4.7 \mu\text{m}$ have been detected toward more than a dozen Herbig Ae and T Tauri stars (Brittain et al. 2003, Najita et al. 2003, Rettig et al. 2004, Blake & Boogert 2004). The lines often show a double-peaked profile whose width varies from 5-10 km/s to more than 100 km/s and correlates with the inclination angle (see Fig. 12). Thus, a spectral resolving power of $R \sim 50000$ is well suited to resolve the lines. The kinematic information provides constraints on the location of the emitting gas in the disk. Both collisional excitation in the inner dense warm gas ($<1 \text{ AU}$) and resonance fluorescence in the outer disk play a role in the CO excitation, and extended CO has been detected out to radial distances of $\sim 20 \text{ AU}$ ($0.3'' \text{ } \varnothing$ at 150 pc). A particularly interesting question is if gas is still present in the gaps in images of a dust disk. T-OWL can spatially resolve the CO emission in the nearest disks.

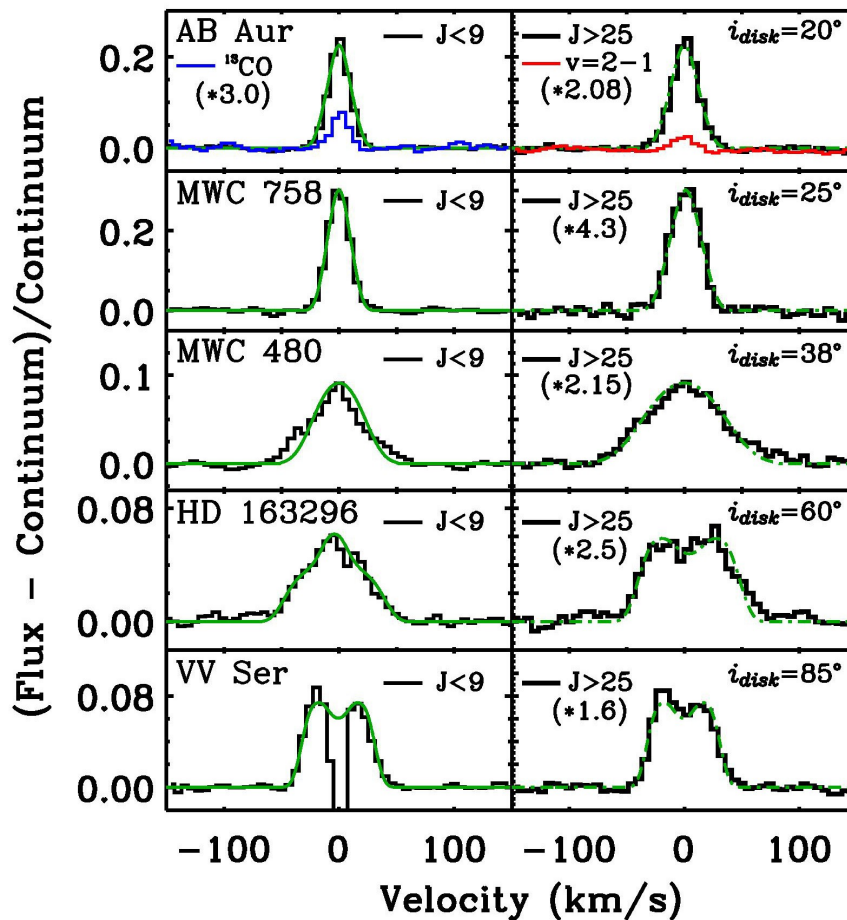


Fig. 12: CO $v=1-0$ line profiles at 4.7 mm obtained with Keck-NIRSPEC at $R=25,000$, produced by averaging over all low- J levels (left panels) and high- J levels (right panels). The green lines represent disk model fits to the data (Blake & Boogert 2004). T-OWL can both spatially and spectrally resolve the CO emission.



T-OWL Concept Level Study

Doc : OWL-CSR-ESO-00000-0161

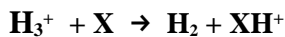


Version 1
Date: 20/10/2005
Page: 38/175

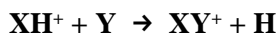
H_3^+ emission at $3.9\mu\text{m}$

H_2 , CO and H_3^+ are the three molecules most fundamental and abundant in the interstellar medium. They often control chemistry and physics whatever their environment.

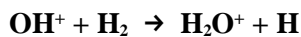
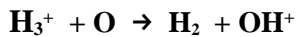
H_3^+ is 10,000 times less abundant than molecular hydrogen in dense molecular clouds, and 10^7 times less in diffuse clouds. However, the molecular ion still plays a pivotal role in the interstellar chemistry. H_3^+ is a universal protonator that works with almost any atoms and molecules of X with few exceptions:



leaving X in the highly reactive state XH^+ , which may further react with Y



resulting in the larger molecule XY^+ . The most relevant reaction among these may be



where H_3^+ opens a critical path to create, e.g., the water on the earth. The detection of the molecular ion in the ISM only goes back a decade (Geballe & Oka 1996) after a long enduring search initiated a quarter century ago (Oka 1981). Despite the significant consequence H_3^+ may have in the chemical network in the ISM, the ion molecules is not yet well understood itself. A simple steady state analysis predicts 3 orders of magnitude less H_3^+ in diffuse clouds than in dense clouds (McCall et al. 1998), while the observations have found similar abundance in both environments. The observation forced to change the zeta, the ionization rate of the molecular hydrogen, which initiates many chemical reactions in the ISM and is the fundamental value for interstellar chemistry (Geballe & Oka 1996, Nature, 384, 334; Oka 1981, RSPTA, 303, 543; McCall, B. J., et al. 2003 Nature, 422, 500; Goto et al. 2002, PASJ, 54, 951; Oka et al. 2005, ApJ, submitted).

The H_3^+ ion has strong emission bands at $3.9\mu\text{m}$. These lines have been detected in the polar regions of Jupiter in our own solar system, and may be prominent as well in exo-planetary atmospheres. A possible detection of H_3^+ lines in the HD 141569 transitional disk has been claimed by Brittain & Rettig (2002), but has not been confirmed by subsequent searches (Goto et al. 2005). Nevertheless, like the H_2 mid-IR lines, these are pioneering attempts to develop previously unexplored spectroscopic diagnostics of the planet formation process, and T-OWL will push these studies significantly deeper.

Note on design requirements

Observation type	TIR/MIR-spectroscopy
Spatial resolution	diffraction
FOV	2"
Spectral resolution	3000, 50000
Wavelength range	3 - $20\mu\text{m}$
Min. telescope size	60m
Special requirements	none
comments	

5.3.4 Organic Molecules in the Planet-Forming Zones

Gas-phase molecules

Besides CO and H₂, several other molecules have vibration-rotation bands at wavelengths accessible from the ground with T-OWL. Molecules such as CH₄ (7.7μm), C₂H₂ (13.7μm) and HCN (14.0μm) are key species in the organic chemistry that occurs in the inner (<20 AU) planet-forming zones of disks. At the high temperatures in these regions, even more complex organic molecules can be formed (Markwick & Charnley 2004), which could be detected via their C-H stretching vibration in the 3-4μm region. Indeed, this wavelength range is the fingerprint region for different hybridized bonds of sp³ (e.g. CH₄), sp² (e.g. C₂H₂) and sp (C₂H₂) type. O-H and N-H bonds also have signatures in this range. ALMA cannot see symmetric molecules without a dipole moment, such as CH₄ and C₂H₂, which are the main building blocks of organics.

The excitation and line widths of these molecules provide additional information on their location in the disk. Models predict that the abundances of CH₄ and C₂H₂ will peak somewhat further away from the star than that of the very stable CO molecule, so their widths are expected to be narrower, requiring high spectral resolution. The ortho/para ratio of methane also provides clues about the conditions during the formation of the solar system (Mumma et al. 2001, Kawakita et al. 2005). High spectral resolution is absolutely crucial to resolve them.

The molecular lines are usually expected to be in emission, except in the case of edge-on disks, where they may be in absorption. An excellent example is provided by IRS46 in Ophiuchus (Fig. 13), for which the Spitzer-IRS spectrum shows surprisingly strong absorption by gaseous C₂H₂, HCN and CO₂ in the 13-15μm region, indicating temperatures of 300-900 K and very high abundances up to 10⁻⁵ with respect to H₂. Its spatial extent is constrained to be less than 20 AU. The origin of this hot gas is currently unclear; the most likely explanation is that the absorption occurs against the warm dust near the mid-plane of the inner disk and that the line of sight intersects the puffed-up inner rim. The width of the lines is estimated to be Δv~10 km/s, as confirmed by spectrally resolved HCN absorption at 3μm. T-OWL will have the spectral resolution to resolve the mid-IR lines and search for other species such as CH₄. Moreover, its high spatial resolution and sensitivity offers the opportunity to do spatially resolved *absorption* spectroscopy against the disk photosphere. Spitzer and ground-based infrared surveys are discovering more of such edge-on candidates and at least two dozen are expected to be known by the time of T-OWL observations.

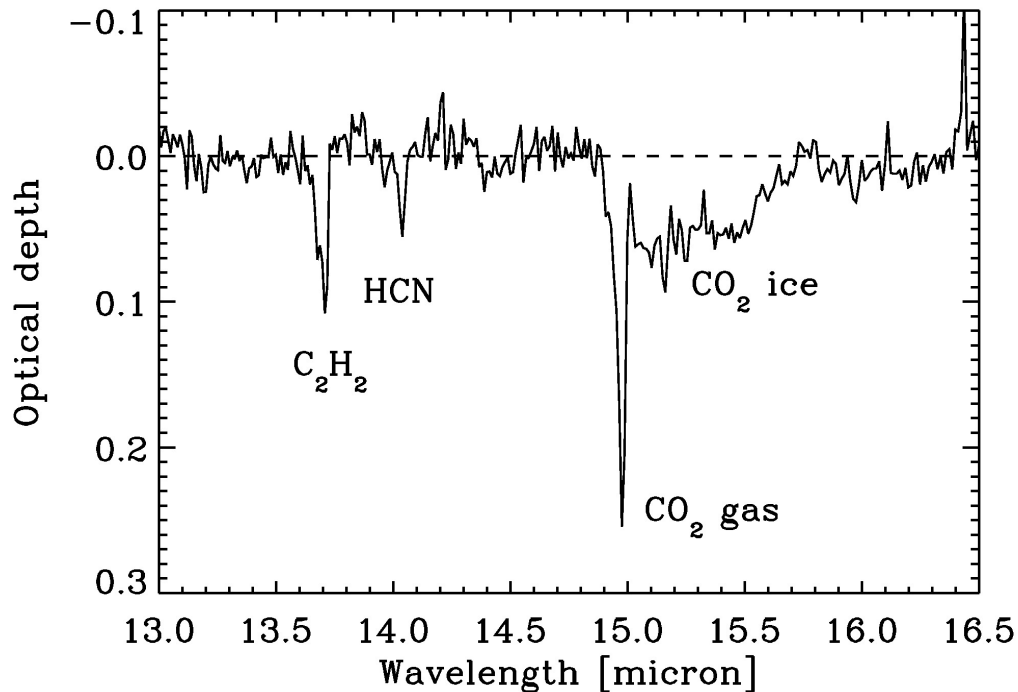


Fig. 13: Spitzer-IRS spectrum at $R=600$ toward the edge-on disk IRS46 in Oph (Lahius et al. 2005).

Ices

At low temperatures (<90 K), the organic molecules will be frozen out as icy mantles on the grain cores where they can also be studied through infrared spectroscopy. Examples are solid H₂O ($3\mu\text{m}$), HDO ($4\mu\text{m}$), CO ($4.67\mu\text{m}$), OCN⁻ ($4.62\mu\text{m}$), CH₄ ($7.67\mu\text{m}$), NH₃ ($9.0\mu\text{m}$) and CH₃OH ($3.5, 9.7\mu\text{m}$) bands, which can be observed from the ground. The line of sight through edge-on disks can intercept also the cold outer layers of the disk where these molecules are frozen out. An example is the edge-on disk CRBR2422.8-3423 whose spectrum shows very deep ice absorptions (Thi et al. 2002, Pontoppidan et al. 2005). A spectral resolving power $R\sim 3000$ is needed to properly sample the line profiles, which vary from source to source and contain interesting information on the ice environment and temperature history. Moreover, high spectral resolution is essential to properly remove the telluric lines, which completely dominate the signal-to-noise ratio that can eventually be reached. A S/N ratio of more than 100 is needed to put limits on interesting ice ratios such as HDO/H₂O for comparison with cometary and solar-system data (Dartois et al. 2003, Parise et al. 2003).

PAHs

PAHs are the largest organic molecules that can be observed in disks. Their strong emission features dominate the structure of the MIR spectrum (Fig. 14) PAHs are not only interesting for the disk chemistry, but are also excellent diagnostics of the UV radiation incident on the disk surface, and thus its flat or flaring geometry (Acke & van den Ancker 2004). Moreover, they are important in heating the gas to temperatures higher than that of the dust through photo-ionization (Jonkheid et al. 2004). In contrast to the thermal dust emission, the PAH features are known to be extended to radii of at least 30 AU, as demonstrated by spatially-resolved spectroscopy on 8-m class telescopes (Habart et al. 2004, Geers et al. 2004). The spatial extent is expected to vary from feature to feature; for example,

the $3.3\mu\text{m}$ feature is predicted to be more compact than the $11.3\mu\text{m}$ feature. These models can be directly tested by spatially resolved spectroscopy with T-OWL at 10 AU resolution.

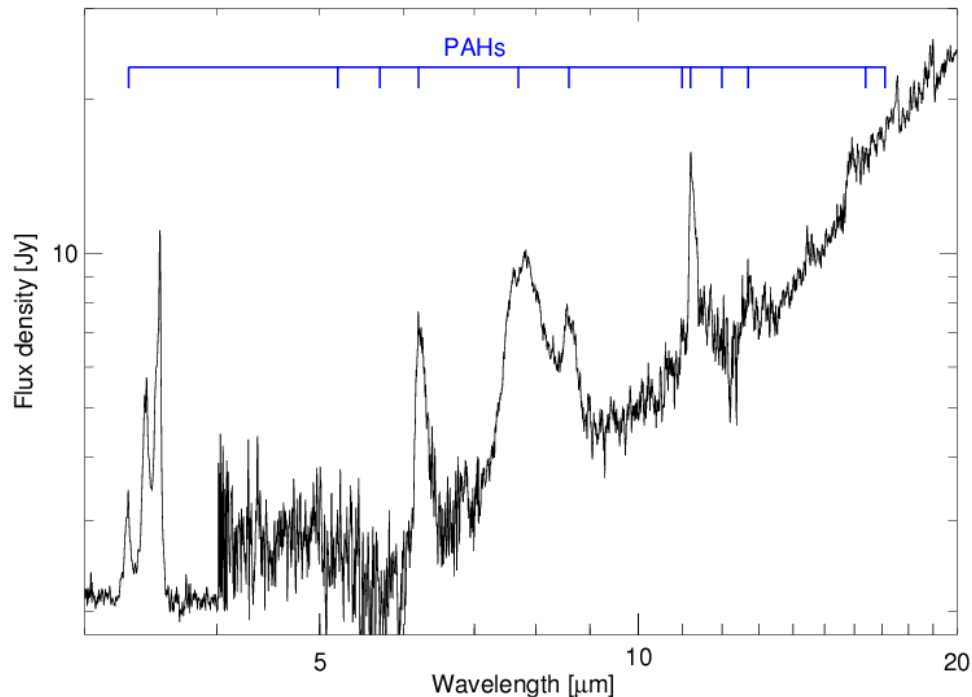


Fig. 14: ISO-SWS spectrum of the Herbig Ae/Be star HD 97048. The strength of the various PAH emission features – predominantly those at 3.3 , 6.2 , 7.6 , 7.8 and $8.6\mu\text{m}$ – makes them important diagnostics tool (van Kerckhoven et al. 2002). The features at 3.3 and $8.6\mu\text{m}$ are easily observable from the ground.

Note on design requirements

Observation type	TIR/MIR-spectroscopy
Spatial resolution	diffraction
FOV	2"
Spectral resolution	50000
Wavelength range	3 - $20\mu\text{m}$
Min. telescope size	30m
Special requirements	none
comments	

5.4 Proto-Stars

Deeply embedded young stellar objects with hundreds of magnitudes of visual extinction are prime targets for high-resolution mid-infrared spectroscopy. Traditionally, efforts have focused on high-mass proto-stars with luminosities of 10^4 – $10^5 L_{\odot}$. The high luminosity sets up a temperature gradient in the gas and dust through the envelope, with temperature up to a few hundred K in the inner part, decreasing to 10–20 K in the outer part. This temperature range is well probed by the CO fundamental ro-vibrational bands at $4.7\mu\text{m}$, and indeed, a forest of strong lines of ^{12}CO and ^{13}CO is routinely detected (e.g., Mitchell et al. 1990). Rotational diagrams such as presented in Fig. 15 provide a direct measure of this temperature gradient. High spectral resolution is essential to resolve the lines, since many of them are highly saturated. Intrinsic line widths are typically a few km s^{-1} , with outflow components of up to 100 km s^{-1} .

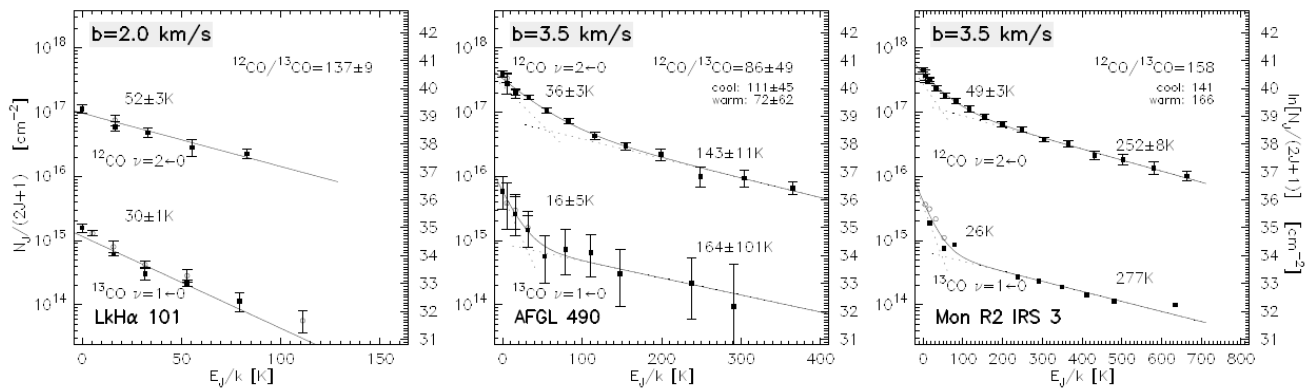


Fig. 15: Rotational diagrams of CO molecules in the hot cores in massive star forming regions. Multiple line observation works as a thermometer (Goto 2005).

Many other molecules can be identified in these spectra. Detections include gaseous CH_4 , C_2H_2 , HCN , NH_3 , HNCO and CH_3 at 7 – $14\mu\text{m}$, indicative of a rich chemistry in the hot cores near the proto-stars (Lacy et al. 1989, 1991; Evans et al. 1991; Boogert et al. 1998; Lahuis & van Dishoeck 2000, Knez et al. 2003). These mid-infrared lines are highly complementary to the sub-millimeter lines of massive YSOs, which are biased toward the cooler outer layers. The infrared spectra of the coldest proto-stars are also full of ices, which can be probed at $R \sim 3000$ (Gibb et al. 2000).

The previous data were limited to the brightest, most massive proto-stars ($> 100\text{Jy}$ at mid-IR); T-OWL would allow solar-mass proto-stars with luminosities comparable to those of our proto-Sun (10 – 100 mJy) to be probed. An exciting prospect is that the line of sight may pass through the flaring layers of the forming circumstellar disk (Boogert et al. 2002, see also section 5.3.3). The physical parameters and kinematics of young disks are still highly uncertain; for example, it is not known whether the disk is hot or cold, and what the velocity pattern of the in-falling and rotating gas is. The lines are usually seen in absorption, so high spectral resolution to enhance the line/continuum ratio is the key. At the high spatial resolution, some emission lines from the inner region may be superposed on the absorption spectrum, as evidenced by VLT spectra (Pontoppidan et al. 2003). The emission can arise either from the disk, from in-fall or from the inner part of the outflow. The integral field unit, combined with the high spectral resolution, can beautifully trace the origin of such emission.



T-OWL Concept Level Study

Doc : OWL-CSR-ESO-00000-0161



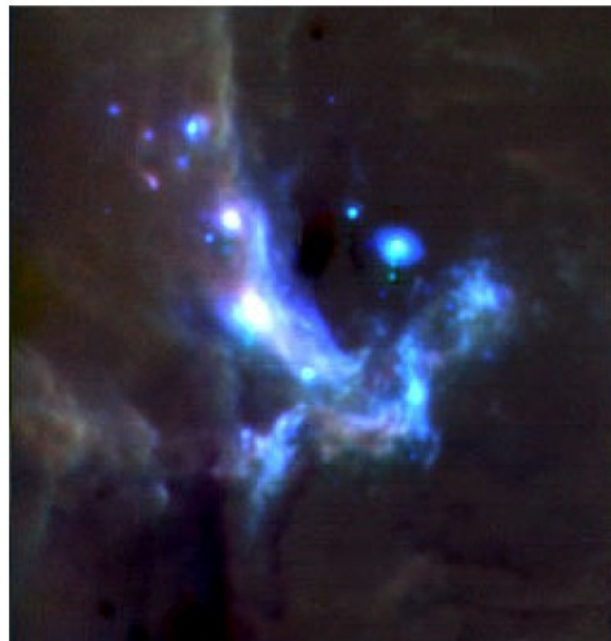
Version 1
Date: 20/10/2005
Page: 43/175

Note on design requirements

Observation type	TIR/MIR-Spectroscopy
Spatial resolution	diffraction
FOV	4"
Spectral resolution	50000
Wavelength range	3 - 20 μ m
Min. telescope size	60m
Special requirements	none
comments	

5.5 The Galactic Center

Even though the GC is largely shrouded by surrounding gas and dust, it is being explored very actively by observations at radio, sub-millimeter, infrared, X-ray and γ -ray wavelengths. All constituents of the inner few parsec, the super-massive black hole, the surrounding cluster of stars, streamers of ionized gas, a molecular dust ring and a supernova remnant as well as their mutual interaction have been studied extensively during the last years. A nice overview is given by F. Melia and H. Falcke (2001).



Colour Composite of the Galactic Centre
(VLT Melipal + VISIR)

ESO PR Photo 16d/04 (12 May 2004)

© European Southern Observatory



Fig. 16: The Galactic Center: Color composite using filters centered at 8.6 μ m (coded blue), 12.8 μ m (coded green) and 19.5 μ m (coded red). Each pixel subtends 0.127 arcsec and the total field of view is $\sim 33 \times 33$ arcsec (North at the top and East to the left). Total integration times were 300, 160 and 300s for the 3 filters, respectively.

High spatial resolution imaging of Sgr A* at NIR, MIR, sub-millimeter and radio wavelengths can ultimately distinguish between different accretion and emission models of the source. Unfortunately, the intrinsic size of Sgr A* has remained fairly unresolved at cm and longer wavelengths because radio waves from Sgr A* are scattered by turbulent interstellar plasma along the line of sight, an effect that is proportional to λ^2 . This effect, which is even atypically strong for Sgr A*, has pushed observations to shorter and shorter wavelengths. ALMA will be a powerful tool for such observations. MIR observations of highest spatial resolution will significantly contribute to this exciting puzzle by improving drastically the sensitivity for point sources in the 3 – 25 μ m wavelength regime: Broad band observations for this regions at present give upper limits that are a factor 2 to 10 above the theoretically expected SED for Sgr A* spectrum calculated based on a variety of accretion- and jet models. In this case, detectivity of Sgr A* is not limited by the thermal background of our atmosphere but by the diffuse emission of the surrounding gas and dust., thus, the point-source detectivity can not be improved by satellite observatories. However, a MIR diffraction limited resolution camera attached to a 60 - 100m-telescope should clearly be able to detect Sgr A* and distinguish between the different models by measuring the broad band flux coming from the central ≤ 17 Schwarzschild radii. To detect Sgr A* at 10 μ m, at least a telescope diameter of 60m seems to be necessary.

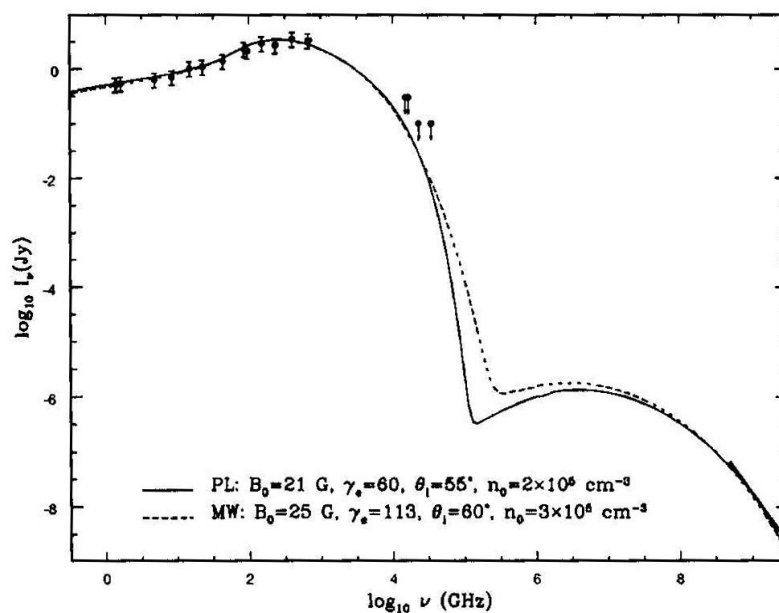


Fig. 17: Broad band spectrum of Sgr A produced by a jet model, with a power-law(PL) and a relativistic Maxwellian (MW) electron distribution, compared to radio and IR observations (From F. Melia and H. Falcke, 2001)*

Similar problem applies to many other galactic nuclei. Building the IR SED of any galactic nucleus still relies on poor resolution spatial data from IRAS, ISO, SPITZER, and seeing-limited near-IR data.

Thanks to the advent of adaptive optics (AO) and mid-IR interferometry in 8-10 m class telescopes, near to mid IR SED of the central few parsec region of galaxies have been possible to produce for a privileged number of them - actually active nuclei only. These “central parsecs” SED are turning to be rather different from what we knew before.

The misleading effect of using large aperture data in interpreting SEDs of nuclear regions is well illustrated in Fig. 18 with the prototype AGN, NGC 1068. Fig. 18 shows the highest spatial resolution SED that we can build today of the nucleus of this galaxy on the basis of AO near-IR data (VLT/NACO, FWHM $\sim 5-10$ pc), mid-IR interferometry data (VLT/MIDI, FWHM ~ 2 pc) and radio data (VLBA, FWHM < 1 pc). The SED is complemented with Chandra X-ray data (FWHM ~ 70 pc) and millimetric interferometry data (FWHM ~ 110 pc). NGC 1068 nucleus is fully absorbed in the UV-optical, hence the data gap in this range.

Focusing in the IR, the figure also includes *{best extracted nuclear fluxes}* from HST/NICMOS, ground-based mid-IR and ISO (from Alonso-Herrero et al. 2004), and IRAS/ISO beam-resolution data. To guide the eye, all these IR data are connected with a line. It is obvious from the figure that the trend outlined by the high resolution NACO and MIDI IR-data is very different from that traced by the larger-aperture defined by the line-envelope, in shape and integrated power. The progressive change in the SED between the large-aperture and MIDI data can already be seen by comparing with seeing-limited mid-IR nuclear fluxes extracted from de-convolved Keck/MIRLIN images (Bock et al. 2000, AJ 120, 2094), also shown in the figure.

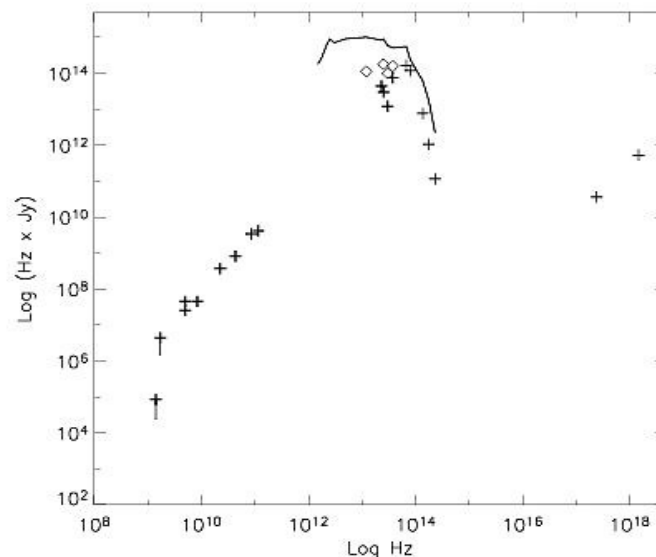


Fig. 18. Today’s highest spatial resolution SED of the nucleus of NGC 1068, based on NACO, MIDI and VLBA data (crosses). X-ray data from Chandra and EXOSAT is also included. The effect of large-aperture data is illustrated with the tick-line which outlines extracted nuclear fluxes from HST/NICMOS, ISO and IRAS. Diamonds are Keck mid-IR nuclear fluxes extracted from de-convolved images. Compilation by A. Prieto.

The change in the SED simply illustrate the effect of sampling different physical regions with increasing spatial resolution. It points out the risk of getting misleading interpretations when limited to data that includes information from distinct physical regions. MIDI with a 100 m base-line

configuration provide us spatial resolutions comparable to that of OWL at 10 μm ; yet MIDI is restricted to the brightest objects in the sky, and to a very reduced spectral range. TOWL will provide us with parsec-scale resolutions in the 3-20 μm range of any galactic nuclei up to the Virgo distance. This means the possibility of producing, together with VLBI, ALMA and OWL near-IR data, the most genuine SED of the core region of galaxies regardless of galaxy morphological-type or activity level. The physics of accretion by the putative BH in the centers of galaxies will then be possible to test in the galaxies of today and in comparison with our Galactic Center.

In the 10 -20 μm range, JWST will provide spatial resolutions comparable to what we can get today with the VLT under Paranal “average-seeing” conditions in the optical. Thus, albeit JWST sensitivity, only instruments as TOWL will provide the quantum jump in resolution that is needed.

Note on design requirements

Observation type	MIR-imaging/spectroscopy
Spatial resolution	diffraction
FOV	2“
Spectral resolution	300, 3000
Wavelength range	8 - 25 μm
Min. telescope size	60m
Special requirements	IFU
comments	

5.6 The IMF in Star-Bursts

Star-bursts represent a fundamental mode of galaxy evolution and star formation. In a star-burst, a galaxy undergoes – within a short period of time (less than 10^8 years) – major changes in luminosity, morphology, color, spectral energy distribution (SED), stellar population, gas and dust content, and metallicity. Star-bursts are central to our understanding of the Hubble sequence and the evolution of galaxies as a whole. In addition, star-bursts often go hand-in-hand with the phenomenon of active galactic nuclei (AGNs), which will be addressed below. Given the increased merger rate at higher redshift, and the fundamental role that merging events play in the evolution of the galaxy population, the physical conditions in obscured star-bursts are of central importance to our understanding of galaxy evolution. The initial stellar mass function (IMF) plays a central role in this context.

Star-burst galaxies are usually heavily dust extincted, and therefore only accessible at infrared wavelengths. A dramatic illustration of this effect is found in the nearby merging system NGC 4038/4039 (the "Antennae", Fig. 19 and 20). The Hubble Space Telescope (HST) revealed hundreds of compact young star clusters. However, MIR images obtained with ISO and Spitzer show that most of the star formation takes place in an optically obscured region where the two disks interact directly. One spectacular super star cluster in this regions accounts for more than 15% of the luminosity of the entire galaxy at 15 μm , yet it is optically almost totally invisible.



Fig. 19: Spitzer-IRAC colour composite of the 3.6 μ m, 4.5 μ m, and 8 μ m filter bands.



Fig. 20: HST-WFPC2 image (below) and a larger scale DSS image showing the tails that gave it its nickname.

Basically, there are two general methods to study the IMF in a dusty star-burst system, namely via the dynamical mass estimates of super star clusters (SSC), and via star-burst modelling. Both will be discussed in the following sections.

5.6.1 Dynamical Masses of Super Star Clusters

Deriving the total masses, densities, and IMFs of super star clusters would be of greatest interest regarding their future evolution toward globular cluster systems, the origin of the galactic field star population, and the time scales and sub structures of luminous star-bursts.

At 3.5 μ m T-OWL could provide seven times higher spatial resolution than HST/WFPC-2 for the study of heavily embedded super star clusters – while the negative impact of extinction is minimized. The importance of high angular resolution is illustrated in Fig. 21, which shows R136, one of the most nearby dense star-burst clusters, artificially shifted toward larger distances. Fig. 22 shows the derived cluster core radius that would be measured at a given distance. Obviously, only the highest possible spatial resolution is barely sufficient to derive the correct light profiles of such a system. Even at the resolution of HST such estimates can be off by an order of magnitude.

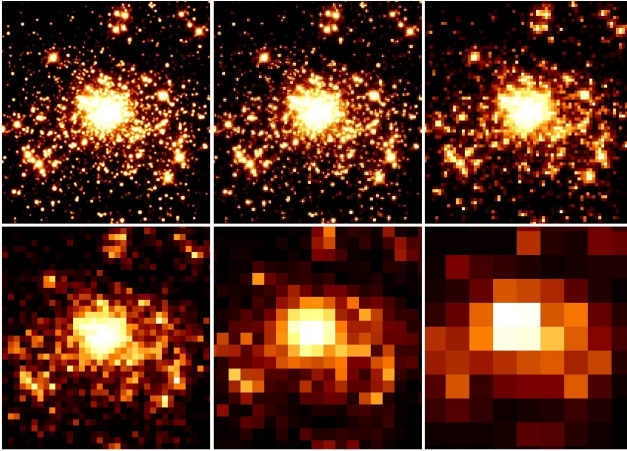


Fig. 21: HST/NICMOS image of R136 re-binned by factors of two (from left to right: x2, x4, x8) to simulate greater distances (Brandl et al. 2004).

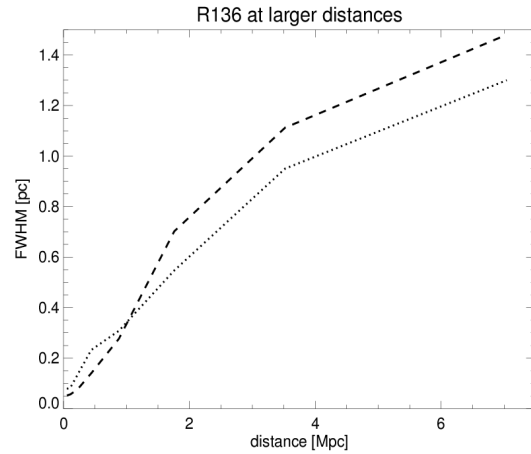


Fig. 22: The core radius derived by a simple Gaussian fit to the cluster at a given “distance”.

Once the cluster radius r_{hl} has been determined from high resolution imaging, and the cluster velocity dispersion σ has been measured by medium resolution spectroscopy (at high angular resolution, requiring an IFU), the dynamical masses of these systems are derived via:

$$M_{dyn} = \eta \frac{\sigma^2 r_{hl}}{G}$$

Measuring the total luminosity then allows to derive the mass-to-light ratio, and to infer the IMF for a given cluster. Current estimates are rather uncertain with errors dominated either by extinction, spatial resolution or poor signal-to-noise. T-OWL will provide a breakthrough in this field.



T-OWL Concept Level Study

Doc : OWL-CSR-ESO-00000-0161



Version 1
Date: 20/10/2005
Page: 49/175

5.6.2 Star-burst modelling

Spectroscopy in the MIR region is of fundamental importance to star-burst research. The spectral range covered by T-OWL contains a large variety of unique diagnostic tools, from polycyclic aromatic hydrocarbons (PAHs), molecular hydrogen, and forbidden transitions of fine-structure lines, to silicate features. Altogether, these diagnostics provide excellent measures of the local kinetic temperatures and gas densities, and the properties of the exciting radiation field. Table 1 lists the main diagnostics within the TIR and MIR bands shortward of $20\mu\text{m}$.

Table 2 The main spectral diagnostics for star-bursts in the L, M, N and Q bands.

Feature	Wavelength	Excitation or mode
Br- α	$4.05\mu\text{m}$	
H (7-6)	$12.37\mu\text{m}$	
[Ar III]	$8.99\mu\text{m}$	27.6 eV
[S IV]	$10.51\mu\text{m}$	34.8 eV
[Ne II]	$12.81\mu\text{m}$	21.6 eV
H ₂ S(3)	$9.66\mu\text{m}$	1015 K
H ₂ S(2)	$12.28\mu\text{m}$	510 K
H ₂ S(1)	$17.03\mu\text{m}$	170 K
PAH	$3.3\mu\text{m}$	C-H stretching
PAH	$8.6\mu\text{m}$	C-H in-plane bending
PAH	$11.3\mu\text{m}$	C-H out-of-plane bending
PAH	$12.7\mu\text{m}$	C-H out-of-plane bending
Silicate	$9.7\mu\text{m}$	Si-O stretching
Silicate	$18.0\mu\text{m}$	O-Si-O bending

The combination of several spectral features provides an excellent basis for star-burst modelling. However, since the spatial extent and distribution of higher excitation regions with respect to lower excitation regions varies on parsec-scales, spectroscopy at highest angular resolution is crucial.

The problem of low spatial resolution is illustrated in Fig. 23: the ratio of the two ionization states of Neon [Ne III] / [Ne II] is a good measure of the hardness of the ionization field and hence a probe of the most massive stars (and thus the IMF) in a star-burst. However, the measurement from ISO-SWS (Fig. 23) indicate a much lower ratio of [Ne III] / [Ne II] than model predictions based on a Salpeter-like IMF. The most likely explanation is an aperture effect, caused by the wide ISO-SWS slit. The medium resolution IFU spectrograph of T-OWL will provide 500 times narrower “slits” making it possible to model the properties of physical regions rather than spatially averaged systems. For instance, the spatial resolution of the T-OWL IFU at $10\mu\text{m}$ corresponds to only 0.4 pc at the distance of NGC 5253. Unfortunately, the [Ne III] line lies outside the atmospheric window, but for the purpose of these studies it can be replaced by the [S IV] line (see Tab. 2).

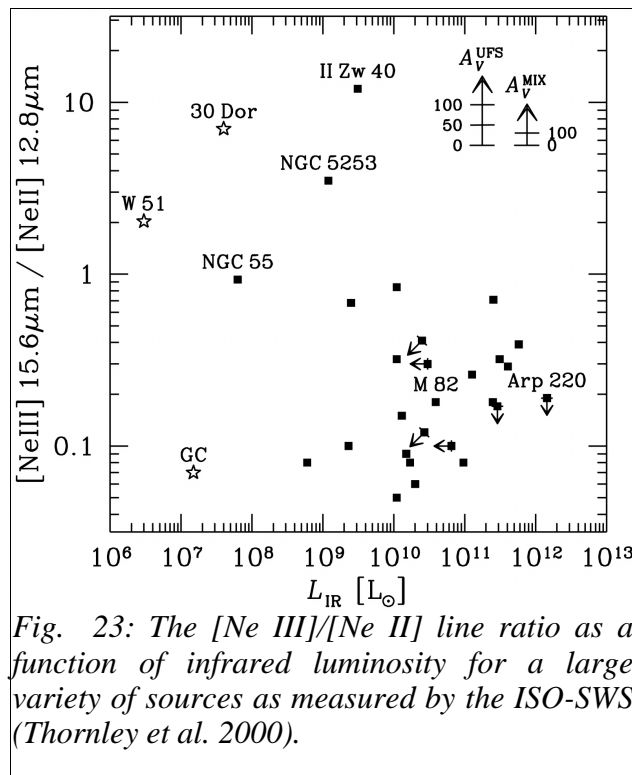


Fig. 23: The $[Ne\ III]/[Ne\ II]$ line ratio as a function of infrared luminosity for a large variety of sources as measured by the ISO-SWS (Thornley et al. 2000).

Note on design requirements

Observation type	TIR/MIR-imaging/spectroscopy
Spatial resolution	diffraction
FOV	4"
Spectral resolution	3000
Wavelength range	3 - 20 μ m
Min. telescope size	60m
Special requirements	IFU
comments	

5.7 Active Galactic Nuclei at Low Redshift

Numerous models have been proposed to describe the scales, mechanisms and components within active galactic nuclei (AGN). Fig. 24 illustrates the “standard unification model” for AGN. From this figure it becomes clear that the relevant scales to probe the inner regions of AGN are in the order of fractions of parsecs. T-OWL will be able to resolve 1.4 pc at the distance of NGC 1068, i.e., the molecular torus, and hence the broad line region, can be resolved! With NACO today we resolve 1pc only in the nearest AGN, with T-OWL we will resolve 1.5 pc in *any* galaxy – regardless extinction- at the Virgo distance.

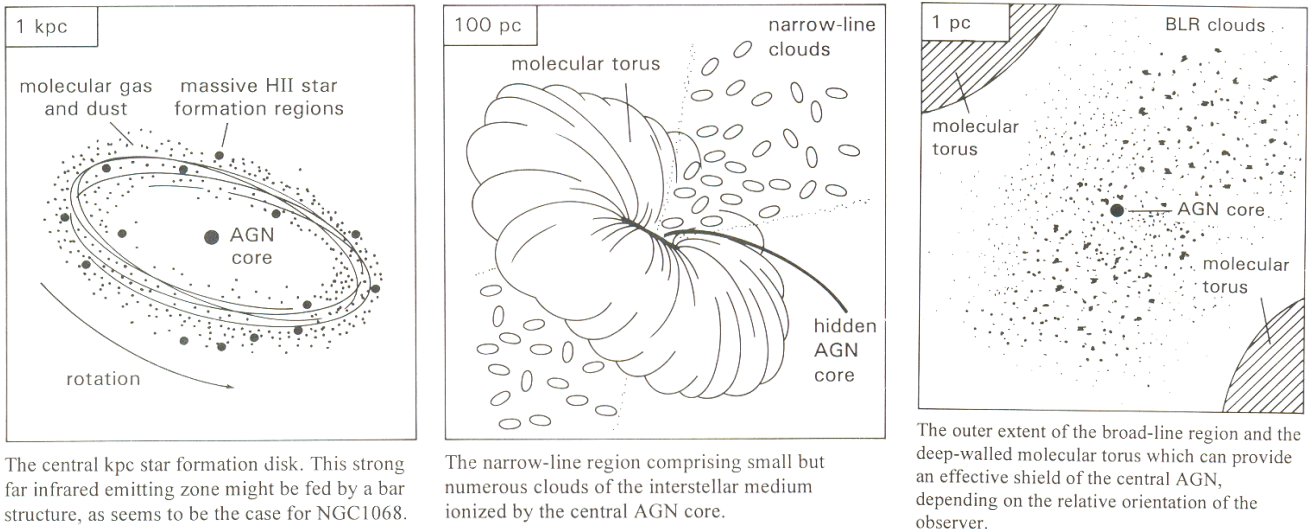


Fig. 24: The relevant length scales of structures around an AGN (from Robson 1996, Fig. 9.9)

Geometrically, molecular tori around AGN act similar to circumstellar disks. A dusty AGN serves as a background illumination source to observe the foreground CO absorption on their continuum spectra. However, obscured Seyfert-2 AGN are usually by far fainter ($M \geq 9$ mag) than the intragalactic sources ($M < 7$ mag). The CO absorption line at $4.7 \mu\text{m}$ has been detected only for a handful of AGN. The first successful attempt had to wait for high resolution spectrographs available at 8-m class telescopes, newly uncovering an intriguing picture of molecular tori unknown before (Shirahata et al. in prep.; Spoon et al. 2004, ApJS, 154, 184). The lines of sight are typically filled with high velocity infalling gas and outflow, with velocity dispersions up to ~ 250 km/s. The temperature of the gas is bifurcated into several components of cold ($T < 50\text{K}$) and hot gas ($T > 300\text{K}$). The critical density of CO and its temperature constrains the location of the gas as close as 0.01 pc to the central heat source, proving a novel means to access the central engine. Observations at spectral resolutions above $R \sim 5,000$, which would reveal the kinematics of the molecular gas, have not been possible so far due to insufficient sensitivity of 8-10m class telescopes. The rotational levels as high as $J > 20$ are populated because of the high temperature in the molecular tori.

VLT/VISIR has recently observed NGC 1068 in the [Ne II] line, imaging the angular structure around the AGN in unsurpassed detail (Fig. 25). T-OWL will have more than $12\times$ the resolution of VISIR and be able to zoom in much closer to the nucleus to reveal the distribution of material and the motion of the accreting matter.

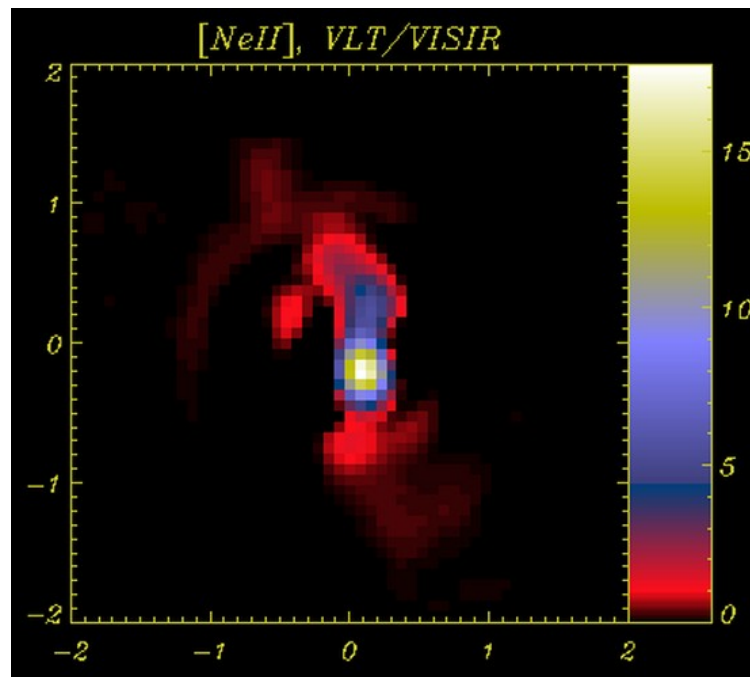


Fig. 25: VISIR map of NGC 1068 in the [Ne II] line.

The conditions around an AGN can also be probed via the shape of the silicate dust feature around $10\mu\text{m}$. Jaffe et al. (2004) used the VLTI-MIDI to investigate the conditions around the nucleus of NGC 1068 on milli-arcsecond scales. Figs 26 and 27 show MIDI spectra taken with a large beam (corresponding to traditional ground based resolution in the mid-IR) and a zoom-in on the very centre with VLTI resolution. Not only does the strength of the silicate absorption feature change significantly (indicating that the central nucleus is heavily dust enshrouded), but the shape of the feature changes as well (indicating that the dust grains have been processed by the strong radiation field from the AGN). Jaffe et al. argue that the modified shape indicates a larger fraction of amorphous aluminium-rich silicates – possibly crystallized – which require rather high condensation temperatures.

T-OWL would be able to provide images and 2-dimensional spectra at even higher angular resolution for a much larger sample of objects in two dimensions, enabling the study of the distribution of grain properties relative to the dust tori, accreting matter and jets from the black hole.

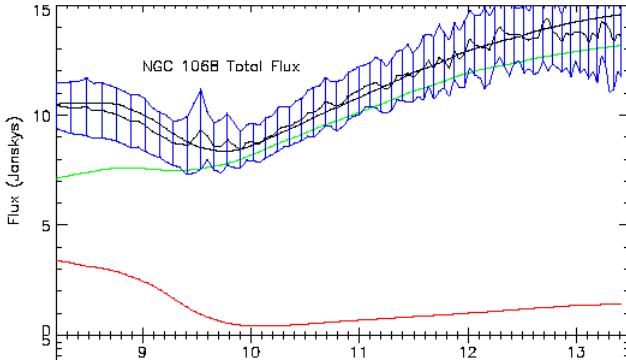


Fig. 26: Spatially integrated VLT/MIDI N-band spectrum of the nuclear region of NGC 1068 (Jaffe et al. 2004).

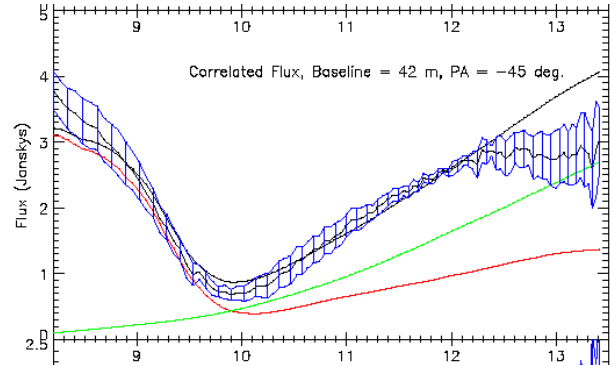


Fig. 27: VLT/MIDI N-band spectrum of the very center of NGC 1068 (Jaffe et al. 2004).

Note on design requirements

Observation type	TIR/MIR-imaging/spectroscopy
Spatial resolution	diffraction
FOV	2"
Spectral resolution	3000
Wavelength range	3 - 20 μ m
Min. telescope size	60m
Special requirements	IFU
comments	

5.8 Ultra-Luminous IR Galaxies (ULIRGs)

The most extreme star-bursts are found in mergers of gas-rich galaxies, where the dissipative gas components quickly sink to the centre of the potential well, resulting in an intense burst of star formation. The ultra-luminous infrared galaxies (ULIRGs) are a manifestation of this phenomenon, and approach quasar-like luminosities, which are, however, almost entirely emerging in the infrared. Based on the high luminosities, it has been suggested that powerful AGN are born in the obscured cores of gas-rich mergers. Observational studies of this important phenomenon require very high angular resolution at MIR wavelengths, which can only be attained with an aperture greater than 50 meters.

Locally, ULIRGs are rare objects and of little importance in the overall star formation budget. However we now know that this was fundamentally different at higher redshifts. Indeed, recent sub-millimetre surveys have revealed a rich population of high- z ULIRGs, which are responsible for a large fraction of the integrated sub-millimetre background and are plausibly the progenitors of present-day elliptical galaxies. This would imply that the origin of the relation between spheroid mass and nuclear black hole mass, which is believed to lie in the formation mechanism of these galaxies, is related to the ULIRG phase.

Many ultra-luminous infrared galaxies contain an intense star-burst as well as an AGN. Does the occurrence of an extreme star-burst trigger the formation of an AGN? How does this depend on parameters of the star-burst? In the earlier stages the build-up of the stellar population and/or the central black hole may be a violent and mostly obscured process (after the first chemical enrichment and thus dust formation has taken place). All of these questions are directly relevant to our understanding of the formation and evolution of galaxies and their components. However, to answer these questions it is necessary to perform imaging spectroscopy in the mid-IR range at an angular resolution of about 20 milli-arcseconds at $10\mu\text{m}$, provided by a diffraction limited 100m OWL telescope.

In the nearest ULIRGs like Arp 220 (Fig. 28), the resolution provided by a 100m aperture will allow to spatially resolve AGN, individual supernova remnants, SSCs, and HII regions, and spectrally classify these components.

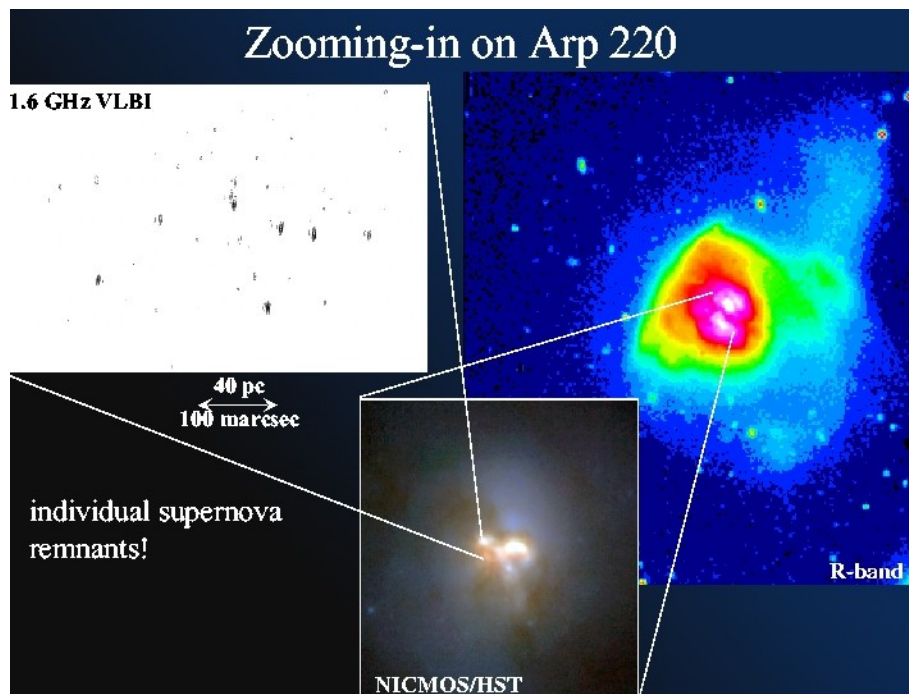


Fig. 28: A zoom-in on the nuclear region of the nearest ULIRG, Arp220. At a resolution of $0.02''$, the detailed structure of the central power source can be resolved.

Fig. 29 shows a [Ne II] velocity map of the star-burst/Seyfert galaxy NGC 7582, taken with VLT/VISIR in HR mode (Wold et al. 2005). From various models an upper limit on the black hole mass of $\leq 5 \cdot 10^7 M_{\odot}$ could be derived for this galaxy. To appreciate the power of and need for angular resolution, we note that the nearest ULIRG, Arp220, is already at a relatively large distance of 75 Mpc. For a rather limited sample of ULIRGs we must already reach out to distances of ~ 200 Mpc. At 200 Mpc distance, even a 100m OWL telescope has only a resolution of 50 pc at $10\mu\text{m}$ – which is still sufficient to reveal unprecedented details of the nuclear region.

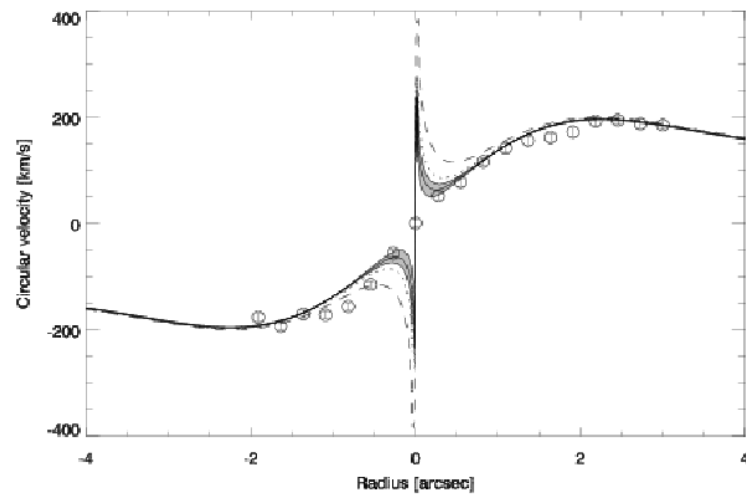


Fig. 29: *[Ne II]* velocity map of the starburst/Seyfert galaxy NGC 7582, taken with VLT/VISIR in HR mode (Wold et al. 2005).

The various spectral features listed in Tab. 2 probe different environments in the nuclear region: the ionic lines probe the photo-ionized gas, PAH emission arises from UV-irradiated photo-dissociation regions (PDRs) and traces massive star formation, H₂ lines probe the warm molecular gas, the broad silicate feature, which covers a large fraction of the N-band, contains information on the amount of absorbing material along the line of sight and additional information on the AGN. In the vicinity of the AGN significant PAH emission features are usually not observed (e.g., Sturm et al., 2000), because the PAH molecules are most likely being destroyed by the hard X-ray radiation. This effect can be used to separate the contributions from star-burst and AGN to the total mid-infrared output of the ULIRG, sufficient spatial resolution provided. In addition, the variation in physical conditions can be studied in detail by tracing ionization structure with the [S IV] 10.5 μ m emission line, the distribution of warm neutral gas using the H₂ S(3) 9.66 μ m line and from the amount and nature of the material obscuring the source by modelling the silicate absorption feature.

The power of this approach lies in the *direct* measurement of the origin of the infrared luminosity. Other methods for separating star-burst and AGN components (e.g., via [NII]/H α ratio, presence of broad or high-excitation lines, presence of a non-thermal radio VLBI nucleus, presence of a hard X-ray nucleus) can (and have) all be used – but not to determine how much the AGN component contributes to the far-IR luminosity. In the wavelength range targeted by T-OWL, the heating source of the dust is probed directly, allowing a direct link with the power source of the far-IR emission.

The only facility comparable to OWL in terms of resolution for this application will be ALMA in its widest configuration at high frequency. This comparison also directly shows the unique and important synergy between the two facilities. T-OWL provides the necessary information at the short wavelength (Wien) side of the Planck curve, probing the energetic thermal and non-thermal processes directly associated with the star-burst and the central AGN. ALMA probes at the long wavelength (Rayleigh-Jeans) side the cooler bulk material. Hence, a 100m OWL is the perfect MIR complement to ALMA.

Note on design requirements

Observation type	TIR/MIR-spectroscopy
Spatial resolution	diffraction
FOV	5"
Spectral resolution	3000
Wavelength range	8 - 20 μ m
Min. telescope size	60m
Special requirements	IFU
comments	

5.9 Active Galactic Nuclei at High Redshift

Coronal lines are collisionally excited, forbidden transitions within low-lying levels of highly ionized species with an ionization potential of 100 – 400 eV. These lines can only form in extreme energetic environments such as AGNs, and are good discriminants between AGN and star-burst dominated environments. These high ionization lines are present from X-rays to IR and are common in AGN regardless of their type (Penston et al. 1984; Marconi et al. 1994; Prieto & Viegas, 2000; Rodríguez-Ardila et al. 2002; Reunanen et al. 2003). The strongest coronal lines actually lie in the 1 – 40 μ m range: [Si VI] ... [Si IX], [Ne V] ... [Ne VI], [Mg VII], [Ca VII], etc. Their strength is comparable to that of lower-ionization atomic or molecular lines present in this spectral range. The K-band rest frame lines of [Si VI] 1.96 μ m and [Si VII] 2.48 μ m are particularly strong (Fig. 30).

A characteristic kinematic feature of coronal lines is their asymmetric profiles and broad line widths of $v > 1000$ km/s, broader than those measured in the narrow line region but still narrower than those of the broad line region. These features are a consequence of the proximity of the lines to the active nucleus. An important aspect is the fact that these lines are seen with similar strength in either obscured or un-obscured AGN (e.g. Penston et al. 1984; Reunanen et al. 2003; Siebenmorgen et al. 2005; Yan et al. 2005), which implies that the location of the coronal region although very close to the nucleus is still outside the broad line region. This means that coronal lines could be rather unique tracers of obscured AGN in particular at high redshift.

The strength of the IR coronal lines, their exclusive ubiquity in AGN, and their low susceptibility to extinction makes them ideal tracers of AGN activity, in particular of optical obscured AGN, at high redshift. Fig. 30 illustrates which coronal lines would be accessible for a given redshift. Obviously, the N-band alone provides good coverage out to $z = 6$. If metals are sufficiently abundant at these redshifts, the sensitivity of a 100 m telescope should allow us to detect these lines.

For $z > 1$, the shortest-wavelength coronal lines, [Si VI] 1.6 μ m and [Si VII] 2.4 μ m, move beyond ~ 4 μ m; for the critical redshift range $4 < z < 10$, these lines fall in the 10 – 20 μ m range. Thus, these will identify AGN by follow up spectroscopy in the mid-IR of candidate sources found in surveys with JWST in the near-IR.

NACO at the VLT has shown that the real extension of the coronal region is a few 100 pc radius at most from the active nucleus. At $z \sim 4$, these sizes would be comparable to the diffraction limit

resolution of OWL at $10 \mu\text{m}$, 25 mas , and thus, the coronal line region could be considered as a truly unresolved point-like source as detection limits concern.

[Si VI] $1.6 \mu\text{m}$ and [Si VII] $2.4 \mu\text{m}$ are the strongest coronal lines in the IR. Their expected line flux is about $\sim 10^{-14} - 10^{-15} \text{ erg cm}^{-2} \text{ s}^{-1}$ at $z = 0$ and $\sim 10^{-21} \text{ erg cm}^{-2} \text{ s}^{-1} \text{ A}^{-1}$ line peak at $z \sim 5$, 3σ detection in should be possible in 4 h.

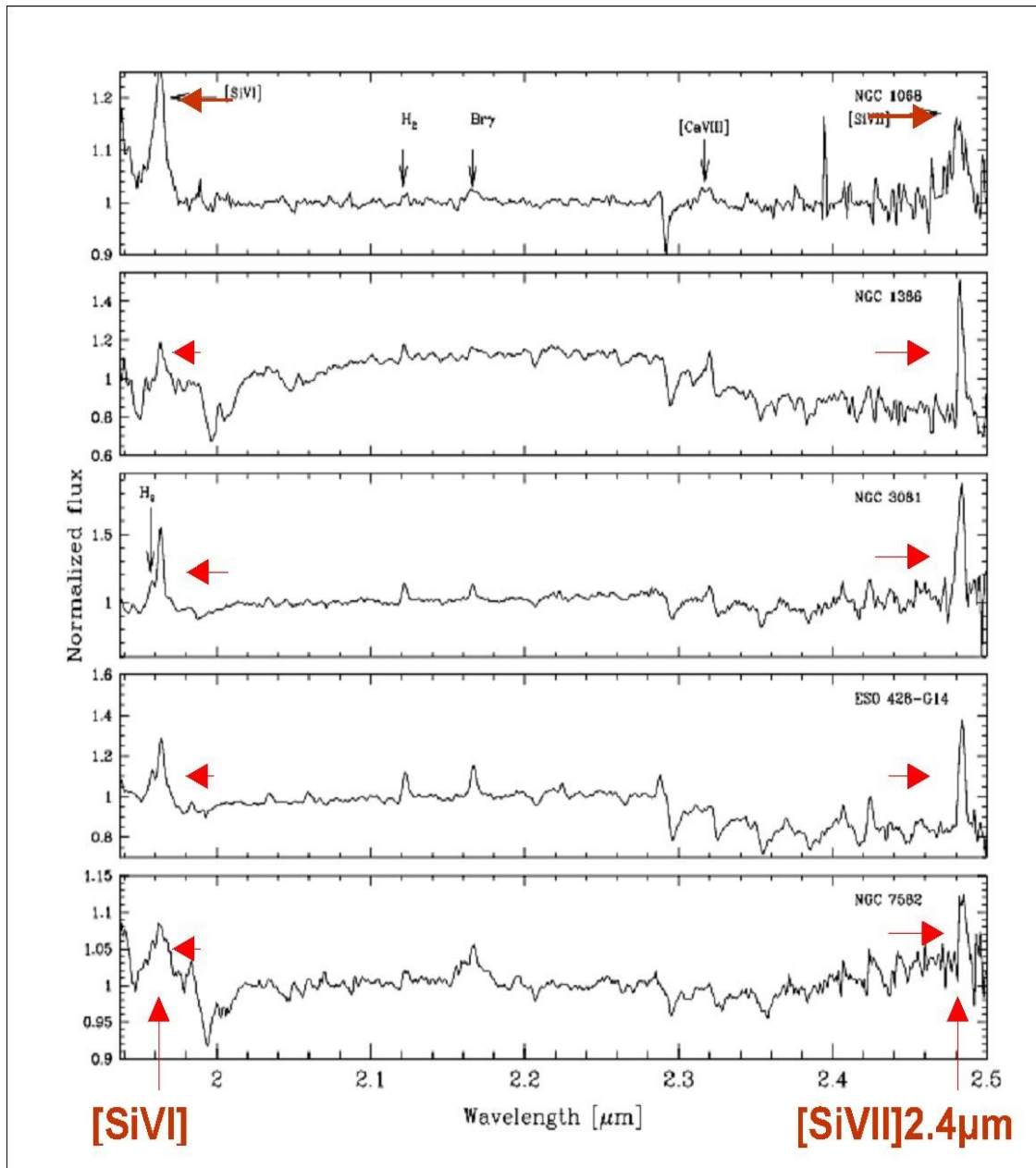


Fig. 30: K-band spectra of typical AGN, including NGC 1068 on the top (adapted from Reunanen et al. 2003). The coronal lines [Si VI] $1.6 \mu\text{m}$ and [Si VII] $2.4 \mu\text{m}$ are the strongest lines in these spectra. These lines shift into the $10\text{--}20 \mu\text{m}$ range for $z > 4$.

At even higher redshifts, other lines may be of interest. During the past decades, the technique of H- α imaging proved immensely useful to quantify star-formation in nearby galaxies. T-OWL could reach the culmination of this technique: star-formation at extreme redshifts ($z \geq 5$) in both star forming proto-galaxies as well as AGN (radio galaxy hosts) imaged in redshifted H- α . Highly redshifted Balmer or – following the famous example of M87 (Ford et al. 1999) – higher ionization lines, such as [OII] and [OIII], could be used, exploiting the unique spatial resolving power with a velocity resolution of at least 100 km/s. Spatially unresolved gas can be used to derive the black hole masses. This is now – with much effort – done for QSOs using the Balmer emission lines, as well as MgII and CIV [e.g., Willott et al. (2003), who derive the mass of a $z=6.4$ massive BH]. Using T-OWL these studies could be taken to extreme redshifts. However, the power of using H- α instead of lines at shorter wavelengths would make also red, star-forming QSOs accessible, which suffer from dust obscuration and would be undetectable at optical/ultraviolet rest frame wavelengths. Hence T-OWL would provide a more unbiased view of active galaxies in the early Universe!

L α moves beyond 2.5 μ m for $z > \sim 20$:

$$\begin{aligned} \text{Line peak L}\alpha / \text{CIV} &\sim 2 \times 10^{-17} \text{ erg cm}^{-2} \text{ s}^{-1} \text{ \AA}^{-1} \text{ at } z=6.3 \\ \Rightarrow &\sim 5 \times 10^{-8} \text{ Jy at } z = 20 \text{ (assuming } q_0 = 0.5, H_0 = 50 \text{ km/s Mpc}^{-1}\text{)} \\ \Rightarrow &5 \text{ sigma in the line peak with 5 minutes integration with OWL.} \end{aligned}$$

This is particularly interesting considering that OWL outperforms JWST in spec at 3.5 μ m by a factor 11 (T. Hawarden, 2000). These estimates are based on results from Pentericci et al. (2002) on the most distant quasar known $z=6.28$.

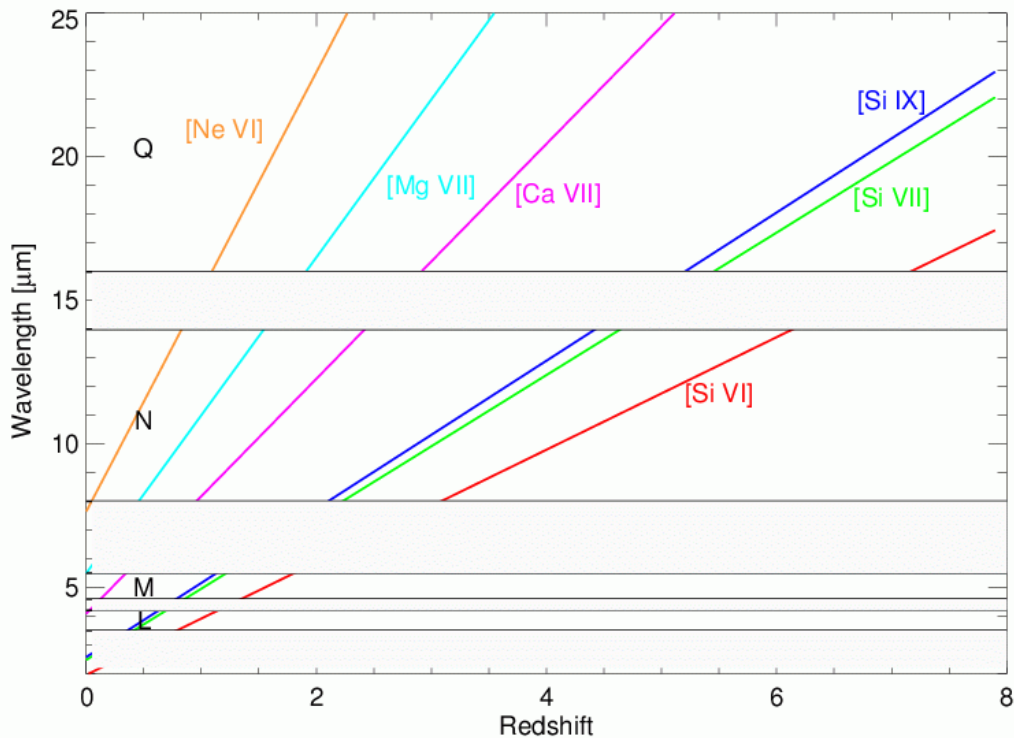


Fig. 31: Illustration of the detectability of the strongest coronal lines within the atmospheric windows for a wide range in redshift. The atmospheric windows are the ones listed in Tab. 13.

It should be added that JWST/MIRI will be able to do similar studies, with access to continuous redshift coverage. However, given its rather short lifetime MIRI will not be able to provide a

complete census of AGN at extreme redshifts, in particular as many potential targets will be discovered during or even after the end of operation of JWST.

Note on design requirements

Observation type	MIR-spectroscopy
Spatial resolution	diffraction
FOV	2"
Spectral resolution	3000
Wavelength range	3 - 20 μ m
Min. telescope size	100m
Special requirements	IFU
comments	

5.10 Gamma-Ray Bursts

Since their *published* discovery in 1973 gamma-ray bursts (GRBs) have been one of the most exciting areas of extragalactic astronomy. Besides being extremely interesting events by themselves they can be used to probe the ionization state and metal content of the intergalactic medium (IGM) at high redshifts. They are – at least for a short period of time – the most energetic, and hence brightest, events in the distant Universe. They seem to occur preferentially in star forming, dusty environments, and they are point sources. At $z=10$ an observed wavelength of $\lambda_{\text{obs}}=2\mu\text{m}$ corresponds to a rest frame wavelength of $\lambda_{\text{rest}}=182\text{nm}$, which is in the UV regime and potentially strongly affected by dust extinction. All these points make GRBs ideal candidates for observations with T-OWL.

Fig. 32 illustrates the predicted flux densities from GRBs as a function of redshift. The figure makes two important points: (i) to detect gamma-ray bursts at $z \geq 5$ observations at infrared wavelengths are needed. (ii) since the brightness of the GRB declines rapidly with time the flux densities drop strongly on time scales of hours. A GRB observed only a few hours after it “ignited” has a flux density of about 0.1 mJy, which is well within the capabilities of the T-OWL medium resolution spectrograph. At that flux level (or higher) one would expect about 10^{-4} GRBs at redshift $z = 6$ (!) per square degree [Fig. 33] (Ciardi & Loeb 2000).

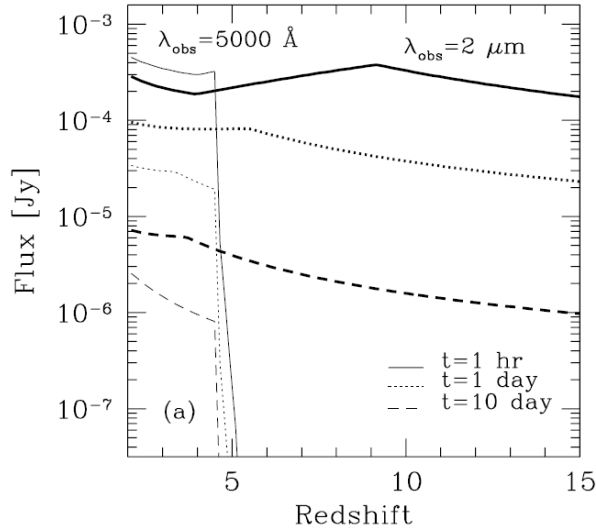


Fig. 32: GRB flux density as a function of redshift for different observing wavelengths and times after the burst started (Ciardi & Loeb 2000).

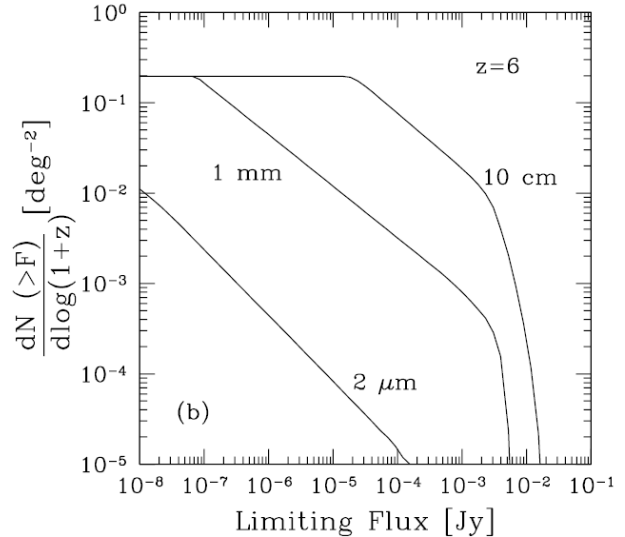


Fig. 33: GRB number counts as a function of flux density for different observing wavelengths (Ciardi & Loeb 2000).

With its rather small field of view T-OWL will not be well suited to *discover* GRBs – this task has to be done by a dedicated survey satellite like *SWIFT*. The main challenge here will be to identify those GRBs at very high redshifts, and separate them from the majority of GRBs that will occur at lower redshifts. This strategy will require further work, but is not subject to the T-OWL study. However, once a good GRB candidate has been identified, T-OWL should be able to follow-up on this detection within hours after its discovery. This is a clear advantage over JWST/MIRI which has a much longer response time to targets of opportunity – almost prohibitive since the GRB will have faded away in the meantime.

T-OWL spectroscopy could not only verify the exact redshift of the GRB Pa- α (1.87) could be seen from $z = 3.0 - 6.2$ and Pa- β (1.28) from $z = 4.8 - 9.5$) but also the spatial structure of its environment.

Note on design requirements

Observation type	MIR-spectroscopy
Spatial resolution	diffraction
FOV	2"
Spectral resolution	3000
Wavelength range	3 - 14 μ m
Min. telescope size	60m
Special requirements	IFU
comments	

5.11 Summary of the Science Requirements

5.11.1 Conclusions Concerning Aperture Diameter

A 100m telescope provides twice the diffraction limited resolution and four times the collecting power of a 50m aperture. Most of the science cases for T-OWL benefit from both, sensitivity and resolution. However, there is (only) one science case which requires a 100m (or larger) aperture: the detection of terrestrial exoplanets. A direct detection and spectroscopic follow-up will not be possible with a significantly smaller aperture.

For most other cases the discussion of a 100m vs. 50m aperture is similar to the comparison VLT vs. NTT. While it is unquestionable that the VLT has enabled breakthrough science, many programs – technically -- could have done with the NTT, IF (!) the TAC would have assigned a full week of NTT time to a program that takes the VLT half a night. But practically this does not happen. Many T-OWL observations of very faint sources across all science cases could -- technically -- be done with a smaller aperture telescope, but practically they never will be done. In many cases -- from protoplanetary disks to active galactic nuclei – it is not sufficient to study the closest one or two examples, but a larger sample is needed to draw any meaningful conclusions.

As stated before, the optical design of OWL is not optimized for the thermal infrared regime. If the telescope aperture has to be less than 100m (on which our sensitivity calculations in Chapter 8 are based) part of the loss in sensitivity due to a smaller aperture could eventually be regained by an optimized MIR telescope design. The loss in spatial resolution, however, cannot be recovered. It would critically affect the following science cases:

- IMF in starbursts
- AGN at low redshift
- ULIRGs

reducing the number of objects that can be studied significantly. However, it is likely that the impact of observations with a telescope aperture NOT smaller than 50m will still be tremendous.

5.11.2 Conclusions Concerning T-OWL Capabilities

The following table summarizes the science requirements on a TIR/MIR instrument for OWL.

Table 3: Summary of scientific requirements on a TIR/MIR instrument for OWL.

Science case	Spatial res	FOV [']	$\lambda / \Delta\lambda$	$\Delta\lambda$ [μm]	Min. \O_{tel} [m]
Seismology of giant planets	0.050	5 – 10	IM	8 – 20	30
Volcanism in the outer solar system	0.050	1	IM, 300	3 – 20	60
Comets and ices and dust	0.050	60	300, 50000	3 – 5	30
Exoplanet follow-up	diff.lim.	2	IM, 100, 50000	8 – 12	100
Signatures of planet formation	diff.lim.	4	IM	3 – 20	50
Evolution of dust grains	0.050	2	300	8 – 12	60
Chemical evolution of the gas	0.050	2	3000, 50000	3 – 20	60
Organic molecules in planet formation	diff.lim.	2	50000	3 – 14	30
Protostars	diff.lim.	4	IM, 50000	3 – 20	60
Galactic center	diff.lim.	2	IM, 300, 3000	8 – 25	60
IMF in starbursts	diff.lim.	4	3000	3 – 20	60
AGN at low redshift	diff.lim.	2	IM, 3000	3 – 20	60
Ultra-luminous infrared galaxies	diff.lim.	5	IM, 3000	8 – 20	60
AGN at high redshift	diff.lim.	2	3000	3 – 20	100
Gamma-ray bursts	diff.lim.	2	3000	3 – 14	60

The *most important conclusions* for T-OWL are:

1. Observations at the diffraction-limited resolution of the Owl aperture are crucial to basically all science cases. First, the targets are either point-like or reveal the most interesting structures on spatial scales close to the diffraction limit. Second, because of the high thermal background, the largest gain in sensitivity will be achieved for unresolved sources.
2. In most cases the required field of view is in the order of a few arcseconds only. A multi-object capability is not required. For the spectrograph, an integral field unit (IFU) is mandatory (see discussion in section 10.3.2 for more details).
3. The main scientific emphasis is on L, M, N, and part of the Q band up to about 20 μm . The scientific importance of the Q band strongly depends on the actual T-OWL sensitivity at that wavelength range, which depends on the atmospheric conditions at the OWL telescope site (Fig. 40). *If* the site will provide low water vapour conditions there are good reasons to extend the spectral coverage out to 27 μm , which corresponds to detector cut-off wavelength.
4. T-OWL requires four different observing modes to cover all science cases:
 - a broad- and narrow-band imaging mode (all applications)
 - a low resolution ($R \sim 300$) slit spectroscopic mode
 - a medium resolution ($R \sim 3000$) IFU spectroscopic mode, mainly for extragalactic science, where line widths are typically in the order of 100 km/s and a wide spectral coverage is desirable.

- A high resolution ($R \sim 50000$) spectroscopic mode, mainly for molecular spectroscopy of Galactic sources, where line widths are typically in the order of 5 km/s.
5. Almost all science cases presented here require an OWL aperture of 50–100 m in diameter for both sensitivity and resolution.

A few more details on the requirements for *high resolution spectroscopy* are necessary here. High spectral resolution for very narrow emission or absorption lines is important for three reasons. First, to resolve and separate close spectral features (a resolution of $R > 30,000$ is needed to simply discern disk emission from ambient nebular lines without ambiguity). Second, at $R > 50,000$ narrow atmospheric windows can provide higher sensitivity than the band average. Third, higher spectral resolution means better line sensitivity, even for absorption lines, since the signal-to-noise in the continuum decreases as \sqrt{R} for background-limited performance. This is impressively illustrated in Figs. 34 and 35.

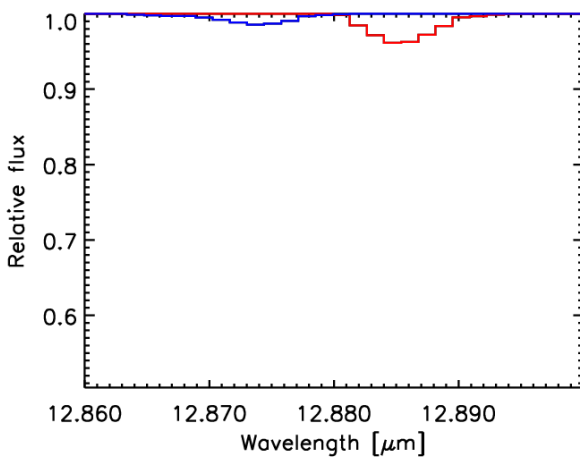


Fig. 34 Model spectra of C_2H_2 at 900K and HCN at 600K (assumed Doppler broadening ~ 4 km/s) at a resolutions of $R=2000$ (Fig. provided by F. Lahuis).

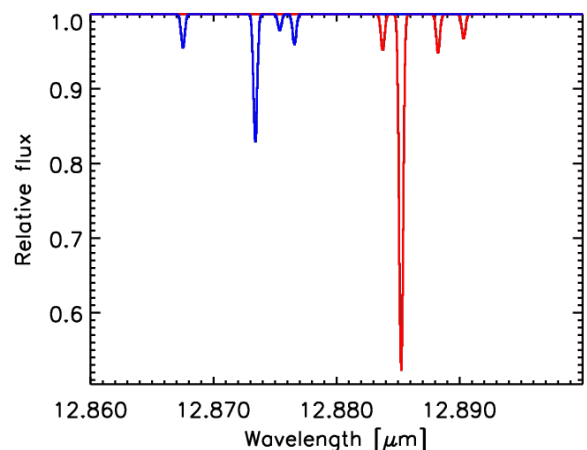


Fig. 35: Model spectra of C_2H_2 at 900K and HCN at 600K (assumed Doppler broadening ~ 4 km/s) at a resolutions of $R=50000$ (Figure provided by F. Lahuis).

One advantage of infrared over radio molecular spectroscopy is the coverage of multiple rotational lines within a short infrared wavelength interval. The rotational levels of the molecules in the thermal equilibrium are populated according to Boltzmann's principle $N_j/N \sim \exp(-E_j/kT)$. The simultaneous measurement of multiple lines therefore can serve as a practical measure of temperature, density, and the fractional abundances of different molecules, including their isotopes. While simultaneous measurements could, in principle, be done sequentially it will practically be very difficult to extend the OWL telescope time accordingly. Furthermore, the temporal variations of the sky introduce systematic uncertainties if lines are measured sequentially. Hence, for best observatory efficiency and scientific results T-OWL will provide the largest possible *spectral coverage* for all spectral modes.

6 Study of Seeing / AO Requirements

As mentioned before, TIR and MIR observations from the ground should concentrate on highest achievable spatial resolution to be compatible to MIR space astronomy:

1. Due to the high background, the RO frame rate has to be quite high to avoid saturation. Smaller pixel scales are helpful here with growing telescopes and array sizes.
2. Ground based telescopes in general are much larger than space telescopes, diffraction limited spatial resolution for largest ground based telescopes is unbeatable from space.
3. Highest sensitivity comparable to that achievable by space telescopes can only be reached for unresolved sources. Thus, there is a special advantage in observing very compact sources – especially when embedded in diffuse emission from surrounding dust and/or gas.

In consequence, adaptive optics is essential for MIR ground based observations with an ELT.

In general, seeing and AO requirements are much more relaxed at thermal or Mid infrared wavelengths compared to the near infrared or even optical regime. However, keeping in mind the very high spatial resolution in principle achievable with an 100m-telescope, some atmospheric effects still can affect the image quality seriously.

6.1 Chromatic Atmospheric Effects

The refractive index affects mainly in two ways the wave-front propagation in astronomical applications.

1. Firstly, we have a geometric effect due to the dispersion of the refractivity ($N=n-1$, where n is the refractive index) that depends on the wavelength and acts as a modification of the direction of wave-front propagation when this last propagates along directions different from the zenith. This effect should be taken into account when one works in a not monochromatic regime.
2. Secondly, the random variations of the refractive index due to the atmospheric turbulence produced by temperature and humidity fluctuations induce a spreading and a balancing of the image obtained at the focus of telescope.

We treat here the effects due to the dispersion of the refractivity in IR wavelength ranges i.e. the wavelengths range of T-OWL that is the effect (1).

This chromatic effect has been studied by Roddier and Roddier (SPIE, 628, 1986, pp. 298) at different wavelengths (included those we are treating on) for application to the AO techniques. The Adaptive Optics technique is based on a simple principle: wavefront perturbations are measured at a wavelength λ_1 and the scientific target is observed at a wavelength λ_2 after correction of the wavefront perturbations. In general, the two wavelengths are different and in general, the observation wavelength (λ_{obs}) is larger than the wavelength at which perturbations are measured (λ_{meas}). This means that, in principle, if the refractivity depends strongly on the wavelength, we could have a displacement of the image position obtained at the two different wavelengths taken into account. The criterion used to define if such an error is negligible or not is to estimate if the difference of optical path (d) is larger or smaller than r_0 . The effect is negligible if d is much smaller than r_0 i.e. if $d/r_0 \ll 1$.

Roddier and Roddier calculated d/r_0 at different wavelengths for typical seeing values above astronomical sites: $r_0 = 10$ cm at $\lambda = 0.5$ μm . In this paper, $\lambda_1 = 0.5$ μm and λ_2 spans the range [0.5-10] μm . The general trend observed is that the larger is the wavelength, the smaller is d/r_0 . More precisely,

for a maximum air mass of 60 degrees, we have $d/r_0 = 0.052$ at the maximum $\Delta(\lambda) = \lambda(10 \mu\text{m}) - \lambda(0.5 \mu\text{m})$.

In the work by R&R (1986) it is not clear (it is not mentioned explicitly) if the authors take into account the contribution of the water vapour in the variations of the refractive index. In the visible range it is known that contributions to the variations of n coming from the dry air are dominant on the water vapour contributions.

In the IR range, contributions from water vapour and CO_2 become more important because the refractivity is affected by the absorption resonances inside the IR pass-bands and between the IR pass-bands. This effect is overlapped to a gentle relation $n = n(\lambda)$ as shown in Colavita et al. 2004 (Fig. 1).

Of course this fact has substantial consequences in interferometry because difference in the optical paths due to this chromatic effect can strongly modify the interferometric pattern. In the application to the AO technique the impact is less clear and evident. For this reason we investigated a slight deeply this topic.

We planned to use with T-OWL a $\lambda_{\text{meas}} = 3 \mu\text{m}$ and a $\lambda_{\text{obs}} = 10 \mu\text{m}$. For wavelengths larger than $10 \mu\text{m}$ the angular resolution is not any more advantageous. Looking at Fig.1 (Colavita et al. 2004, PASP, 116, 876) we can retrieve that $[n(\lambda_{\text{obs}}) - n(\lambda_{\text{meas}})]$ is of the order of 0.2×10^{-6} .

The displacement d obtained for wave-front propagating at an angle θ with respect to the zenith is of the order of:

$$d \approx \text{tg}(\theta) \cdot \Delta(h) \cdot [n(\lambda_1) - n(\lambda_2)]$$

Where h is the depth of the atmosphere that we are considering crossing by the wavefront and affected by the water vapour fluctuations.

If we take as a first approximation $h = 20 \text{ km}$ (depth of the troposphere) and $\theta = 60^\circ$, we find $d \sim 0.6 \text{ cm}$.

If we take a more reasonable depth of the atmosphere in which the water vapor fluctuation can affect the refractive index as equal to 3 km (Masciadri et al. 2000, SPIE, 4006, 1136; Thompson, Moran, Swenson, Interferometry and Synthesis in Radio Astronomy, John Wiley & Sons, 1986) we find $d \sim 0.1 \text{ cm}$. The water vapour is indeed present in the first 2-3 km above the ground.

We know that:

$$r_\theta(\lambda) = r_\theta(0) \cdot (\lambda/\lambda_0)^{6/5}.$$

A $r_\theta = 10 \text{ cm}$ at 0.5 micron (typical of a good astronomical site) corresponds to $r_\theta = 836 \text{ cm}$ at $10 \mu\text{m}$. If we consider the maximum angle of $\theta = 60^\circ$ we have:

$$d/r_\theta(\lambda_{\text{obs}}) \cdot (\cos \theta)^{3/5} = 0.1/836 \cdot 0.63 = 1.8 \times 10^{-4}$$

We conclude, therefore, that the effects induced by the dispersion of the refractivity can be negligible in our application. We note that d/r_θ is proportional to $\Delta(n)$.

Assuming a $\Delta(n)$ larger than a factor 10^2 we should remain with a d/r_θ of the order of 10^{-2} .

This means that also for λ in the range 5-8 microns in which sharp fluctuations of n is observed because the absorption resonance (Mathar et al. 2004), we should start to be worried only for $\Delta(n)$ larger than 10^2 .

For what concerns the random turbulent fluctuations of the refractivity (**2.**) it is known (Colavita et al.2004) that the constant of the structure function C_N^2 is:

$$C_N^2 = ST^2 \cdot C_T^2 + SQ^2 \cdot C_Q^2 + 2ST \cdot SQ \cdot C_{TQ} \quad (1)$$

SQ depends in a much more strong way on the wavelength than the ST (Table 2, Colavita et al. 2004). Besides this, at IR range, the ST factor is dominant with respect to SQ in its absolute value. To have a precise estimate of C_N^2 we should know also C_Q^2 that depends on the $\Delta(q)/\Delta(z)$ (Masciadri et al. 2000). It would be interesting to estimate the order of magnitude of $\Delta(q)/\Delta(z)$ compared to $\Delta(T)/\Delta(z)$ to have a more precise order of magnitude of the first two factor of Eq. (1). In alternative to this calculation we can retrieve some conclusion starting from the work of Colavita et al. (2004).

The authors estimated that the seeing contributions coming from water-vapour in the IR range is roughly 1/7 of the seeing contribution coming from the temperature fluctuations. In spite of the fact that this ratio is equal to 1/19 in the visible range, the authors estimate that also in the IR the water-vapor contribution can be considered negligible.

We conclude that, based on previous literature results adapted to our applications, both refractivity effects (dispersion and turbulence) do not introduce major problems for T-OWL.

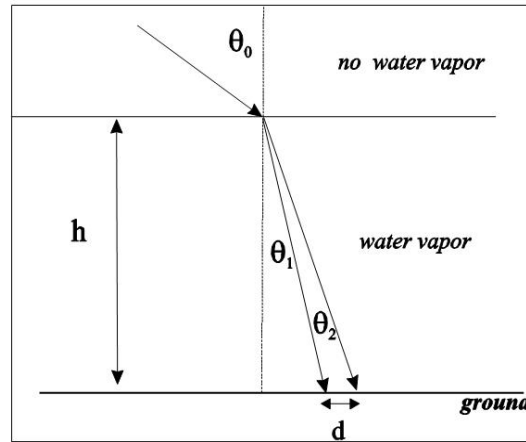


Fig. 36: Schematic ray path to demonstrate chromatic atmospheric effect

6.2 Strehl Ratio

OWL has been specified to reach a Strehl Ratio of 20% (requirements) or 30% (goal) at $0.5\mu\text{m}$. To calculate the expected Strehl Ratio for the TIR and MIR wavelength region, the following dependencies are used:

$$S = e^{-\sigma^2}$$

$$\sigma^2 = 0.35 \cdot [(D/r_0)^2 \cdot (\pi/4N)]^{5/6}$$

$$r_0 = r_{00} \cdot (\lambda/0.5\mu\text{m})^{6/5} \cdot \cos^{3/5}\xi$$

where σ is the wavelength distortion, D the telescope diameter, r_0 the Fried parameter, r_{00} the Fried parameter at $0.5\mu\text{m}$, N the number of actuators and ξ the zenith distance. Assuming a Fried parameter of 20cm at $0.5\mu\text{m}$, we calculate the Strehl ratios for different numbers of actuators over the wavelength range from 0 to $30\mu\text{m}$. The result is given in Fig. 37.

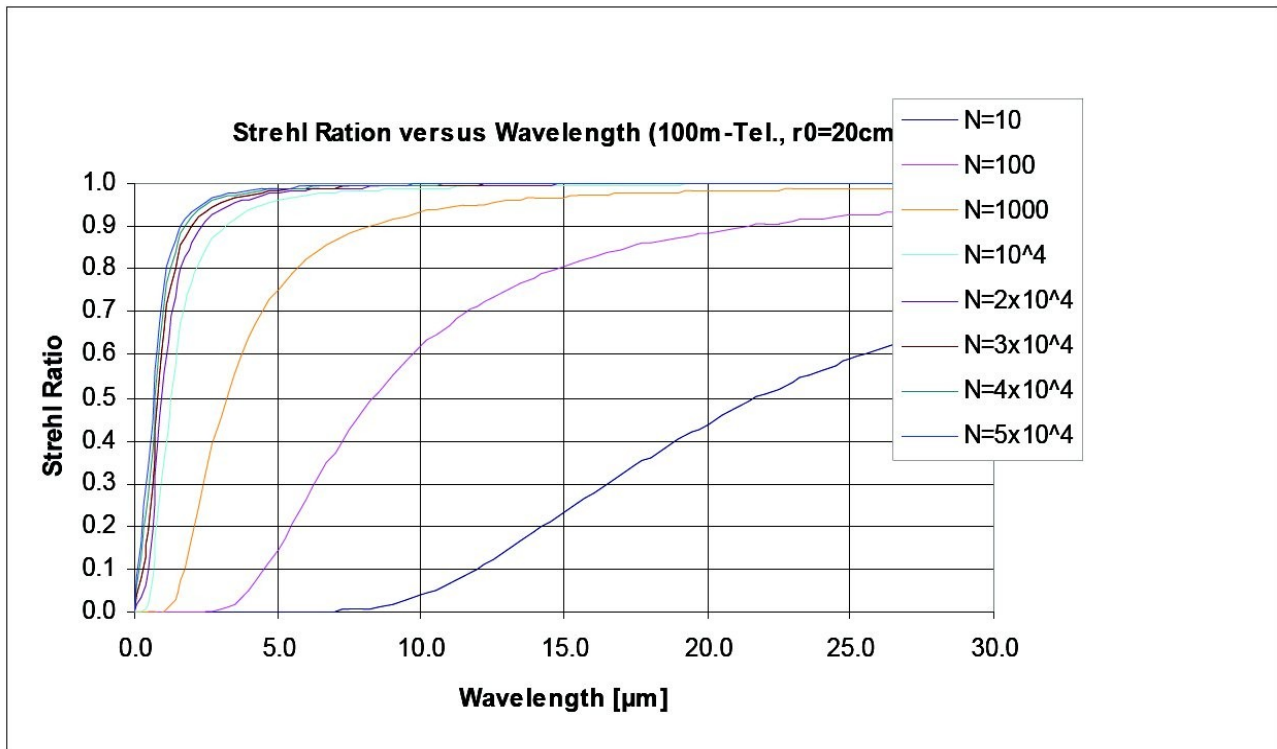


Fig. 37: Strehl ratio versus wavelength assuming a Fried parameter of 20cm at $0.5\mu\text{m}$. This wavelength dependence is given for different numbers of actuators N . To reach the goal of 20% SR at $0.5\mu\text{m}$, at least 10000 actuators are required.

It turns out that for any adaptive optics system that provides a Strehl Ratio significantly beyond 10% in the visible, the resulting Strehl Ratio in the thermal IR – and even more pronounced in the MIR – is expected to be better than 90%. To calculate the Strehl Ratio $S(\lambda)$ for any wavelength from a given Strehl Ratio $S_{0.5}$ at $0.5\mu\text{m}$, we have to raise $S_{0.5}$ to the power of $-\lambda/0.5$.

Table 4: Expected Strehl ratio for TIR and MIR bands extrapolated from a given Strehl ratio at $0.5\mu\text{m}$

$S[0.5\mu\text{m}]$	$S[1\mu\text{m}]$	$S[5\mu\text{m}]$	$S[10\mu\text{m}]$	$S[20\mu\text{m}]$
10%	56.2	97.7	99.4	99.8
20%	66.9	98.4	99.6	99.9
30%	74.0	98.8	99.7	99.9
40%	79.5	99.1	99.8	99.9

Thus, for the wavelength region discussed here we can assume diffraction limited resolution.

6.3 Isoplanatic Patch

The OWL thermal and mid infrared camera critically depends on the operation of the AO-system. The resulting spatial resolution is by a factor of 10 better than achieved with any projected mission seen at the horizon, and its high sensitivity for point sources is due to the small pixel scale, which again makes sense for diffraction limited resolution only. In consequence, the field of view is limited by the isoplanatic patch provided by the efficient AO system.

This isoplanatic angle is equal to:

$$\Theta = 0.3 \cos\gamma r_0/h$$

where γ is the zenith angle, r_0 the Fried-parameter and h the mean height of turbulences. As r_0 goes with the power of $6/5$ of λ , even for poor visual seeing conditions of 0.7 arcsec – which corresponds to a Fried parameter of 10cm at 0.5 μ m), at 3 μ m the isoplanatic radius angle is about 26 arcsec (assuming a medium turbulence height of 2km). Thus, a detector of more than 7,000 x 7,000 pixel is required to fill the isoplanatic patch with Nyquist sampling sensors. This is a conservative estimation, medium seeing is assumed, no MCAO system is assumed which will open the FOV for OWL. In summary, the isoplanatic angle will not restrict the FOV of a diffraction limited thermal IR camera for a 100m- telescope.

7 Detailed Best Effort Calculations of Performance

7.1 Instrumental Background

T-OWL itself will be cooled down to operational temperatures for which the emissivity of cryogenic optical components is negligible. Thus, the instrumental background is given by warm components within the optical beam (for simplicity and lack of information we assume a common overall temperature of 10°C):

Table 5: Instrumental Background conditions

Item	emissivity	partly blocked	Comments
M1-M6	12.0%	12.0%	2% each, 280K
Central hole	10.90%	0.00%	Cold pupil stop
Spiders	3.80%	0.00%	Cold pupil stop
Gaps	2.20%	2.20%	100%, 280K
Dust...	0.50%	0.50%	50%, 280K
Entrance window	1.00%	1.00%	1%, 280K
Total	30.40%	15.70%	280K

Thus, beside emission from the individual optical surfaces, that can be minimized by optimizing the reflection coating, the gaps between the mirror segments are expected to form the main contributor to the instrumental background. The image of the 14mm gaps into a 100mm pupil diameter results in 14 μ m thick structures. It will be very challenging to reduce this effect by a cold stop, as well concerning the optical quality as pupil image stability.

Thus, thermal emission from the gaps between M1 segments should be reduced by reducing the emissivity itself, e.g. by special coating. This should be carefully investigated to avoid mirroring contributions from the warm structure parts into the optical beam: There is the danger of increasing thermal background and straylight.

7.2 Atmospheric Transmission

It is well known that the atmospheric transmission in the thermal and mid-infrared is reduced by molecular absorption bands mainly due to H₂O, CO₂, O₃, N₂O, CH₄, O₂, NO... In Figs. 38 and 39 standard transmission is shown for a mid-latitude winter and summer atmosphere as modeled with HITRAN. Largest variations are observed at those spectral bands where atmospheric absorption is produced by H₂O, that is within L,M,N and Q band. Especially the Q-band is strongly dependent on dry rest-atmosphere: In Fig. 40 we show how the Q-band transmission improves with elevation of the telescope site. Thus, for ground based MIR observations it is extremely important to minimize the content water molecules within the line of sight. The OWL site should be dry and at high elevation.

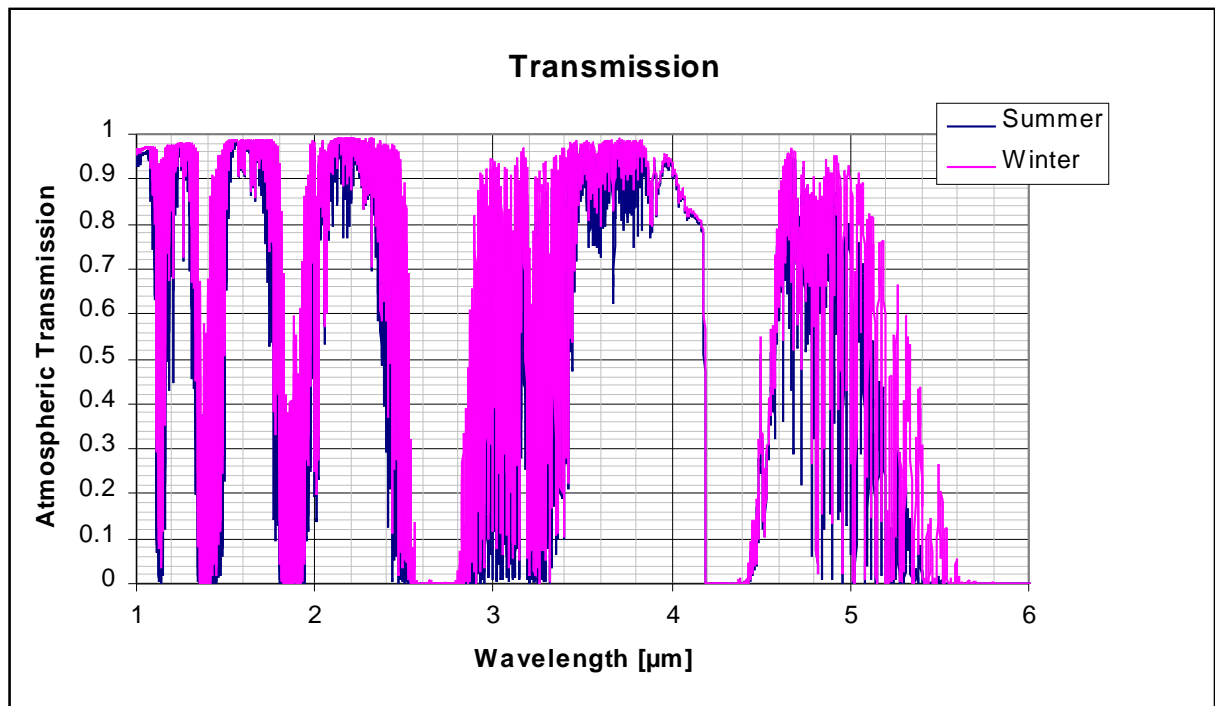


Fig. 38: Atmospheric transmission from 1 to 6 μm at mid-latitude in summer and winter time for a moderate elevation of 2km

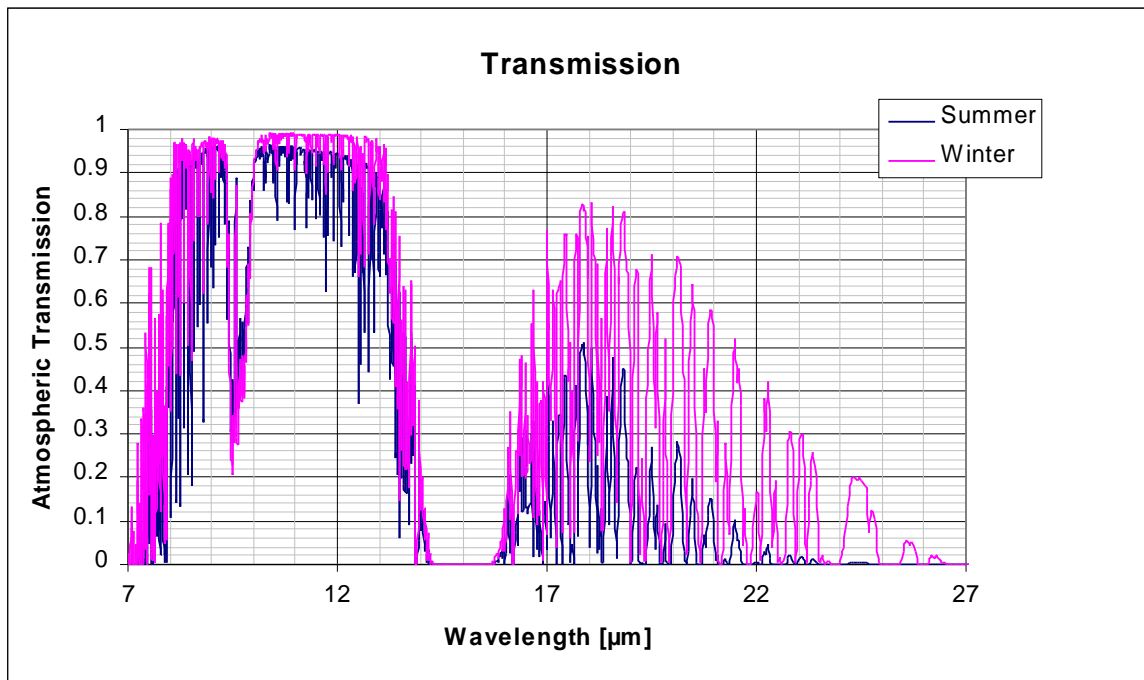


Fig. 39: Atmospheric transmission from 7 to 27 μm at mid-latitude in summer and winter time for a moderate elevation of 2km

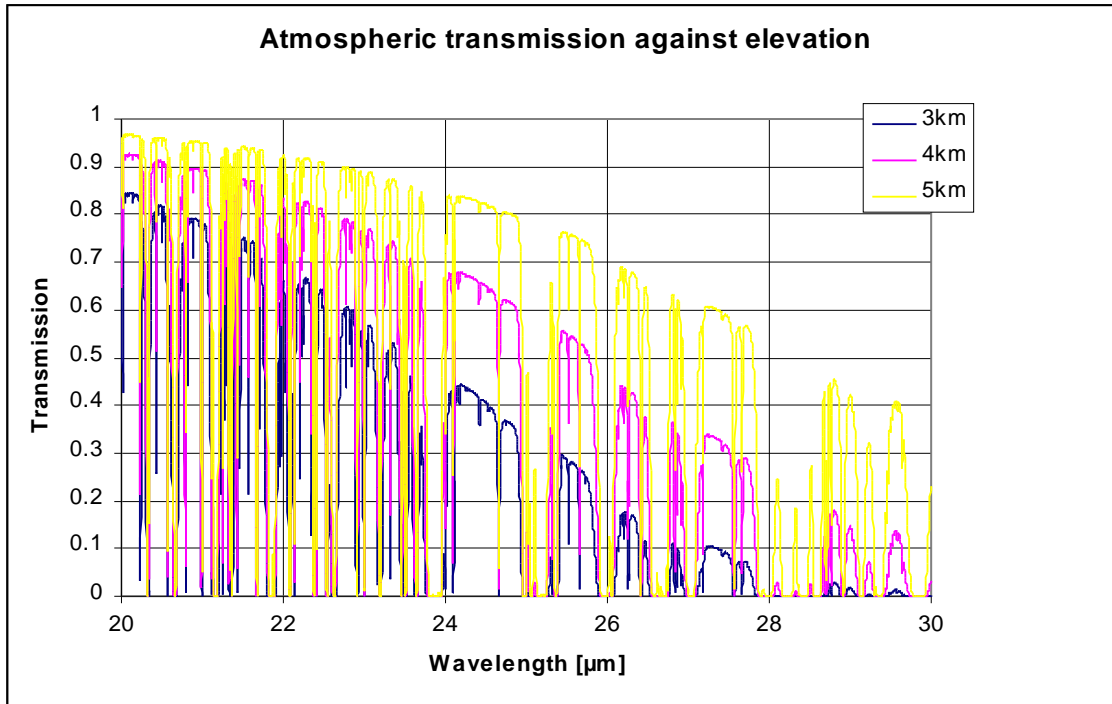


Fig. 40: Variation of 20-30μm atmospheric transmission with elevation of observing site, Zenith mid-latitude winter standard model.

7.3 Atmospheric Emission

7.3.1 Atmospheric Background for BB Imaging

TIR and MIR sky background (including thermal emission from the telescope) is variable with time and thus depends on site and atmospheric conditions. As long as the OWL site is not definitely fixed, we assume sky background conditions as measured for Paranal (see Cuby et al., The Messenger 101, p3 (2000)).

Unfortunately, these values are given only for the NIR and TIR region. Beyond the M-band, we assume 251Jy per square arcsec in N-band and 2610 Jy for the Q band (broad band application).

Table 6: Background flux for broad band applications.

Atmospheric band	BG [mag/arcsec ²]	BG [JY/arcsec ²]	BG[γ/s/arcsec ²] For 100m Tel.	BG[γ/s/N-pixel]
J	16.5	0.39 10 ⁻⁴	1.17 10 ⁺⁷	7.8 10 ⁺¹
H	14.4	1.74 10 ⁻³	6.80 10 ⁺⁷	7.9 10 ⁺²
Ks	13.0	4.15 10 ⁻³	2.17 10 ⁺⁸	4.5 10 ⁺³
L	3.9	7.96 10 ⁺⁰	6.74 10 ⁺¹¹	3.6 10 ⁺⁷
M	1.2	5.40 10 ⁺¹	6.53 10 ⁺¹²	7.2 10 ⁺⁸
N	-2	2.51 10 ⁺²	5.96 10 ⁺¹³	2.5 10 ⁺¹⁰
Q	-6	2.61 10 ⁺³	1.24 10 ⁺¹⁵	2.1 10 ⁺¹²

N-pixel means a Nyquist-sampling pixel for diffraction limited resolution.

7.3.2 Atmospheric Background for Spectroscopy

To estimate the atmospheric radiance (and transmission) we have used standard atmospheric models in PCLNWin (HITRAN). Typical wavelength dependence of atmospheric radiance are given in Fig. 41 and Fig. 42 for the full thermal and mid infrared region available from the ground (up to 30 μ m).

The difference between summer and winter model is mainly due to temperature variations, even some line absorption variation especially due to varying water content can be observed.

Several data sets of low and medium spectral resolution have been produced to provide atmospheric input data for the sensitivity spread sheet presented in chapter 8.

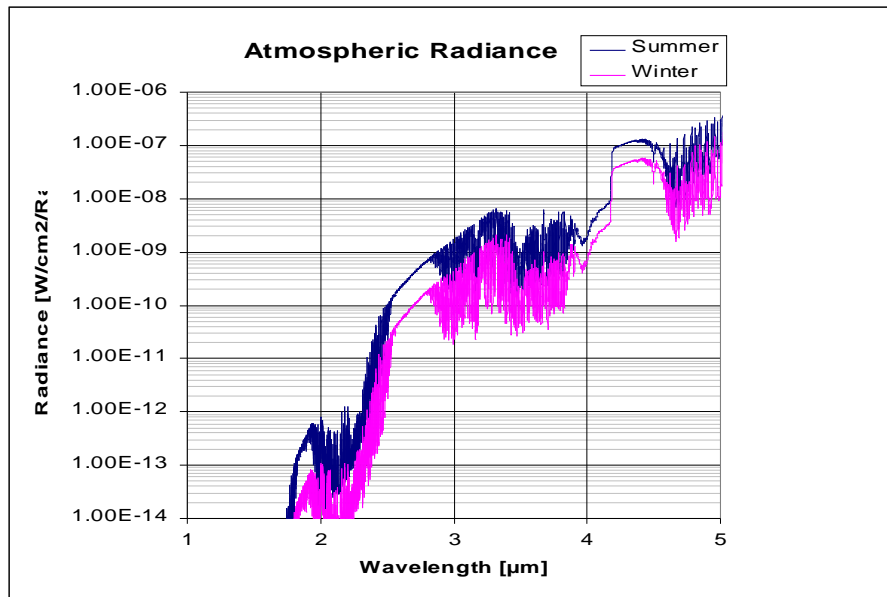


Fig. 41: Atmospheric radiance at mid-latitude in summer and winter time for the 1 to 5 μ m region. Observatory height of 3500m is assumed.

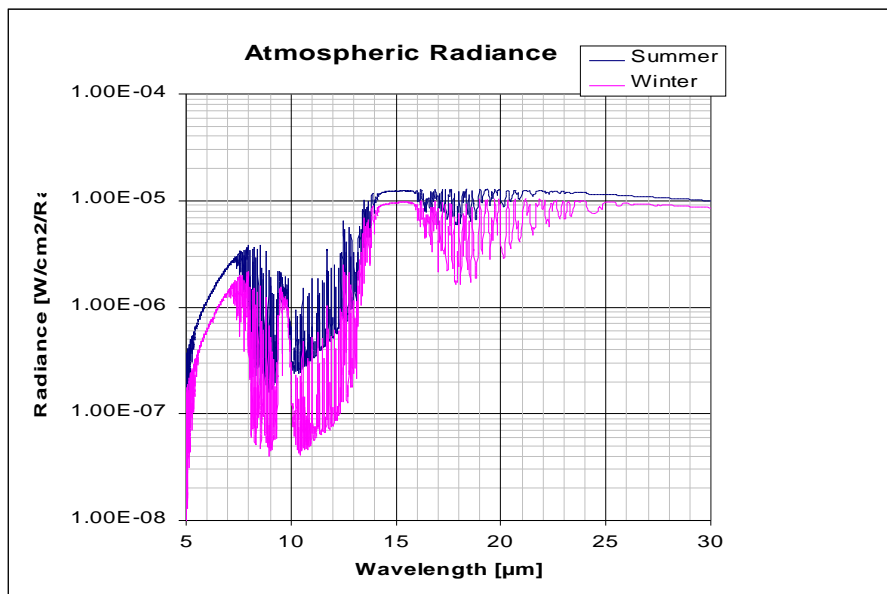


Fig. 42: Atmospheric radiance at mid-latitude in summer and winter time for the 5 to 30 μ m region. Observatory height of 3500m is assumed.

7.4 Atmospheric Dispersion

For seeing limited astronomical observation, at optical wavelengths atmospheric dispersion is a known effect producing significant image distortion especially at high zenith angles. As distortion becomes smaller and the diffraction limit is growing with increasing wavelengths, even for diffraction limited observation at 8m-class telescopes significant deterioration of the Strehl ratio by atmospheric dispersion is expected up to near infrared wavelengths only. However, the step from an 8m-class telescope to the 100m-class reduces the FWHM of the PSF down to the mas region, thus, even at thermal IR wavelengths this effect gives significant Strehl Ratio reduction.

In Fig. 43 the atmospheric dispersion is given for the 0.5-30 μm wavelength region as recently published by R. J. Mathar (2004). These data are compared to the standard formula for refraction index of air given by Seidelmann (1992). The Seidelmann formula fits quite well for wavelength regions below 5 μm , however, beyond this limit there is a significant deviation, in contrast to R. Penndorf statement “*The computed n values are considered as very reliable for the spectral range from 0.2 to 20 μm* ”.

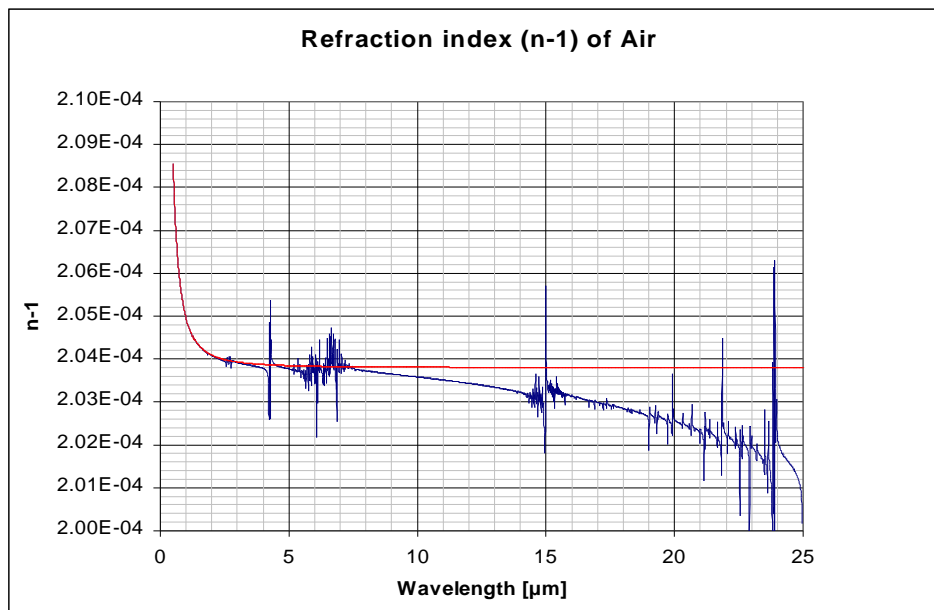


Fig. 43: Atmospheric refractivity versus wavelength. The blue graph represents the data given in Mathar (2004), the red one is the generally accepted (Joint Commission for Spectroscopy 1952) one as represented by Edlén’s formula given in Edlén (1953) (for details see text).

However, this deviation is mainly due to the water content of the atmosphere: The data given by Mathar (2004) are based on a atmospheric water content of 10^{23} molecules per m^3 , that is about 65% relative humidity 10C. However, observations within the Q-window will be possible for low humidity values only. Thus, dispersion correction beyond 5 μm is not required for a diffraction limited 100m-telescope.

There are several ways to overcome the loss of spatial resolution by atmospheric dispersion: Direct imaging could be restricted to narrow band application or to the region near the zenith. For IFU-units this effect has to be taken into account within the data reduction pipeline. Long-slit spectroscopy

could handle this problem by aligning the slit parallel to the dispersion direction. Or the dispersion effect has to be corrected by a special device as discussed in Chapter 12.3.4.

7.5 Instrumental Polarization

All off-axis components of T-OWL are gold or silver coated, well protected inside the cryostat. A typical TMA will produce an internal polarization effect of 0.17%, the arrangement of imaging optics could even reduce these internal effects by optimizing the tilt direction.

However, the current telescope design includes one 1.6m diameter mirror (M6) which is inclined by 20deg. This mirror is within the common path of all instruments, thus, will not be optimize for individual requirements like low thermal emission or low polarization effect. It may be worth wile studying an automatic exchange mechanism of M6 to optimize instrument specific requirements.

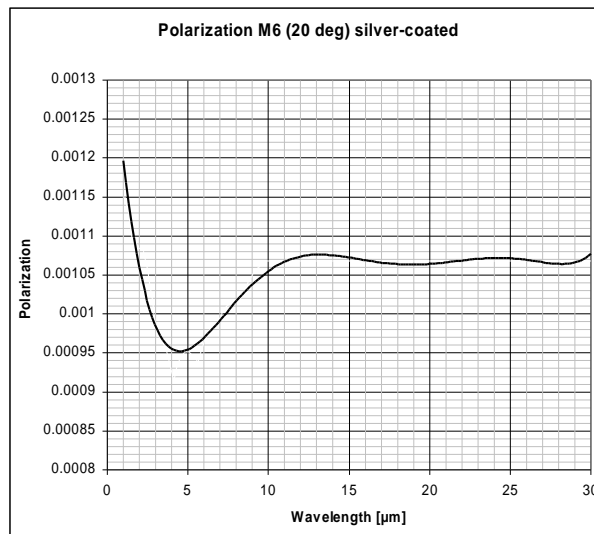






Fig. 44: Instrumental polarization produced by M6 (20deg incidence angle) for pure silver coating. Polarization for protected silver coating will be somewhat higher, however significantly depending on the materials used for over-coating.

Thus, the total instrumental polarization of the telescope itself will be quite small, dominating polarization effects may be produced by T-OWL if not optimized in this sense. In consequence, the design of T-OWL will significantly depend on the question if this instrument should be used for high precision polarization effects.

	<h1 style="text-align: center;">T-OWL Concept Level Study</h1> <p style="text-align: center;">Doc : OWL-CSR-ESO-00000-0161</p> <div style="display: flex; justify-content: space-around; align-items: center;">    </div>	<p>Version 1 Date: 20/10/2005 Page: 75/175</p>
---	--	--

However, the T-OWL team decided not to include the polarization mode into this pre-phase A study, mainly driven by the consideration that AO-supported high precision polarimetry at MIR-wavelengths needs high sophisticated polarimetric measuring methods, that requires a special instrument. Nevertheless, this item remains as an open item to be investigated in more detail beyond this T-OWL study.



T-OWL Concept Level Study

Doc : OWL-CSR-ESO-00000-0161



Version 1
Date: 20/10/2005
Page: 76/175

8 T-OWL Sensitivity

8.1 Preface: Point Source Versus Extended Source Sensitivity

All estimates below assume a diffraction-limited point source. This is clearly the best case in terms of best sensitivity since the angular diameter of a diffraction limited source shrinks linearly, relative to the extended background, and the signal-to-noise (S/N) of a detection increases approximately with D^2 , and hence the observing time needed to achieve a certain S/N drops with D^{-4} .

If the pixel scale is matched to the diffraction limit, bigger telescopes provide only the same sensitivity to extended emission (per pixel) than smaller telescopes do. However, if the instrument provides sufficient FOV and only extended features are of interest, pixel re-sampling will gain back sensitivity. Re-sampling the pixel scale to the one of a smaller telescope, the sensitivity improves with D and the observing time needed to achieve a certain S/N drops with D^{-2} in this case. This is another reason for using an IFU in the spectrograph design.

The most interesting sources discussed for the science case have interesting structures close to the diffraction limit of the telescope, or they are close point sources. Thus, we limit our discussion here to point source sensitivities.

8.2 Imager Sensitivity

Broad band sensitivity in the TIR and MIR varies with atmospheric conditions, telescope temperature, single, number of readouts etc. A rough (optimistic) estimate for BB direct imaging can be deduced from background data as given in Tab. 6.

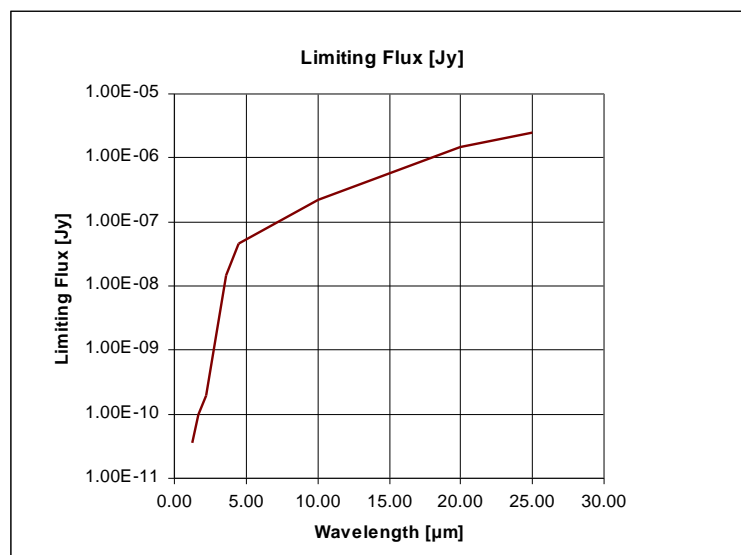


Fig. 45: Point source sensitivity of a 100m-telescope under medium atmospheric conditions (typical for Paranal).

8.3 Spectrograph Sensitivity

8.3.1 Introduction

The sensitivity of the T-OWL spectrograph has been estimated at various resolutions for the L, M, N and Q bands using a complex spreadsheet¹. This chapter describes the assumptions that went into the calculations and presents the results.

The calculations are based on atmospheric transmission and emission spectra calculated with HITRAN-PC for an observatory at 4 km altitude, at a mid-latitude location, and observations at zenith during winter time at the two spectral resolution $R=250$ and $R=10000$.

Other relevant, wavelength-independent input parameters are listed in Table 7.

Table 7 Parameters used in the spreadsheet for the spectrograph sensitivity calculations

Parameter	Value	Comment
Telescope primary mirror diameter	100m	
Secondary mirror obscuration	33m	
Effective temperature of the atmosphere	10°C	
Effective temperature of the telescope mirrors	10°C	
Emissivity of mirrors M1 – M6	0.120	
Emissivity of gaps in M1	0.071	
Emissivity of central obscuration	0.00	requires effective blocking
Emissivity of telescope spiders	0.00	requires effective blocking
Emissivity from dust contamination	0.005	
Total emissivity	0.196	sum of the above 5 contributions
Reflectivity of individual telescope mirror	0.98	
Total number of warm telescope mirrors	6	
Number of cold reflective surfaces	10	
Reflectivity of individual cold surface	0.985	
Grating efficiency	0.7	
Fractional slice transmission	0.8	
Filter transmission	0.8	
Spatial pixels per resolution element	2	
Spectral pixels per resolution element	2	
Physical detector pixel size	25 μ m	
Read noise per frame	100e ⁻	
Dark current	10 e ⁻ /s	
Photoconductive gain	1.0	
Detector quantum efficiency (average)	0.6	λ dependency can be added
Overhead to due to chopping or other techniques	0.5	

¹ A copy of the EXCEL file and a more detailed description of the individual cells of the spreadsheet can be obtained directly from Bernhard Brandl (brandl@strw.leidenuniv.nl).



T-OWL Concept Level Study

Doc : OWL-CSR-ESO-00000-0161



Version 1
Date: 20/10/2005
Page: 78/175

Parameters that have been varied between the calculations shown below:

- Spectral resolution
- Waveband (and the corresponding f/# at the detector)
- Total observing time
- Frame time (depends on spectral resolution)
- Anticipated signal-to-noise ratio (S/N)

The calculations are performed as follows:

The minimum detectable flux density from a source, S_{src} [photons s⁻¹ cm⁻² μm⁻¹], is given by:

1. The signal-to-noise ratio $\sigma_{S/N} \equiv \frac{S_{src}}{N_{tot}}$

2. The total noise², which depends on the background noise per pixel and the number of pixels n_{pix} to be combined from each resolution element in both the spectral and the spatial direction:
$$N_{tot} = N_{back} \sqrt{n_{pix}} .$$

3. The detected signal S_{el} in [e-], which depends on the source flux density S_{src} , the integration time t_{int} , the effective collecting area of the telescope A_{tel} , the throughput of the atmosphere η_{atm} , the total throughput of telescope and instrument η_{tot} , the detector responsivity $\eta_D G$, and the width of the resolution element $\Delta\lambda$:

$$S_{el} = S_{src} \Delta_{tel} \eta_D G_{atm} \eta_{tot} t_{int}$$

Combining (1.) – (3.) yields:

$$S_{src} = \frac{S_{el}}{\Delta_{tel} \eta_D G_{atm} \eta_{tot} t_{int}} = \frac{\sigma_{S/N} N_{back} \sqrt{n_{pix}}}{\Delta_{tel} \eta_D G_{atm} \eta_{tot} t_{int}}$$

Before we calculate the resulting detection threshold with a given S/N we need to discuss the other quantities that enter the above equation:

The total system throughput η_{tot} without the atmosphere, and (currently) constant with wavelength is the product of:

1. the total reflectivity of all telescope mirrors η_T
2. the total reflectivity of all instrument mirrors η_I
3. the fractional slice transmission η_{fsr} . As the PSF grows with wavelength the relative slice width gets narrower and diffraction broadening of the beam leads to light losses. Therefore the medium resolution spectrograph will consist of several modules with minimum wavelengths of $\lambda_{min}^{LM} = 3.5\mu\text{m}$, $\lambda_{min}^{N1} = 8.0\mu\text{m}$, $\lambda_{min}^{N2} = 10.6\mu\text{m}$, $\lambda_{min}^Q = 17\mu\text{m}$. We assume a slice width of λ_{min}/D with a maximum fractional slice transmission of 80% and a linear decrease with wavelength.

² We only consider noise from the background here; shot noise from the source signal is neglected.



T-OWL Concept Level Study

Doc : OWL-CSR-ESO-00000-0161



Version 1
Date: 20/10/2005
Page: 79/175

4. the transmission of filters and dichroics η_{dic} , and
5. the grating efficiency η_g .

Hence:

$$\eta_{tot} = \eta_T \eta_I \eta_{fst} \eta_{dic} \eta_g$$

The total background intensity [$\text{W cm}^{-2} \text{sr}^{-1} \mu\text{m}^{-1}$] at the focal plane is the sum of the contributions from the warm telescope B_T and the atmosphere B_A times (approximately) the total system throughput η_{tot} :

$$B_{tot} = (B_T + B_A) \eta_{tot}$$

where the background signal from the warm telescope assumes black-body emission:

$$B_T = \frac{2hc^2}{\lambda^5} \left[\frac{\epsilon}{e^{\frac{hc}{k_B T}} - 1} \right]$$

and B_A as provided by the HITRAN simulations.

The total signal S_{back} per pixel [e^- /s] from the background is the number of electrons that are being generated solely by the background flux every second in a detector pixel. It is the product of total background intensity B_{tot} , the pixel “field of view” $A \times \Omega$, the width $\Delta\lambda$ of a resolution element, and a conversion factor, which relates the photons of energy hc/λ to a given “light power” [W] for a given wavelength and detector responsivity $\eta_D G$:

$$S_{back} = B_{tot} \cdot A \cdot \Omega \cdot \frac{\eta_D G}{hc} \cdot \Delta$$

The $A \times \Omega$ product at the detector plane in [$\text{cm}^2 \text{steradians}$] is the field-of-view over which each detector pixel sees the background. The f-number at the detector used for the computation is determined by design considerations (to sample the slice width with two pixels), namely 14.3, 6.3, 4.7, and 2.9, for the LM, N1, N2, and Q band, respectively.

$$A \cdot \Omega = 2 \left(1 - \cos \left(\arctan \left(\frac{f}{2D_D} \right) \right) \right) D^2_{pix}$$

The sampling in the spatial dimension is different due to anamorphic optics. Instead of $1.22\lambda/D$ the spatial sampling is at $1.5\lambda_{min}/D$. Although the camera is slightly slower in the spatial direction this is not (yet) included in the spreadsheet calculations.

The total noise per pixel for a given integration time t_{int} is a combination of three components (assuming Poissonian error distributions for three statistically independent components):

1. the noise associated with the background signal: $\sqrt{(S_{back} \times t_{int})}$,
2. the noise associated with the detector dark current: $\sqrt{(I_d \times t_{int})}$, and
3. the detector read noise and the number of frames: $N_{read} \sqrt{n}$

Hence, the total background noise [e^- /pixel/ t_{int}] is: $N_{back} = \sqrt{S_{back} t_{int} + I_d t_{int} + N_{read}^2 n}$

With the above equations we can now compute the two most important quantities: the flux an unresolved line S_{line} and the continuum sensitivity S_{cont} .

The line flux S_{line} in [$W m^{-2}$] can be derived from the minimum detectable signal from a source S_{src} in [$photons s^{-1} cm^{-2} \mu m^{-1}$] via: $S_{line} = \frac{hc}{\lambda} S_{src} \Delta \cdot 10^4$

With $S_{\lambda} \left[\frac{W}{m^2 \mu} \right] = S_{\nu} [Jy] \cdot 10^{-26} \frac{c}{\lambda^2}$, the continuum sensitivity S_{cont} [Jy] can then be calculated to:

$$S_{cont} = \frac{hc}{\lambda} S_{src} \cdot 10^4 \cdot \frac{\lambda^2}{c} \cdot 10^{26} = h_{src} \cdot 10^{30}$$

Those are two quantities that are plotted in the following sections for the various wavebands and resolutions.

8.3.2 Low Resolution $R=300$ Spectrograph

Note: *The low-resolution sensitivities were calculated with the spreadsheet described above which assumes an IFU spectrograph. However, the low resolution module is more likely to be part of the imaging channel using a different optical setup based on a grism. Hence, the graphs within this subsection can only serve as a rough guideline.*

At low resolution the main interest is the sensitivity to the continuum or broad spectral features. Fig. 46to 48 show the LM, N, and Q band sensitivities, respectively.



T-OWL Concept Level Study

Doc : OWL-CSR-ESO-00000-0161



Version 1
Date: 20/10/2005
Page: 81/175

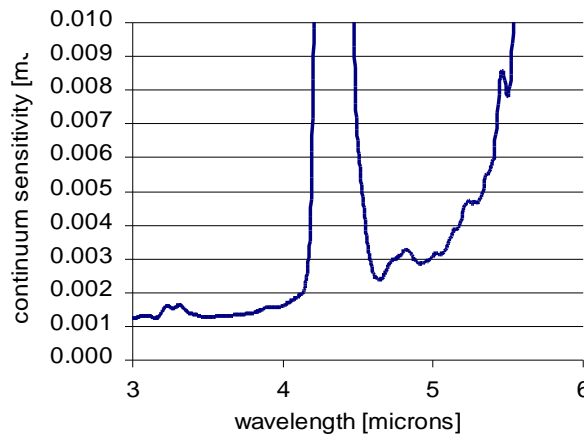


Fig. 46 – $10\text{-}\sigma$ continuum point source sensitivity in L and M-band at $R = 300$ for one hour wall clock observing time.

At LM bands astronomers often think in units of magnitudes rather than Janky. The corresponding magnitudes to the limiting 10σ , 1hr flux densities in Fig. 46 are:

Band	λ [μ m]	mag	Flux
L	3.45	20.9	$1.3\mu\text{Jy}$
M	4.80	17.6	$3.2\mu\text{Jy}$

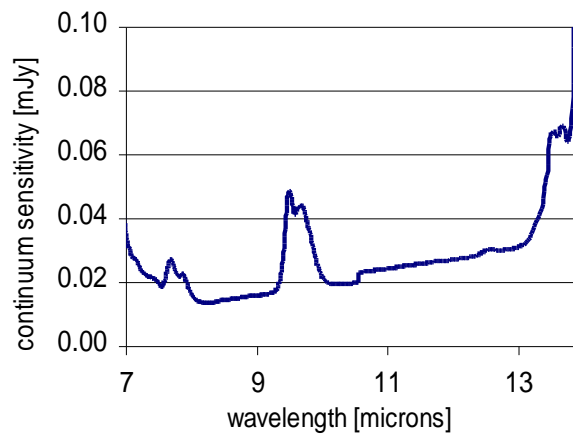


Fig. 47 – $10\text{-}\sigma$ continuum point source sensitivity in N-band at $R = 300$ for one hour wall clock observing time.



T-OWL Concept Level Study

Doc : OWL-CSR-ESO-00000-0161



Version 1
Date: 20/10/2005
Page: 82/175

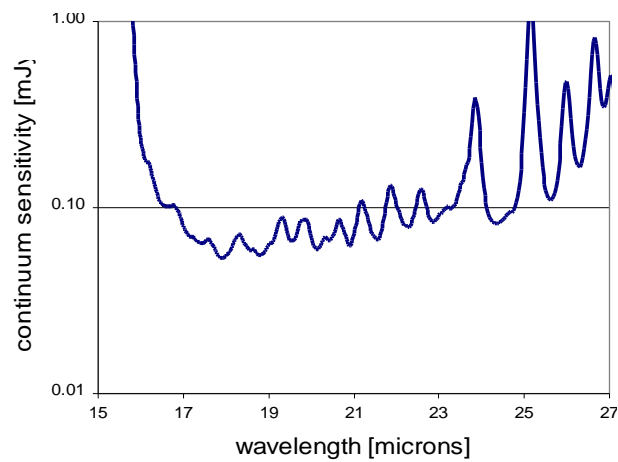


Fig. 48 – $10\text{-}\sigma$ continuum point source sensitivity in Q-band at $R = 300$ for one hour wall clock observing time.

8.3.3 Medium Resolution $R = 3000$ Spectrograph

At medium resolution the interest is the sensitivity to both continuum and line fluxes. Hence, Fig. 49 to Fig. 54 show the LM, N, Q band sensitivities in units of both mJy and Wm^{-2} .

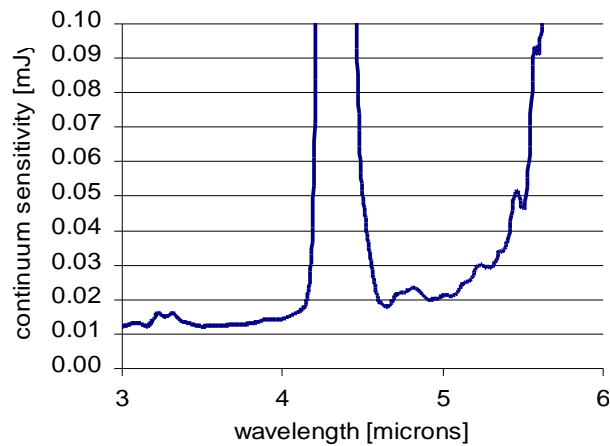


Fig. 49 – $10\text{-}\sigma$ continuum sensitivity to a point source in LM-band at $R = 3000$ within one hour wall clock time.



T-OWL Concept Level Study

Doc : OWL-CSR-ESO-00000-0161



Version 1
Date: 20/10/2005
Page: 83/175

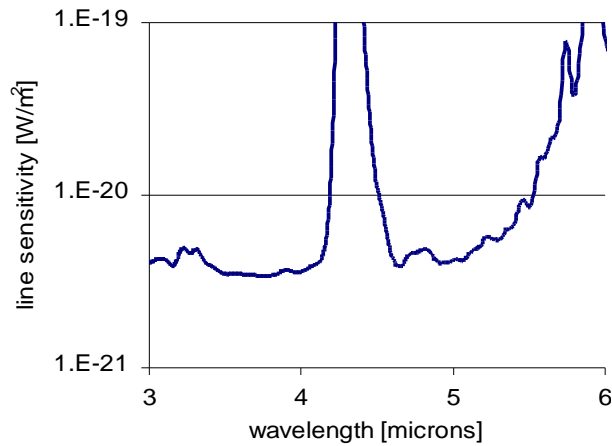


Fig. 50 – $10\text{-}\sigma$ line sensitivity to a point source in LM-band at $R = 3000$ within one hour wall clock time.

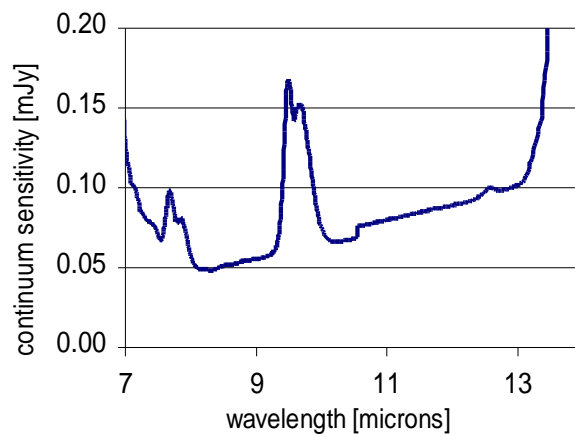


Fig. 51 – $10\text{-}\sigma$ continuum point source sensitivity in N-band at $R = 3000$ within one hour wall clock time.

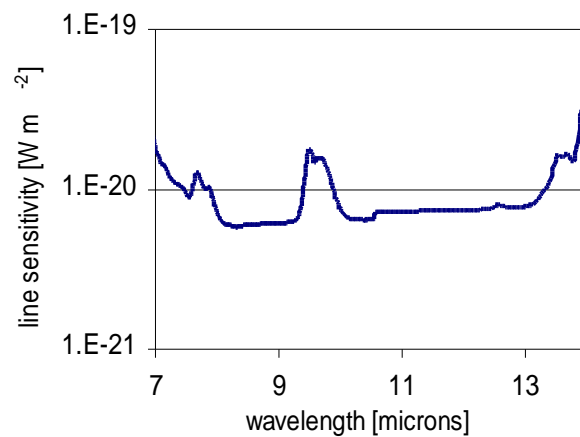


Fig. 52 – $10\text{-}\sigma$ line sensitivity to a point source in N-band at $R = 3000$ within one hour wall clock time.



T-OWL Concept Level Study

Doc : OWL-CSR-ESO-00000-0161



Version 1
Date: 20/10/2005
Page: 84/175

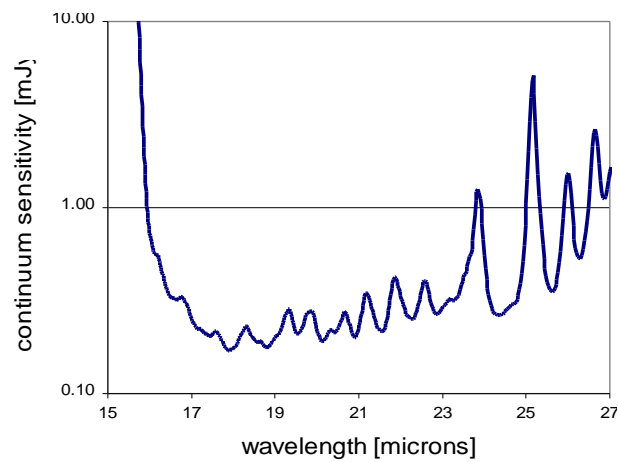


Fig. 53 – $10\text{-}\sigma$ continuum point source sensitivity in Q -band at $R = 3000$ within one hour wall clock time.

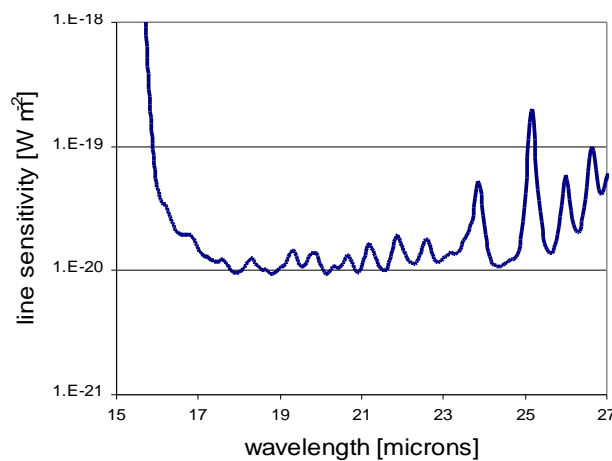


Fig. 54 – $10\text{-}\sigma$ line sensitivity to a point source in Q -band at $R = 3000$ within one hour wall clock time.

8.3.4 High Resolution $R = 50000$ Spectrograph

At very high resolution the interest is in the sensitivity to very narrow spectral features. Fig. 55 to Fig. 59 show the sensitivities in units of W m^{-2} towards some unresolved emission lines within the LM, N, and Q bands.



T-OWL Concept Level Study

Doc : OWL-CSR-ESO-00000-0161



Version 1
Date: 20/10/2005
Page: 85/175

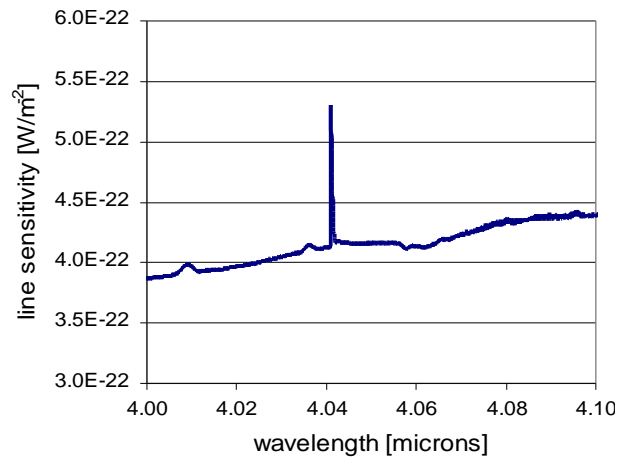


Fig. 55 – $10\text{-}\sigma$ line sensitivity to a point source around the Br- α line ($4.05\mu\text{m}$) in L-band at $R = 50000$ within one hour wall clock time.

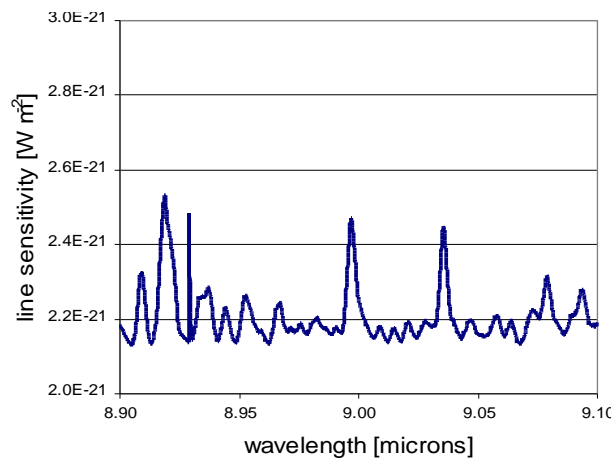


Fig. 56 – $10\text{-}\sigma$ line sensitivity to a point source around the [Ar III] line ($8.99\mu\text{m}$) in N-band at $R = 50000$ within one hour wall clock time.

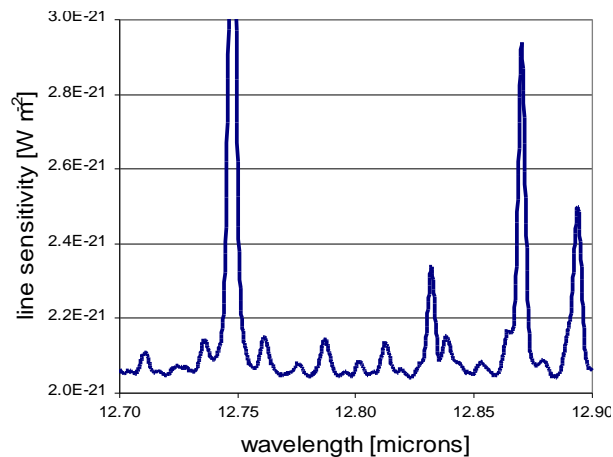


Fig. 57 – $10\text{-}\sigma$ line sensitivity to a point source around the [Ne II] line ($12.81\mu\text{m}$) in N-band at $R = 50000$ within one hour wall clock time

In Q-band the sensitivity at high resolution depends strongly on the actual wavelength since the atmosphere has numerous narrow windows of poor transmission. However, at high resolution, it is possible to obtain much better sensitivity by observing between these more opaque wavelengths. In some sense, the situation is similar to the OH lines in the NIR H-band.

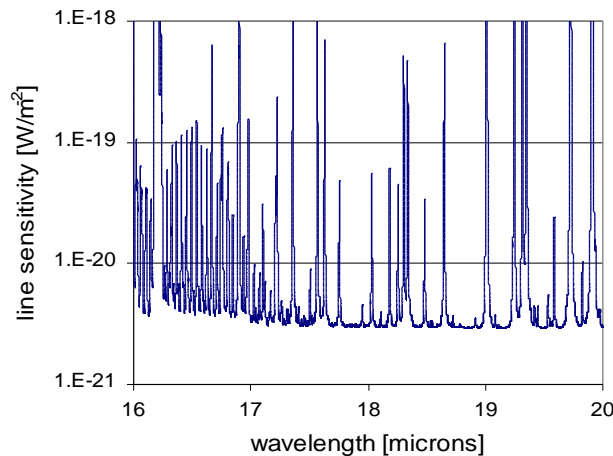


Fig. 58 – $10\text{-}\sigma$ line sensitivity to a point source in the short wavelength part of the Q-band at $R = 25000$ within one hour wall clock time. Numerous spectral features, such as the $H_2 S(1)$ line, fall into windows of good atmospheric transmission and can be observed at unsurpassed sensitivity.

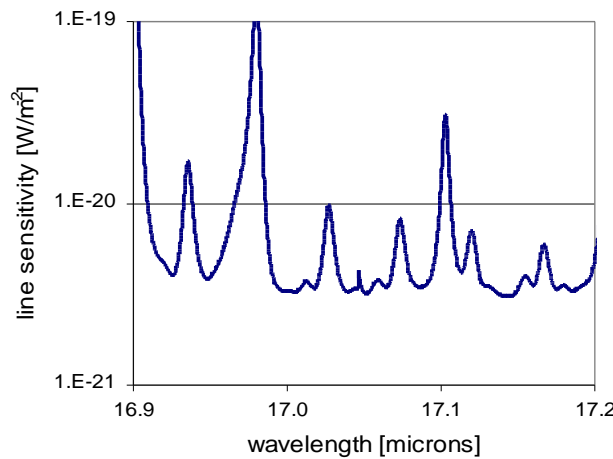


Fig. 59 – $10\text{-}\sigma$ line sensitivity to a point source around the $H_2 S(1)$ line ($17.03\mu\text{m}$) in Q-band at $R = 25000$ within one hour wall clock time.

8.3.5 Conclusions

Fig. 60 compares the line sensitivities at $R=3000$ that can be obtained with a T-OWL-like instrument on a 8m, 30m, and 100m telescope in the N-band. The 8m case has been added for comparison with existing instruments like VISIR at the VLT and MICHELLE at GEMINI; the good agreement with the actually achieved sensitivities there gives us good confidence in our sensitivity estimates for T-OWL.

The **most important conclusions** from the above discussion are:

- The line sensitivity in N-band provided by T-OWL at R=3000 is basically the same as for JWST/MIRI (see Fig. 60 and Fig. 61).
- Because of 1. and the fact that T-OWL will have 15 times better spatial resolution, a 100m (T)-OWL is an equal competitor to JWST/MIRI. However, a significantly reduced OWL aperture, e.g., 30m, will not be able to compete with JWST in terms of sensitivity.
- The high resolution spectrograph (R=50000) will provide unsurpassed sensitivity to unresolved lines, and hence be a much more powerful tool to study very narrow spectral features than JWST/MIRI within the atmospheric windows.

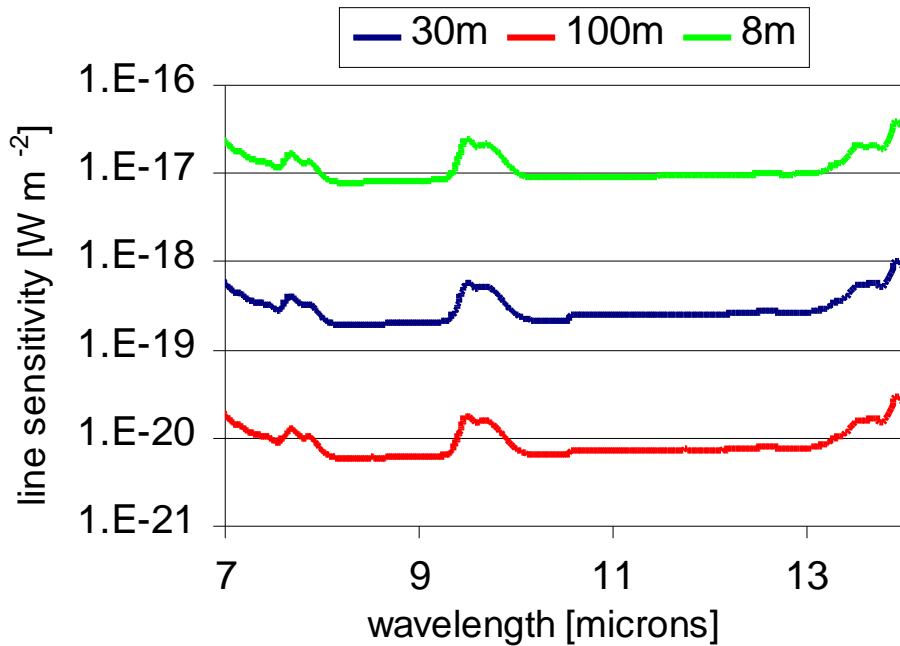


Fig. 60 – Impact of the telescope aperture size on the N-band line sensitivity (10σ in 1hr) at R=3000.



T-OWL Concept Level Study

Doc : OWL-CSR-ESO-00000-0161



Version 1
Date: 20/10/2005
Page: 88/175

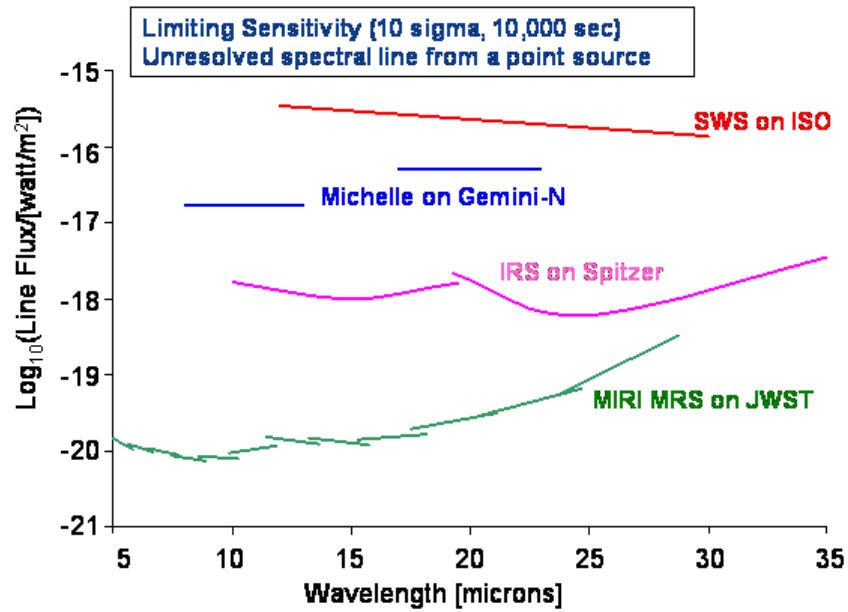


Fig. 61 – Comparison of the line sensitivity between existing and future T-OWL spectrograph “competitors” (courtesy Alistair Glasse).

9 Comparison to Ground Based Facilities and Space Missions

9.1 Mid Infrared Instrumentation at 8m-Class Telescopes

Table 8: Observational capabilities of MIR-instrumentations at existing 8m-class telescopes

Telescope	Instrument	Wavelength coverage [μm]	Pixel scale [arcsec/pixel]	Detector size	Spec. Res.	Window
Gemini N	Michelle	7 - 26	0.10	320x240	200@7-14 110@16-26 1000@7-26 3000@7-26 30000@7-26	KBr
Gemini S	T-ReCS	8-26	0.10	320x240	100@10 80@20 1000@10	KBr, ZnSe, KRS-5 (real time)
GTC	CanariCam	8-26	0.08	320x240	150@10,20 1300@10 900@20	ZnSe, KBr, KRS-5 (real time)
Hobby-Erberly	-	-	-	-	-	-
Keck	LWS	3.5-25	0.085	128x128	270@10 540@20 4000@10 4000@20	KBr+ZnSe
LBT	-	-	-	-	-	-
Subaru	Comics	8-26	0.13	320-240	250,2500,10000 @10 2500 @ 20	ZnSe, KBr few hours
VLT	Visir	8-24	0.075 0.127 0.2	2x256x256	350@10 3200@10 25000@10	

All currently available 8m-class telescopes are offering a MIR instrument that combines direct imaging and spectroscopic capabilities. It is interesting to see that VISIR at the VLT is the only MIR that offers imaging pixel scales well beyond the optimum diffraction limit sampling.

A second aspect that can be learned from this list, is the choice of the entrance window. Windows are exchangeable, sometimes within few hours, sometimes in realtime. To our knowledge, no diamond window is in use.

The third point we want to emphasize here, is the dimension of the typical detector array. Groundbased MIR instrumentation is dealing with array sizes that correspond to NIR arrays of the 1985s.

9.2 Expected Contemporaries of T-OWL

9.2.1 Introduction

Spitzer has been successfully launched in August 2003. With its new, large format MIR arrays Spitzer is orders of magnitudes more sensitive than its predecessors and opened up a new observing space, discovering hundred thousands of new infrared sources in our Galaxy as well as at higher redshifts. During its five year cryogenic lifetime Spitzer will deliver many exciting results, but also an extremely rich dataset for high resolution follow-up observations with T-OWL and the facilities listed below. The catalogs that are being compiled from the Galactic GLIMPSE survey and the extragalactic, deep GOODS and wide-field SWIRE surveys will provide an extremely rich database for many years to come, just as the IRAS catalogs have been serving infrared astronomers for more than 20 years.

9.2.2 James Web Space Telescope

JWST will be launched in 2012 (status July 2005) from an expandable launch vehicle into an orbit at the L2 Lagrange point. An operational life time of at least 5 years is planned, possibly elongated to a maximum of 10years (cooling exclusively provided by closed cycle cooler). Thus, even for the longest assable operational lifetime JWST will have ended its operation when OWL becomes fully operational. Nevertheless, JWST with MIRI will be a main compator for T-OWL. Therefore, its observational capabilities as well as some mission informations are presented here in some more detail:

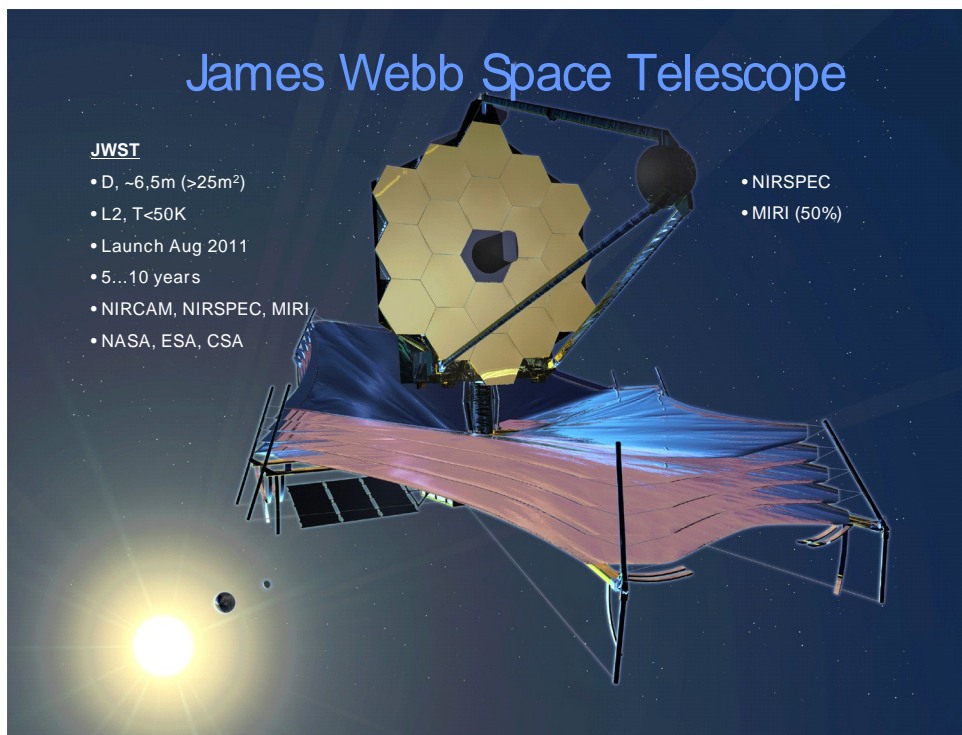


Fig. 62: JWST placative description

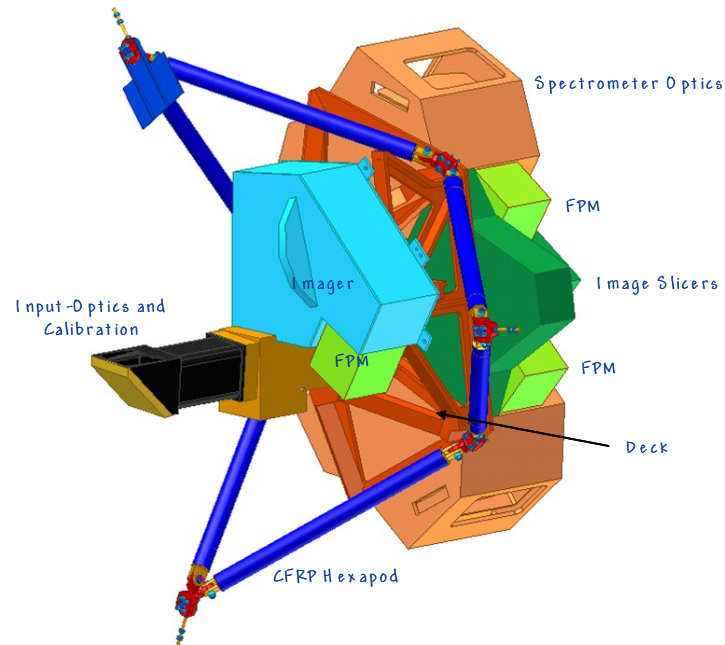


Fig.63: JWST MIRI Optical Module

JWST – Scientific Objectives:

1. The End of the Dark Age: First Light and Re-ionization
2. The Assembly of Galaxies
3. The Birth of Stars and Protoplanetary Systems
4. Planetary Systems and Origins of Life



T-OWL Concept Level Study

Doc : OWL-CSR-ESO-00000-0161



Version 1
Date: 20/10/2005
Page: 92/175

Level 1 Baseline Science Requirements (Mission Success Criteria)

4.1.1.1 Measure the space density of galaxies to a $2 \mu\text{m}$ flux density limit of $1.0 \times 10^{-34} \text{ W m}^{-2} \text{ Hz}^{-1}$ via imagery within the **0.6 to $27 \mu\text{m}$** spectral band to enable the determination of how this density varies as a function of their age and evolutionary state.

4.1.1.2 Measure the spectra of at least **2500 galaxies** with spectral resolutions of approximately **100 (over 0.6 to $5 \mu\text{m}$)** and **1000 (over 1 to $5 \mu\text{m}$)** and to a $2 \mu\text{m}$ emission line flux limit of $5.2 \times 10^{-22} \text{ W m}^{-2}$ to enable determination of their redshift, metallicity, star formation rate, and ionization state of the intergalactic medium.

4.1.1.3 Measure the physical and chemical properties of young stellar objects, circumstellar debris disks, extra-solar giant planets, and Solar System objects via spectroscopy, and imagery within the **0.6 to $27 \mu\text{m}$** spectral band to enable determination of how planetary systems form and evolve.

JWST – 39 Science Requirements

(„JWST should be capable of/provide...“)

- SR-1 ..wavelength range 0.6 – $27 \mu\text{m}$
- SR-2 ..imaging ($3 < R < 200$) with ≥ 16 discrete filters over $0.6 < \lambda < 27 \mu\text{m}$
- SR-3 ..coronagraphic imaging capabilities over $2 < \lambda < 27 \mu\text{m}$
- SR-4 ..spectroscopy with $50 < R < 5000$ over $0.6 < \lambda < 27 \mu\text{m}$
- SR-7 ..simultaneous spectra of ≥ 100 objects (NIRSPEC)
- SR-10 ..primary mirror, unobscured, $\geq 25 \text{ m}^2$
- SR-11 ..diffraction limited imaging at $\lambda = 2 \mu\text{m}$
- SR-16 ..sensitivity
 - $1.2 \cdot 10^{-34} \text{ W m}^{-2} \text{ Hz}^{-1}$, SN=10, 10^4 s , R=4 (NIRCAM)
 - $1.2 \cdot 10^{-33} \text{ W m}^{-2} \text{ Hz}^{-1}$, SN=10, 10^4 s , R~100 (NIRSPEC)
 - $7 \cdot 10^{-33} \text{ W m}^{-2} \text{ Hz}^{-1}$, SN=10, 10^4 s , R=5 (MIRI)
- SR-17 ..ZL background limited imaging over $0.6 < \lambda < 10 \mu\text{m}$
- SR-20 ..calibration accuracy: imaging 5%, coronagraphic imaging 15%, spectroscopy 15%
- SR-21 ..FOV [arc min^2] > 9.4 NIRCAM...> 3.5 MIRI
- SR-26 ..observing anywhere within celestial sphere, over 1 yr
- SR-27 ..> 35% of sphere accessible anytime
- SR-32 ..mission lifetime $\geq 5 \text{ yr}$ (propellant for 10 yr)
- SR-34 ..observing efficiency (on scientific target) > 70%
- SR-37 ..general observer and archival research (peer review of science proposals)

Celestial calibration standards: solar type G-stars in clusters, A stars (SPITZER)

Systematic errors: dark current drifts, flat fields, latent images, gain drifts, cosmoics,...

Table 9: Sensitivity estimates for the MIRI Imager and Spectrometer

Imager					
Band (μm)	Bandpass (μm)	Estimated Background (e/s)	Frame Pattern	Detection Limit (μJy) ($10\text{-}\sigma$ in 10000sec)	
				EOL	BOL
5.6	1.2	6	SLOW, 480 sec	0.19	0.15
7.7	2.2	45	FAST, 120 sec	0.28	0.23
10	2	94	FAST, 120 sec	0.7	0.5
11.3	0.8	52	FAST, 120 sec	1.7	1.15
12.8	2.5	222	FAST, 120 sec	1.4	0.9
15	4	526	FAST, 60 sec	1.8	1.1
18	3	672	FAST, 30 sec	4.3	3.1
21	5	2354	FAST, 15 sec	7.3	5.7
25.5	3.9	7677	FAST, 6 sec (512x512 sub-frame)	29	25
Spectrometer					
Wavelength	$\lambda/\Delta\lambda$	Estimated Background (e/s)	Frame Pattern	Detection Limit ($10^{-20} \text{ W m}^{-2}$) ($10\text{-}\sigma$ in 10000sec)	
				EOL	BOL
6.4	2400	0.04	SLOW, 960 sec	1.2	0.8
9.2	2400	0.08	SLOW, 960 sec	1	0.75
14.5	1600	0.5	SLOW, 480 sec	1.2	0.8
22.5	1200	3.5	SLOW, 480 sec	5.6	5

9.2.3 SAFIR

Safir (the Single Aperture Far InfraRed Observatory) is a large (10m-class) cold (4-10K) space telescope for wavelengths between 20 micron and 1mm. This project has been selected for a Vision Mission study currently being performed by the NASA centers GSFC, JPL, MSFC and JSC in collaboration with Ball Aerospace, Lockheed-Martin and Northrup-Grumman. With a wavelength region of 20-800 μm , Safir is poised to bridge the spectrum between JWST and ALMA, improving the point source sensitivity compared to Herschel and/or Spitzer by up to three decades (see Fig. 65).

Safir is planned to be launched on a Delta IV-H rocket at middle JWST lifetime in 2015-2020. Several concepts are currently under discussion to optimize the deployable telescope assembly and the corresponding cooling concept. Main telescope requirements are:

- Aperture diameter >8m
- Temperature ~ 4K
- Wavelength range 20 – 800 μm
- Diffraction limited for $\lambda > 40\mu\text{m}$ (1 arcsec)
- Pointing accuracy 0.5 – 1 arcsec
- Pointing stability ~ 0.1 arcsec
- Lifetime > 5 years

Safir will be injected into a quasi-stable L2 halo orbit. Currently planned instruments (Strawman Instrumentation) are:

- Camera for the 20-600 μm wavelength region
- Low resolution spectrometer for the wavelength region 20-800 μm (R~100)

- Mid resolution spectrometer for the entire wavelength region (20-800 μ m) R~2000
- High resolution spectrometer for the 25 to 520 μ m region (R~10⁶)

Following these specifications, SAFIR could be a very powerful complementary facility to future MIR instrumentations like T-OWL and JWST/MIRI. Within the small overlapping wavelength range between 20 and 27 μ m, compared to ALMA, SAFIR provides by a factor of 10 higher sensitivity for point sources but a factor of at least 10 lower spatial resolution.

9.2.4 ALMA

Following the current time-scale ALMA will detect first light using the full array in 2010. The baseline frequency bands available are: 86 – 116GHz, 211 – 275 GHz, 275 – 370 GHz, and 602 – 720GHz. Spatial resolution can be changed between 350 arcsec/Freq[GHz] and 4.2arcsec/ freq[GHz] depending on the chosen configuration. Thus, the maximum spatial resolution is achieved at 86GHz (417 μ m) with 6mas.

9.2.5 Darwin

The European Space Agency has selected the "InfraRed Space Interferometer - Darwin" as a mission for its Horizons 2000 programme. Selection of a launch date, probably at or after 2015, will be made on cost, science and technology grounds sometime before then.

Darwin will use a flotilla of three space telescopes, each at least 3 metres in diameter, and a fourth spacecraft to server as communications hub. The telescopes will operate together to scan the nearby Universe, looking for signs of life on Earth-like planets. This is a daunting challenge and will require a number of technological innovations before the mission launches in the middle of the next decade.

9.2.6 VLTI

At MIR wavelength, VLTI is in operation already since few years (MIDI). As interferometric device, it can not be competitive to a 100m telescope in sensitivity, however, the spatial resolution is of the same order as T-OWL.

9.2.7 WISE

WISE will provide an all-sky survey from 3.5 to 23 microns up to 1000 times more sensitive than the IRAS survey. WISE has been selected by NASA as its next Medium-Class Explorer. With this decision the WISE mission will proceed into Phase B (Definition Phase).

A 40cm-telescope is collecting the light into four channels to produce a complete four colour survey of the sky at 3.3, 4.7, 12 and 24 μ m, which will provide an excellent data base for JWST and other MIR pointing facilities like OWL. Thus, WISE is not competitive to JWST and/or T-OWL, neither in resolution nor in sensitivity, but will prepare a detailed study of selected astrophysical objects.

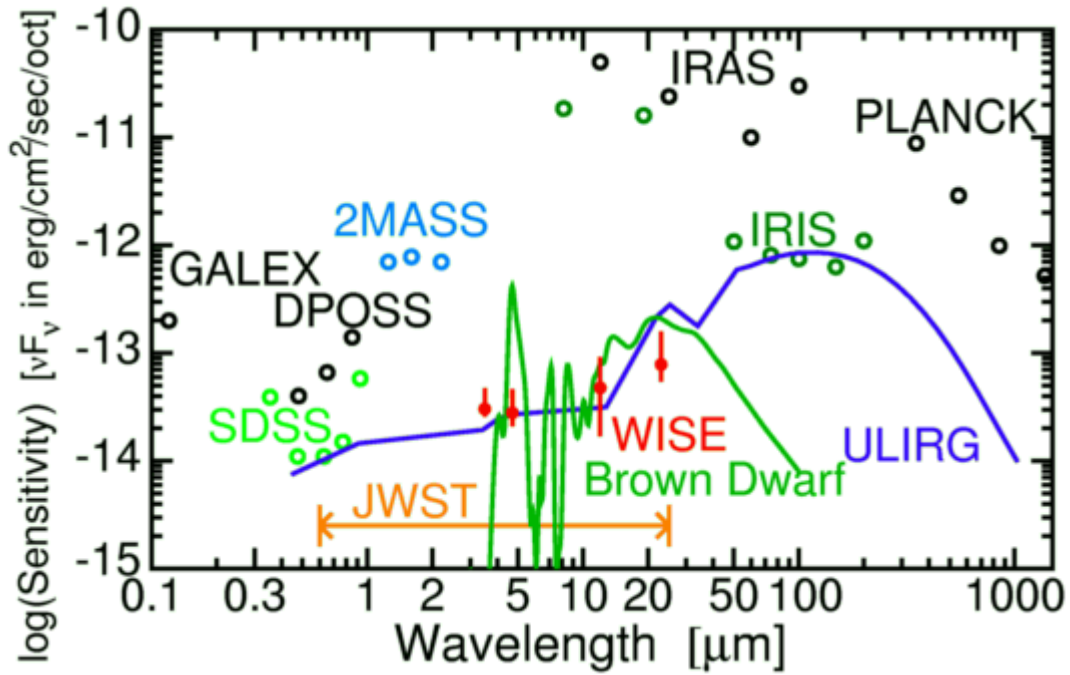


Fig. 64: Sensitivity of WISE

Table 10: Comparison of the main MIR competitors of T-OWL

Project	Wavelength range [μm]	Telescope diameter [m]	Telescope temperature	Diffraction limit @5μm [mas]	FOV [arcmin]	Launch
JWST (MIRI, NIRCam)	0.6 – 28	6.5	50 K	159	2.3 x 2.3	2012
OWL	1 – 27	100	290 K	10	20 x 20	2021
SAFIR	30 – 500	10	5K	100		2020
Spitzer IRAC	3.6 – 8	0.85	70 K	1213	5 x 5	2003
WISE	3.5 – 24	0.40	15K	2580	45 x 45	2008

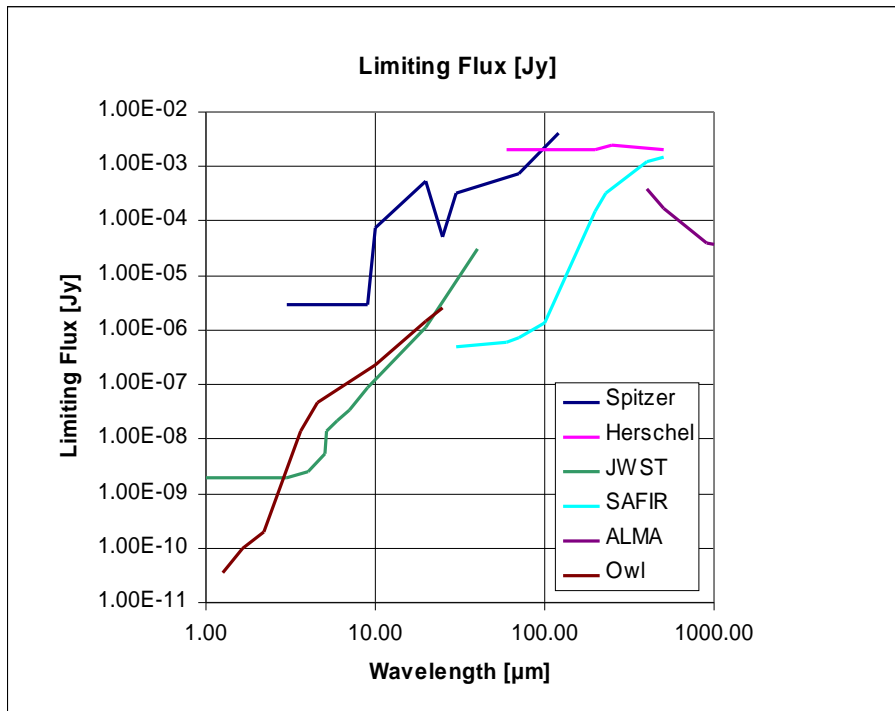


Fig. 65: Comparison of point source detectivity of contemporary IR and sub-millimeter instrumentations to a MIR instrumentation at OWL.

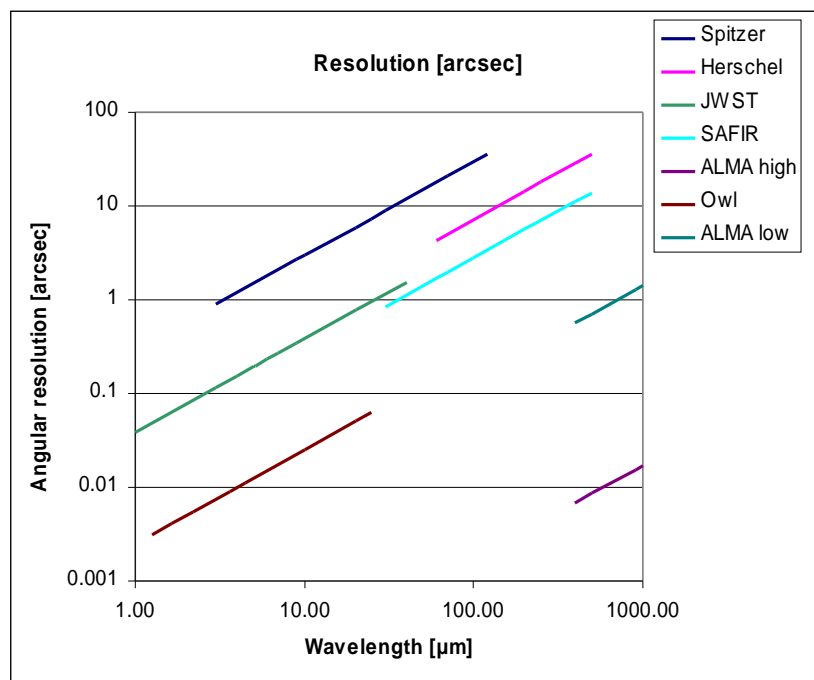


Fig. 66: Comparison of spatial resolution of contemporary IR to sub-millimeter projects to MIR-instrumentation at OWL.

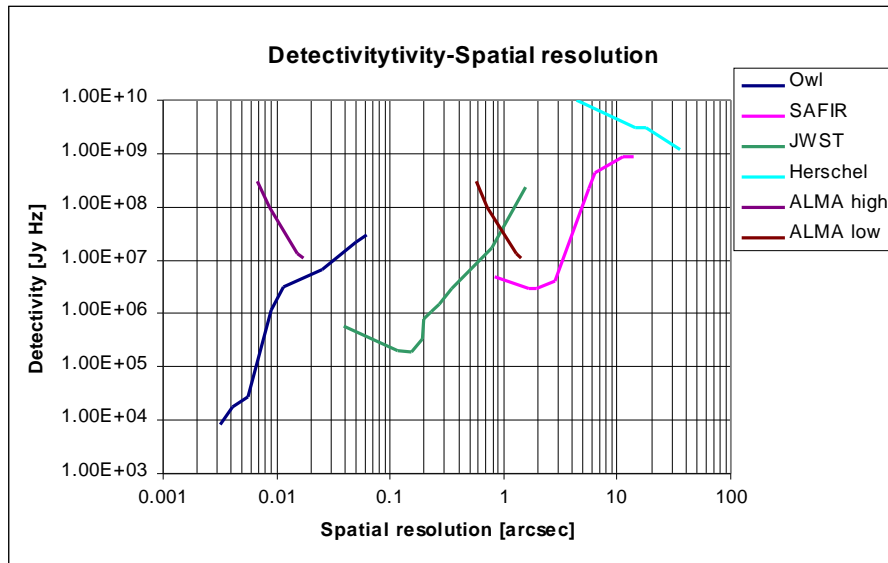


Fig. 67: Comparison of point-source detectivity versus spatial resolution of IR to sub-millimeter contemporaries to an OWL MIR-instrument

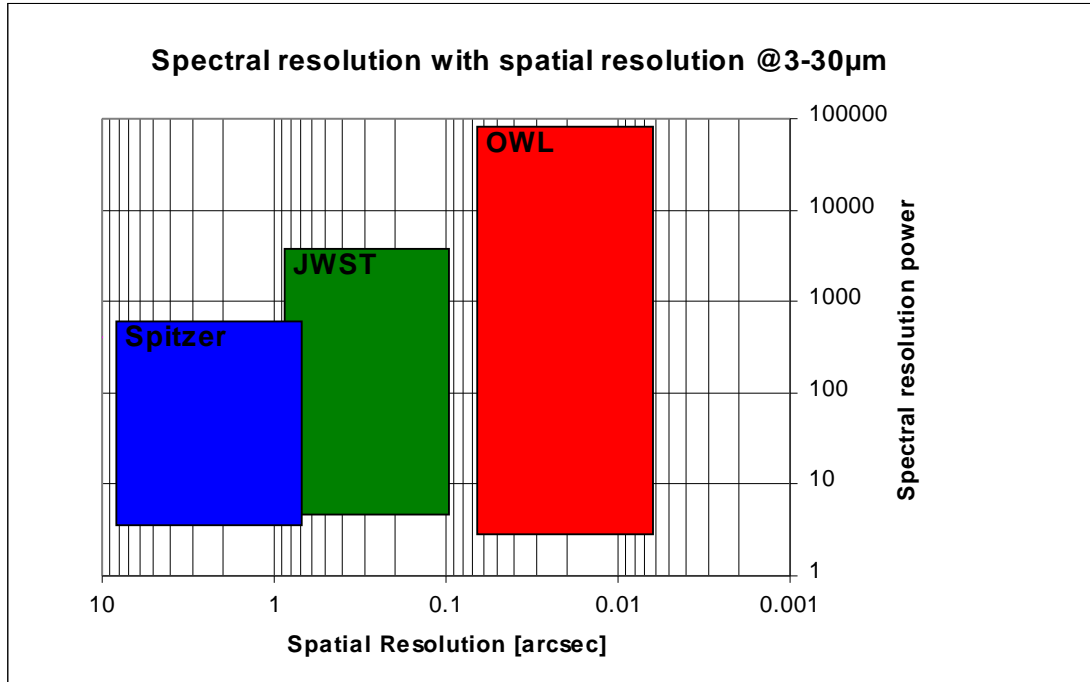


Fig. 68: Comparison of possible field of observational capabilities of T-OWL compared to those of JWST/MIRI and Spitzer.

9.2.8 Summary

Most of the currently planned projects are less competitive than more complementary to T-OWL. SAFIR and ALMA will work in an other wavelength range than T-OWL JWST and WISE will not have the resolution of OWL and VLTI and Darwin will not have the sensitivity as T-OWL. Taking also in account that space missions will have a much more limited lifetime than a ground based telescope and instrument, T-OWL would clearly fulfil the need of highly sensitive, long living and flexible mid-infrared instrument providing high spatial resolution.

10 Scope of the Ideal Instrument

10.1 Wavelength Range

The choice of the wavelength region of a ground based thermal to mid infrared instrument is driven by the atmospheric transmission windows. The lower limit of the wavelength band taken into consideration here is $2.5\mu\text{m}$ to avoid overlap to any NIR instrumentation discussed for OWL. On the other hand, beyond $30\mu\text{m}$ even for best 10% conditions at extreme altitudes of 5km elevation level, the atmospheric transmission is too poor to rectify instrumental development for ground based observations.

Even the $20\text{-}30\mu\text{m}$ region is strongly restricted by atmospheric absorption bands (mainly water), only single narrow band imaging observations are possible with significant sensitivity.

We propose to combine two detector types to cover the full wavelength range from 2.5 to $27\mu\text{m}$: The InSb-detector (type ALADIN e.g.) covers the thermal IR region with exceptional QE values, an additional Si:As-detector will be sensitive from 5 to $27\mu\text{m}$ (see chapter 12.4.6).

As we favorite an all reflected optical system, only the entrance window material will depend on the decision if the cut-off wavelength will be $20\mu\text{m}$ or $27\mu\text{m}$.

10.2 Imaging Mode

10.2.1 Pixel Scale

For the following collection of top level requirements we assume an f-ratio of the telescope of F/6 (see OWL ICD-document). The resulting scale is 0.344arcsec per mm, or 2.909mm per arcsec. To determine the maximum FOV the TIRC should be able to re-image, we assume a 1024×1024 pixel array for the MIR region detector and 2048×2048 pixel array for the $1 - 5\mu\text{m}$ region. The camera should be able to Nyquist sample for the smallest wavelengths, thus, the resulting FOV is $1024 * 7.0\mu\text{m}/D/2$ in arcsec, which is $7.4\text{arcsec} \times 7.4\text{arcsec}$. In linear scale this is $21.5\text{mm} \times 21.5\text{mm}$. For the smallest wavelength of the TIR detector ($3\mu\text{m}$) the corresponding calculations is $2048 * 3\mu\text{m}/D/2$ which gives $6.3 \times 6.3 \text{arcsec}^2$. We propose a pixel scale of 3.5mas and 7.0mas for the TIR and the MIR wavelength region, respectively. Thus, common maximum FOV for imaging application is $7 \times 7 \text{arcsec}^2$.

The following list gives the required f-ratio of the re-imaged beam, assuming different pixel scales of $27\mu\text{m}$, $50\mu\text{m}$ and $75\mu\text{m}$. Fortunately, linear pixel scales are adjusted to Nyquist sampling of



T-OWL Concept Level Study

Doc : OWL-CSR-ESO-00000-0161



Version 1
Date: 20/10/2005
Page: 99/175

diffraction limited application at a typical central wavelength for a typical f-ratio between 12 and 16, which is independent from telescope size: 27 μm e.g. is an optimum value for f/10 at 5 μm , thus, for diffraction limited application, the re-imaging magnification is not too far away from unit.

As shown in chapter 12.2, a larger FOV of up to 3 x 3 such sub-fields (that is 21 arcsec x 21 arcsec) could be built up by mosaicing such optical camera systems including the entrance window. However, at present there are no high priority science cases which could drive such development.

pixel	Wavelength				
	3	5	8	14	20
27 μm	18.0	10.80	6.75	3.86	2.70
50 μm	33.33	20.00	12.50	7.14	5.00
75 μm	50.00	30.00	18.75	10.71	7.50

Table 11: F-ratio of re-imaging beam required for Nyquist sampling at different wavelengths and for three most common pixel sizes. Most favourable combinations are highlighted in yellow.

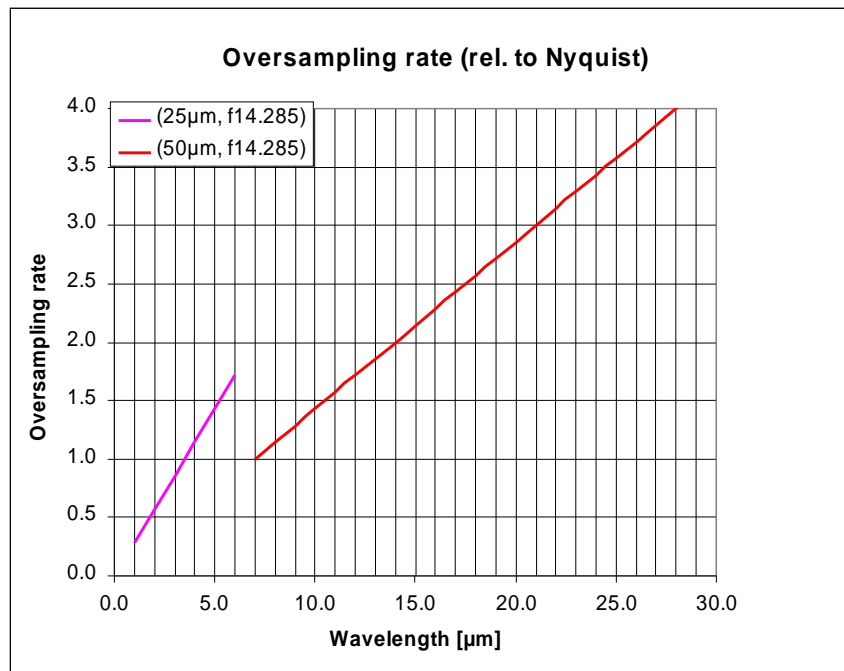


Fig. 69: Over-sampling rate (compared to Nyquist sampling) for 3mas (respectively 6mas) pixel size within the 1-5 μm (respectively 7-25 μm) region.

We propose a pixels scale that provides Nyquist sampling at 3.5 μm and 7.0 μm , respectively. Assuming 25 μm and 50 μm pixel pitch values for the TIR array and the MIR array, respectively, the optimum f-ratio is 14.285 for all the entire wavelength region. T-OWL will be optimized for the 3 – 27 μm region, thus under-sampling rates below 3 μm are acceptable. For the MIR region best choice of

a fixed camera is a scale that provides Nyquist sampling at the lower end at $7\mu\text{m}$, accepting over-sampling within the Q-band.

10.2.2 Chronagraphy

The cryogenic focal plane contains some change mechanism to insert field stop masks, slit masks and coronagraphic masks. At a minimum, the following coronagraphic masks should be provided:

- Full spot 5λ @ $3\mu\text{m}$ 30mas diameter
- Full spot $5\lambda/D$ @ $10\mu\text{m}$ 100 mas diameter
- Full spot $5\lambda/D$ @ $20\mu\text{m}$ 200mas diameter
- 10^{-4} spot $5\lambda/D$ @ $3\mu\text{m}$ 30 mas diameter
- 10^{-4} spot $5\lambda/D$ @ $10\mu\text{m}$ 100mas diameter
- 10^{-4} spot $5\lambda/D$ @ $20\mu\text{m}$ 200 mas diameter
- quarter phase plate

10.2.3 Pupil Masking

At the position of the cryogenic pupil image pupil masks can be inserted. As T-OWL will not be rotated, the pupil position is fixed, no pupil rotation is provided, thus, for normal operation only a small number of Lyot-stops is required. However, if observations with a partly assembled M1 are provided, several blocking masks are necessary.

All masks are slightly undersized to make sure that the effective pupil is defined by the cryogenic mask. The Lyot stops are designed to block out all warm structures of the telescope except for the gaps between mirror segments. Whether the $14\mu\text{m}$ structure of these gaps can be reduced significantly should be considered in a subsequent study.

10.2.4 Low Resolution Spectroscopy

While the following chapter will deal with the spectroscopic mode of T-OWL as a whole, the low resolution spectroscopy is treated as part of the imaging mode: For resolution power between 100 and 300 ($\Delta\lambda$ per 2 pixels) the dispersing element will be a grism, optionally inserted into the collimated beam of the imager, near to the pupil image. A long slit mask is inserted into the cryogenic focal plane. Due to the limited number of useful optical materials for the mid-IR region, low resolution spectroscopy by prisms is not recommended. For details see chapter 12.4.5.

10.3 Spectroscopic Mode

10.3.1 General Spectroscopic Concept (Spectral Modes)

In the overall layout of the T-OWL instrument the imager and spectrometer are physically separated. The main reason for this separation lies is to be able to implement a high resolution spectroscopic mode and to optimise the spectroscopic performance.

Early on for spectrometry, three main settings for the resolution were required from science:

- low resolution spectroscopy ($R \sim 100-300$)
- medium resolution spectroscopy ($R \sim 3000$)
- high resolution spectroscopy ($R \geq 50000$ (N) and 25000(Q))

In the design process, the low resolution spectroscopy was separated from the other modes by incorporating the low resolution mode in the imager.

The instrumental parameters derived in Section 5.11 drive the design. The design wavelength range does presently not consider the actual atmospheric transmission windows, and some cuts may have to be made. Furthermore, as will be discussed later, the maximum spatial resolution of the OWL telescope can only be reached by designing the instrument fully diffraction limited. For spectrometers, a diffraction limited design, requires optimal slit selection, certainly when a reasonable throughput and instrumental dimensions are required. This necessitates the splitting of the overall wave-length range into different bands.

Table 12: Top level technical requirements for the spectrometer

Parameter	Values
λ_{\min}	3 μm
λ_{\max}	27 μm
R_{low}	100-300
R_{medium}	3000
R_{high}	~ 50000
HR-mode	<512 resolution elements
MR-mode	1.7 μm per exposure (@10 μm)
FOV	3''x3'' continuous
Multi-object	NO
Wide FOV	reduced spatial resolution allowed
Polarimetry	no strong drivers as yet
	not yet required for R 50000
Parallel read-out	not required

10.3.2 IFU Versus Long-slit

The medium resolution slit spectrograph concept could be either based on a more conventional long-slit or an integral field unit (IFU). A careful evaluation of the pros and cons for each concept lead to strong support of the IFU concept despite its higher complexity, costs, and reduced flexibility. The main arguments in favor of an IFU are:

1. In most cases where MIR source are surrounded by a more complex environment, their nominal position on the sky is insufficiently well known from previous observations by other instruments (on the here relevant scales of 10 milli-arcseconds or less). However, even if the spectroscopic observations would be preceded by a T-OWL broadband filter image, the scientifically interesting position of e.g., an emission line source produced by outflows, may be spatially offset from the continuum peak.

2. In many scientifically interesting cases, such as YSO or AGN, the point source is surrounded by an equally interesting structure on very small scales. To study the interplay between the central source and its environment in two dimensions with a conventional long-slit spectrograph would require an enormous overhead in time and very stringent limits on the pointing and tracking stability over long periods (in the order of hours).
3. An IFU with an approximately square field of view can rotate on the target during the observations, i.e., field rotation caused by the telescope tracking does no longer have to be corrected in real-time but can be taken out in software. In fact, the field rotation in combination with an IFU provides the potential to reduce the negative effect of detector artifacts (bad pixels).
4. Although an IFU will lose a small fraction of the light due to diffraction, these losses are approximately constant with position within the FOV and can be well calibrated out. Diffraction limited long-slit spectrograph on the ground depend critically on accurate coordinates, short-term image motions, and long-term tracking. The literature on MIR spectroscopy is full of examples where source fluxes were given by an order of magnitude fainter than what would have been observed with an accurately centered long-slit. This problem does not exist for IFUs.

In an early stage, the conclusion was reached that for OWL scale observations, a long-slit spectrometer will be too limited for the required science goals. Cost arguments for this scale of instruments on the OWL observation platform are not considered consistent as the cost trade-off between observation time versus investment strongly pushes to be most observation efficient.

10.3.3 Atmospheric Windows

Full spectral coverage in the TIR/MIR is not possible from the earth surface. Atmospheric gases like water and CO₂ have wide absorption structures in the spectral region. Fig. 38 to 40 show the transmission bands in the spectral region of interest. Careful analysis shows that only the regions indicated in table 13 have sufficient atmospheric transmission to be included in the spectrograph design.

Table 13: Spectral ranges

Spectral band	Broad band imaging	band spectroscopy	remarks
L	3.4 – 4.2 μm	2.9 – 4.2 μm	
M	4.6 – 5.1 μm	4.5 – 5.4 μm	Absorption structure between 4.7 and 4.85, many small absorption lines here
N	8.5 – 13.0 μm	7.5 – 14.0 μm	
Q	17 – 21 μm	16 – 25 μm	Strongly dependent on humidity

10.3.4 Efficiency Considerations

For a diffraction limited spectrometer, the Airy disk is the minimum resolution element available for obtaining spatial information. In the MIRI study for JWST, the effect of the dimension of the slices/slits on throughput has been analysed, as over-dimensioning the slice widths results in spatial

resolution loss and under-dimensioning of the slice width results in increasing diffraction problems and therefore reduction in efficiency. Oversizing of components in the optical train after the slices/slits allows one to recover part of the diffracted light, but this oversizing grows rapidly making the instrument too big and even impossible to design. This is illustrated in figures 70 - 72. showing a worked out example for the MIRI-spectrometer of the JWST.

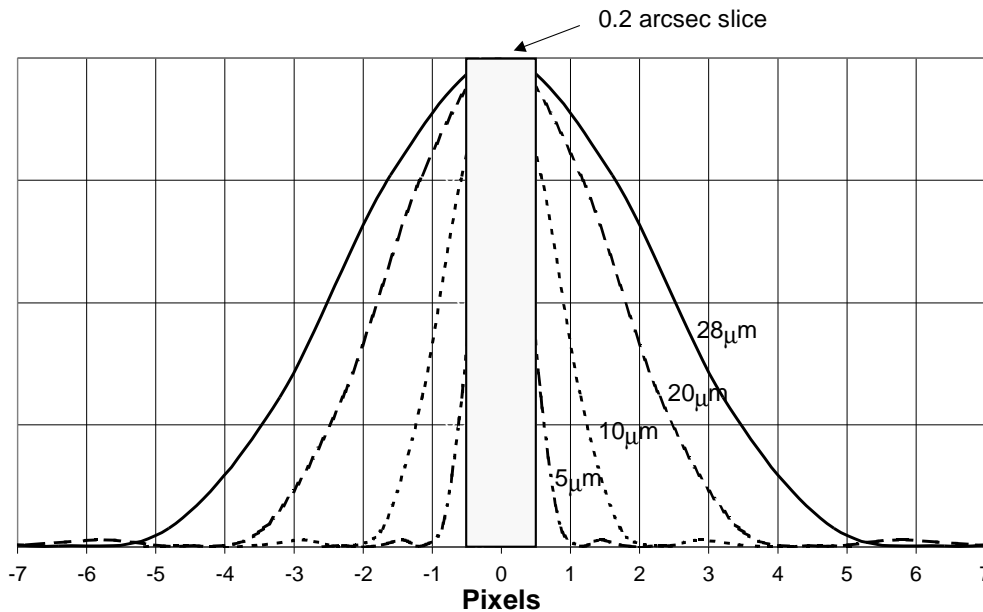


Fig. 70: As example, the Airy pattern broadening with wavelength for JWST compared to a slice width of 0.2 arcsecond.

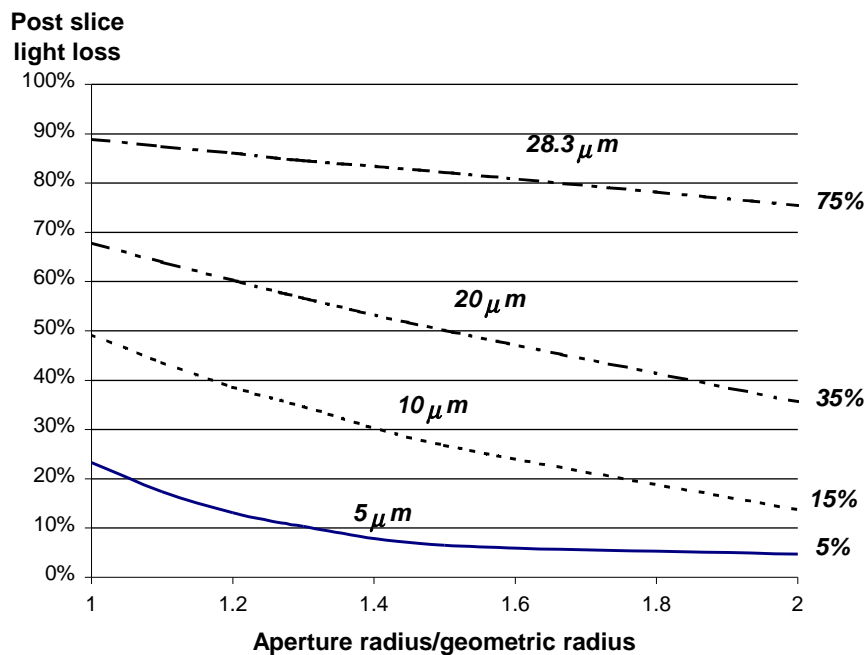


Fig. 71: The recovery of lost light as function of oversizing in the post slice optics for the slice of Fig. 70.

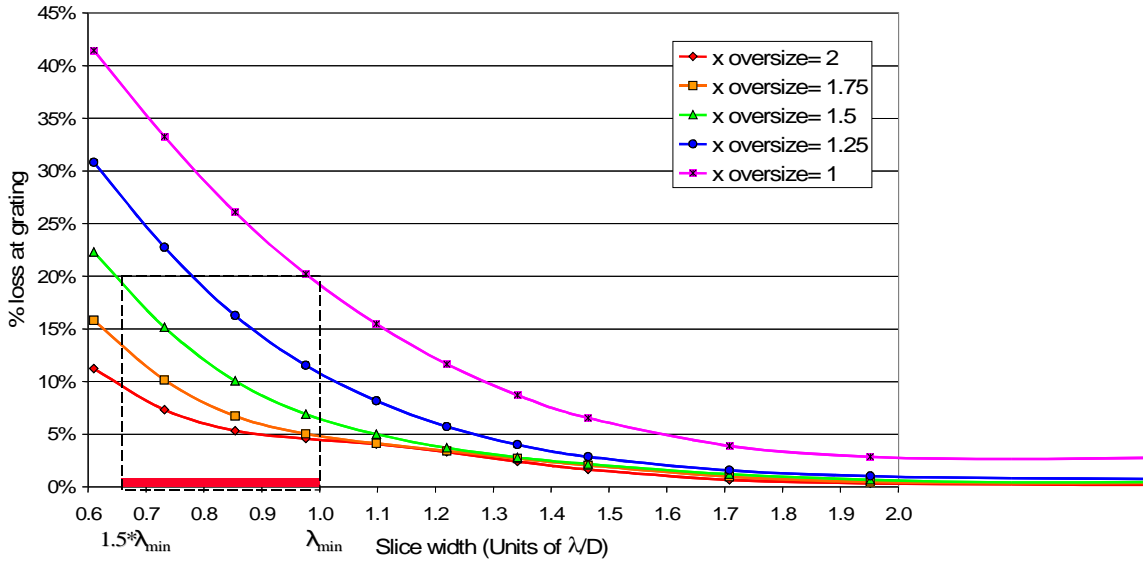


Fig. 72: The efficiency loss as function of slice width for various degrees of oversizing.

These figures show that a slice or slit width smaller than λ/D requires significant oversizing in the optics to limit the diffraction losses. In a spectrograph, the slice will be chosen for a certain wave range region for optimizing spatial sampling while maintaining sufficient efficiency. Therefore an optimized slice/slit dimension should remain close to the wavelength under consideration, i.e. from λ_{\min} to $1.5 \cdot \lambda_{\min}$. One should realise, that this property is the consequence of any slit/slice that cuts in the Airy pattern. So, a spectrograph can only be efficient and diffraction limited when the wavelength range ratio ($\lambda_{\max}/\lambda_{\min}$) is limited to a factor 1.5. Similar arguments hold for many components in the optical train: the grating efficiency, efficiencies of coatings.

Therefore, one need to reassess the wavelength range as is required for the instrument. The overall wavelength range is very large and can not be covered at once. From detector perspective, the L+M band separate from the N and Q band, so we can already split the L+M band from the rest of the spectral range. The remaining N+Q do have a very large spectral window ($\lambda_{\max}/\lambda_{\min} > 3$). We obtain an optimized diffraction limited spectrograph for this wavelength range when we separate the spectrograph in 4 channels, using the ranges as indicated in Table 14.

Table 14: Spectral ranges that should be covered by T-OWL

Spectral band	For T-OWL	$\lambda_{\max}/\lambda_{\min}$
L+M	3.5 – 5.5	1.57
N _{low}	7.5 – 11	1.37
N _{high}	11 – 14	1.27
Q	16 – 25.5	1.56

10.3.5 Spatial Sampling

One of the first limitations for an integral field spectrometer is the availability of detector pixels.

Due to the wave nature of light, the spatial (angular) resolution of the image depends on the wavelength of light according to

$$\omega_R \approx \frac{\lambda}{D} \text{ [rad]} \quad (1)$$

resulting in the change of resolution of any telescope/instrument with wavelength. In the wavelength domain under consideration here (3-25 μm), this change is very significant and has serious consequences for the amount of information in any FOV. The major advantage of any ELT like OWL in the infrared compared to space missions like JWST is the superior angular resolution the large aperture offers. So there is a strong push to maintain the highest angular resolution at instrument level, both for the imager and spectrograph.

When sampling at the highest resolution, loosely applying the sampling theory, two pixels are required per resolution element. For a two dimensional FOV the amount of pixels needed depends quadratically on field size. Current spectrograph designs taking care of both a FOV consisting in two dimensions of more than one resolution element, reserve one dimension on the detectors for the spectral information and the other dimension for the spatial information³.

Assuming for the spectrograph that the spectral information uses completely the 1024 pixels in one dimension of the 2D array detectors, the spatial information is stored along the other and a 2D FOV has to be remapped.

Table 15: Effect of angular resolution on required number of detectors for full spatial sampling of an 1*1 square arcsec FOV

Wavelength	(μm)	3,5	5,5	10	20
λ/D	(marcsec)	7,2	11,3	20,6	41,3
#resolution elements in 1 arcsec		139	88	48	24
#pixels for sampling		277	176	97	48
<i>Estimation of # of 1024*1024 pixel detectors for 1*1 arcsec FOV</i>					
<i>Slicing one dimension and fitting the slices on the detector</i>					
<i>Assume 50 pixels at the edge and 5 pixels per slices as required free space</i>					
#slices fitting on one detector		3,5	5,4	9,6	18,2
integral #slices		3	5	9	18
#detectors for 1*1 arcsec FOV		46,2	17,6	5,4	1,3
Telescope diameter	(m)	100			

Table 15 shows a calculation example of the numbers of detectors needed for a full square 1 arcsec FOV, assuming 1024*1024 pixel detectors. The sole purpose of this calculation is to demonstrate that the number of detectors start to explode when full sampling is required of a fixed FOV over the

³ For low resolution spectroscopy, the development of “colour” sensitive detectors seems very promising, but for medium and high resolution, this does not seem to be a viable option.

wavelength range for T-OWL. So optimization of the required FOV and the number of detector pixels has to be made for each individual channel of a spectrometer. The trade-off where the spatial sampling should be most optimal is very essential.

Another important consideration in the spatial sampling trade-off is the fact that in the spectral direction, the slicing results in another sampling density. In the spectral direction, the spatial resolution is under-sampled by a factor of two. So there is the question whether we can optimize the spatial sampling and slicing in another way.

For maintaining high efficiency, we stick to the a slice width of λ_{\min}/D . In spatial direction we can chose a different sampling density. Sampling λ/D with 2 pixels is already slightly oversampling the spatial information, but taking λ_{\min}/D results for most of the wavelength range a big oversampling. To create a more averaged sampling density both in spectral and spatial direction and to remove the large oversampling at longer wavelengths, we propose to optimise the spatial sampling close to $\lambda_{\min} * 1.5$. This reduces the number of detector pixels approximately to 2/3 and provide full spatial sampling at the other end of the wave range.

Fig. 73 shows the angular resolution as function of wavelength. This figure shows the theoretical line, the spatial resolution element in spectral direction and the propose matched spatial sampling.

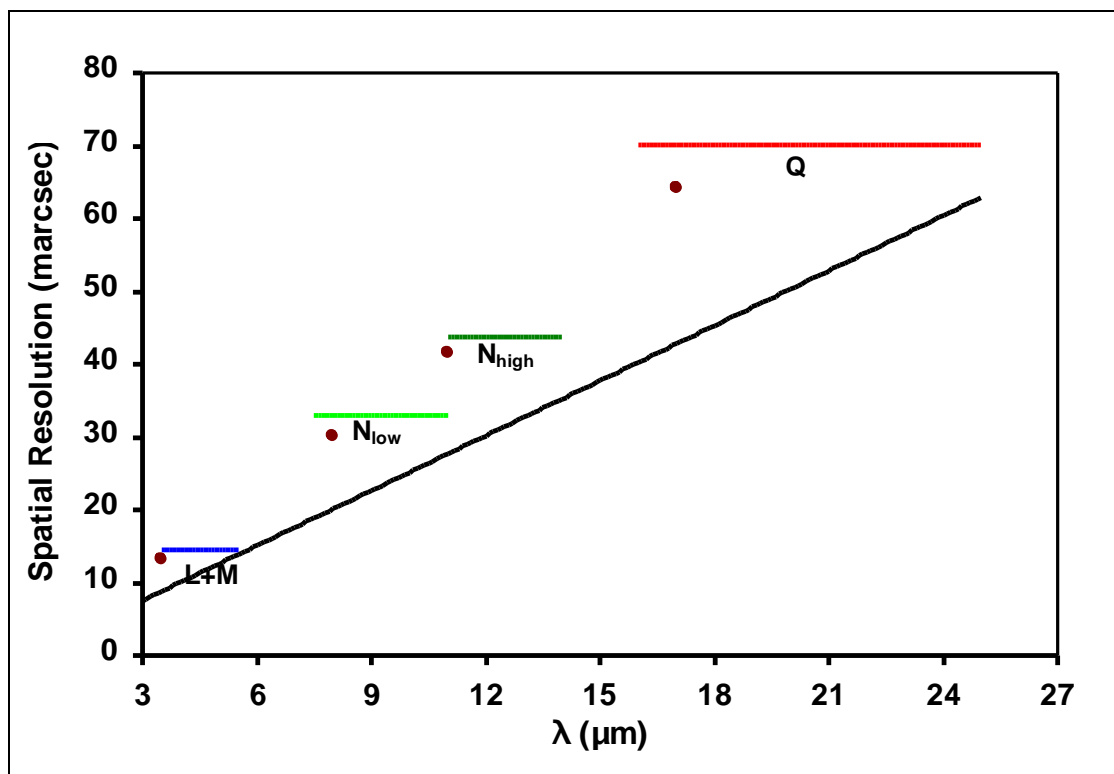


Fig. 73: The dependence of spatial resolution elements as function of wavelength for a 100 meter telescope (solid black line). The sampling in spectral direction by the slices (coloured lines), and the proposed spatial sampling by $1.5 * \lambda_{\min} * D$ (dots).

10.4 Use of the Instrument with an Incomplete M1

Following the development plan of OWL as described in the OWL-ICD document chapter 3.2, the primary aperture will be progressively filled over 5 years, starting with year +10. During this time any available instrument could use the telescope already with a partly filled aperture. The filling factor and the distribution of single segments over the aperture will influence both, the PSF and the point source sensitivity.

MIR spectroscopy, could be done during the implementation phase, if the high spatial resolution of the full 100m-telescope is available from the beginning, that is for filling strategy 2 and three.

10.4.1 PSF of Progressively Filled Aperture

In AD1 a rough schedule is given for the progressively filled aperture, however, to discuss the corresponding PSF some information should be added about the distribution of segments over the full area: Neglecting mechanical or management arguments, in the following we distinguish between four strategies:

1. The aperture will be filled from center to margin. This has the obvious advantage of an always filled aperture, an aspect that is important especially at thermal IR wavelength: The thermal emission of the not yet used part of M1 can be effectively suppressed by an adequate pupil stop. The full resolution, however, will be achieved only at the very end of the integration.
2. The aperture will be filled from margin to the center. Assuming 254 segments to be mounted the first year and assuming a total number of segments of 3048, nearly two circles could be filled during the first year. The full resolution of an 100m telescope could be reached from the first year on, paid by a quite poor PSF. Thermal background blocking is easily done as for the solution above.
3. Filling the aperture could be started building up a full 100mx100m cross of single elements. After one year this cross could consist in a full double line cross. Again the full diffraction limit of the 100m telescope is reached with a quite poor PSF, thermal blocking is easily provided. But in contrast to filling strategy 2, there are position angles with highest contrast from the very beginning.
4. Finally the aperture could be progressively filled in some MonteCarlo method. This might be a theoretically optimum way of building up the aperture, however, we will disregard this method here, as it has significant disadvantages for the thermal IR: Dark parts of M1 could be baffled only by very complicate pupil masks, High pupil imaging quality is required, free-standing apertures are impossible and a huge number of pupil masks would be required to take the daily modification into account.

For the following discussion of the PSF we approximate the filled part by its continuous surrounding, disregarding the hexagonal form and the space between single elements. Thus, continuous circular rings and rectangles, respectively, are assumed the area of which is equal to the number of mirrors mounted at the corresponding time, corresponding to a optimum adapted Lyot stop.

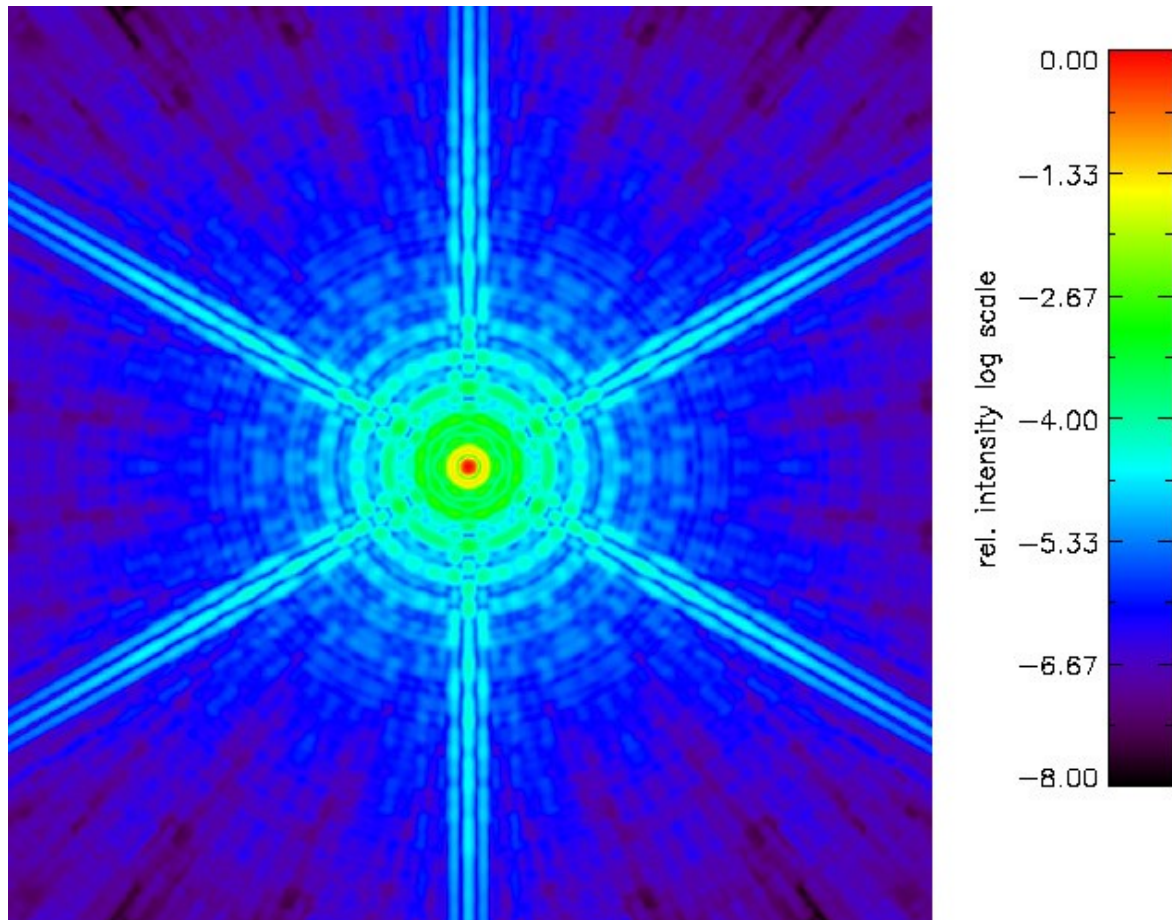


Fig. 74: PSF of OWL at 10 μ m, broad band $R=10$, 2arcsec \times 2 arcsec), completely filled M1 and M2.

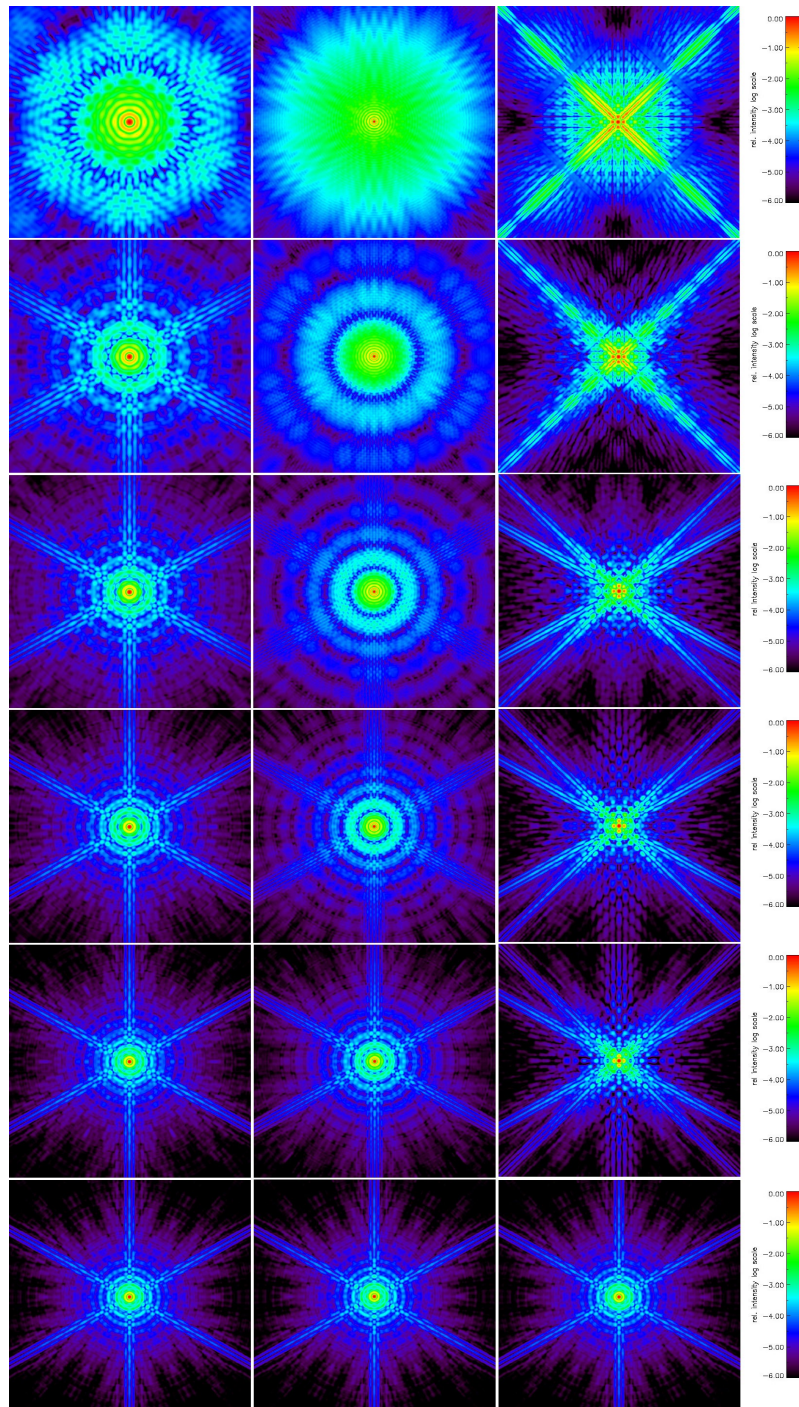


Fig. 75: 10 μ m point spread function of OWL during progressive filling of aperture: top row one year after start of mirror mounting, lower row final configuration. First column: filling from margin to center. Second column: filling from center to margin. Third column: Starting with 100m x100m cross. Image size is 2 x 2 arcsec.

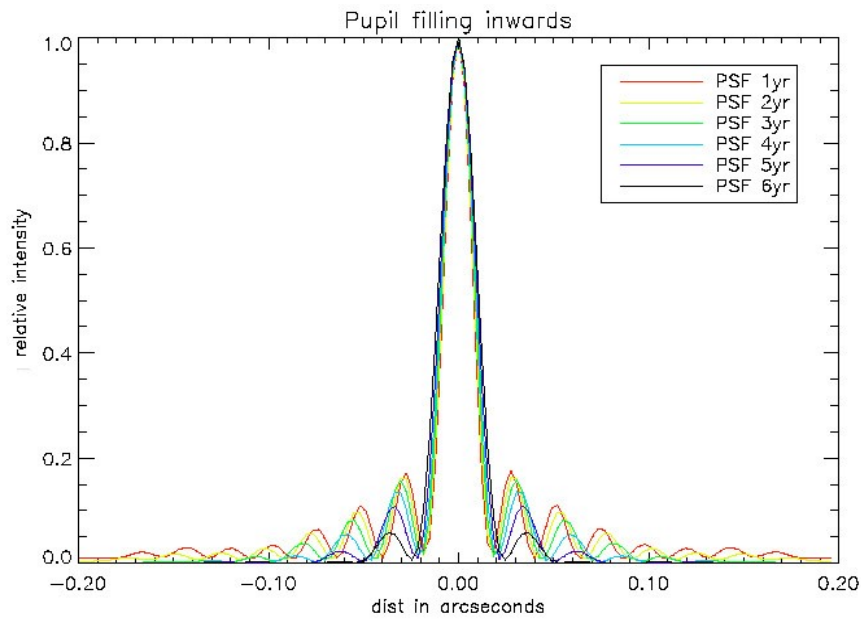


Fig. 76: Comparison of PSF for a continuously growing MI filling from margin to center)

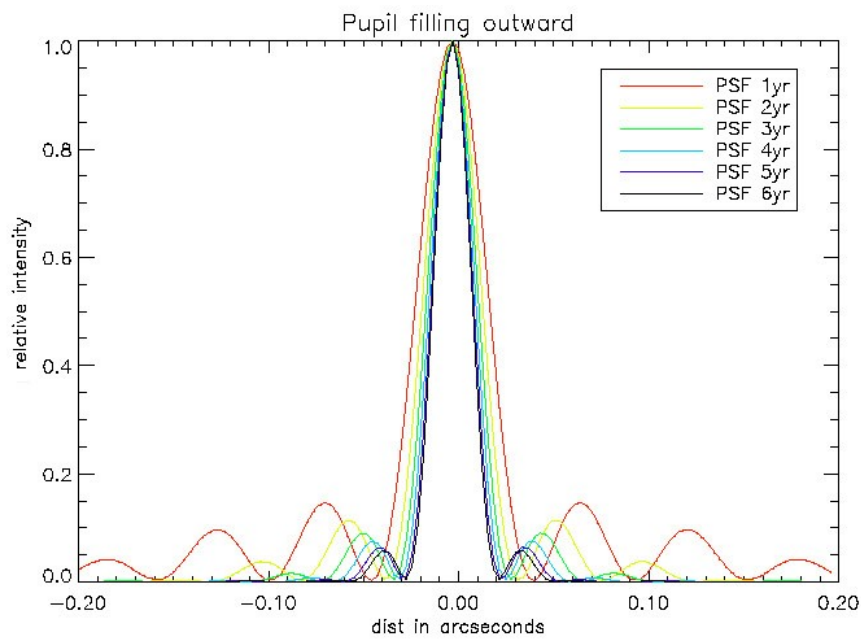


Fig. 77: Comparison of PSF for a continuously growing MI filled from center to margin (see text).

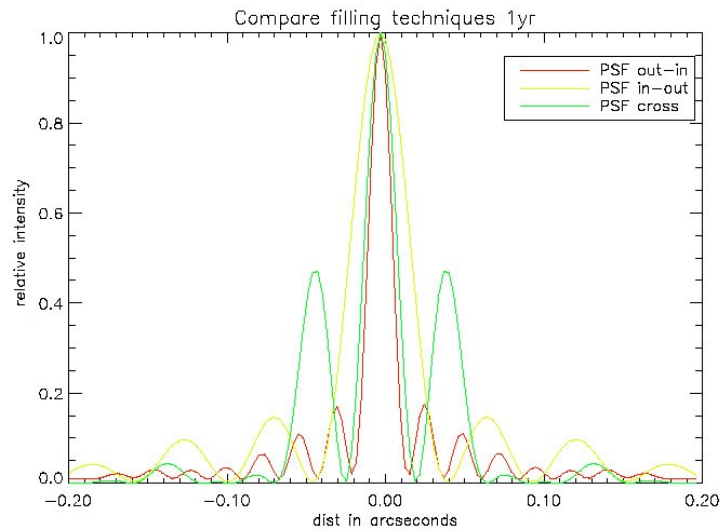


Fig. 78: Comparison of PSF for different filling models after one year (see text).

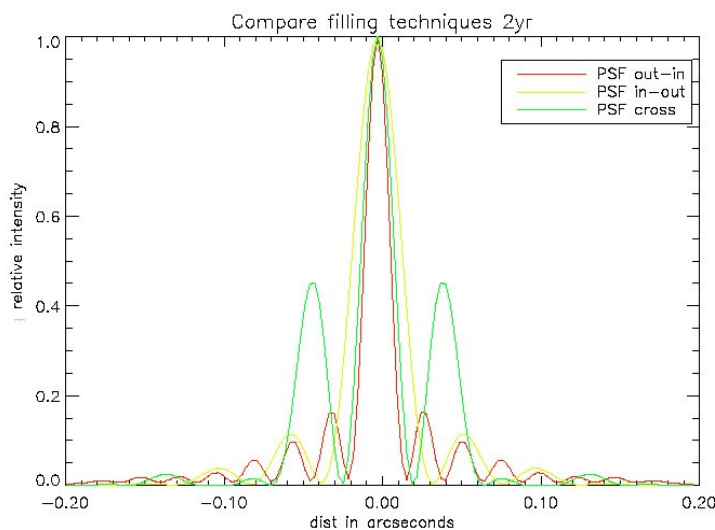


Fig. 79: Comparison of PSF for different filling modes after two years (see text).

10.4.2 PS Sensitivity for a Progressively Filled Aperture

MIR-observation using a partly filled M1 mirror plane can achieve compatible sensitivity only if the un-filled parts of the mirrors can be suppressed by a adapted cold pupil stop. This limits the number of modes to fill the mirror: the mount segments should form continuous planes within the M1/M2 area, e.g. For arbitrary distributed segments cryogenic blocking will be extremely difficult.

T-OWL is proposed to offer one single pixel scale, optimized to offer diffraction limited resolution of the full aperture, thus, even for sensitivity reasons we conclude that mode 2 or 3 are the optimum strategies.

11 Observational Technicalities

11.1 Field- and Pupil Rotation

The maximum (meridian) velocity of field rotation is given by :

$$w = dp/dt = w_0 \cos(F) \cos(A) / \cos(a)$$

where p is the parallactic angle, F is the observatories Latitude, A the azimuth (measured westwards from the south-point), a is the altitude (measured zenith-wards from the horizon) and w_0 is the sidereal rotation rate.

$$w_0 = 15 \text{ arcsec/s}$$

The maximum (meridian) velocity of field rotation is given by:

$$w_{\max} = w_0 \cos(F) / \sin(\delta - F)$$

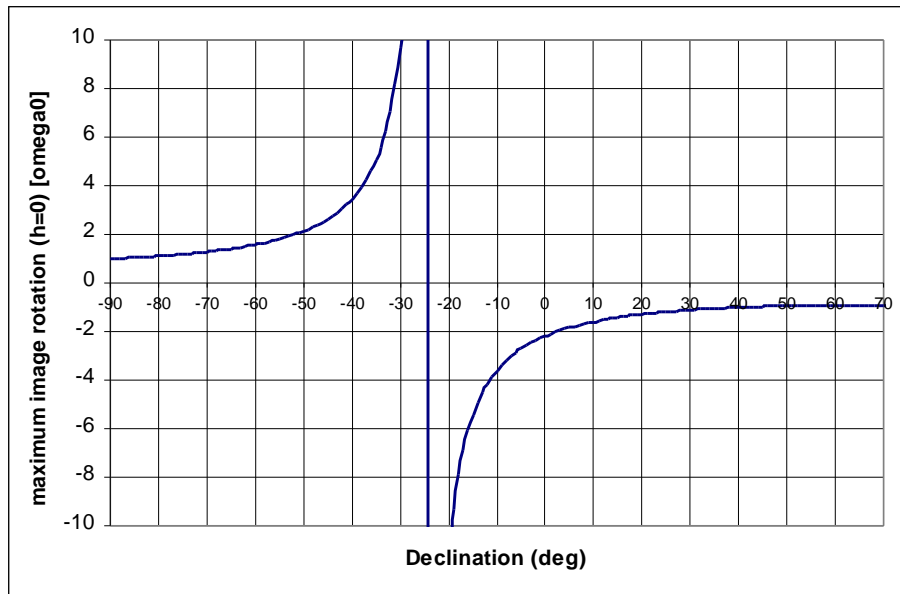


Fig. 80: Maximum (at meridian) field rotation versus declination for Paranal.

Maximum integration single time (DIT) will be 60mas (see VISIR ITC). Assuming that for a 2048x2048 pixel array at the edges the rotation during DIT should be smaller than 0.1pixel at any time, the minimum allowed zenith distance without application of an image de-rotator is 3.5deg. Even for an array of 2x2 such detectors, the minimum zenith distance of 7deg then is acceptable.

In case of the IFU, integration times may be significant longer, the FOV, however is much smaller. Assuming a FOV of 128x128 pixels, the single integration times can be larger by a factor of 16, thus, DITs up to 1s are acceptable down to a zenith distance of 3.5deg without de-rotation.

As long as the instrument is fixed to the OWL focal station, there is no pupil rotation. Image de-rotation should not be provided by rotating the whole instrument or by optical parts in front of the Lyot-stop, as in this case counter-rotation of the pupil-mask becomes necessary.

Even though for T-OWL we do not propose any de-rotation facility (de-rotation is performed by post-processing), in the following possible mechanisms of de-rotation are summarized.

11.1.1 Instrumental De-Rotation

Mechanical de-rotation is best suitable for instrumentations of large FOVs with compact optical design. The whole instrument is rotated around the optical axis. As T-OWL will be moving with the telescope, flexure problems due to changing direction of gravity should be compensated by some (slow) TT-mechanism. The same TT-loop could compensate for flexure effects due to the mechanical rotation. As mentioned above, this de-rotation mode introduces the need of counter-rotating the pupil stop.

11.1.2 Detector De-Rotation

De-rotation by rotating the detector in general is a solution, too, but should be avoided for IR-detector arrays due to their high sensitivity to EMC-effects, to changing wiring and thermal coupling problems.

In addition, detector de-rotation can be applied in imaging mode only. Thus, this is not a solution for T-OWL.

11.1.3 Optical De-Rotation

Optical de-rotation is best suitable for small FOV diameters. The largest advantage is the small amount of weight that has to be rotated, flexure effects can be kept small and no cable twister is required. These advantages are paid by additional optical components that might be much larger than the FOV. For MIR-instrumentations these components contribute additional thermal background if they are not included into the cryostat.

If high accuracy polarimetry is required, de-rotation should be done by non-optical methods: The large tip-angle required for compact de-rotators are producing serious instrumental polarization effects.

An optical de-rotator is quite incompatible with the modular design of 9 parallel instruments, which is optionally proposed here.

11.1.4 De-Rotation by Post-Processing

De-rotation by post-processing is only possible if single integration time, the FOV and the zenith distance are small enough such that the rotation near the corner or the FOV is small compared to the pixel pitch. Single integration time at TIR and MIR wavelengths in general are short enough in this sense, however, in general it is not necessary to store the individual frames, single DITs can be co-added on-line, only the mean value and standard deviation are stored. Thus, de-rotation by post-processing – if not provided on-line – will drastically increase the data flow. We favorite here de-rotation by post-processing. If however larger FOVs by mosaicing is proposed, some field rotator might be required.

11.2 Chopping

All observations within the thermal and mid-infrared wavelength region requires some kind of differential imaging to perform background reduction. In general, this is done by chopping. In addition, nodding can be applied.

It looks very challenging to provide a chopping capability with M6 beyond the current requirements of tilt correction: on sky 1" at 1 Hz maximum. Please note that M6 unit is a 2.4 m adaptive mirror and therefore large stroke tilt will be very difficult to provide at frequency higher than 0.1 Hz.

To include an instrumental chopping device seems favorable at a first glance especially because the AO-system would not see chopping activities within the non-common path. However, trying to design such optical device it turns out that due to the large linear scale within the focal plane, quite large inclination angles are expected for the required chop throw of 30arsec, thus, instrumental background will vary significantly. Instrumental chopping devices might introduce larger effects compared to those it should correct for. One solution could be to increase the instrument, however, then the advantage of compact instruments for diffraction limited application is completely lost, compared to 8m-telescope the instrument must be 10times greater. Nevertheless, an instrumental chopper with moderate chop-throw and an intermediate instrumental size might be a solution.

Alternatively, the solution might be to operate a MIR-instrument offering two modes: One mode uses T-OWL in poor wobbling mode, using M6 or the hole telescope for slow differential observations. The second mode provides chopping against a cold shutter, rejecting 50% of the time but offering accurate reference signals.

The chopping problem should be addressed in a more detailed separate study.

12 Instrument Concept Design

12.1 Top Level Requirements

Based on the science cases (see Tab. 3) and the considerations given in Chapter 10 and 11 the following top level requirements (TLR) are deduced for T-OWL:

Wavelength range:	3 – 20 μ m (requirement), 3 – 27 μ m (goal)
real, high quality pupil imager	required for efficient blocking of instrumental thermal BG
TADC	3 – 5 μ m optional
FOV (imaging)	1x1 2048 ² -arrays 7x7arcsec, 20x20mm (f/6.0) @TIR 1x1 1028 ² -array 7x7arcsec, 20x20mm (f/6.0) @MIR 3x3 mosaic optional
Imaging Pixel scale:	3.5 mas per pixel @ 3 – 5 μ m 7.0 mas per pixel @ 7 – 14 μ m and 16 - 25 μ m
Spectroscopy	long-slit R = 100 - 300 @ 3 – 20 μ m IFU R = 3000 @ L,M (4.7 μ m), N1 (10 μ m), N2 (13.5 μ m), and Q (20.5 μ m) R = 50000 @ L,M (3.5 μ m), N (10 μ m), and R = 25000 @ Q (20 μ m)
Polarimetry	Not proposed here
Pupil mask rotation	not required
Field De-rotation	Field-de-rotation is done by data post-processing
Chopping	Needs further investigations
TT-Stabilization	optional

12.2 General Concept Considerations

Developing a scientific instrument starts with the definition of its scientific capabilities. This instrument should be tuned to optimum use at a special application, maximum sensitivity e.g. or special time resolution ... However, for several reasons it is unrealistic to build a special instrument for any individual scientific program, thus, an astronomical instrument at a ground based telescope, should always meet a *limited* number of requirements of scientific programs. So, versatility is required, but as far as possible without losing individual capabilities. For several reasons, this gets easily in contradiction: Highest efficiency can be reached for a narrow wavelength band only, or highest spectral resolution can not be combined with wide field imaging capabilities and so on.

On the more technical level, there is a similar contradiction between instrumental reliability and complexity. The probability of having a malfunction is steeply increasing with complexity and versatility.

In addition, the instrumental design will be influenced by external limitations as maximum available budget, maximum allowable mass and torque, or even by the limit of technical feasibility.

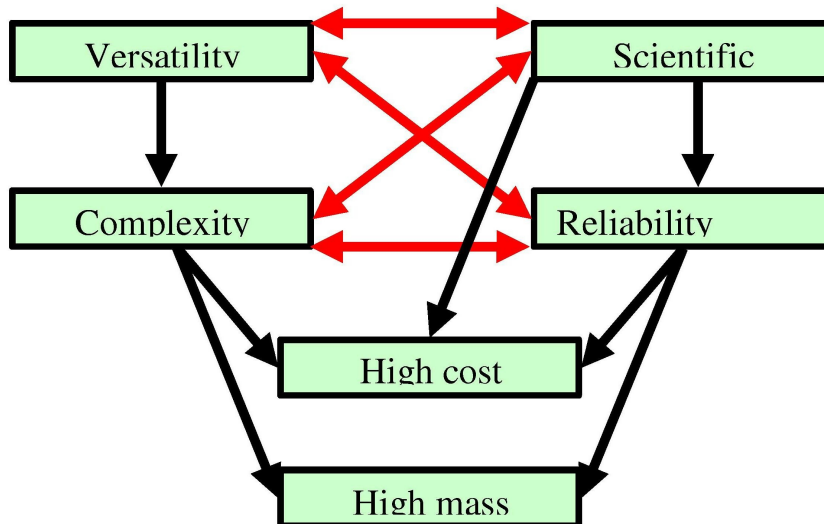


Fig. 81: Schematic showing conflicts between versatility, complexity, cost and mass limitation, reliability and scientific requirements.

In general, a typical astronomical camera design has started with the maximum field of view, the required spatial resolution and the given or expected detector size and pixel size that is or might be available at phase C/D. For TIRC a cold image of the entrance pupil is required to suppress the thermal background, thus, at least one re-imaging optics is needed. Following the general concept of designing this optics as one single system, that re-images the full field into one single detector plane, for a 100m-telescope we are running into serious problems:

The FOV for a diffraction limited TIRC for OWL is limited to 3arcmin in diameter at $1\mu\text{m}$ by specification (visually diffraction limited FOV of OWL, see e.g. Ref. 5). To use the inner squared field, such FOV requires an entrance window of at least 370mm x 370mm. Such window designs are feasible for near infrared applications, for thermal and mid infrared applications, however, this will cause serious problems: CVD-diamond window of such size e.g. would cost several million Euros, Fraunhofer Institute IAF gives a rough price estimation of 15–20€ per mm^3 e.g., while KRS5, TiBr, TiCl are not available in blanks larger than 150mm. In contrast, splitting the full FOV into 9 sub-fields, the individual window is 90mm x 90mm, half of which could be equipped with diamond windows for the 10/20 μm wavelength region (see Fig. 82).

To re-image the full FOV into one focal plane, the optics will become significantly larger. In consequence, thermal stability and flexure problems will be significantly more serious.

The filter size is another limiting factor: The monolithic solution requires filter sizes of 300mm in diameter (near the pupil stop) or 300mx300mm near the detector.

Alternatively, the design could split the full FOV into several sub-fields and re-images these smaller fields in parallel by individual optical systems. For such multi-optics solution all problems mentioned above can be reduced with increasing number of subfields. For example, assuming nine sub-frames, a moderate filter size of two inches in diameter would fit.

For thermal IR region, there is an additional advantage of the split concept: The monolithic solution has to be extremely folded, thus, highly efficient baffling will be very difficult. For the multi-optics

solution in contrast the individual sub-systems can be completely separated optically from each other, baffling is much easier and much more efficient.

But there are some dis-advantages of the multi-optics design as well: First of all, the FOV is no longer homogeneous, the “filling factor” of the 300mmx300mm FOV is about 64%. To obtain the full FOV dithering is required – which has to be done anywhere for background reduction.

In summary, in Tab. 16 advantages and dis-advantages of the multi-optics design are listed.

Table 16: Advantages (and disadvantages) of the multi-optics concept.

Advantage	Dis-advantage	Comments
Compact design		Easier cryogenic concept, Smaller flexure problems
Small pupil		Smaller filter, better baffling
Less challenging optics		Easier alignment, cheaper fabrication (Offner relay) , smaller number of mirrors
High efficiency		Smaller number of folding mirrors required
Efficient baffling		
	Inhomogeneous FOV	Dithering required
	FOV filling factor <1.0	e.g. 64% achievable
Small Windows		
Individual windows	1-5 μ m-Window 8-25 μ m window	
Easier Mosaicing of detectors		

Starting with the top level requirements as given in Chapter 12.1, there is no need for mosaicing at present: A maximum single FOV of 7 x 7 arcmin is proposed for both imager wavelength channels, which can easily be achieved by one single optics. The mosaicing design here is considered as an optional design for the case larger FOVs are required.

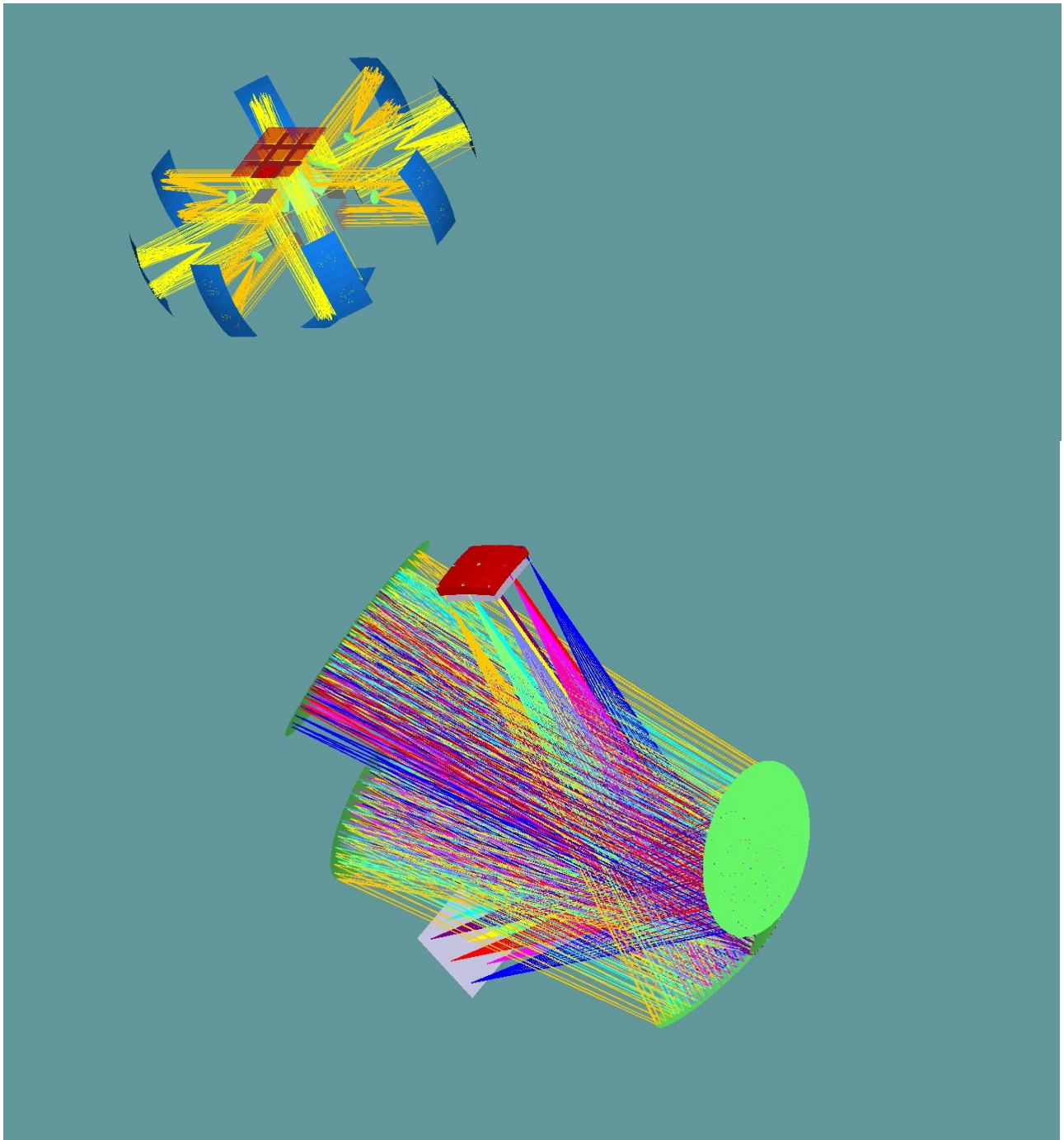


Fig.82: Comparison of multi-optics design to the monolithic design. The same FOV is shown in similar scale.

12.3 General Instrument Concept in Optical Train

The low cryogenic temperatures required for T-OWL are a very strong driver to keep volume and mass low. Thus, once the individual optical concept of imager and spectrograph are fixed, an optimum combination of both instruments should be carefully considered. In general, we strongly favour to keep both parts within a common cryostat: Partly for a quick possibility to fast switch between imager and integral field spectrograph, possibly to be able to use the spectrograph as one imager field and the rest as a general field (for extended sources) and practically, use the same infrastructure efficiently (available instrument bays, cryogenic equipment ...).

Figs. 83 to 86 compare the overall design proposed for T-OWL with those of similar instruments as NACO (CONICA), VISIR and COMICS (Subaru).

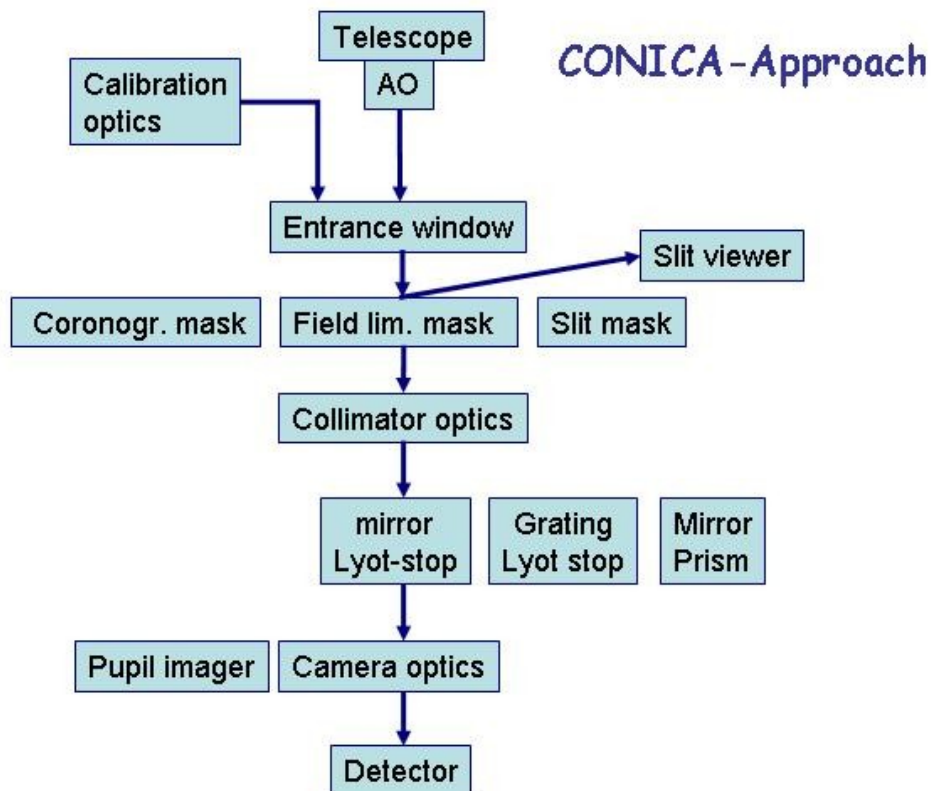


Fig.83: Schematic overview of the CONICA-approach: The first collimated beam is used for all analysing optics, including spectroscopy. Advantage: Very compact overall design, optics completely common for imaging and spectroscopic mode. No trade-offs for imaging mode. Disadvantage: Pupil-stop identical to grating/grism-position. No separate pixel scale optimization, spectroscopic resolution is limited.

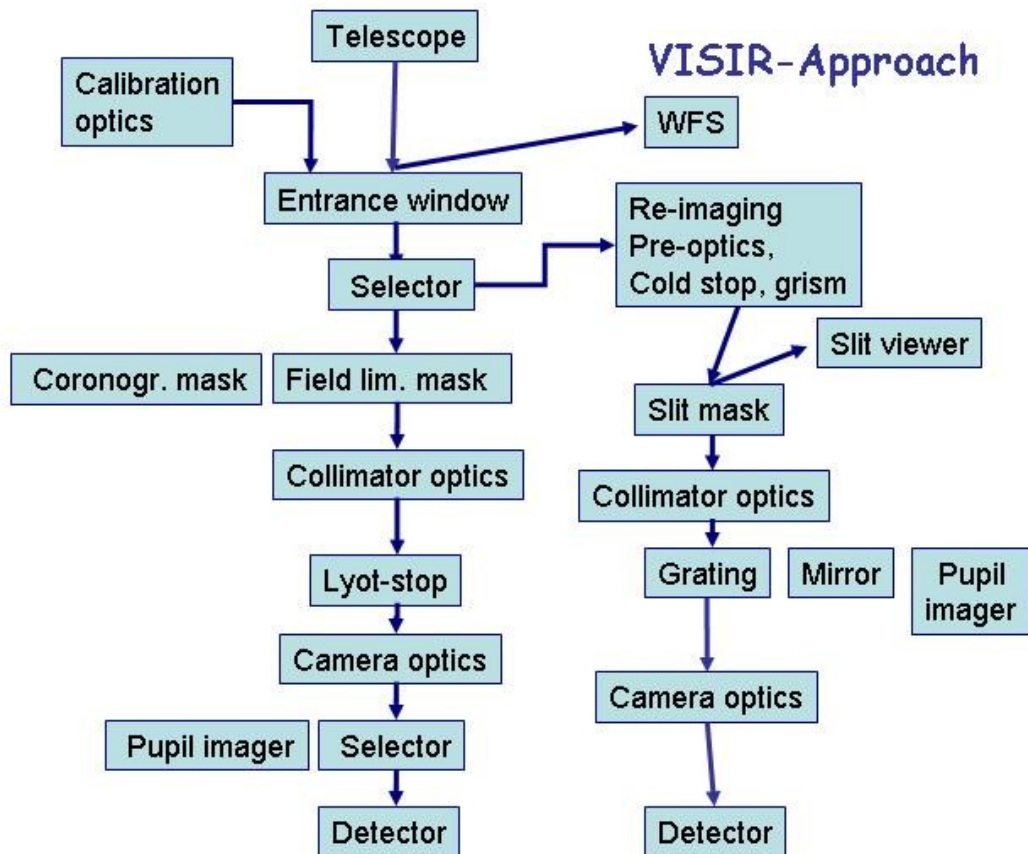


Fig. 84: VISIR approach: the detectors are not shared between imager and spectrograph; this could indeed be an advantage of the design if there were different detectors to pick from

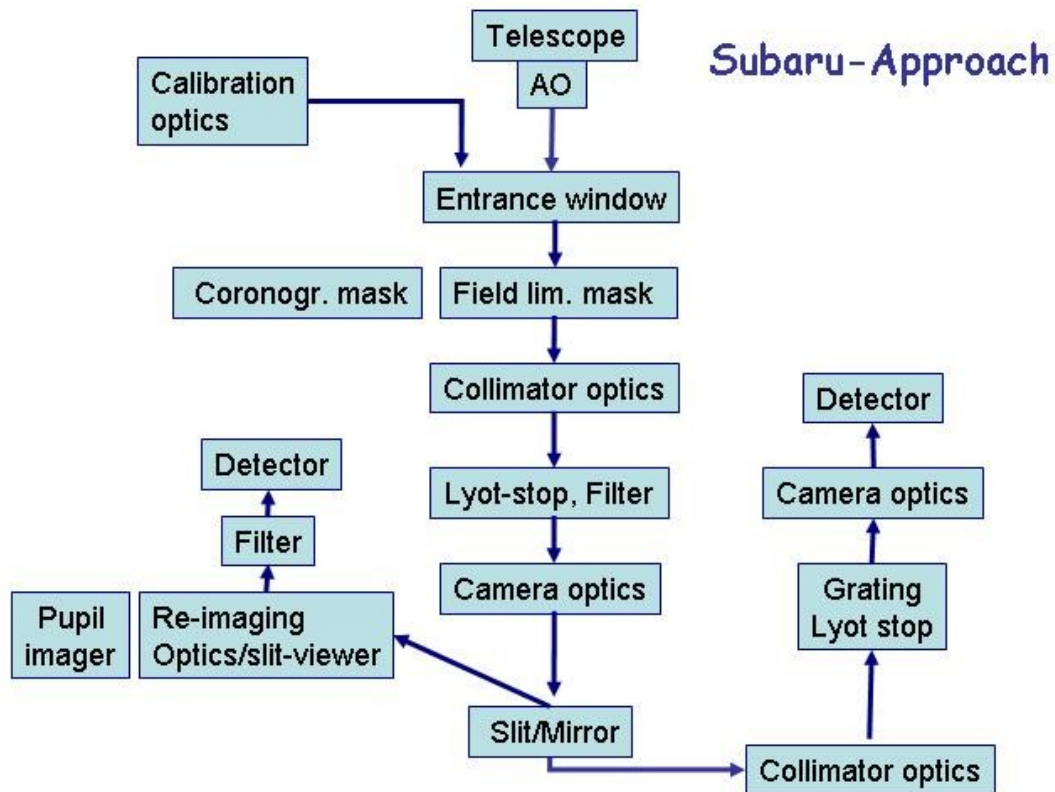


Fig. 85: The SUBARU-Approach: Cold fore-optics, common detector for slit-viewer and imaging mode, separate detector for spectroscopy. Advantage: Imager used as slit-viewer. Pre-optics until slit position is common. Disadvantage: Two detectors required (slit-viewer detector not optimized), additional re-imaging optics in imaging mode.

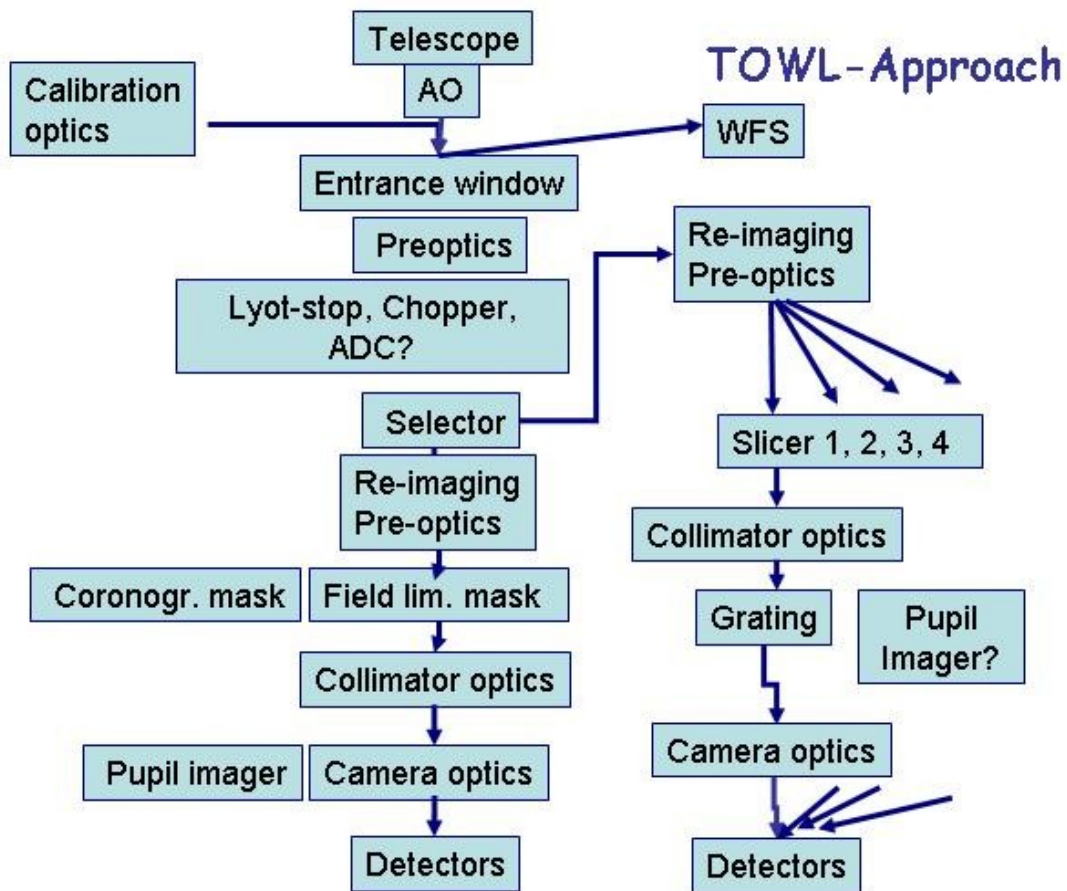


Fig. 86: Proposed T-OWL approach: Common pre-optics including entrance window, cold pupil stop, chopper, ADC and de-rotator(if required) within a common cryostat, however, imaging and spectroscopic instrument are entirely separated, additional detectors are required.

This T-OWL schematics does not indicate the two channels for TIR and MIR applications. Indeed, this point actually is not fixed yet, as it significantly depends on the pixel sizes available once the instrument will be built. If optimum sizes of $25\mu\text{m}$ for the TIR region and $50\mu\text{m}$ for the MIR region will be developed, the same optics can be used for both channels, a dichroic mirror (or solid gold mirror) will split into (or flip between) the two channels. However, if $25\mu\text{m}$ pixel sizes are to be assumed for both channels, individual imaging optics is required, the splitting mirror will be placed between collimator optics and camera optics. Anyway, both channels will see the same FOV in arcsec, the TIR channel using one single 2048×2048 pixel array, the MIR channel a 1024×1024 detector. Increasing the total FOV by mosaicing has been addressed before, the basic version of T-OWL we are proposing here does not make use of such possibilities.

T-OWL should be developed as an instrument with an optimised performance in all crucial instrument modes, requiring an integral field spectrometer including a high resolution mode, big FOV imager, etc.. As a consequence, imager and spectrometer should be separated, with individual detector arrays. Furthermore, the requirement of optimised sampling, pixel efficiency and efficient use of observing time, leads to the necessity of using parallel channels in the spectrometer. Observing time with OWL is very expensive, so compromising here is very cost inefficient!

12.4 Imager Design Details

12.4.1 Optical Design of the Imager

The optics of the T-OWL imager should provide a diffraction limited achromatic re-imaging onto the detector array with the f /ratio given in Table 12. In addition, an intermediate high quality real pupil image is required to suppress the instrumental thermal background. Grisms are planned to be inserted into the beam, thus, the pupil position is optimized for the collimated beam. At the same time, this is the best position to insert filters.

We propose here a design that is composed by two TMAs, the collimator TMA and the camera TMA (see Fig. 88). Fig 86 and 87 are shown to demonstrate that such optics could occupy a very small volume within the OWL design. Thus, there is enough room to increase the FOW and/or the pupil diameter (spectral resolution, blocking requirements).

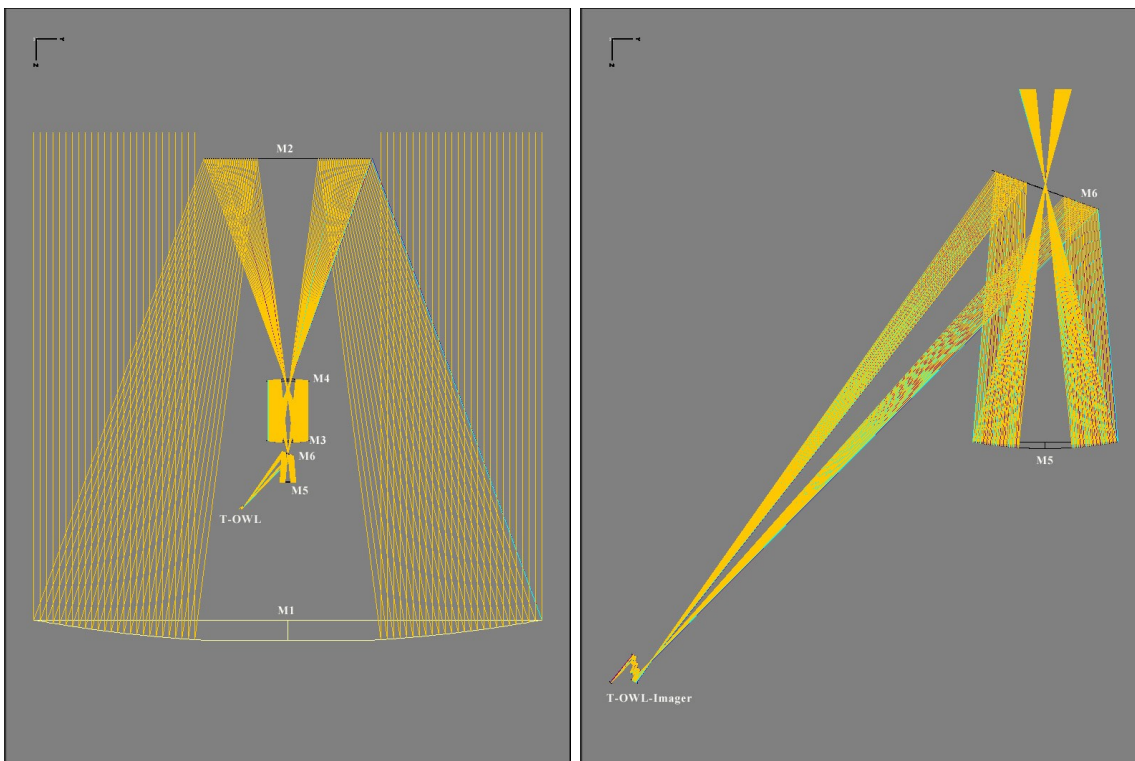


Fig. 87: Pure reflective imaging optics of the T-OWL Imager, attached to the telescope.

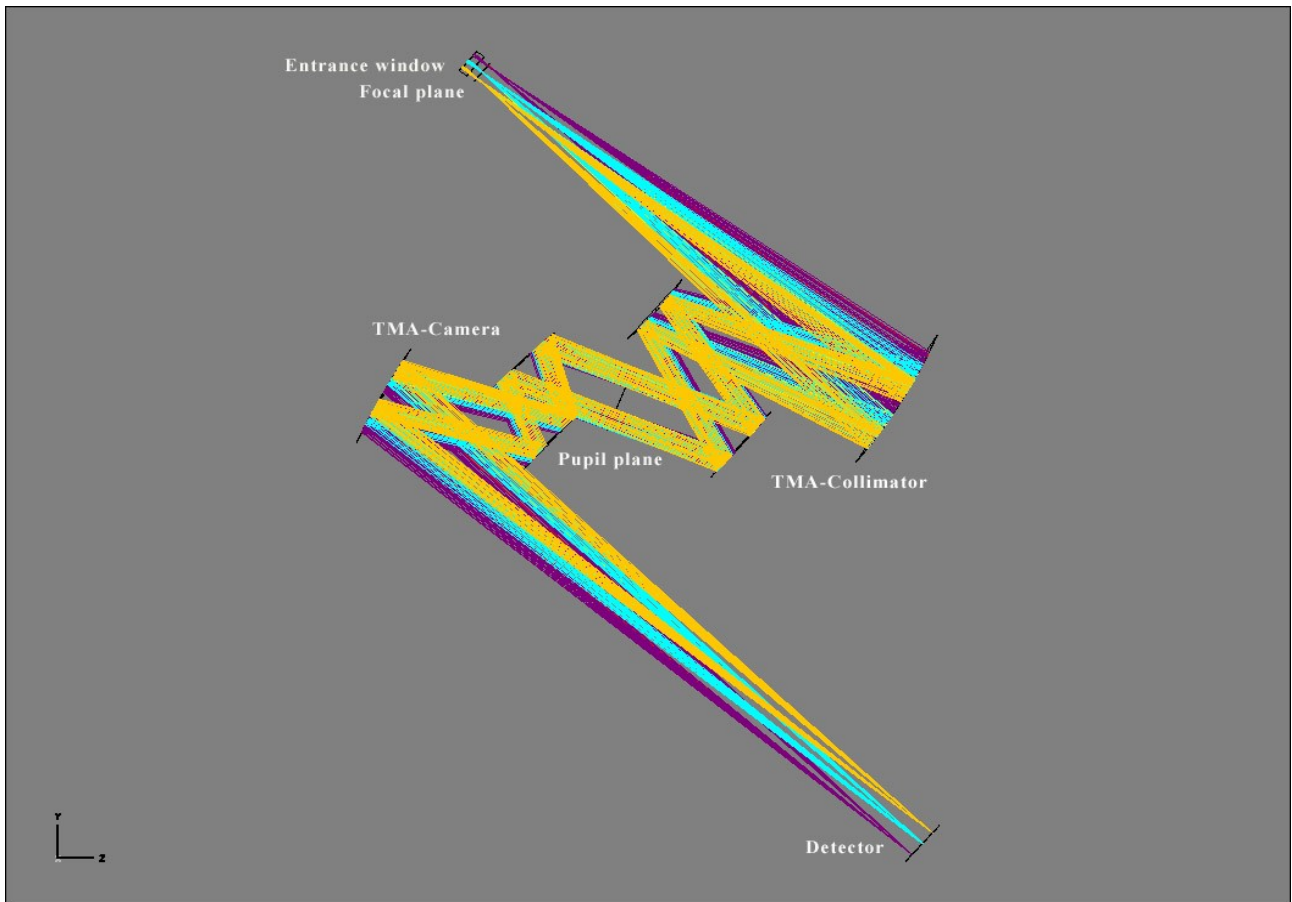


Fig. 88: Conceptual optical design of the T-OWL imager.



T-OWL Concept Level Study

Doc : OWL-CSR-ESO-00000-0161



Version 1
Date: 20/10/2005
Page: 125/175

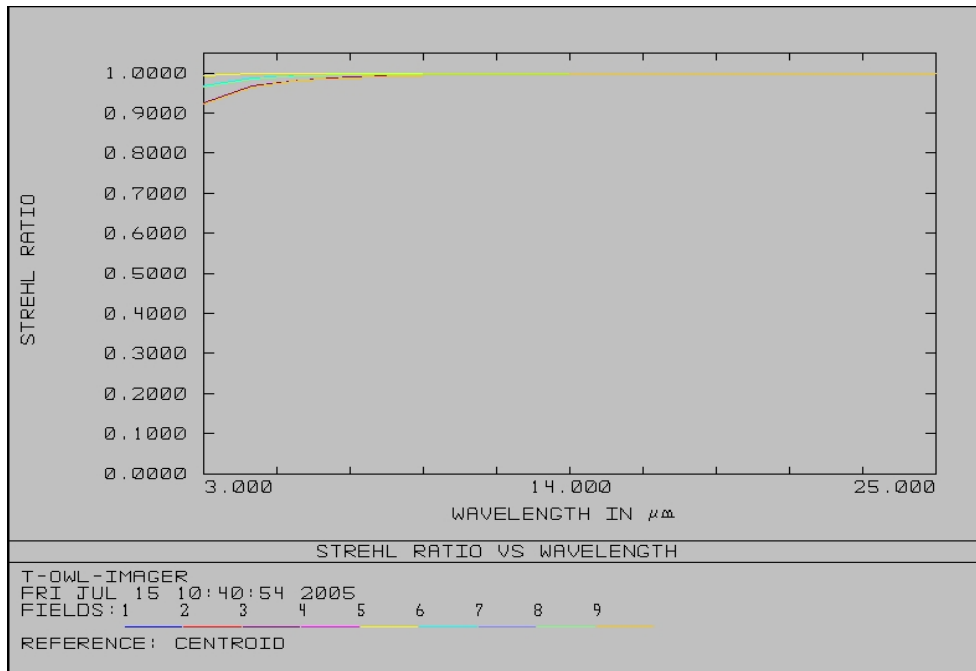


Fig. 89: Image quality of T-OWL-imager: Strehl ratio for different field positions versus wavelength

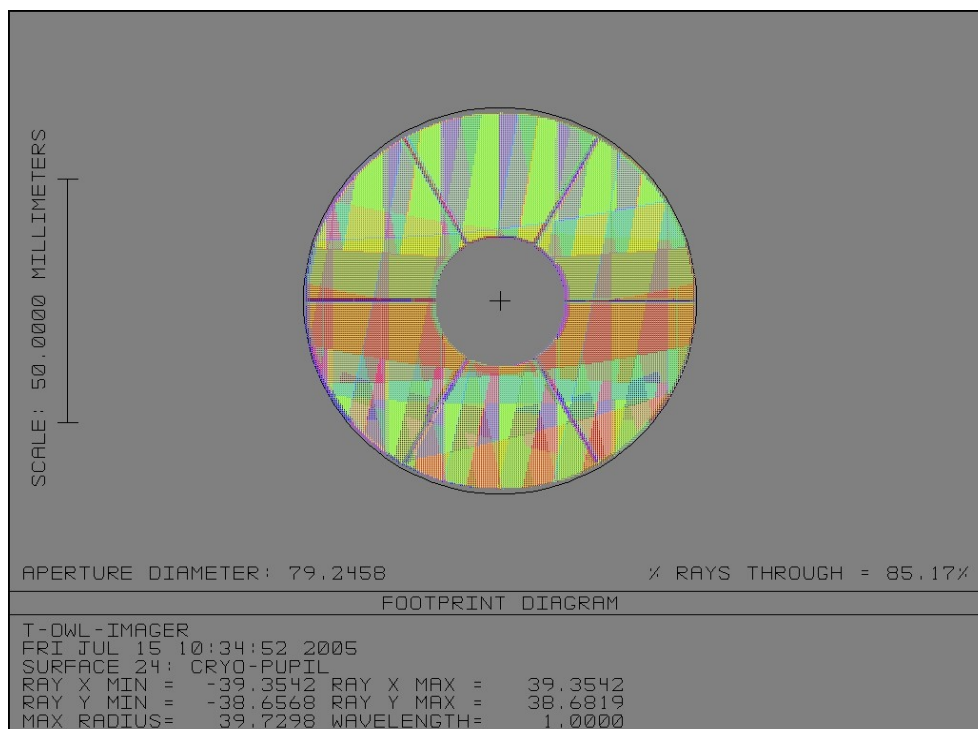


Fig. 90: Pupil image quality (cryogenic pupil)

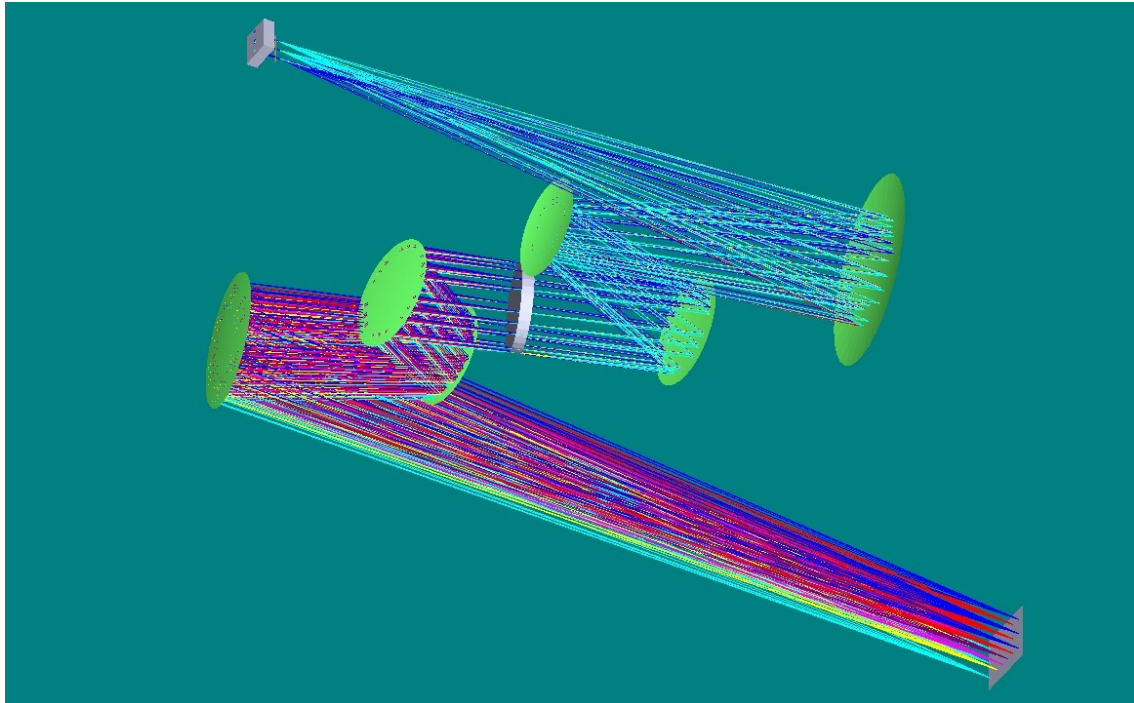


Fig. 91: T-OWL imager with low resolution grism

12.4.2 Entrance Window

The optimum window material critically depends on the cut-off wavelength up to which T-OWL should be able to observe:

For the 1 – 21 μm region clearly the optimum solution is ZnSe, offering high internal transmission all over the entire wavelength band without intermediate absorption gaps. CVD Diamond, in contrast, is the optimum solution if observations beyond 21 μm (up to 30 μm) are required. This material however is very expensive and shows an absorption gap between 4 and 6 μm , thus, Diamond is useless for M-band observations. All other TIR and MIR materials are quite soft, instable and inhomogeneous, thus, using them as cryostat window will cause stability and optical quality problems.

There is no optimum material for the full wavelength range from 1 μm to 27 μm : Low refractive index materials best suitable for the NIR and TIR region (CaF₂, BaF₂...) are useless beyond 10 μm , MIR materials like CsI, KRS5 etc. are difficult to polish, too soft to be used as vacuum window and/or hygroscopic. Diamond could be a material all over the required wavelength range if the absorption feature between 4.5 and 5.5 μm would be missing and the production would not be that expensive. Thus, to overcome these problems, sometimes a window exchange mechanism has been discussed. Rotatable plates with ferro-fluidic sealing up to diameters of 80cm have been produced, operating under high vacuum conditions (10⁻¹⁰ mbar). Such device could be used to flip between ZnSe- and Polyethylene-window e.g., or a larger number of different materials and AR coatings. However, for an array of entrance windows, such mechanism would no longer be applicable.

Three alternative solutions for the entrance window of a thermal/mid-infrared instrument are proposed:



T-OWL Concept Level Study

Doc : OWL-CSR-ESO-00000-0161



Version 1
Date: 20/10/2005
Page: 127/175

1. A single KBr window for the whole TIR/MIR wavelength region
2. An exchangeable window (online, ferro-fluidic sealing) KBr, KRS-5, ZnSe, (Diamond)
3. For the optional solution of a mosaicking design, an array of 3x3 entrance windows, 5 CaF2 or ZnSe windows for the TIR region, 4 for KBr or Diamond windows for the MIR regions is proposed.

In all cases easy replacement of the KBr-window is desired, thus, some kind of airlock is recommended to be able to replace the window without warming up the whole cryostat (for solution 1 this is mandatory). Only for solution 3 with Diamond there is no need of such device.

Table 17: Window materials for the thermal and mid-infrared wavelength region, materials useful beyond 25 μ m are high-lighted (grey).

Material	Refraction index [μ m] @2.0 μ m	Wavelength region [μ m]	Solubility , Comments
AgBr	01.02.30	0.5 – 30	12e-6/100, toxic, soft
AgCl	2.07	2 – 25	0
AMTIR (GeAsSe-glass)	2.5	0.9 - 16	0
BaF2	1.46	0.2 – 13	0.17/100 (23C)
CdSe	2.47	1.0 – 20	0
CdTe	2.67	1-21	0, Irtran-6
CsBr	1.67	0.4 – 40	124/100 (20C), soft
CsI	1.74	0.5 – 50	44/100 (0C), soft
Diamond (CVD)	2.37	0.3 – 4, 6 - 300	0, expensive (15-20 $\text{€}/\text{mm}^3$), 10 μ m-absorption
GaAs	3.33	2-14	0
Ge	4.00	3 – 13	0
KBr	1.53	0.5 - 31	53/100 (0C)
KCl	1.	0.4 – 21	35/100
KI	1.63	1 – 12	127/100 (0C)
KRS5 (Thallium Bromo-Iodide)	2.37	0.8 – 32	0.05/100 (20C), toxic, soft
NaBr		0.2 – 15	
NaCl	1.52	0.4 – 14	36/100 (0C), very soft
Polyethylene	1.54	17 - 300	0, excellent for FIR
NaI		0.4 – 21	
Si	3.40	1 – 10, 20 - 200	0
ThBr	See KRS5		
ThCl	See KRS5		
ZnSe	2.20	0.6 – 21	0
ZnTe		0.7 – 48	0

In table 17 all materials are listed that may be used for the thermal infrared camera entrance window. Materials suitable from 3 μ m to at least 13 μ m are listed, those transparent at least up to the 25 μ m band are high-lighted (gray).

For the optional solution of a mosaicking design, the optimum number of sub-windows is 3x3 for the following reason: Splitting the full FOV of 300mm x 300mm into 2x2 subfields, the size of the individual windows still is too large to be practicable. For larger numbers of subfields than 9 there is the problem of space: Keeping in mind that for the large wavelength region from 3 to 27 μ m at least

partly a reflective optics is mandatory, we need more space behind the individual window than given by the projected surface. For an array of 3x3 the surrounding space can be used, for larger numbers this is no longer possible. The size of the individual FOV is about 80mm x 80mm, central stripes of 30mm widths are lost. To optimize the filling factor, the focal plane must be near the entrance window.

Two different types of window material/coating are proposed in this optional case: In Fig. 92 the turquoises squares indicate the shorter wavelength FOV (1 – 5.5 μ m), the red one the long wavelength region FOV (7 – 27 μ m). Continuous fields are achieved by dithering. The central channel in addition will contain a spectroscopic mode.

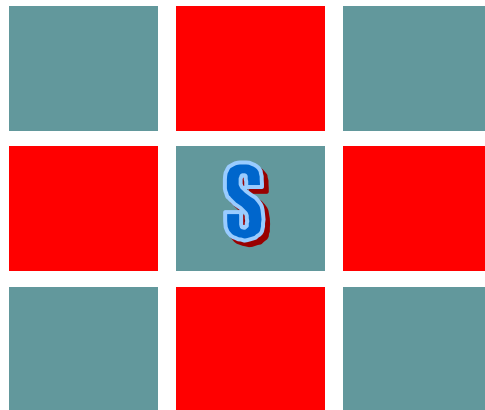


Fig. 92: Schematic distribution of entrance windows

12.4.3 Tunable Atmospheric Dispersion Corrector (TADC)

If we could realize an evacuated volume in front of the telescope aperture, the front surface of which is always horizontal, the rear surface is perpendicular to the line of vision (as it is above the atmosphere), the dispersion effect would be completely corrected for all wavelengths. Unfortunately, this is technically more challenging than the 100m-telescope itself.

As a less challenging solution, we could imagine to put an evacuated prism into the collimated beam near the focal plane (or a air-filled prism into the vacuum), however, the required dispersion effect goes with D/d , where D is the entrance pupil diameter and d the diameter of the collimated beam. To compensate the atmospheric dispersion using such air prism within a 100mm diameter collimated beam, e.g., a thousand times higher pressure is required! Again this is not a really feasible solution. In consequence, materials are used that show a dispersion effect proportional to - but much stronger than that of the atmosphere.

For the Optical and NIR wavelength region up to 2 μ m, a huge number of glasses and crystals are available, thus, there is no problem to find combinations suitable to compensate for the atmospheric differential dispersion effect. One of the best choices for the 1-2 μ m region is the combination of SF1 and SK10, which gives excellent correction within ± 0.2 mas! (See Fig. 93).

The best choice for the 2.5-5 μ m region combine Ge, Si, CsBr, IRG100. In Fig. 93 three solutions are shown, that fulfill our requirements.

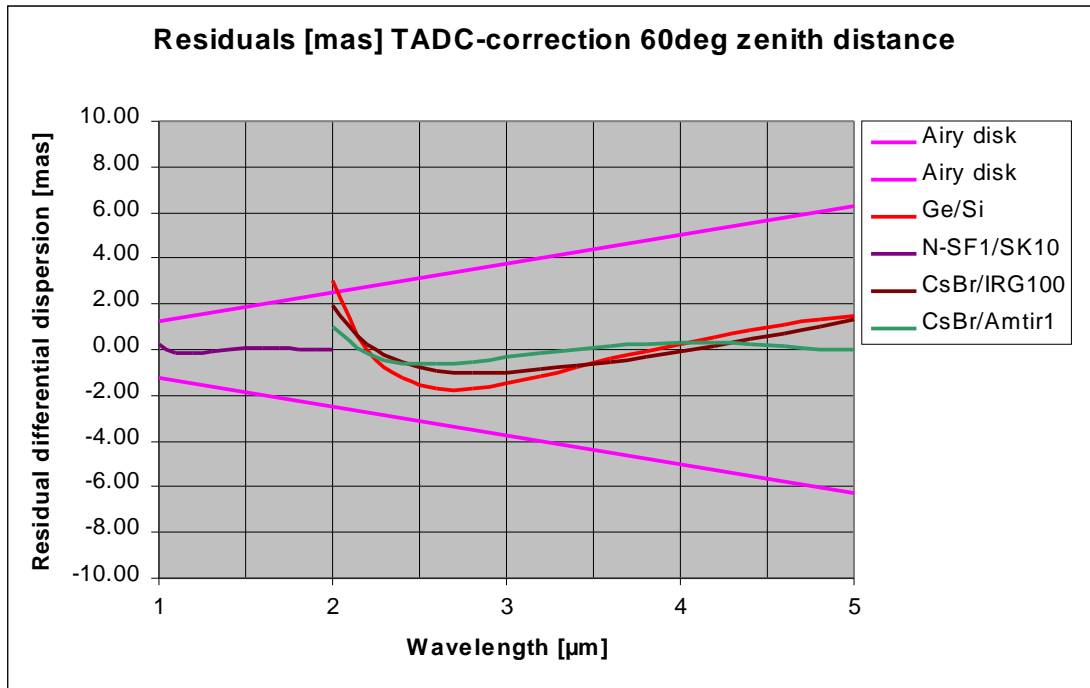


Fig. 93: Residual atmospheric dispersion effects using optimized TADC concepts of different material combinations (two components, 2-5 μ m region). Zenith distance of 60 deg, atmospheric temperature 293K, 1013mbar (ground layer).

The TADC will operate within the collimated beam, that is inside the cryostat. In addition, it will be an important contributor to the overall emissivity, which is another reason for putting it into the cryogenic environment. Thus, as the 4 single glass components can not be cemented, careful AR coating has to be applied, which is easier due to the fact that we have to split the wavelength region anyway.

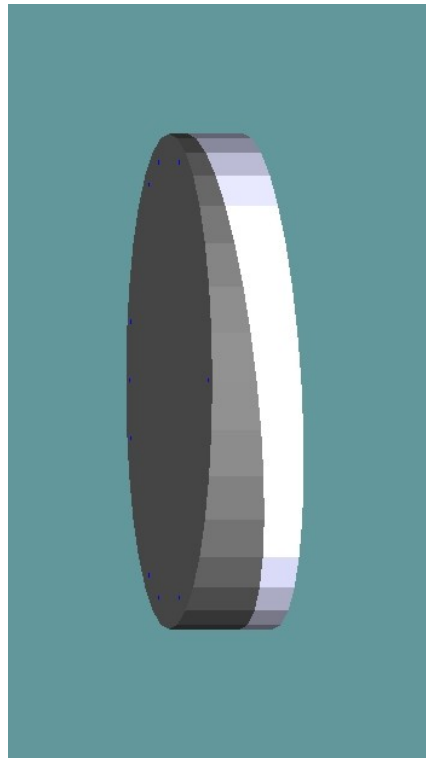


Fig. 94: As an example, one TIR TADC double wedge plate of the TADC is shown (CsBr/Amtir1)

In summary, technical solutions can be found that compensate atmospheric dispersion effects up to 60deg zenith distance down to a residual level well below the Airy disk of an 100m-telescope.

However, these components reduces overall transmission and increases the background, strategies mentioned before to avoid atmospheric dispersion effects in some passive way should be used as far as possible.

12.4.4 Filters

The requirements of interference filters for the MIR wavelength region has been studied intensively by the VISIR Astronomical Filter Consortium (VAFC) see e.g.

<http://www.irfilters.reading.ac.uk/library/presentations/hawaii/index.htm>

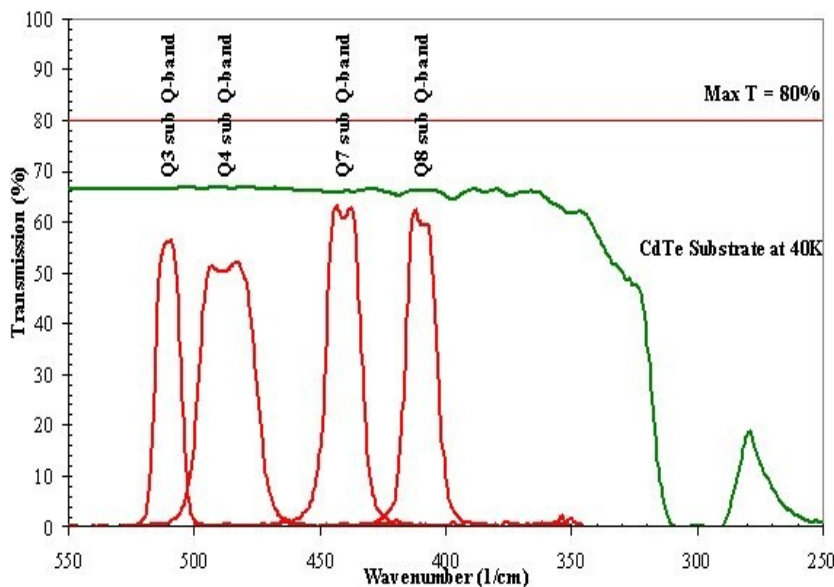
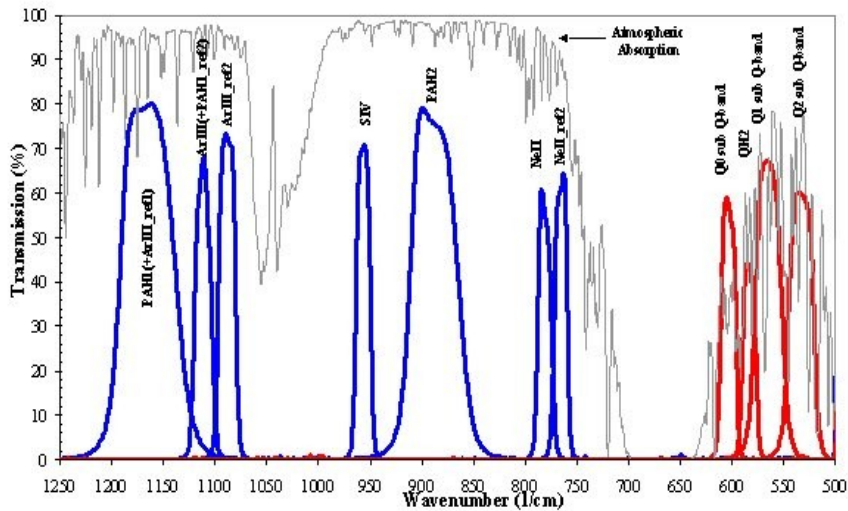


Fig. 95: MIR filter set proposed for VISIR by the VAFC (see webpage given above)

The following filter list is based on these recommendations:



T-OWL Concept Level Study

Doc : OWL-CSR-ESO-00000-0161



Version 1
Date: 20/10/2005
Page: 132/175

Table 18: List of proposed filters

Identifier	Central λ [μm]	FWHM [μm]	FWHM [%]	Comments
NB3.21	3.21	0.05	1.6	
NB3.28(PAH)	3.28	0.05	1.6	
L	3.78	0.58	15	
NB3.80	3.8	0.06	1.6	
NB4.07	4.07	0.07	1.7	
M	4.66	0.1	2	
N1	8.6	1.4	16	
N2	10.7	1.4	13	
N3	12	1.4	12	
NNB1	8.3	0.6	7.2	
NNB2	9	0.6	6.7	
NNB3	9.7	0.6	6.2	
NNB4	10.4	0.6	5.8	
NNB5	11.1	0.6	5.4	
NNB6	11.8	0.6	5.1	
NNB7	12.5	0.6	4.8	
PAH1	8.59	0.42	4.9	
Ar III	8.99	0.14	1.6	
SIV_1	9.82	0.18	1.8	
SIV	10.49	0.16	1.5	
SIV_2	10.77	0.19	1.8	
PAH2_1	10.67	0.4	3.7	
PAH2	11.26	0.59	5.2	
SiC	11.85	2.34	19.7	
PAH2_2	11.88	0.37	3.1	
Nell_1	12.27	0.18	1.5	
Nell	12.8	0.21	1.6	
Nell_2	13.03	0.22	1.6	
Q1	17.65	0.83	4.7	
Q2	18.72	0.88	4.7	
Q3	19.5	0.4	2.1	



T-OWL Concept Level Study

Doc : OWL-CSR-ESO-00000-0161



Version 1
Date: 20/10/2005
Page: 133/175

12.4.5 Dispersive Elements

Due to a FOV of 60mmx60mm within the focal plane of the telescope and an f-ratio of 6, the collimated beam will have a diameter size of at least 50mm.

Directly ruled KRS5-grisms up to 100mmx120mm can be produced by Zeiss (Jena), optimized for the L/M, N and Q-band windows. The exact grism dimensions will depend on the final choice of the camera focal length and the required spectral resolution. Here we assume an f-ratio of 14.3 and a pupil diameter of 120mm (as given by the preliminary optical design), resulting in a focal length of about 870mm. Given a pixel scale of 27 μ m the resulting grism design parameters are quite moderate (see Tab. 19).

Table 19: Main parameters of proposed Grisms

<i>Titel</i>	<i>band</i>	<i>Resolution $\lambda/\Delta\lambda$ per 25μm pixel</i>	<i>Wedge angle [deg]</i>	<i>Grooves/mm</i>
Grism 1	LM	1000(4.1 μ m)	2.3	14.8
Grism 2	N	1000(10 μ m)	2.5	6.1
Grism 3	Q	1000(20 μ m)	2.5	2.8
Grism 4	NQ	1100(10,20 μ m)	2.9	3.4
Grism 5	LMNQ	500(15 μ m)	1.26	2.0

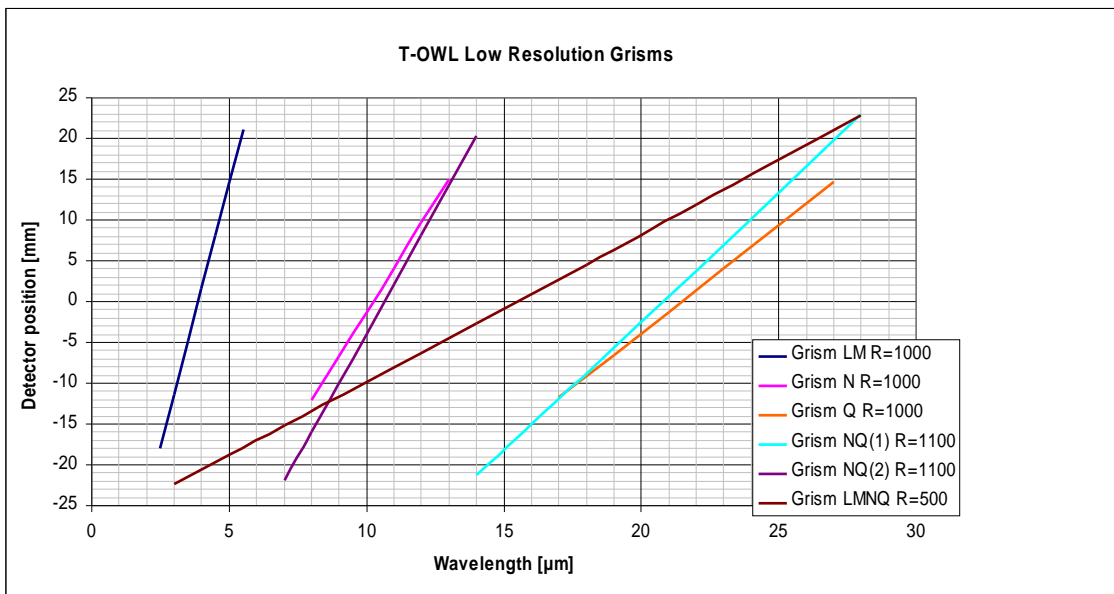


Fig. 96: Spectral distribution over the chip for proposed grisms.

12.4.6 Detector

During the last decades the size of available CCD and IR detectors has continuously increasing up to a value of 1024x1024 in 2004 for the thermal IR (InSb) and 2028x2028 for the NIR region (HgCdTe). Considering a concept of a next generation TIRC that might see first light in 2021, the development of growing detector size has to be taken into account. Extrapolating the known trend between 1975 and 2004, for 2020 we would expect infrared detector sizes of $10^6 \times 10^6$ pixels or even $2 \times 10^6 \times 2 \times 10^6$ pixels. Using such detector arrays for Nyquist sampling at $10\mu\text{m}$ e.g. would require a 30m x 30m FOV in the focal plane of a 100m telescope of an f-ratio of 6, which can hardly be handled within any cryogenic environment. Two trends are visible already to overcome this problem: The pixel pitch values are getting smaller with larger number of pixels (Hawaii 4RG will have a pitch value of $8\mu\text{m}$, e.g.), and there is a tendency of arranging individual arrays in mosaics. Best example for application of buttable arrays at present is the design of VISTA 4x4 2Kx2K arrays.

Concerning the thermal IR region up to $5\mu\text{m}$, the maximum detector array currently available is the 2Kx2K array developed for ORION/Phoenix delivered by Raytheon. This array can be combined in larger mosaics. The maximum MIR detectors beyond $5\mu\text{m}$ (for high BG application) are the 256x256 DRS (Boeing) Si:Ge array and the 340 x 240 Raytheon array, not yet optimized for dense mosaics. The larger Si:As BIB array of 1Kx1K is available only for low BG application at present.

For T-OWL we assume the availability of a MIR 2Kx2K or a two side buttable 1Kx1K Si:As detector array. $2096 \times \lambda \cdot N/2$ at $8\mu\text{m}$ for an f-ratio N of 6 is 50.3mm. Thus, assuming additional margin, the imaging optics should be able to re-image a FOV of 60mm x 60mm.

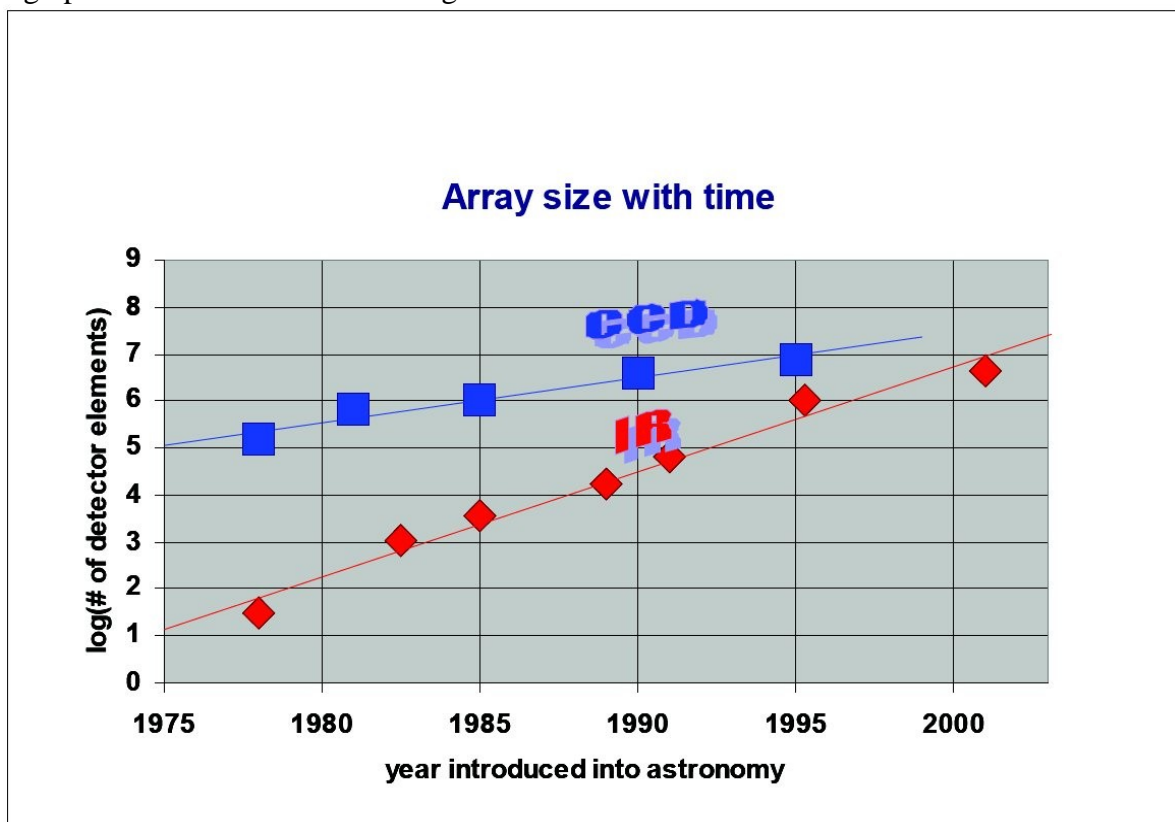


Fig. 97: Historical development of pixel sizes for optical and infrared detector arrays.



T-OWL Concept Level Study

Doc : OWL-CSR-ESO-00000-0161

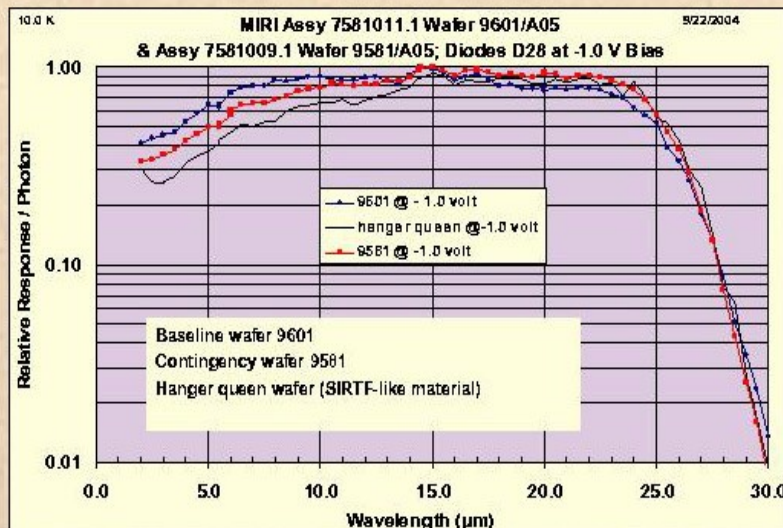


Version 1
Date: 20/10/2005
Page: 135/175

Aquarius: 1024 × 1024 Si:As IBC for Ground-Based Astronomy

- Developing a large-format Si:As IBC array for higher backgrounds
 - Ground-based astronomy requires larger well capacity and higher frames rates than current MIRI readout
- Propose to use the same detector format as MIRI
 - 1024 × 1024 pixels
 - 25 μm pitch
 - Same spectral response as MIRI
- Readout features
 - Direct injection unit cell
 - High gain: 1 × 10⁶ e- well capacity
 - Low gain: 15 × 10⁶ e- well capacity
 - Selectable integration modes: snapshot or rolling integration
 - Selectable number of outputs
 - 16 or 64
 - Up to 120 Hz frame rate for full 1024 × 1024
 - Windowing available for higher frame rates

Relative Spectral Response Comparisons





T-OWL Concept Level Study

Doc : OWL-CSR-ESO-00000-0161



Version 1
Date: 20/10/2005
Page: 136/175

MegaMIR

Megapixel Mid-Infrared Focal Plane Array

KEY FEATURES

- 1024 x 1024 format
- Si:As sensor array
- 6K optimized direct injection multiplexer
- 2-side buttable (2048x2048 possible)
- variable integration time
- center windowing mode
- non-destructive readout

The MegaMIR FPA is the first in a new generation of mid-infrared products for ground based astronomy and other imaging and spectroscopy applications.

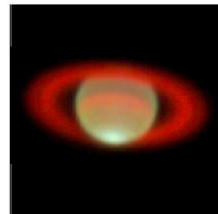
The MegaMIR FPA consists of a Si:As detector array hybridized onto a customized multiplexer with a direct injection architecture appropriate for ground based applications. In addition to the megapixel class format, the MegaMIR features 2-side buttable layout (to enable up to 4 megapixels in one package), optimized operation at 6K, variable integration time, center (256x256)

windowing mode (extendible to 512x512 for chips butted together),

JPL is leading the development efforts with DRS Technologies. We are currently seeking partners interested in the application of the MegaMIR FPA in ground based astronomy. Interested parties are encouraged to communicate with the contact given below.

Dr. John Hong
(john.hong@jpl.nasa.gov)

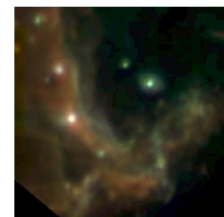
Parameter	Value	Units	Comments
Format	1024 x 1024		
Integration Mode	Ripple		
Pixel Pitch	18	um	
Detector Material	Si:As		
Band	5-28	um	
Integration Control	Variable		
Read Noise	< 1000	e ⁻	10 msec integration time
Dark Current	< 12,800	e ⁻ /s	at 10K
	< 10	e ⁻ /s	at 6K
QE	> 57%		
Well Capacity	≤ 5.0E+06 Max ≥ 96E+03 Min	e ⁻	Controlled by gain select
Operability	> 99%		
Non-uniformity	< 2%		Limited by measurement accuracy
Nonlinearity	< 1%		
Frame Rate	< 100	Frames/sec	
Number of Outputs	16		
Data Rate	≤ 7E6	Pix/s/output	



Saturn as seen in one MegaMIR FOV at 12, 18, 25 um

Photo Illustrations based on MIRLIN camera observations (JPL/Keck)

The Galactic Center at 9, 13, 21 um in one MegaMIR FOV (photos courtesy M. Ressler, JPL)



PRELIMINARY
v. 4.2

Overview of MIR-detectors

Table 20: List of available TIR and MIR detector arrays

Company	Type	Pixel pitch	Pixel number	Wavelength range	High/low BG
Raytheon (SBRC)	Aladdin III InSb	27	1024x1024	0.9 – 5.4	low
Raytheon (SBRC)	InSb (ORION)	25	2048 x 2048	0.9 – 5.4	low
Raytheon (SBRC)	Si:As IBC (JWST)	25	1024 x 1024	2 - 28	low
Raytheon (SBRC)	Si:As	50	320 x 240	2 – 28	low/high
Raytheon (SBRC)	Si:As	75	126 x 126	2 - 28	low/high
DRS (Boeing)	Si:As BIB	50	256 x 256	2 – 28	low/high
DRS (Boeing)	Si:As BIB	75	126 x 126	2 - 28	low/high
Sofradir/AIM	HgCdTe	15	640 x 480	8 - 12	low
Sofradir/AIM	HgCdTe	15	320 x 256	0.8 – 11	low
LETI/LIR ¹	Si:Ga	75	128 x 196	2 - 17	low/high
JPL	Si:As	18	1024x1024	5-25	high
Raytheon (SBRC)	Si:As	25	1024x1024	5-28	high

¹ Lucas et al., 1994

Need for detector development ?

Obviously, the well known detector industry is aware of the ground based detector requirement of next generation MIR-detectors. A 1024x1024 Si:As IBC array with the option of two side buttability is a first step in fulfilling the ELT MIR detector requirements, even though for optical design reasons (see 10.2.1 of this document) and for high dynamic range reasons a larger pixel scale (e.g. 50 μ m) for the 8-25 μ m detectors is recommended.

For the thermal IR region (Aladdin) the next step to a 2048x2048 detector array for ground based application is recommended, based on the design of the ORION-detector.

12.4.7 Wave Front Sensor

The reflected light from the entrance window is used for wavefront sensing. The entrance window should transmit all light beyond 2.6 μ m. On the other hand, the sensing wavelength should be as close as possible to the observing wavelength, thus, we propose to us a NIR wavefront sensor for T-OWL.

12.5 Spectrograph Design Details

12.5.1 Spectrometer Concept

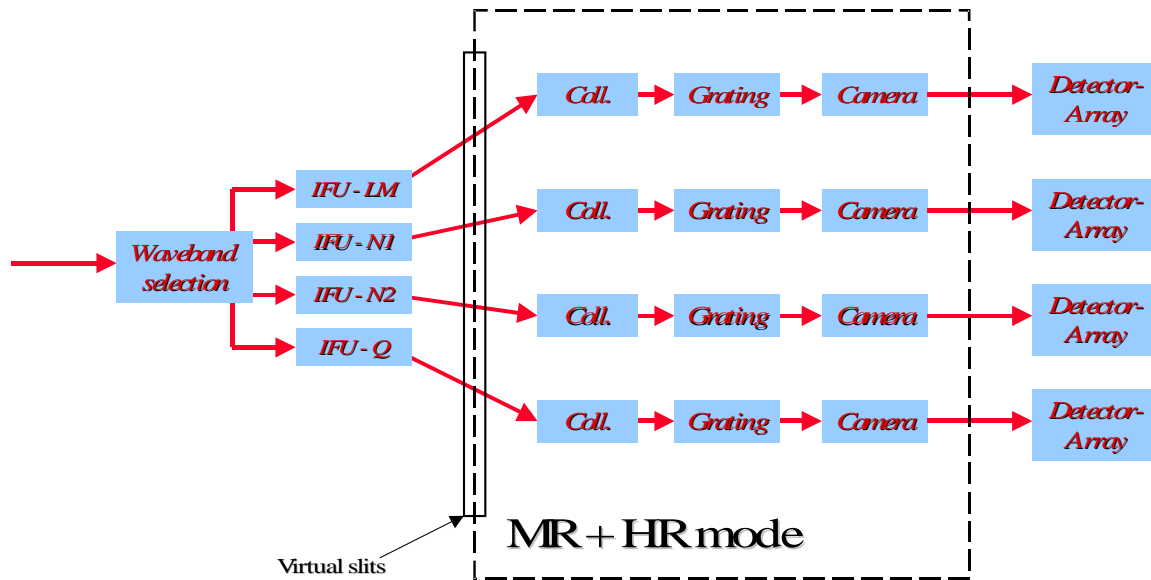


Fig. 98: General lay-out of the spectrometer

Fig. 98 shows the general lay-out of the spectrometer. After the common pre-optics with the image, a switch sends the collimated beam into the spectrometer. The first part of the spectrometer consists of a dichroic filter system in which the waveband separation takes place. After the waveband separation, the full FOV will be sliced in a for each waveband optimised IFU. The slices are projected on top of each other creating a very long “slit”. In the IFUs, the beams are re-imaged again to produce a well defined image at their exits and thus create access to an intermediate pupil and image to reduce the stray light generated in the system and offer the required output beam parameters independently of the internal IFU requirements.

The exit of the IFUs is an image of the slit that serves as input for the collimator system. The collimator produces a collimated beam with sufficient diameter to ensure the proper spectral resolution. The dispersion will be provided by gratings in almost Littrow mounting, where the angle of incidence on the grating equals the angle of diffraction. The camera makes an image of the spectrum on the detector array providing the required pixel scale for optimised sampling.

12.5.2 IFU⁴

Slicing and detector sampling

In the general spatial sampling consideration (section 9.3.5), the number of required detectors and slices were estimated for a FOV of 1 square arcsecond at a 100 meter telescope, resulting in both an

⁴ More details on the IFU design are planned for the future. This part is not critical for the interface to OWL.

unrealistic number of slices and detectors for the shortest wavelength channels. In this section we make the trade-off to more conservative values for the possible number of slices and detectors. Using the sampling considerations of the previous section we get the results as shown in Table 21.

Table 21: Slicing and sampling parameters

Channel		L+M	N _{low}	N _{high}	Q
λ_{\min}	(μm)	3,5	8	10,6	17
λ_{\min}/D	(marcsec)	7,2	16,5	21,9	35,1
$1,5 \cdot \lambda_{\min}/D$	(marcsec)	10,8	24,8	32,8	52,6
#slices		48	45	45	36
FOV across slice (spectral)	(arcsec)	0,35	0,74	0,98	1,26
#spatial resolution elements in square FOV		32	30	30	24
#pixels for sampling		64	60	60	48
#slices fitting on one detector		14,1	15,0	15,0	18,4
integral #slices/detector		14	14	14	18
#detectors for square FOV		3,4	3,2	3,2	2,0
Acceptable #detectors		4,0	3,0	3,0	2,0
FOV along slices (spatial)	(arcsec)	0,4	0,7	1,0	1,3
Telescope diameter	(m)	100			

λ_{\min} is not always taken as lowest point of the wavelength range. The atmospheric windows tend to limit certain parts of the wavelength range and we tried to optimize that the best part of the window (including interesting lines and features) were sampled optimally.

The configuration and pixel mapping is done in each channel independent of the parameters of the other channels. For the future, another trade-off parameter, the relative change in slice widths, must be taken into account. Full spatial recovery for all spectrometer channels simultaneously with the minimum number of pointings require a further optimization in the slice width. This might deviate from the otherwise optimal value.

12.5.3 Optical Design

The overall concept for the pre-dispersion optics of the spectrometer is shown in Fig. 99. The proper FOV for the spectrometer is directed from a switchable mirror at the end of the common pre-optics from T-OWL. This collimated beam is directed towards a dichroic switch-yard where the light is separated in different spectrometer bands going to the individual IFUs.

The optics between the switch mirror and the IFU slicing mirrors performs two functions:

1. Provide a section of beam in which the folded light path through the dichroic filters can be accommodated
2. Magnify the image to the appropriate size at the image slicer, and adjust the relative scaling between spatial and spectral direction

It is assumed at this stage that the pupil in the collimated beam was used for a Lyot stop in the common pre-optics. The anamorphism between the spatial and the spectral sampling is created in the re-imager before the image slicers, similar to the JWST-MIRI design.

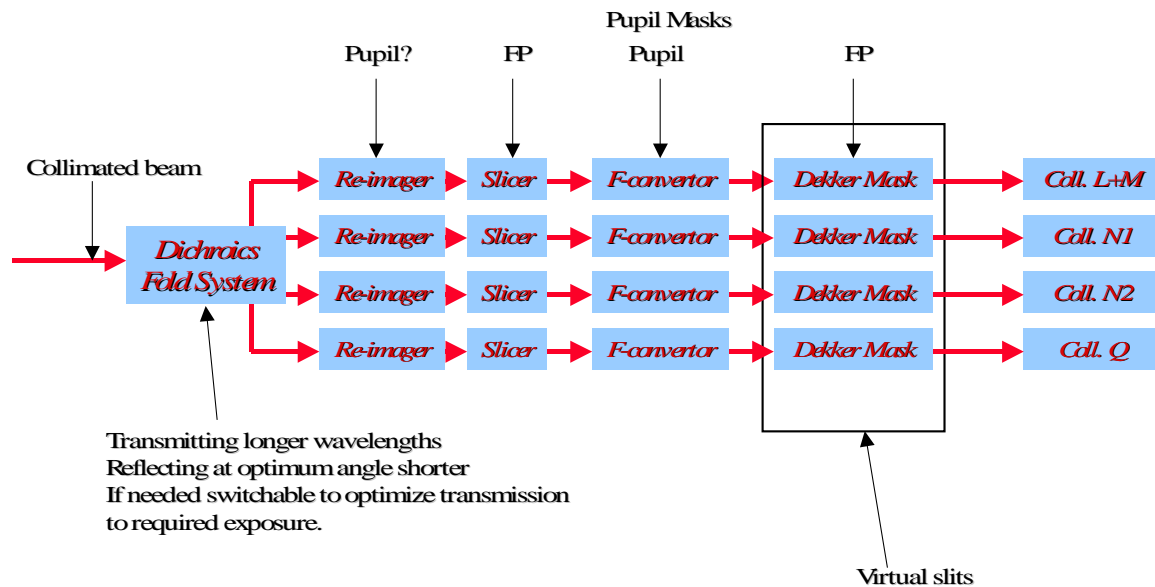


Fig. 99: Schematic representation of the pre-optics for the spectrometers

The re-imaging optics after the slicer has the following functions:

- provide additional baffling before the light can enter the spectrometer (pupil and image baffling), to suppress the scattering produced by the image slicer
- provide a well defined “virtual slit” plane with sufficient optical quality by reorienting the slices
- adapt the f-ratio of the exit beam to the needs of the spectrometer channels
- control of the pupil location with respect to the diffraction elements

In the medium resolution mode, Decker masks are provided to reduce stray light in the image plane, for the high resolution spectrometer, the Decker masks are modified/changed to reduce the FOV of the IFUs, as well.

The dichroic system will be described after the spectrometer channels are discussed, as the detailed filtering requirements follow from the band and required order separation.

12.5.3 Medium Resolution Spectrometer

For each spectrometer channel the instrument parameters need to be established. Drivers for the spectrometer channels are:

1. high efficiency
2. similarity between the different channels
3. weight and size (instrument needs to be cryogenic)
4. maximum wavelength coverage in few exposures

Due to the dense packing of spatial information on the detectors, image distortions and curved spectra should be prevented. Optimizing the efficiency of the spectrometer is easiest accomplished by using the gratings in first order, to prevent the need for additional order suppression. Fig. 100 shows the parameters for the spectrometer elements (collimator, grating, camera). The following consideration led to these values:

1. gratings in first order
2. optimize for efficiency
3. keep beam dimensions reasonable
4. prevent fast or extremely slow collimator parameters (baseline F/6)
5. Pixelsize of the detector is defined to be 25 μm

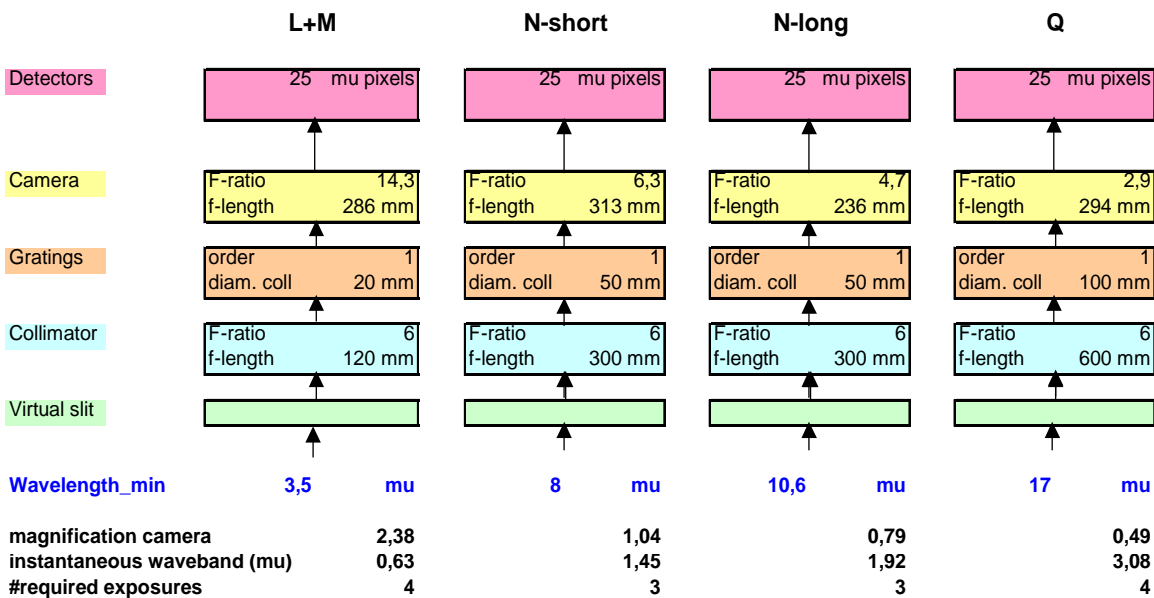


Fig. 100: Global design parameters for the medium resolution spectrometer channels

For obtaining high efficiency in the gratings, the parameters were established by taking each grating step slightly larger than the maximum λ for the spectrometer channel. Requiring $R=3000$ leads to a minimum of 3000 steps for the beam on the grating, resulting in the collimated beam diameter and, therefore, the collimator dimensions.

The F-ratio of the camera is defined by the requirement to sample the slice width by two pixels. This results in fast cameras for the longest wavelength. However, the f-ratio of 2.9 for the Q-band is still considered doable. The overall focal lengths needed and the F-ratios of the systems seem to be very acceptable, similar or relaxed to existing instruments or instruments in development.



T-OWL Concept Level Study

Doc : OWL-CSR-ESO-00000-0161



Version 1
Date: 20/10/2005
Page: 142/175

Table 22: Details for the different exposures in all channels and the grating parameters

Spectrograph channel		1	2	3	4
Atmospheric Window		L+M	N _{low}	N _{high}	Q
Wavelength requirements		3,5 5,5	8 10,6	10,6 14	16 25
Diffraction limit (m-arcsec)		8,8 13,8	20,1 26,7	26,7 35,2	40,3 62,9
Spectral resolution R		3000	3000	3000	3000
Collimated beam Ø (mm) ²		20	50	50	100
Grating constant (l/mm)		141,5	57,5	55,6	28,7
Grating angle		19,4	16,7	22,0	17,1
Opening angle Blaze (1/2 intensity)		40,4	34,4	46,4	35,2
Central wavelength for R		4,7	10	13,5	20,5
Exp. 1	Wavelength range ¹	3,5 4,0	7,5 8,5	10,3 11,7	16 18,2
	R _{eff}	4029 3558	4000 3530	3932 3463	3844 3375
	Angle ³	14,7 16,6	12,7 14,3	17,2 19,3	13,5 15,3
Exp. 2	Wavelength range	3,85 4,4	8,3 9,5	11,2 12,9	18 20,8
	R _{eff}	3662 3195	3614 3147,6	3616 3149	3417 2952
	Angle ³	16,1 18,3	14,0 16,0	18,6 21,1	15,1 17,4
Exp. 3	Wavelength range	4,25 4,9	9,3 10,9	12,2 14,2	20,5 24,2
	R _{eff}	3318 2854	3226 2762,7	3320 2856	3000 2540
	Angle ³	17,7 20,3	15,6 18,0	20,1 23,0	17,1 20,0
Exp. 4	Wavelength range	4,7 5,6			24 29,2
	R _{eff}	3000 2540			2563 2108
	Angle ³	19,4 22,6			19,8 23,6
Wavelength limits (on detector)		3,5 5,6	7,5 10,9	10,3 14,2	16 29,2
IFU	FOV (along * across)(arc)	0,4 * 0,35	0,7 * 0,74	1,0 * 0,98	1,3 * 1,26
	# slices	48	45	45	36
	slice width (marcsec)	7,2	16,5	21,9	35,1
#Detectors		4	3	3	2

Table 22 shows the grating parameters and the different spectral channels in more detail. The resolution of the grating depends on the wavelength. In order to ensure $R=3000$ for the whole range, the grating is defined such that $R=3000$ is obtained close to the maximum wavelength in each channel. The choice is quite arbitrarily and can easily be adapted to other values. The full wavelength range can only be mapped on the detector in several exposures as shown in Table 22. Switching between exposures takes place by tilting the grating angle in fixed steps⁵. The blaze of this grating is sufficient wide to ensure a good efficiency over all tilt angles. More details on the grating parameters will need a full grating analysis, which we consider outside the scope of this conceptual study.

⁵ Another option is to use different gratings for each exposure. This will lead to the use of 14 instead of 4 Medium resolution gratings. The advantage of this solution is that the resolution does not change significantly between various exposures, although the resolution drop within each exposure will be more or less similar.

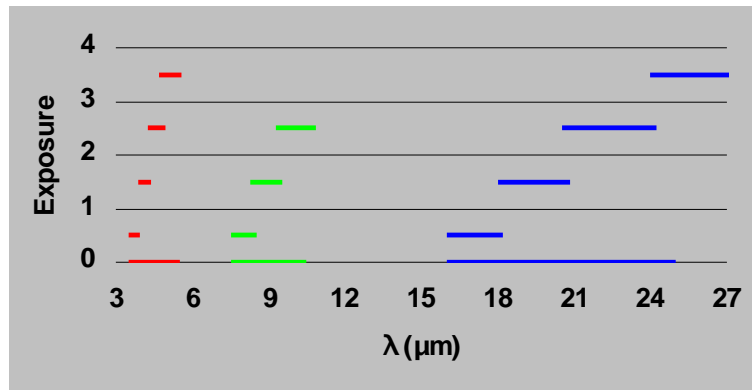


Fig. 101: The wavelength coverage in the four channels with their different exposures.

As a consequence of using the grating with different tilt angles the spectral resolution changes with wavelength (see Fig. 102).

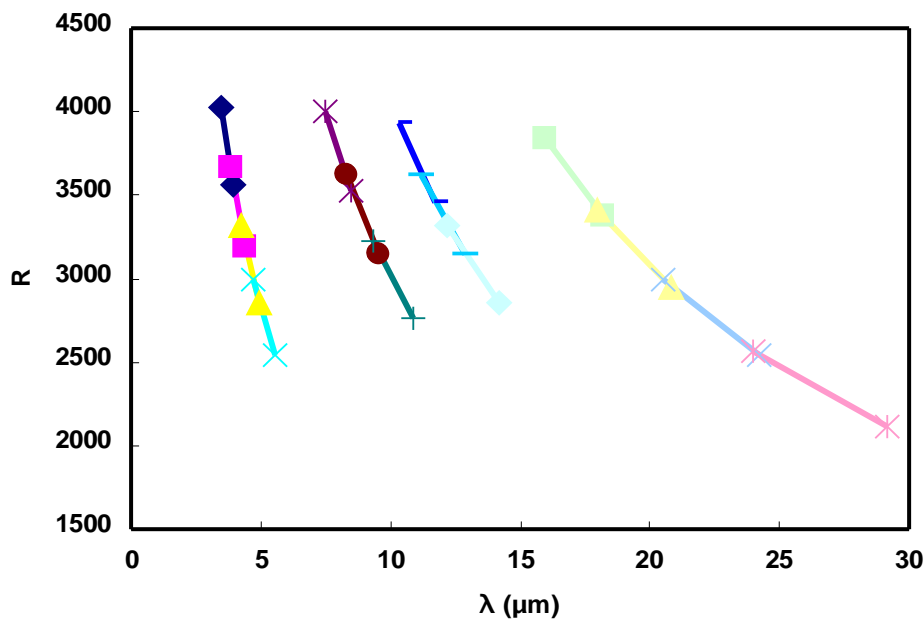


Fig. 102: The change of the resolution for different wavelength in the four spectrometer channels.

12.5.4 HR Spectroscopy

For obtaining sufficient resolution while keeping the size of the optics limited, gratings are used in the Echelle mode, where the optical path difference over the grating is increased by using deeper steps and working in higher orders. This automatically means that overlapping orders become a serious issue that need careful analysis.

Here we follow the same line of constraining parameters as has been done in the MR case. However, in the HR mode, the differences between the various wavebands become again very marked and each band will be treated separately. Again, we consider solely the Littrow configuration for the gratings.

We start the analysis with the 10 μm case, the heart of the mid-IR regime. Here we have a very clean atmospheric window and this domain should be considered as the most prominent wavelength range for the instrument.

N-band

For the high resolution spectroscopy, the main worries in the design were:

- maintaining high efficiency if possible
- preserving a large FOV, if possible
- solving order overlap
- obtaining sufficient instantaneous wavelength coverage.
- ensuring a full coverage of the spectral windows for the high resolution mode

As discussed in the earlier presentation, using $R = 50000$ on 500 resolution elements (1024 pixels), provides an astronomical important velocity resolution of 6 km/s over a sufficient wide range of velocities (3000 km/s). Nevertheless, for a more complete coverage in wavelength many exposures may be needed. If possible, a bigger instantaneous coverage should be accomplished, which can be done, when we can trade spatial pixels for spectral pixels.

Overlapping orders is another important issue. The order separation can be accomplished by:

1. filtering
2. cross dispersion

The filtering has been dropped from our discussion, fixed filters tend to make the instrument inflexible and probably many expensive and technically difficult filters are needed. Another option might be via tunable FP-filters, where the gap is adjustable. However, a cascade of filters is required to select one single wavelength range. This option requires a high risk technology development, which might turn out to be not realistic. So, for this study only the cross dispersion is considered.

Fig. 103 shows a possible solution to the issues both to solve the order overlap issue and recovering some instantaneous wavelength coverage as well. Different orders will be on the different detectors. The choice for three orders will become clear in the discussion of Fig. 105.

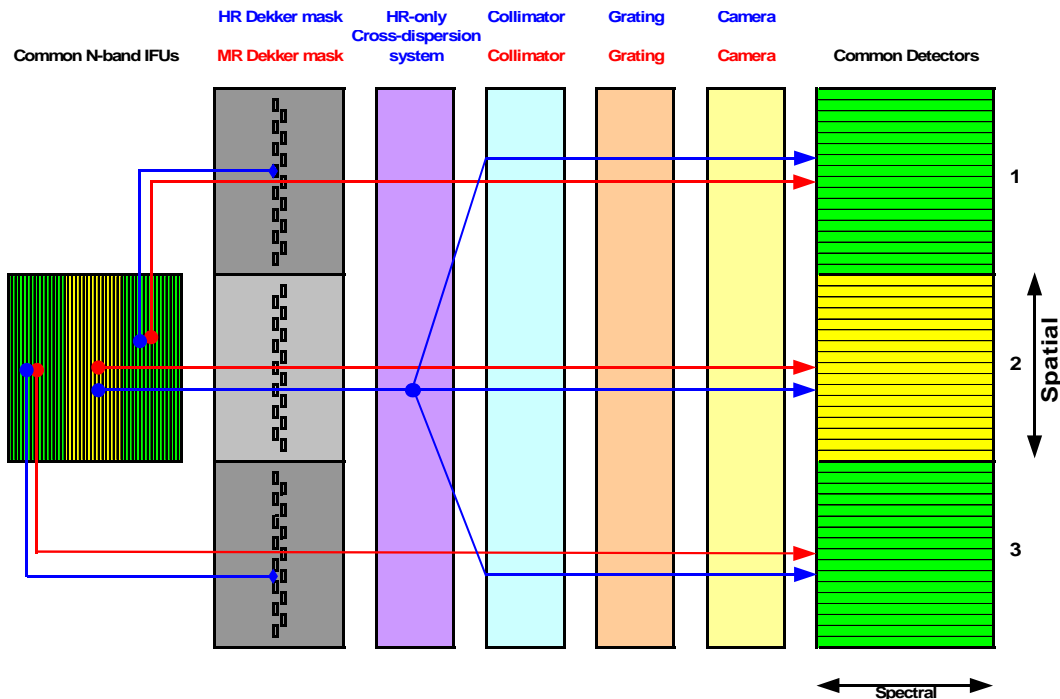


Fig. 103: Mapping of information in N-band channels on the detectors. The Decker mask can be changed to block the outer IFU slices, to free two detectors for cross-dispersion. “Common” refers to common to both MR and HR mode. Blue refers to HR mode, red to MR mode.

In first instance, the scale of an Echelle spectrograph was estimated from a scaled up version of VISIR. As can be seen in Fig. 104 the overall beam parameters seem quite reasonable for this spectrometer mode. However, more detailed analysis for the grating in Echelle mode is required to check both the issues of the capability for covering the whole spectral range and the cross dispersion. Results of this analysis are shown in Fig. 105 for both N-band spectrometer channels.

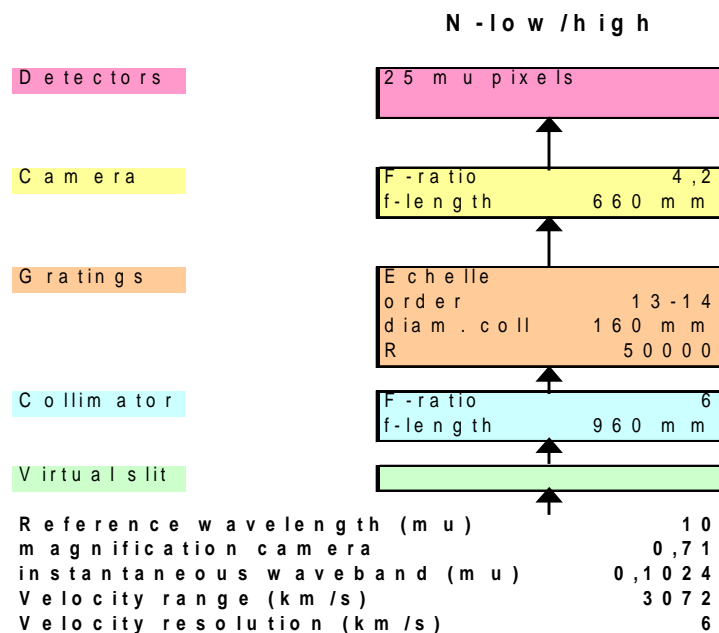


Fig. 104: Estimate of the beam parameters for the high resolution N-band spectroscopy, scaled version from VISIR.

In the top-left corner of Fig. 105, the relation between wavelength coverage in different order is established, using the free spectral range formulas. Testing and trying various settings (orders and central wavelength) showed clearly that full coverage could be obtained for the two N-bands with three orders per spectrometer channels, using the orders and central wavelength as indicated in Fig. 105. These parameters lead to the grating parameters. The only additional input needed here is the tilt angle of the grating (Θ). A further constraint results from the fact that the Echelle should be capable to fill the wave length range continuously by tilting the Echelle, putting severe constraints on the selection of possible combination of orders and central wavelength.

The next big box in Fig. 105 shows the camera parameters for proper pixel matching in both channels. The lower-right corner boxes show the dispersion in the various channels and orders in more detail. From these calculations, it is easy to assess the amount of cross dispersion that is required to separate the orders, where we need to displace the different orders over at least the full width of one detector. This cross dispersion can be created by gratings⁶ with the grating constant as given in the box in the lower-left corners of Fig. 105, which seem to be doable.

The cross dispersion should be performed in a collimated beam, but the dimension of the collimated beam for the high resolution dispersion drives the grating dimensions significantly. A possible solution could be to produce in an earlier stage a collimated beam with smaller dimensions according to Fig. 106. A reduction of collimated beam diameter of at least a factor three is considered possible, but this needs further verification.

⁶ Why grisms or gratings: Main advantage of grisms is that considerable diffraction can be obtained without refracting the beam. The prism compensates the refraction induced by the grating while the dispersive power of the grating is maintained. Disadvantages: transmissive optics, limited materials, losses due to absorption, ruling on materials difficult, coating difficult. Presently for the spectrograph we opt for a high efficiency grating while the low resolution spectroscopy is realized by Grisms. .



T-OWL Concept Level Study

Doc : OWL-CSR-ESO-00000-0161



Version 1
Date: 20/10/2005
Page: 147/175

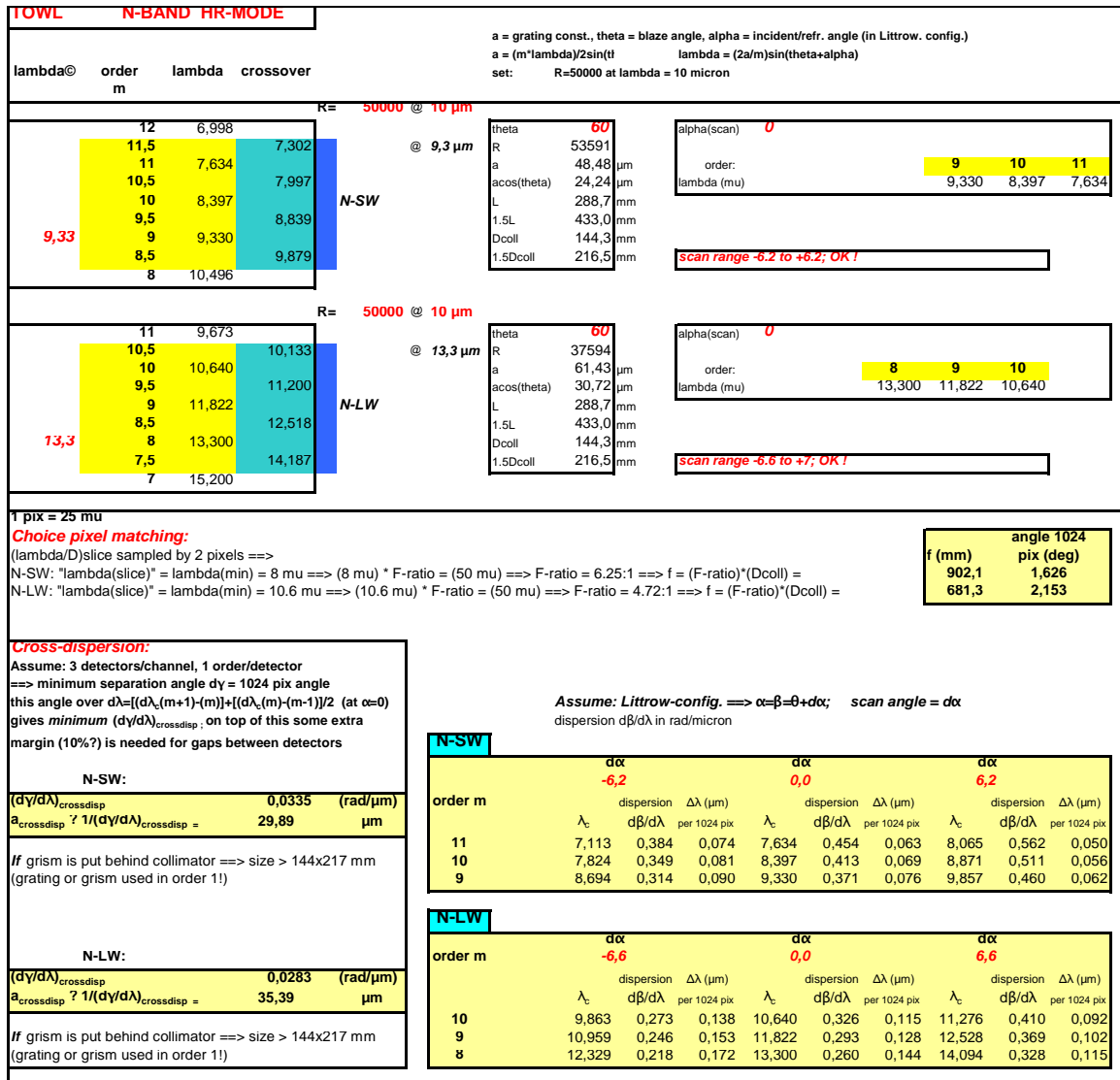


Fig. 105: Echelle mode and cross dispersion for the N-band

Fig. 107 shows the wavelength covered in the HR mode for the N-band. One additional requirement came from the dichroic selection, to separate the band for N_{low} and N_{high} sufficiently for dichroic filter. As can be seen from this figure, we accepted in this conceptual stage to use the HR gratings beyond their crossover wavelength. In a full design, these parameters need further optimisation to ensure a proper use of the gratings.

One of the bonuses with this selection of orders is the capability to extend the spectral coverage down to 7 µm. The instrument will not be optimised for the light between 7 and 8 µm, but will be able to operate in this range.

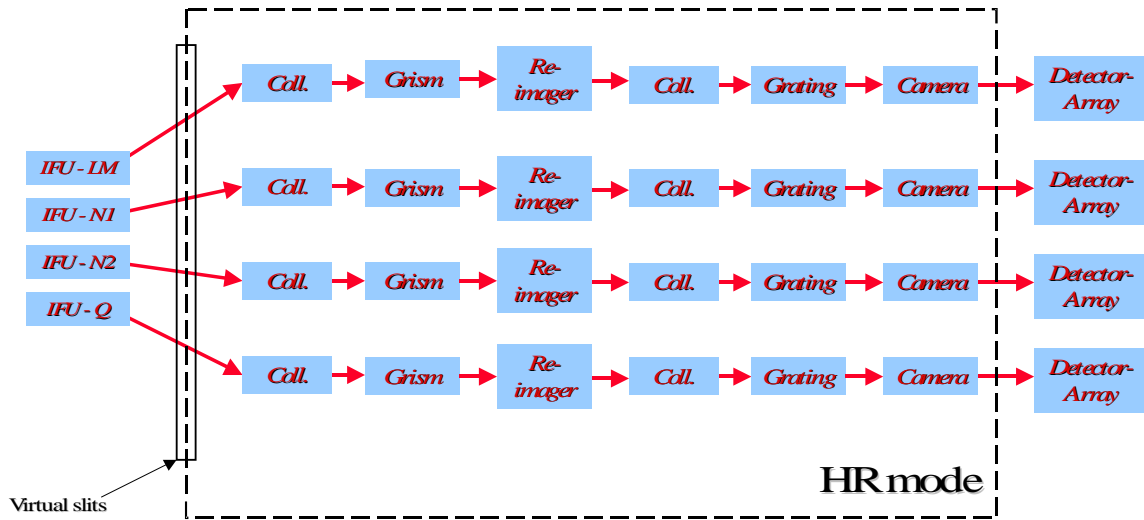


Fig. 106: Possible optical design for the HR spectroscopy

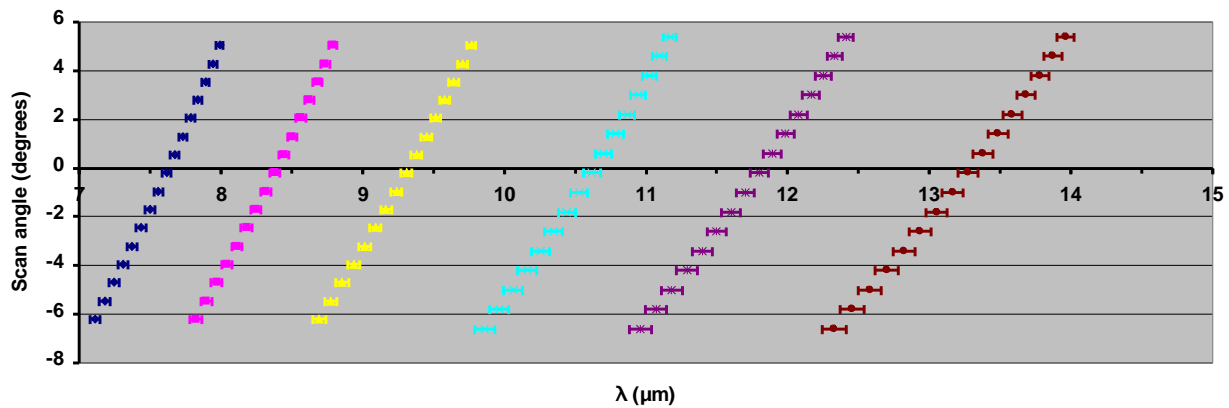


Fig. 107: Spectral coverage of the HR-mode for the N-band. Full coverage with 16 exposures. Still unequal overlap in SW and LW channels. Can be further optimized with additional fine tuning.

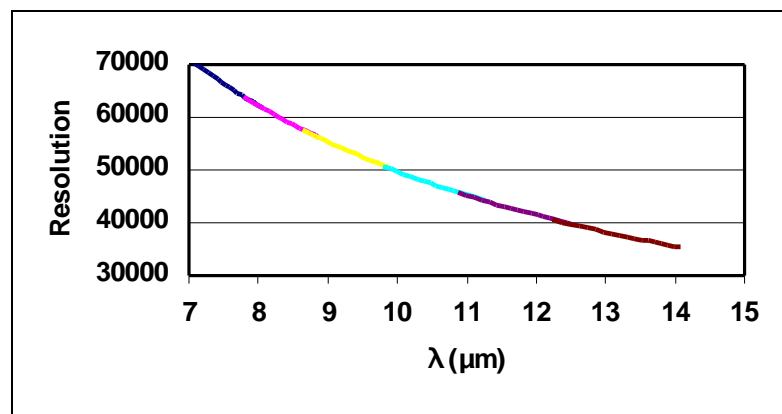


Fig. 108: Resolution drop within the N-band channels

Fig. 108 shows the resolution obtained with these spectrometer parameters. In principle, the resolution can be adjusted independently for the two N-band channels, but for the current design we chose to keep the resolution a continuously degrading function over this wave length region.

As conclusion, the HR mode spectroscopy in the N-band seems feasible within reasonable instrument parameters.

Q-band

For the Q-band, the increase wavelength by a factor of two leads for a similar resolution as the N-band to twice the instrument dimensions. The length of such an Echelle would exceed the size what can be produced nowadays. Although it is not directly ruled out as possibility to combine smaller Echelle gratings to an effective longer one, as is done in other instruments (even for visible light), we accepted a reduced resolution in the Q-band ($R=25000$) as we did not encountered crucial drives for $R=50000$ in the by the atmosphere severely compromised Q-band.

The type of analysis is similar as has been done in the N-band and the results are shown in Figure 109. As can be seen, here four orders are needed to ensure the full coverage in the HR-mode, in the region up to $24.8 \mu\text{m}$. Although, this part of the spectrum is not a driver from the science cases, it is one of the most clear areas in the Q-band. Due to the need of four orders and keeping the philosophy similar as in the N-band, we need to block out three quarters of the FOV in the Q-band, which is less severe than it first appears due to the larger FOV in the Q-band compared to the N-band (Figure 111). The extension up to $25 \mu\text{m}$ is not compromising in the required performance.

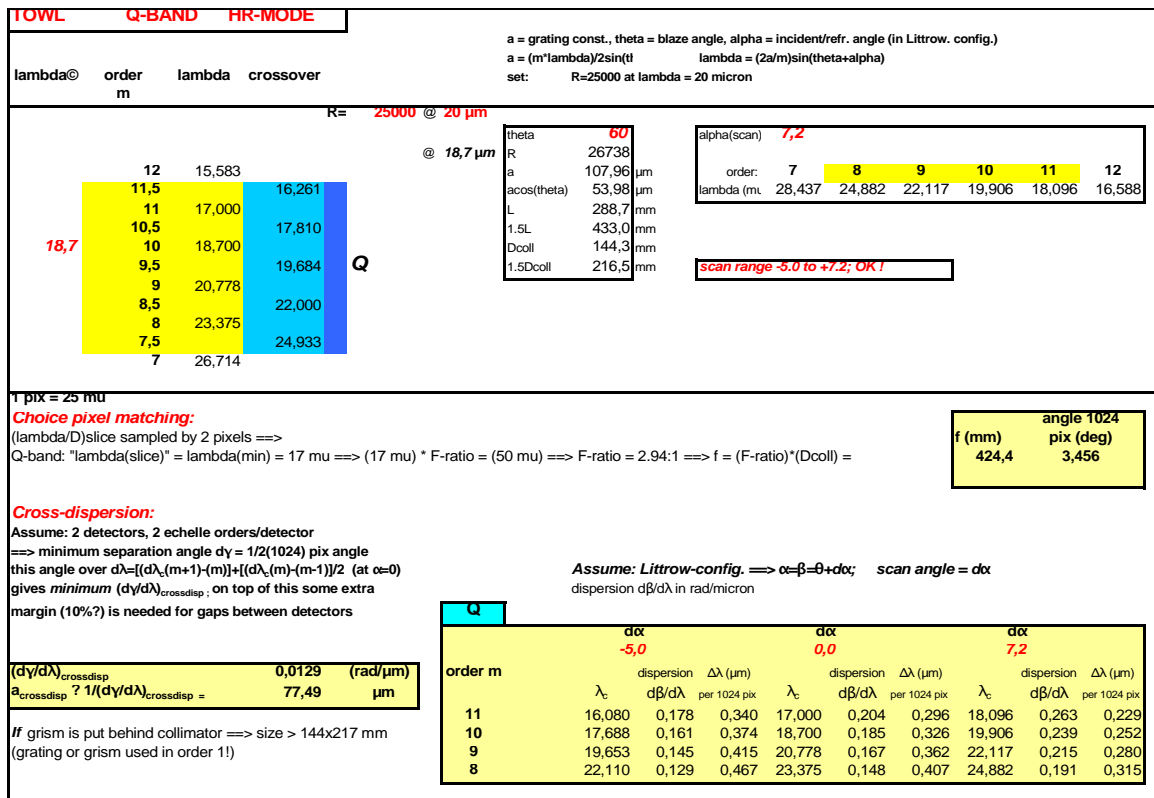


Fig. 109: Echelle mode and cross dispersion for the Q-band

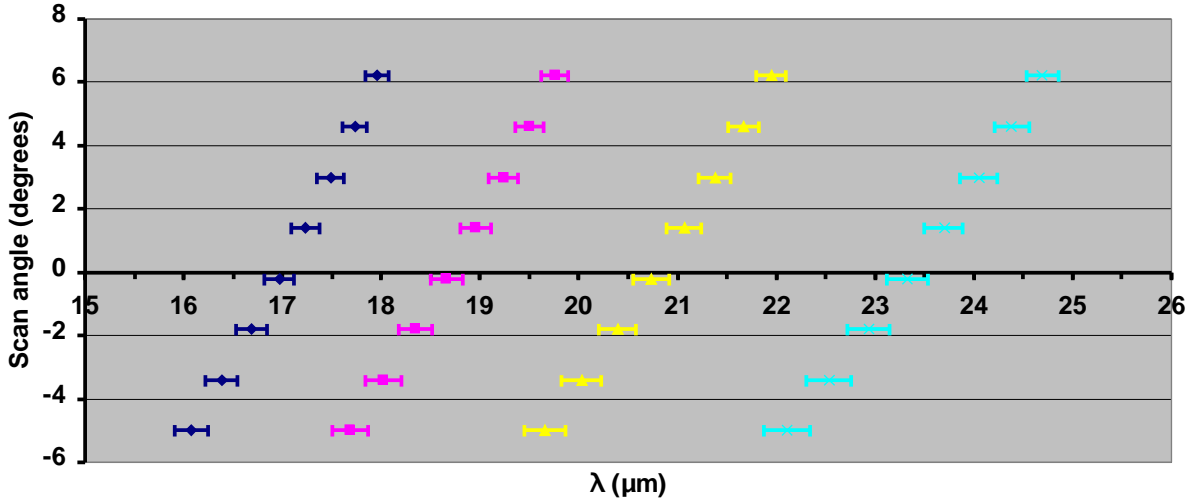


Fig. 110: Spectral coverage of the HR-mode for the Q-band. Full coverage within 8 exposures.

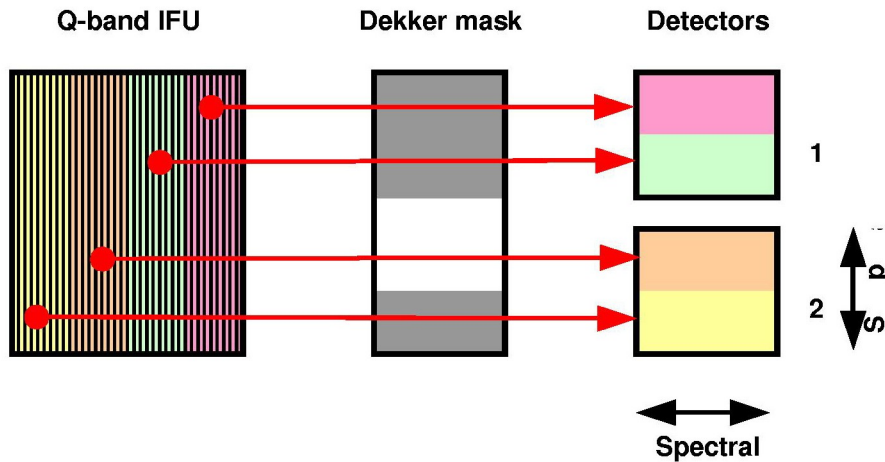


Fig. 111: Mapping of information in Q-band on detector. The Decker mask can be changed to block the outer IFU slices, to free three quarters of the two detectors for the cross-dispersion orders.

As conclusion, the HR mode for the Q-band seems feasible within reasonable instrument parameters. The main worry is the F-ratio of the camera in combination with the field size.

L+M band

The FOV in the L+M band is already quite small. In addition, the wavelength is much smaller making HR spectroscopy “easier” from dimensional perspective. We chose to push this and removed the need for order separation by going to a low order grating (even though still as Echelle). By going to second order, the need for cross dispersion is removed and simple filtering will sufficient. The parameters of this mode are shown in Fig. 112. The required scan range and scan step size might start to push the present cryogenic mechanisms, but it seems still feasible. The disadvantage of this choice is the very

small instantaneous wavelength coverage, however, the atmospheric continuity of the transmission in the L+M-band is also poor. In how far this is acceptable requires fine tuning during phase A study.

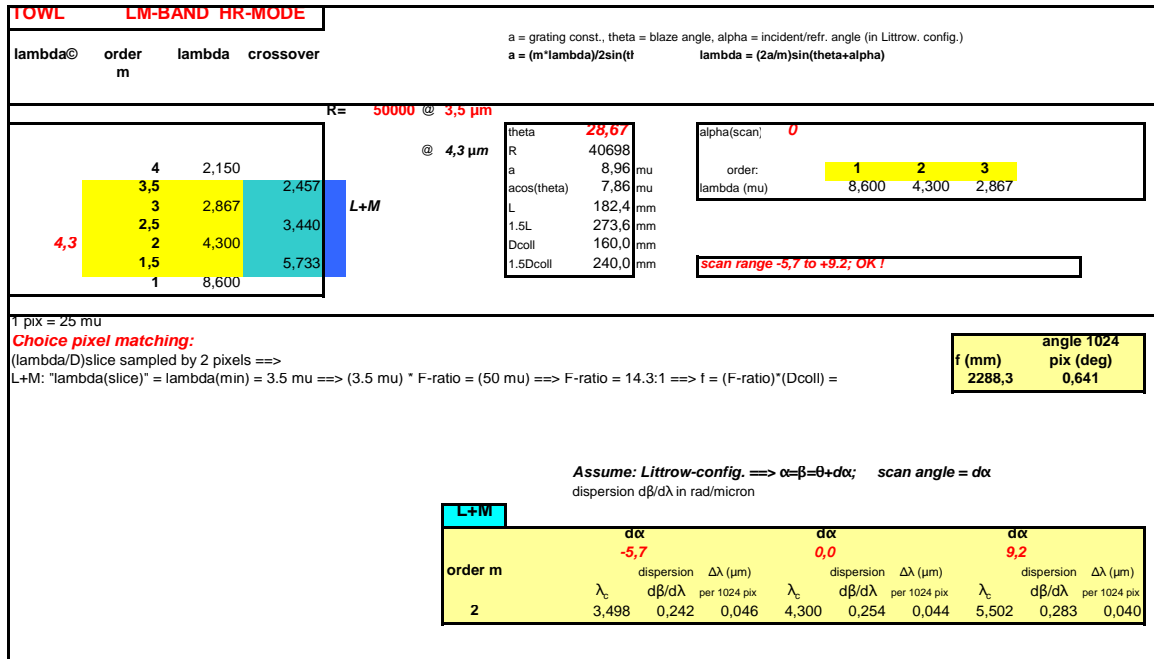


Fig. 112: Echelle mode and dispersion parameters for the L+M-band

Cross Dispersion

The cross dispersion solutions for the N-band and Q-band channels is however not completely solved yet. Different scan angles in the grating result in different spectral spacing between the orders. Therefore, the required amount of cross dispersion depends on the scan angle of the grating. Various solutions can be considered, like reserving additional space on the detector (resulting in a loss of pixel efficiency) or reconfiguration of the detectors (complicating the instrument). In addition, the spectra are tilted by the cross dispersion. As the cross dispersion is approximately 1/10 of the main dispersion, this results in approximately 100 pixels tilt over the full 1024 pixels of each spectrum. However, we consider these open issue not as killers and will postpone further analysis to a later stage.

Summary HR mode

Table 23 presents an overview of the parameters of the HR mode of the spectrograph. The listed IFU parameters include the consequences of masking for freeing space on the detectors for the cross dispersion.



T-OWL Concept Level Study

Doc : OWL-CSR-ESO-00000-0161



Version 1
Date: 20/10/2005
Page: 152/175

Table 23: Overview of the HR spectrometer parameters

Spectrograph channel		1	2	3	4
Atmospheric Window		L+M	N _{low}	N _{high}	Q
Wavelength requirements		3,5 5,5	7,5 9,8	9,8 14	16 24
Diffraction limit (m-arcsec)		8,8 13,8	18,9 24,7	24,7 35,2	40,3 60,4
Spectral resolution R		50000	50000	50000	25000
Collimated beam Ø (mm)		160	150	150	150
Grating constant (l/mm)		111,6	20,6	16,3	9,3
Grating angle (degrees)		29,0	60,0	60,0	60,0
Echelle orders		2	9, 10, 11	8, 9, 10	8, 9, 10, 11
Central wavelength for R (µm)		3,5	10	10	20
Order A	Spec. order Δλ	2 0,04	9 0,08	8 0,12	8 0,30
	Tilt range (degrees)	-5,7 9,2	-6,2 5,5	-6,6 5,4	-5,0 6,2
	Spectral range (µm)	3,5 5,5	8,6 9,8	12,2 14,0	21,9 24,8
Order B	Spec. order Δλ		10 0,07	9 0,13	9 0,33
	Tilt range (degrees)		-6,2 6,2	-6,6 6,6	-5,0 7,2
	Spectral range (µm)		7,8 8,8	10,9 12,5	19,4 22,1
Order C	Spec. order Δλ		11 0,06	10 0,15	10 0,36
	Tilt range (degrees)		-6,2 6,2	-6,6 6,6	-5,0 7,2
	Spectral range (µm)		7,1 8,0	9,8 11,2	17,5 19,9
Order D	Spec. order Δλ				11 0,41
	Tilt range (degrees)				-5,0 7,2
	Spectral range (µm)				15,9 18,1
#Exposures for full coverage		50	16	16	8
IFU	FOV (along * across)(arc)	0,4 * 0,35	0,7 * 0,25	1,0 * 0,33	1,3 * 0,32
	# slices	48	15	15	9
	slice width (m-arcsec)	7,2	16,5	21,9	35,1
	λ _{min} (µm)	3,5	8	10,6	17
#Detectors		4	3	3	2

12.5.5 Dichroic Separation

Dichroic filters are used to create separate wave range channels. To avoid potential introduction of astigmatism, dichroic filters should be used within the collimated beam. In Mid-IR regime, the production of dichroic filters is more difficult as it is for visible wave length range and very sharp cross-overs are hard to produce. In the JWST design for MIRI, dichroics are used, where the dimensions of the cross over range can be expressed by:

$$\frac{\lambda_{max}^{refl.}}{\lambda_{min}^{transm.}} = 1.3$$

This design is most critical in the HR mode between the two channels of the N-band, where after some optimisation we reached a factor

$$\frac{\lambda_{max}^{refl.}}{\lambda_{min}^{transm.}} = 1.13$$

which requires a steep crossover in the dichroic filters. This is certainly a subject for further research.



T-OWL Concept Level Study

Doc : OWL-CSR-ESO-00000-0161



Version 1
Date: 20/10/2005
Page: 153/175

Table 24: Dichroic scheme from the MR spectrograph.

Exposure	Blocking		Dichroic cross-over						Blocking	
	L+M		N-SW		N_LW		Q			
	(μm)	(μm)	(μm)	(μm)	(μm)	(μm)	(μm)	(μm)	(μm)	(μm)
1	<3	7	7	9,8	9,8	15,2	15,2	15,2	>28	>28
2	<3	7	7	10,4	10,4	15,2	15,2	15,2	>28	>28
3	<4	7	7	11	11	15,2	15,2	15,2	>28	>28
4	<4	7	NA	NA	NA	NA	15,2	15,2	>28	>28

Due to the optimisation in spatial coverage in the HR-mode and a maximum transition region between the reflected and transmitted beams the number of dichroics is large and even the separation required for MR and HR-mode are not completely matched any more.

Table 25: List of proposed dichroics

Dichroic filter	reflection range (μm)	transmission range (μm)
Blocking-LM-1	NA	3,47 – 25
Blocking-LM-2	NA	4,5 – 25
LM-N _{low} -1	3,47 – 4,6	7,0 – 25
LM-N _{low} -2	4,5 – 5,5	7,0 – 25
N _{low} -N _{high} -1	7,0 – 8,74	9,79 – 25
N _{low} -N _{high} -2	7,1 – 8,82	9,89 – 25
N _{low} -N _{high} -3	7,2 – 8,90	9,99 – 25
N _{low} -N _{high} -4	7,2 – 8,98	10,0 – 25
N _{low} -N _{high} -5	7,3 – 9,05	10,1 – 25
N _{low} -N _{high} -6	7,4 – 9,14	10,2 – 25
N _{low} -N _{high} -7	7,4 – 9,21	10,3 – 25
N _{low} -N _{high} -8	7,5 – 9,28	10,4 – 25
N _{low} -N _{high} -9	7,5 – 9,35	10,5 – 25
N _{low} -N _{high} -10	7,6 – 9,42	10,6 – 25
N _{low} -N _{high} -11	7,7 – 9,49	10,7 – 25
N _{low} -N _{high} -12	7,7 – 9,55	10,8 – 25
N _{low} -N _{high} -13	7,8 – 9,62	10,8 – 25
N _{low} -N _{high} -14	7,8 – 9,68	10,9 – 25
N _{low} -N _{high} -15	7,9 – 9,74	11,0 – 25
N _{low} -N _{high} -16	7,9 – 9,80	11,1 – 25
N _{low} -N _{high} -A	7,5 – 8,5	10,3 – 25
N _{low} -N _{high} -B	8,3 – 9,5	11,2 – 25
N _{low} -N _{high} -C	9,3 – 10,9	12,2 – 25
N _{high} -Q-1	9,97 – 14	15,9 – 25

In the JWST-MIRI design, the dichroics form a cascade splitting off the shortest wavelengths in reflection. However, the scheme should be optimized from efficiency perspective. We do not consider this to be the most critical item for the construction of the instrument, but it certainly requires attention and further development to optimize the efficiency.

12.5.6 Opto-Mechanical Design

In order to get access to budgets and feasibility estimate, some effort was put in estimating the overall dimension needed for a T-OWL as described in this document.

Due to limitations in time, we selected what we considered to be the most difficult channel, the Q-band with its fast camera. Fig. 113 assists in visualising the lay-out of the optical beams, their images and pupil in our proposed design. Additional folds are possible to pack the design in a smaller volume, which we will not try to optimise at this stage.

"Figure 114 shows a possible optical design for the F/2.94 camera for the Q-band channel. Here, we start from the pupil at the Echelle and modelled the optical path until the detector array (2 1*k detectors for the Q-band channel). The separation of the beams is sufficient including the required spectral oversizing (out of paper). The largest dimension in optical components is the M3 of the camera, measuring 540*480 mm².

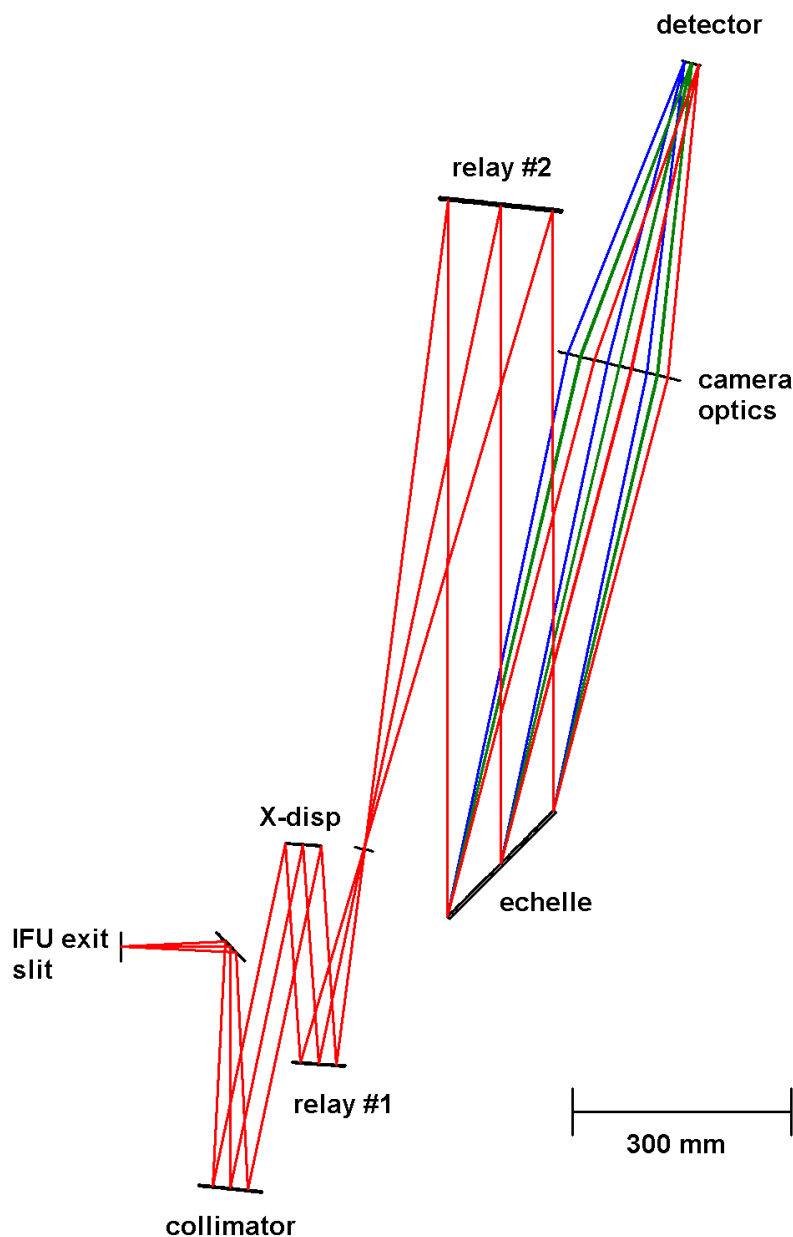


Fig. 113: Paraxial design of the Q-band spectrometer



T-OWL Concept Level Study

Doc : OWL-CSR-ESO-00000-0161



Version 1
Date: 20/10/2005
Page: 155/175

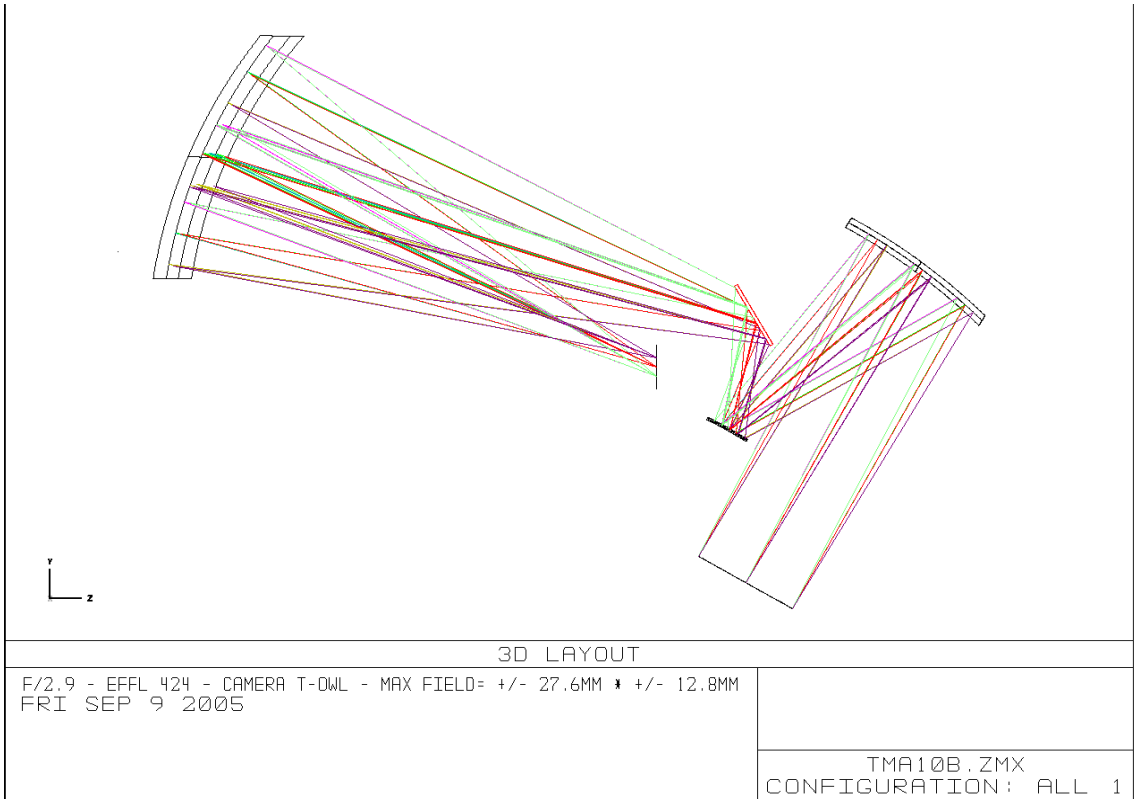


Fig. 114: Optical design for the Q-band channel camera

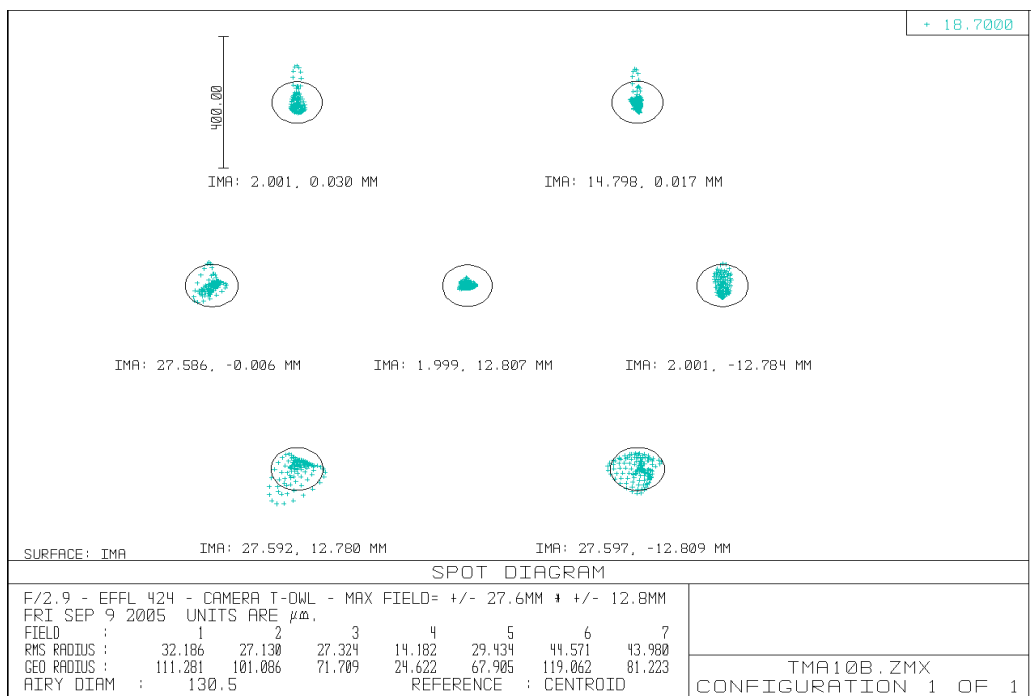


Fig. 115: Spot diagrams for the Q-band channel camera

Figure 115 shows the spot diagrams of the TMA camera. As can be seen from the figure, the quality is not yet sufficient, but we are close to diffraction limited with this system. slit seems possible to get a TMA design for this camera.

12.5.7 Parallel Observing Modes

Explain that due to the 4 parallel channel, parallel read out is possible. The combinations depend on choices in the coupling of mechanisms and how many modes the instrument might have. As baseline, we would suggest to limit the number of modes unless there is a real benefit that various lines or regions can independently be measured. However, the latter case might complicate the dichroic splitting scheme between the N-band channels, for both the HR and the MR spectroscopy.

12.5.8 General Observation Issues

De-Rotation

As baseline, it is decided to exclude the de-rotator from the instrument. This will result in image rotation on the detector, however, on the scale of the TICs, no smearing on the detector will occur. On-line and as post-processing the software needs to correct for the image rotation. The advantage here is the fact that this will lead almost to an automatic dithering of the spatial information due to the image rotation on the detector.

Flexure

Due to the presence of an IFU, also in the HR mode, the need for flexure correction of components before the IFU is minimal. We do not foresee the need of additional flexure compensation. In the spectrometer arms, there are various places where measures could be taken to actively compensate for flexure (like at detector level). Presently we assume that the flexure will be constant in time and that the the majority of the flexure can be calibrated and corrected for.

Conclusions

Conceptually, the spectrometry seems to be feasible. The FOV causes the main difficulty, both for the amount of pixels as well as the division of the FOV. However, we think that the amount of pixels form the major difficulty in this respect.

12.6 Cryo-Mechanical Concept

12.6.1 Packing of the Whole Instrument

Based on this dimensions, Fig. 116 shows a possibility for packaging the whole instrument in a cryostat of reasonable dimension. We assumed that due to the scaling, the sizes of the various spectrometer channels will be similar, both for the HR as for the MR mode. These boxes are $110 \times 100 \times 60 \text{ cm}^3$, the corner can be cut off from the box, making more efficient packing in a cryostat possible.

For the imager we just estimated a volume of $100 \times 100 \times 50 \text{ cm}^3$, similar to the full pre-optics system. The cryostat dimensions are a cylinder of 270 cm diameter and 135 cm height, which will fit easily in the instrument bay as reserved in the OWL ICD.

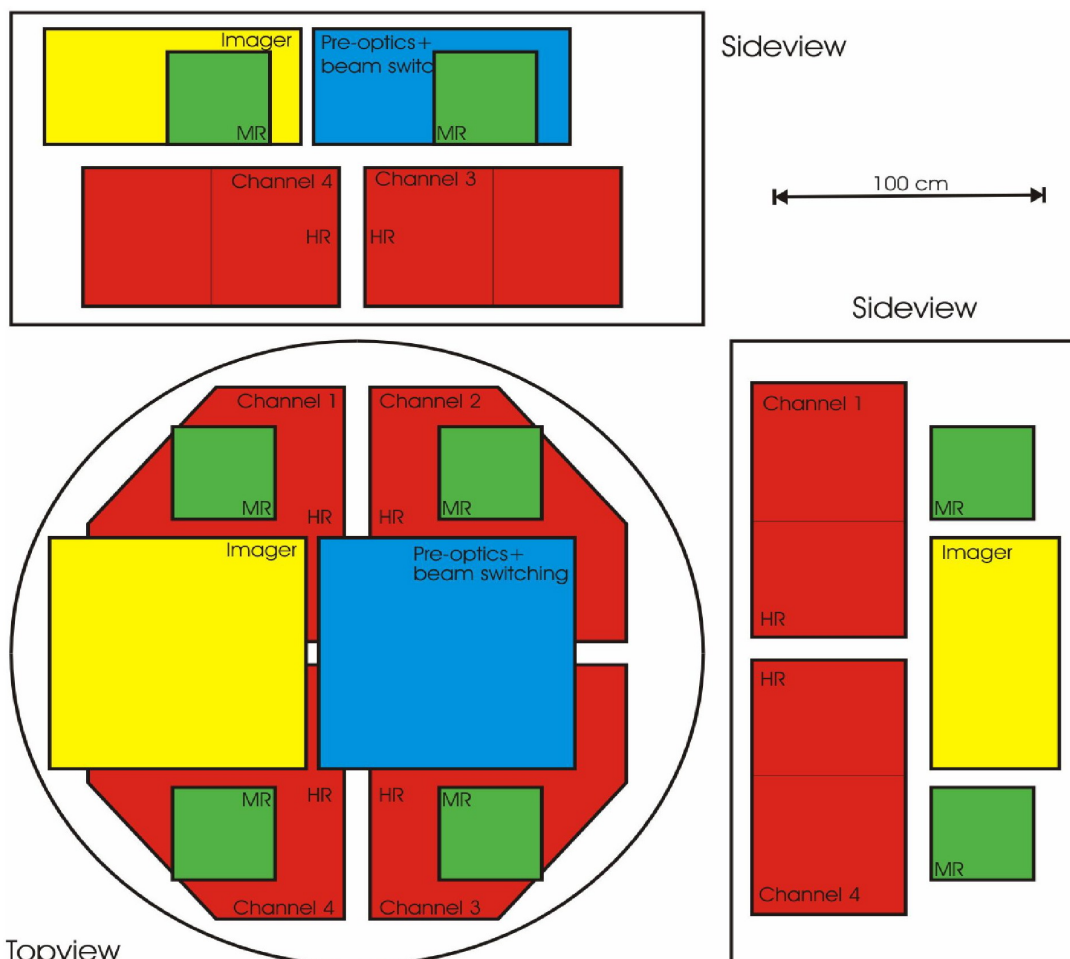


Fig. 116: Packaging the whole T-OWL in one cryostat

12.6.2 Imager Cooling Requirements

Any MIR instrumentation has to be cooled to temperatures below at least 50K, the working temperature of MIR detectors is typically below 5K. To avoid He- continuous flow solutions we propose a Joule-Thomson closed cycle cooler as used for many other astronomical MIR instrumentations (see VISIR e.g.).

To achieve reasonable cooling times of few days, a pre-cooling system of continuous nitrogen will be required. Thus, the focal station should be accessible for maintenance operations, LN2-container available.

For the camera system, the detector at a temperature around 4K is looking into an environment of 15K except for the pupil. This environment encompasses the front end optics, the 15K-radiation shield and the filters. It is surrounded by the 50K environment, containing the collimator optics, the grism wheel, all motor drives and the field limiting mask.

12.6.3 Thermal Consideration for Spectrometer

For observing low level MIR radiation, special cryogenic measures must be taken to keep the background radiation levels sufficiently low. The working temperature of MIR detectors is typically close to or below 5K. Proper shielding of the detector limits the opening angle for the background radiation of the surrounding to enter the detector.

The prime requirement for the cryogenic background, i.e. the inside of the instrument seen by the detector, is that the background flux is small compared to the background from atmosphere and telescope. Although one might guess that the background flux in a cooled cryostat is negligible compared to the flux from the atmosphere and the telescope, this is only true if compared to the same wavelength range and opening angle. In addition, the inside of an instrument behaves as an equilibrated system and has therefore radiates with emissivity=1. Due to the fact that the thermal background of telescope plus atmosphere is most diluted in the HR spectroscopy mode, this observing mode generally is most sensitive to the instrument temperature.

Each detector pixel in the high resolution spectrograph at $R=50000$ (actually, $R=70000$ at 7mm) will only see the sky within a very narrow spectral window and from a narrow opening angle which is matched to the diffraction limit. However, the same detector pixel will also receive photons from a much cooler environment, but from a much larger solid angle (here we assume $\frac{1}{2}$ steradian) and from the entire wavelength range over which the detector is sensitive (here we assume $3 - 27\mu\text{m}$).

The design requirement, that the total background flux per pixel from within the cryostat is small compared to the background from atmosphere and telescope, shows the ratio between internal and external background as a function of wavelength for the most critical regime (fig. 114). For a small ratio (e.g., less than 1%) the temperature of the cryostat has to be less than $T_{\text{cryo}} = 25 \text{ K}$.

The cooling requirements for T-OWL were modelled taking 5K for the detectors, 20K for the cold benches. The temperature of the cold shield was optimized based on the cooling characteristics of the SUMITOMO SRDK-415D cold heads. This resulted in a temperature of 80K for the cold shield. Real numbers for the dissipation of the detectors is presently missing and these values are difficult to estimate. In absence of more elaborate numbers, we tried to make an estimate for the power consumption of the MIRI array, but this dissipation is extremely low, possibly because they just worked with 100 seconds exposure time.

Finally, we decided to stick to 0.1 – 0.3 W per detector, resulting in 1.4 – 4.2W total detector dissipation, requiring two SUMITOMO cold heads (operating only on a 5K stage). In addition three



T-OWL Concept Level Study

Doc : OWL-CSR-ESO-00000-0161



Version 1
Date: 20/10/2005
Page: 159/175

(four) coolers can control the cryostat volume to the required temperatures, resulting in a total of 5 (6) cold-heads.

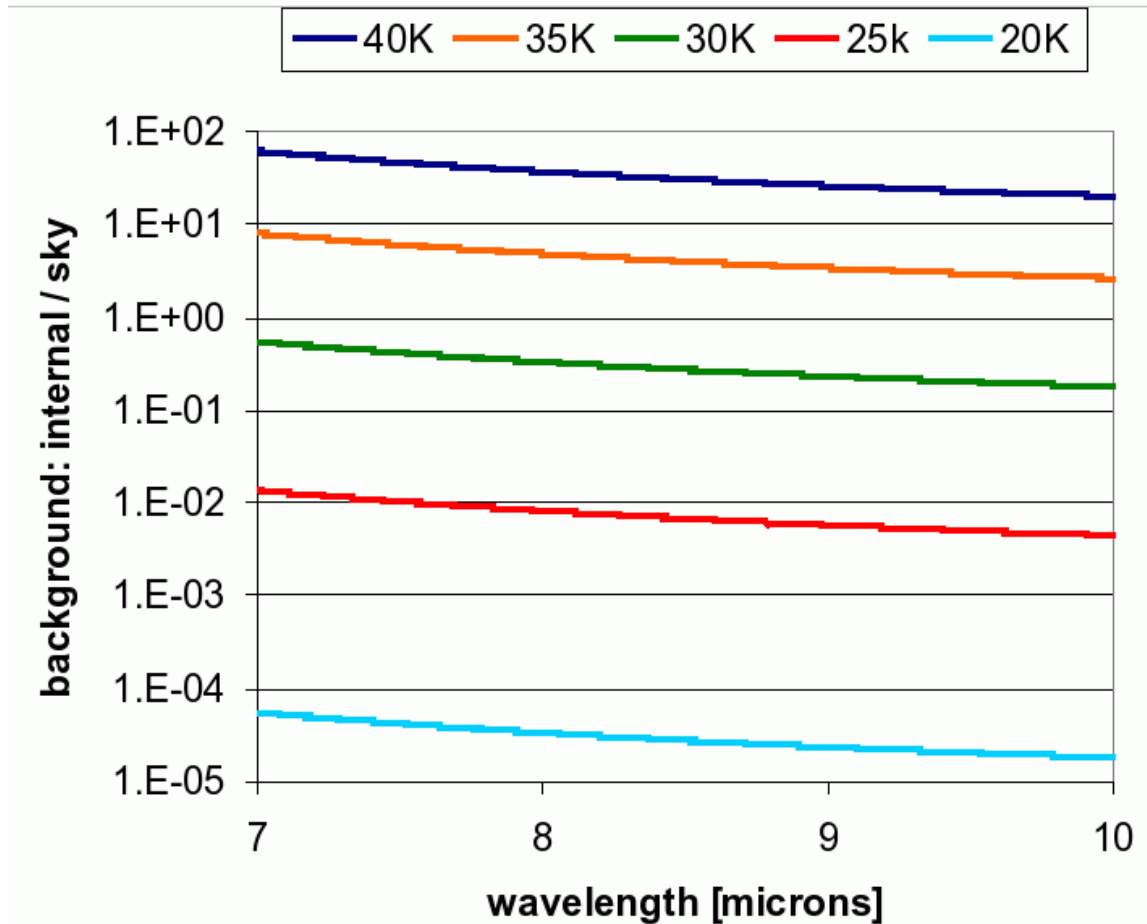


Fig. 117 – Ratio between thermal background from within the cryostat (internal) to the background from atmosphere and telescope (sky) as a function of wavelength for the high resolution spectrograph ($R=70000$ at $7\mu\text{m}$).

12.6.4 Motor Drives

All motor drives should be cryogenic, housed within the 50K environment of T-OWL. This simplifies shielding and opening the cryostat. Reliability of cryogenic drives have reached that of concepts where motor and decoder are mounted externally.

12.6.5 Minimizing Flexure Effects

Flexure effects within the non-common part of the AO-system (for the MIR-instrument this is typically the optical path behind the entrance window of the cryostat) are increasing with mass, dimension and optical magnification of the instrument. Thus, for a diffraction limited MIR-imager flexure problems do not scale with telescope diameter, for T-OWL they are even sever as for NACO e.g.. Nevertheless, we propose a closed loop to compensate slow flexure effects.

13 Data Rates

13.1 Data Rates for the Imager

Maximum data rates for imaging application occur when both channels, the thermal and the MIR channel, are read with highest frequency and are stored individually. For the 3-5.5 μ m 2kx2k detector we assume a maximum frame rate of 100Hz (full frame). The MIR 1kx1k array might have a somewhat higher frame rate, let us assume here a currently optimistic value of 400Hz.

The most adequate frame rate will be individually set as defined by sky background (filter, atmospheric conditions...), field rotation (if not corrected by some field rotator) and atmospheric coherence time.

Assuming in addition a depth of 16bits per pixel, the maximum data rate for the imaging mode is expected to be 13.4 Gbits.

13.2 Data Rates for the Spectrograph

The estimate of the data rates to be expected from the spectrometer are based on the following assumptions:

- Number of detectors 12
- Operation all detectors run in parallel
- Detector size 1024 \times 1024 pixels²
- Readout rate 10 Hz

For spectroscopy, we assume a depth of 32 bits, thus, the data rate is 12 \times 1024² \times 32bits \times 10 frames/s = 4.03 Gbits /s.

This represents an upper limit based on medium resolution spectroscopy. The data rates for high resolution spectroscopy are expected to be an order of magnitude smaller due to slower readout times. It is assumed that all frames get stored; for lower resolution (higher background) where faster frame rates may be necessary, co-addition in a buffer is possible.

14 Calibration: Sketch of Requirements and Solutions

14.1 Introduction

Observations in the MIR are influenced by three main factors which have to be calibrated to improve the signal to noise of the data:

- sky background
- telescope background
- detector variations and non-linearities

To calibrate all the influences different approaches are needed. For some astronomical application there is a further need of a photometric calibration and in the diffraction limited regime a PSF calibration for deconvolution.

14.2 Background Subtraction

The sky can be assumed as blackbody radiator of about 275K, what leads to a peak between 9 and 10 μm . The sky background varies with time. To get a calibration closest to the real condition the calibration frame has to be taken immediately with the science exposure and faster than the background fluctuations. On the other hand we have background through the telescope which varies also over time but much slower. Therefore we propose as calibration scheme chopping and nodding (VISIR User Manual, Michelle User Manual). An image on source and an image off source, only on sky, is taken and subtracted from each other. Doing this fast is called chopping. The size of the chopping distance is given by the size of extended objects and should be equal or larger than 30" for extragalactic objects. Kaeufl et al. (1991) Kaeufl et al have measured the low-frequency power spectrum of the sky in N and Q and found, that there is for N-band 1/f noise up to 8Hz and for Q-band up to $\sim 2\text{Hz}$. Still the observatory experience with 2-4m class telescopes is, that independent of instrument and wavelength chopping, with 1-2Hz is sufficient to avoid excess noise (Kaeufl and Moorwood priv. Comm). Using beamswitching alone a sensitivity reduced by a factor of 2 may follow (see Kaeufl et al., 1998, Allen et al., 1981).

Band	Chopping frequency [Hz]	Source
J	0.2	Allen 1981
H	0.2	Allen 1981
K	0.3	Allen 1981
L	0.3	Allen 1981
M	2	Allen 1981
N	8	Kaeufl 1991

Table 26: Chopping frequency measurements with the AAT in New South Wales (Allen 1981) and at La Silla (Kaeufl 1991). A wavelength dependence is clearly visible.

However, the current OWL design does not provide the possibility of a typical secondary chopping which would require a stroke of 30" at up to 10Hz. Therefore following alternative solutions are proposed:

1. **Internal chopper:** An internal chopper would need a re-imaging of the pupil what complicates the optical design.
2. **Additional of target detectors or self-sky subtraction with blank pixels:** I.e. four small additional detectors at each side of the field should give enough possibility to have off target background measurements (Tarrus 1982). Such technique would need a proper characterisation of the detectors to reduce differential detector noise. The characterisation can be done off sky with a calibration source. Problems with such method, because of noise, are reported by Myata et al. (1999) and there is also a need of a chopping shutter to reject the detector harmonics (Tarrus 1982, Käufel 1991, Käufel 2003).

Depending on the telescope size and the temporal and spatial characteristics of the sky background, chopping might not be necessary at all. The ratio d/D between the atmospheric volume scanned by chopping and the telescope beam does decrease with larger telescope diameter. Where d is the chopping range and D the telescope diameter. Therefore the differential atmospheric volume gets smaller and the chopping frequency can be decreased. While with a 4m telescope and a chopping range of 30" d/D is 0.54 for an 100m it is only 0.0216. Therefore changes through movement of the clouds has less impact. The sky noise between 8 and 13 μm is mainly originated by invisible aerosols/cirrus clouds in an altitude between 1 and 17 km (Käufel 1991). Windspeed between 10 - 16 km are the highest and can go up to 50m/s (Aristidi 2005)

<i>Telescope Diameter [m]</i>	<i>d/D with d for 30''</i>	<i>Frequency@50m/s</i>
4	0.54	12.5
8	0.27	6.25
30	0.072	1.7
50	0.043	1
100	0.021	0.5

Table 27 Dependence of the chopping frequency from the telescope diameter.

If there is a need of chopping at an 100m telescope as to be investigated in more detail in upcoming studies. But it has also to be considered, that new reconstruction methods will handle noisy data much better in future (Lenzen 2005) what might help in the case of self-sky subtraction.

Telescope Background

The optical path of the on and off source image is not the same, what introduces a different telescope background. Such residual is suppressed by nodding. The telescope is moved to the off source position and the same chopping pattern, now inverse, is applied. Before nodding the signals are composed of following:

$$(1) I[\text{star}] + I[\text{Tel1}] + I[\text{sky}]$$

$$(2) I[\text{Tel2}] + I[\text{sky}]$$

subtracting (2) from (1) leads to:

$$(3) I[\text{star}] + I[\text{Tel1}] - I[\text{Tel2}]$$

The signal after nodding are:

$$(4) I[\text{Tel1}] + I[\text{sky}]$$

$$(5) I[\text{star}] + I[\text{Tel2}] + I[\text{sky}]$$

subtracting (4) from (5) leads to:

$$(6) I[\text{star}] + I[\text{Tel2}] - I[\text{Tel1}]$$

adding (3) and (6) ends with $2xI[\text{star}]$ and all telescope background eliminated.

Chopping Requirements	
Chopping distance	$\geq 30''$ (defined by extragalactic objects)
Chopping frequency	≥ 0.5 Hz
Nodding frequency	≥ 30 s

14.3 Flat Fielding

The remaining pixel to pixel variations of the detector are reduced with a flat field division. The flat field can be created either with an artificial calibration source (VISIR User Manual) or with sky flat fields. Sky flat fields have the advantage to be closer to conditions of the observation. However, as especially in N band the sky flux is quite high it is difficult to achieve the accuracy needed (Myata 1999). With the artificial calibration source several flat fields at different temperatures should be created as the detector efficiency varies with wavelength.

Calibration Requirements	
Sky flat fields from chopping data for each band observed.	
Flat field with artificial source from -40°C to $+10^{\circ}\text{C}$ in 10°C steps	

A very promising method using crossed cryogenic polarisers has been proposed by Kaefl et al. (2003). Using constant integration time, the input flux can be modulated by crossing two wire grid analysers to obtain a flux versus signal curve for any individual pixel and integration time. Such a device has to be included into the collimated beam near the pupil image.

14.4 Photometric Calibration

The MIR extinction varies largely with zenith distance and over time. Therefore flux calibration is recommended to be done short in time and close in distance to each science exposure. Standard stars are used, i.e. from the VLT standard star catalogue (VISIR User Manual).

14.5 PSF Calibration

PSF calibration can be done with the standard stars. However if this is sufficient for all purposes has to be studied in more detail.

14.6 Spectroscopic Calibration

The same general principles as discussed above for the imager apply also to the calibration of the spectrograph. There is likely to be a lot of commonality and the calibration unit shall be developed jointly for both imager and spectrograph channels. However, the following sections focus mainly on the specific requirements for the medium and high resolution spectrograph.

14.6.1 Wavelength Calibration

Since all medium and high resolution modes work with fixed grating angle settings the precise monitoring of the wavelength zero points during exposures is not necessary. In other words, no active grating scanner control is required. The atmosphere itself provides numerous narrow lines (at all wavelength bands) that are adequate to verify that there is no change in wavelength during the observation.

The absolute wavelength calibration will be done with gas absorption cells, which can be included in the warm spectrometer pre-optics. (They cannot be inside the cryostat since most gases would freeze out). To cover the wavelength range from 3 to 20 micron 2-3 cells will be required. Gas cells have typical line widths that are narrower than the strongest sky lines, providing a more accurate calibration. In addition they would be available early on for initial calibrations before commissioning or during the day time. Gas cell spectra can only be made with a light source that has a radiation temperature different from ambient; however, such sources are needed for other calibrations anyway (see below).

14.6.2 PSF Calibration

After commissioning of the instrument, PSF calibrations will use stars without infrared excess. However, an internal point source would be extremely useful, especially during lab tests.

The internal point source should have a tunable, stabilized temperature high enough to be observed on the Rayleigh-Jeans part. The location of the point source within the IFU field of view shall be adjustable in both x and y to characterize the PSF quality for all field positions.

A monochromator would be desirable to measure the transmission profiles of dichroics and filters, and to monitor their long-term behaviour. Provided that the point-source mounted at a point of minimum flexure, it can also be used to measure and track internal instrument flexure.

14.6.3 Flux Calibration and Flat-Fielding

Given the relatively small field of view of a few arcseconds only, the relative flux calibration can best be done with an extended, flat source. The calibration unit should contain a uniformly illuminating black-body source with adjustable temperature. The combination of spatially flat sources with well characterized, point-like spectral calibrators in the calibration unit is most important, since no extended, spatially and spectrally flat sources exists on the sky to derive the relative spectral response function (RSRF) to within 10% accuracy.

The absolute flux calibration can be best done on the sky.

Several people involved in this study are also members of the JWST/MIRI spectral calibration team. These efforts include both ground and in-orbit calibration of the medium resolution IFU spectrograph. There will be a lot of overlap between the calibration of MIRI and T-OWL, and the expertise gathered by the Astron/U.Leiden team with ISO-SWS, Spitzer, VISIR, and soon MIRI, will be applied to the T-OWL spectrograph.

15 Conclusions

15.1 Consistency with OWL Interface Document

Table 28: List of consistencies with OWL interface document

<i>ICD Item</i>	<i>Consistency</i>	<i>Comment</i>
D = 100m	Y	
D = 33m	Y	Central obscuration cold baffle
F-ratio 6	Y	Re-imaging needed anyway, useful coronographic scale
Focal plane curvature	Y	Small field, no problem
6-mirror solution	(Y)	Carefully designed MIR are limited by emission from mirrors, thus, number of mirrors should be minimized for MIR application
Alt-az design	Y	Field- pupil rotation can be compensated for
3048 segments M1	(Y)	Gaps should be minimized
Full open-air operation	N	Dust protection critical
Desertic -10-+20C	Y	Cold temperatures preferred
Focal station volume	Y	Imager no problem, spectrograph ?
Allowed instrument weight	Y	Imager no problem, spectrograph ?
No gravitational stability	Y	Imager no problem, Spectrograph needs TT-correction
Mirror coating	Y	Thermal emission is critical, 98% is acceptable, but dust is a problem.
Position of entrance pupil image	Y	
Field size	Y	MIR fields are much smaller
AO-concept	Y	MCAO not required,
Atmospheric sight conditions	Y	Less critical for MIR
Crane handling conditions	Y	
Maximum power	Y	Dominated by cooling power
Maximum data rate	Y	Small arrays, but high frequent RO



T-OWL Concept Level Study

Doc : OWL-CSR-ESO-00000-0161



Version 1
Date: 20/10/2005
Page: 167/175

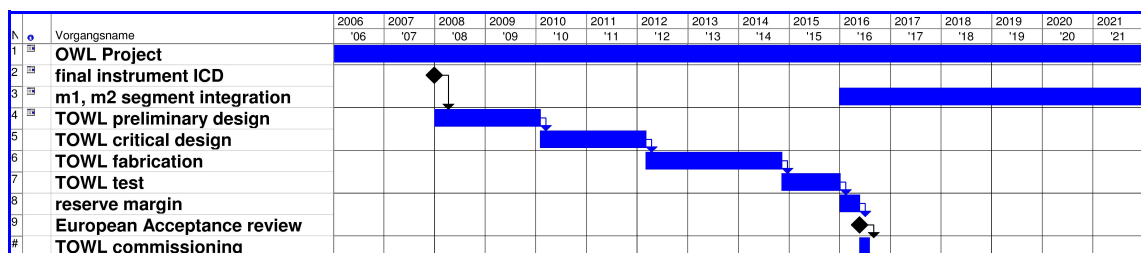
15.2 Main Design Conclusions

1. A TIR/MIR instrument for an ELT like OWL should concentrate on diffraction limited application
2. The site for an ELT using MIR instrumentation should be optimized regarding transmission and thermal background, that means minimum water column (high and dry), low medium temperature, low dust content.
3. A compact direct imaging instrument including low resolution spectroscopic capabilities is within the volume and weight limits of OWL by a large margin.
4. A powerful TIR/MIR mid- and high resolution spectroscopic capability is strongly recommended to satisfy the observational needs. First volume and weight estimates based on a preliminary overall design are consistent with the ICD limits.
5. Instrumental rotation is not required as long as a maximum FOV of 7 arcsec x 7arcsec is considered.

15.3 Schedule

Keeping in mind that T-OWL is an ideal first generation instrument due to its simplicity (at least concerning the imager), due to the reduced AO requirements of OWL and due to the fact that OWL can be used with and incomplete M1, any schedule should base on the 10 year interval given within the ICD for the time between start of OWL design to first M1 segments being integrated. Thus, we assume about 12 years from starting the telescope design to first light of the MIR instrument.

In consequence, T-OWL should be started not much later than 2 years after starting the whole telescope project.



This Schedule is representing the development of a TIR/MIR imager. If the development of the complex mid- and high resolution spectrograph can fit to this schedule, has to be checked in more detail.

15.4 Weight of MIR Imaging Instrument

Table 29: Estimated mass of T-OWL

Item	Weight[kg]	Comments
Optical benches	1270	Optical benches: The (cold) mass for the optical benches is reconstructed from the scaling of the VISIR instrument. Applying standard lightweighting techniques on the all Al-design of the cold bench and components, it turns out that the filling factor of complex instruments is close to 15%. So estimating the volume of the instruments, multiplied by the density of aluminium (2.6) and multiplied by 0.15 yields a mass estimate for the cold benches. (4 HR spectrometer channels times 0.5 m ³ , 4 MR channels times 0.06 m ³ + imager 0.5 m ³ + pre-optics 0.5 m ³ = 3.25 m ³ . Re-enforced polymers will reduce the mass considerable
Cryostat	2500	For the cryostat we scaled the mass of known cryostats. It turns out that volume and mass scale reasonable, were some gain can be achieved by reinforcements at the larger structures. For T-OWL, this results in approximately 2700 kg without additional light weighting, so probably 2500 kg is possible.
CCC	1500	For the cryo-coolers we took as baseline Sumitomo SRDK-415D cold-heads. Standard technique applies one compressor per cooler and without additional development, these compressors need to stay reasonably close to the cold-heads. Here, development is certainly needed, to optimize here. Present assumption 6 coolers and 18+225kg per cooling system.
Control electronic	325	Control electronics: Very rough estimate: 30 mechanisms, some warm (for calibration 5) most cold (25: pre-optics 5, imager 5 and spectrometer 15). So need probably 4 to 5 cabinets a 65 kg per cabinet. With present ESO standard this will be very heavy. But this can't be the standard in 2015 anymore
RO-electronics	100	No real idea, presently we assume 14 detectors, excluding AO detector. Mass of RO electronics?
Vacuum technique	100	
Total weight	5775	Well below ICD limit

15.5 Budget for MIR Imager and Spectrograph

The following table provides a best guess estimate of the total budget for the entire T-OWL project, including hardware and manpower. Please note:

- This is only a zero order approximation. The estimate is on the conservative side; actual costs should be accurate to within less than $\pm 50\%$.
- The estimate are based on a comparison with numerous other existing or presently being developed instruments. We used various approaches to a top-level estimate: like the complexity in relation to other instruments, the estimated project time and the size of the team that would work on it, the relative cost factors between hardware and manpower, etc. The estimates derived in the various ways were reasonably consistent with each other.
- The budget includes 20% contingency but no corrections for inflation.

It is beyond the scope of this study to provide an accurate cost breakdown for stand-alone modules of T-OWL (e.g., for imager, medium-resolution spectrograph, and high resolution spectrograph). However, one can get a good idea about the cost split between imager and spectrograph from the table 30. For the individual spectrograph components this breakdown is less obvious; the majority of spectrometer components are common to both medium- and high resolution spectrograph, such as pre-optics, detector arrays, cryostat, etc. Dropping for instance just the high-resolution mode would result in savings of approximately 3 MEuros in hardware, and about 30 man-yr. T-OWL without the high-resolution mode would result is a cost reduction by about 15% (while a substantial fraction of the most innovative and competitive T-OWL science will be lost).



T-OWL Concept Level Study

Doc : OWL-CSR-ESO-00000-0161



Version 1
Date: 20/10/2005
Page: 170/175

Table 30: Hard-ware cost break down for T-OWL

ITEM	No. of items	Cost/item (kEur)	COST (kEur)	TOTAL (kEur)
COMMON HARDWARE				
Calibration unit			150	
Pre-optics			50	
TADC (if required)			50	
Pre-optics mechanisms	3	50	150	
Pre-optics structure			30	
Cryostat			400	
Cryostat window			50	
Instrument cold bench suspension system			50	
Vacuum equipm.			200	
Heat shield			50	
Cryo-cooler systems	6	60	360	
Temperature control, sensors, heaters			100	
Thermal links			75	
Cabling, connectors			100	
Readout electronics			350	
Control electronics			150	
Handling equipment			100	
Spare parts (10% of total HW)			242	
				2657
IMAGER				
Collimator optics	1	100	100	
Camera optics	1	150	150	
Filters	20	15	300	
Grisms	3	30	90	
Cryomechanism	1	75	75	
Cryomechanics			150	
Harness, cabling, connectors			100	
Models, prototypes			50	
Auxiliary tools, handling equipm., test equipm.			150	
Spare parts (10% of total HW excl. detectors)			117	
Detector arrays	2	500	1000	
Detector test grade	1	200	200	
				2482
SPECTROMETER				
Dichroic beamsplitters	19	15	285	
IFU's	4	100	400	
Collimators	8	100	800	
Cameras	8	150	1200	
Gratings MR	4	50	200	
Gratings HR	4	150	600	
Beam expanders	3	40	120	
Cross dispersers	3	50	150	
Dichroics wheel mechanisms	2	75	150	
Grating tilt mechanisms	8	75	600	
Mode switch mechanisms	2	75	150	
Cryomechanics			300	
Harness, cabling, connectors			250	
Models, prototypes			150	
Auxiliary tools, handling equipm., test equipm.			300	
Spare parts (10% of total HW excl. detectors)			566	
Detector arrays	12	500	6000	
Detectors test grade	2	200	400	
				12621
TOTAL HARDWARE				17759
MANPOWER				
			No. of myrs	
Optical design	Common HW		2	
	Imager		6	
	Spectrometer		12	
				20
Mechanical design	Common HW		6	
	Imager		8	
	Spectrometer		24	
				38
Thermal design	Common HW		12	
	Imager		6	
	Spectrometer		12	
				30
Electronics design	Common HW		20	
	Imager		4	
	Spectrometer		8	
				32
AIT + instrument characterisation	Common HW		8	
	Imager		6	
	Spectrometer		18	
	Integrated instrum.		18	
				50
Instrument control software	Common HW		6	
	Imager		3	
	Spectrometer		6	
				15
Data flow/storage + on-line analysis software				12
Off-line data-analysis software				20
Project management				12
Systems engineering				12
Administrative support				8
TOTAL MANPOWER				249
(@ 150 kEur/myr)				(myr)
				37350
				(kEur)
TRAVEL				
TRANSPORT+INSURANCE				
				400
				100
OVERALL PROJECT COST				
				55609



T-OWL Concept Level Study

Doc : OWL-CSR-ESO-00000-0161



Version 1
Date: 20/10/2005
Page: 171/175

16 Important Aspects for More Future Research

1. Atmospheric dispersion beyond $5\mu\text{m}$, dependence on humidity
2. Chopping requirements for MIR observations at ELT: How to realize chopping on a 100m-telescope, sky-flat stability dependence on telescope diameter
3. A Q-band detector with a pixel pitch of $25\mu\text{m}$ makes the optical design of the camera very complicated. A preferred value for the pixel pitch on the detector is $50\mu\text{m}$ square pixels in a $1\text{k} \times 1\text{k}$ array. IFU design is complicated
4. Feasibility of the dichroic scheme
5. Higher resolution in Q-band requires a study in the feasibility of such a design.
6. ELT/polarimetry at TIR and MIR wavelengths

17 Appendix A: Optical Material Data

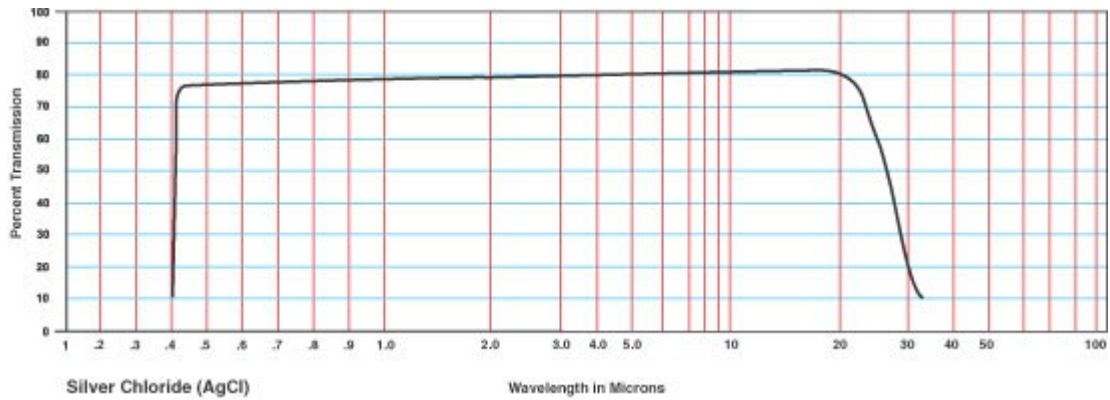


Fig. 118: Transmission of AgCl

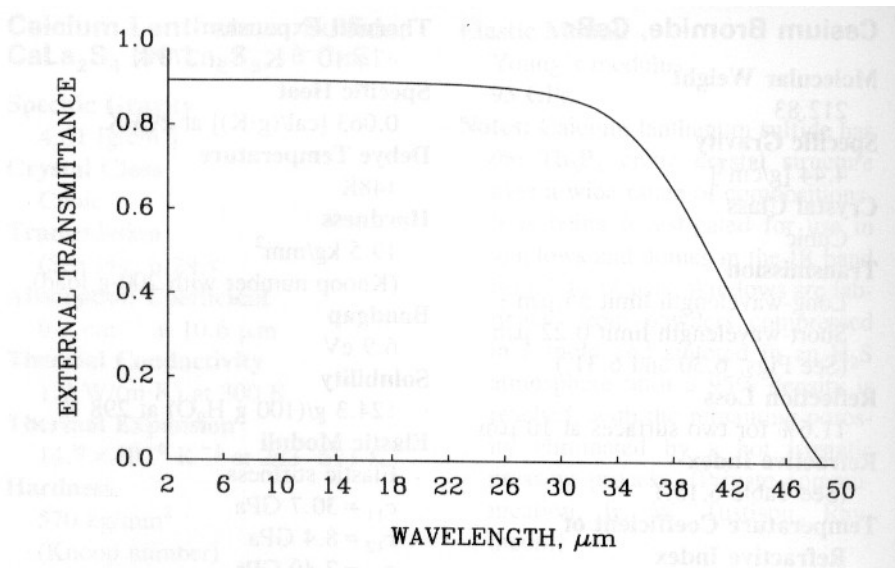


Fig. 119: External transmission of 10mm CsBr

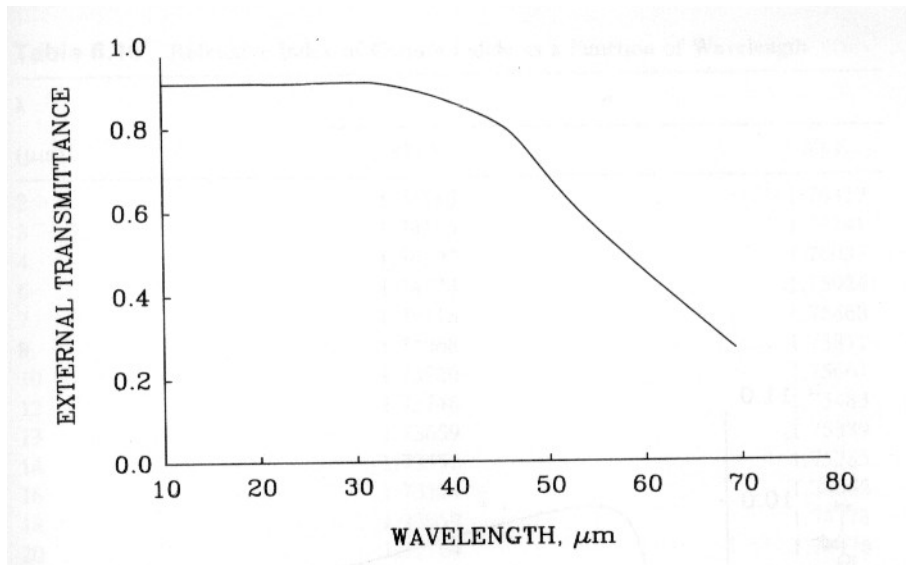


Fig. 120: External transmission of 5mm CsI

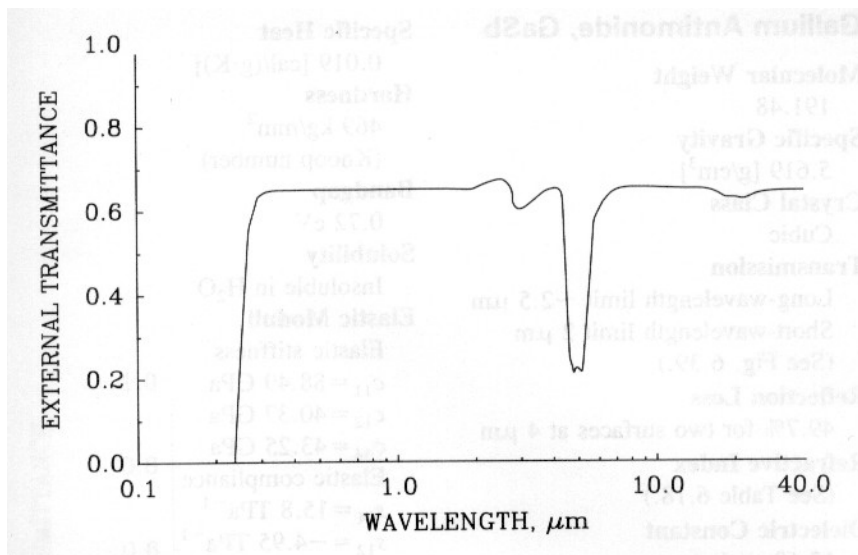


Fig. 121: External transmission of 1mm CVD Diamond



T-OWL Concept Level Study

Doc : OWL-CSR-ESO-00000-0161



Version 1
Date: 20/10/2005
Page: 174/175

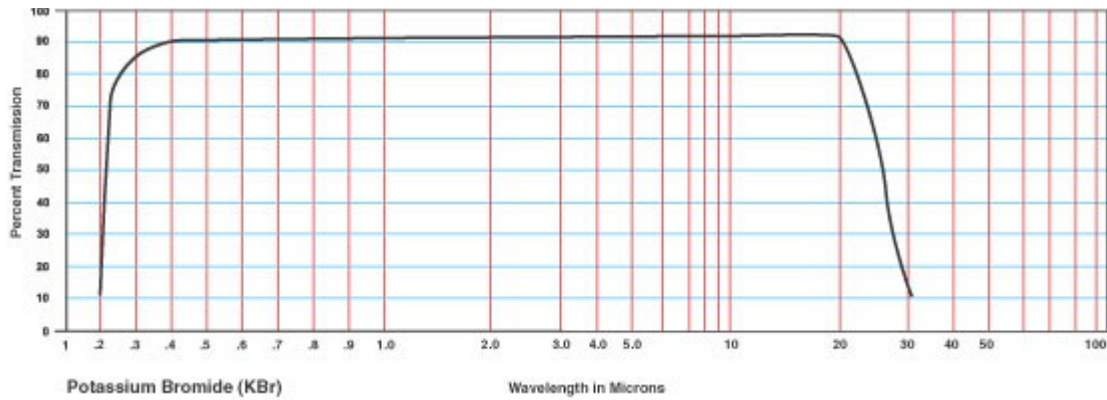


Fig 122: Transmission of KBr

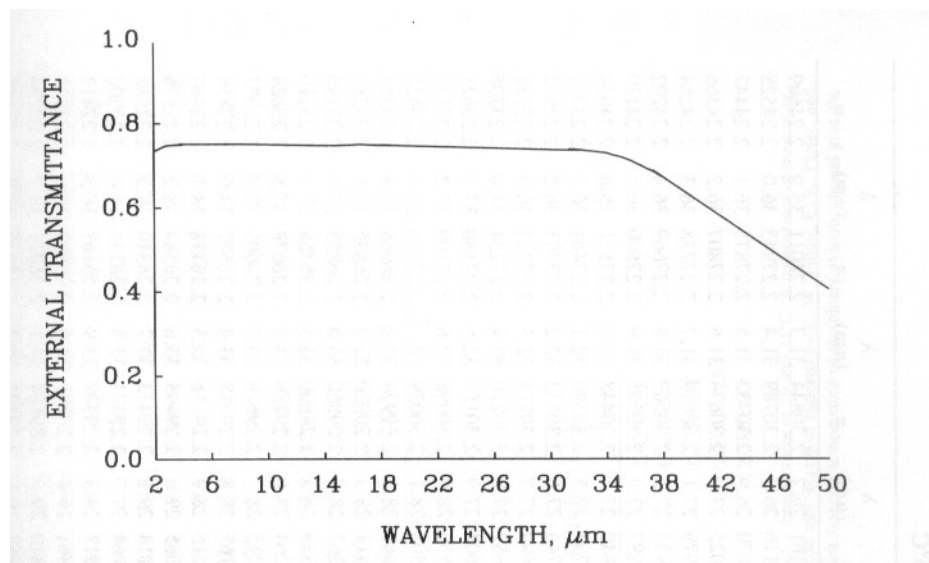


Fig. 123: External transmission of KRS5

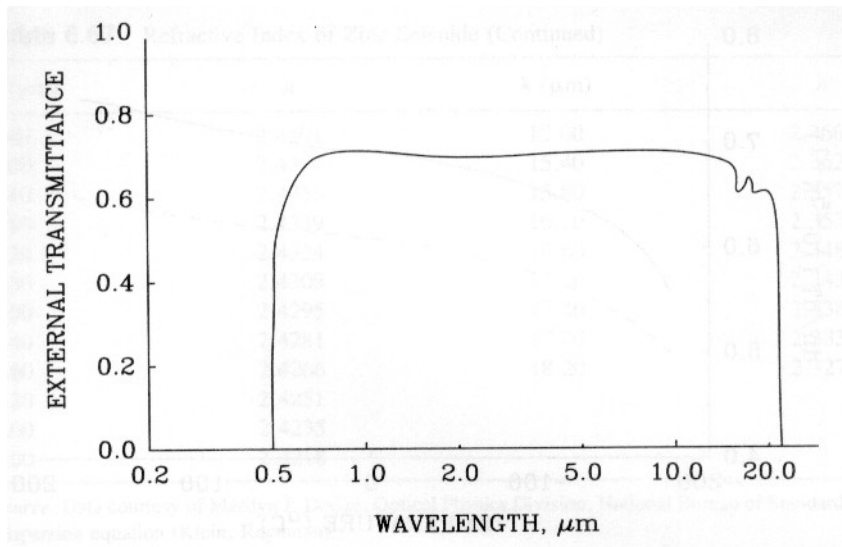


Fig. 124: External transmission of ZnSe.

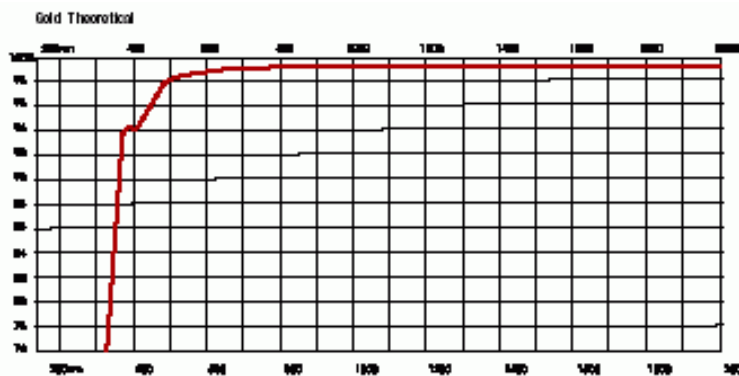


Fig. 125: Reflectivity of JANOS gold coating